ABSTRACT

Title of Dissertation: ESOTAXIS: IDENTIFYING THE FACTORS THAT INFLUENCE NANOTOPOGRAPHIC GUIDANCE OF THE DYNAMICS AND ORGANIZATION OF THE ACTIN CYTOSKELETON AND OTHER MOLECULES INVOLVED IN DIRECTED CELL MIGRATION

Matthew J. Hourwitz, Doctor of Philosophy, 2024

Dissertation directed by: Prof. John T. Fourkas,
Department of Chemistry and Biochemistry

Directed migration is a crucial capability of cells in developmental and immunological processes. Defects in cell migration can lead to negative health outcomes. Cell motion depends on the organization and dynamics of internal components, especially the actin cytoskeleton, and the extracellular environment. Microscale and nanoscale topographical cues, with at least one dimension that is much smaller than most cells, can bias cell motion over long distances, due to the guidance of the organization and dynamics of the cytoskeleton and other molecules and assemblies within the cell.

In this work, I describe a technique to reproduce patterned nanotopographic substrates for use in the study of esotaxis, the guided organization and dynamics of the actin cytoskeleton and other cellular components in response to nanotopographic cues. The guidance of actin drives directed cell motion along a pattern with dimensions much smaller than the cell. The dimensions

of the nanotopography determine the extent to which cellular components are guided. Differences in the physical properties of the plasma membrane and the actin cytoskeleton among cell lines will influence the extent of guidance by nanotopography. Asymmetric patterns can accentuate the distinctions in esotactic responses among cell lines and drive contact guidance in different directions. The cytoskeletal response to nanotopography is a local phenomenon. A cell in contact with multiple nanotopographic cues simultaneously will show distinct organization of actin in the different regions of the cell. The importance of local actin dynamics requires an analysis method, optical flow, that can identify and track the distinct cytoskeletal motions in different parts of the cell. The formation of adhesions attached to the extracellular matrix is a characteristic of the migratory behavior of many types of cells and these adhesions are credited with allowing the cell to sense and interact with the underlying substrate. Actin can sense nanotopographic cues without the widespread availability of adhesive ligands. Although adhesion to the substrate strongly increases the extent of cell spreading and migration on nanoridges, epithelial cells can align with and migrate along nanotopography even with a dearth of adhesive cues. Therefore, actin is a supreme sensor of nanotopography that can drive directed cell migration.

ESOTAXIS: IDENTIFYING THE FACTORS THAT INFLUENCE NANOTOPOGRAPHIC GUIDANCE OF THE DYNAMICS AND ORGANIZATION OF THE ACTIN CYTOSKELETON AND OTHER MOLECULES INVOLVED IN DIRECTED CELL MIGRATION

by

Matthew Jordan Hourwitz

Dissertation submitted to the Faculty of the Graduate School of the
University of Maryland, College Park, in partial fulfillment
of the requirements for the degree of
Doctor of Philosophy
2024

Advisory Committee:
Professor John T. Fourkas, Chair
Professor Wolfgang Losert, Co-Chair
Professor Kan Cao, Dean's Representative
Professor Amy Mullin
Professor Peter Nemes

Acknowledgements

I would like to thank Prof. John Fourkas for the opportunity to work in his lab and for all his support over the years. Thank you for the chance to explore the many fields to which your research can be applied. Thanks to Prof. Wolfgang Losert for his support as well. I never would have imagined working with cells before I was offered a chance to join this project.

Having worked in three different labs during my time in graduate school, I met many smart, kind, and supportive people. I cannot name them all. However, I would like to thank all present and former members of the Fourkas and Losert Labs, as well as all past members of the Nie Lab at the University of Maryland-College Park. Specifically, I would like to acknowledge the following people for teaching or training me: Dr. Sijia Qin for showing me all the steps involved in performing multiphoton absorption polymerization, including sample preparation, beam-path alignment, and the application to microring resonators; Dr. Alison Phillips for also training me on how to perform multiphoton absorption polymerization, as well as soft lithography, and alignment of the laser cavity; Dr. Xiaoyu Sun for showing me the steps involved in nanoimprint lithography; Dr. Sebastian Schmidt for training me on cell culture; and Dr. Rachel Lee for also showing me cell culture techniques and for help with using the spinning disk microscope.

Several members of the Losert Lab were indispensable to my research. Thank you to Dr. Abby Bull for performing the optical flow analysis of actin. I would also like to express my

gratitude to Corey Herr for all his hard work on shape detection and cell tracking, and for helping process the optical flow results.

For mentoring me and showing me the proper approach to performing research and working in a lab, and for his friendship, I would like to thank Prof. Jie He.

I would also like to thank Dr. Amy Beaven for training and support on, as well as maintenance of, the heavily used spinning disk microscope.

I am most grateful to my dissertation committee for their attention, patience, and time. Thank you, again, to Profs. John T. Fourkas and Wolfgang Losert, my advisors. To my other committee members, Prof. Kan Cao, Prof. Amy Mullin, and Prof. Peter Nemes: I am also appreciative of any further insights into my research that your perspectives provide. Thank you for the kind words and encouragement. They truly mean a great deal to me.

Finally, but most importantly, I would like to thank my family. To my parents: thank you for all your support and for always believing in me. I can always rely on you for a good laugh. To my sister: thank you for your kindness and generosity. To my uncle: thank you for taking an interest in my research, and for your humor and generosity.

To anyone I failed to mention so far: I appreciate any lessons or science you taught me and/or any laughs or kind words that you provided me. Please forgive a momentary absence of mind.

Table of Contents

Acknowledgements ii
Table of Contents iv
List of Tables viii
List of Figures ix
List of Abbreviations xi
List of Publications xv
Chapter 1: Introduction 1
1.1. Cell Migration 2
1.1.1. Physiological Relevance 2
1.1.2. Single and Collective Cell Migration 3
1.1.3. Modes of Migration 4
1.1.4. Mechanical Forces 5
1.1.5. Extracellular Cues 7
1.2. Actin Cytoskeleton and Other Cellular Components Involved in Migration 8
1.2.1. Structure of Actin and Mechanism of Polymerization 9
1.2.2. Actin-Binding Proteins 11
1.2.3. Rho GTPases 15
1.2.4. Myosin 16
1.2.5. Focal Adhesions 18
1.2.6. Stress Fibers 21
1.2.7. Microtubules 23
1.2.8. Forces and the Cytoskeleton 25
1.2.9. Examples of Other Molecules that Can Affect the Cytoskeleton 26
1.2.10. Roles of ABPs and Signaling Molecules in Cell Migration 27
1.3. Extracellular Matrix 28
1.3.1. General Characteristics and Composition 28
1.3.2. Structure 29
1.3.3. Cellular Interaction with the Extracellular Matrix 31
1.3.4. Fibronectin 32
1.3.5. Collagen 33
1.3.6. Collagen IV 35
1.3.7. The Extracellular Matrix and Its Relation to Health and Disease 36
1.4. Development of Nano- and Micro-Scale Patterned Surfaces for Biological and Biomedical Applications 39
1.4.1. Devices/Systems 39
1.4.2. Materials 40
1.4.3. Fabrication Techniques 41
1.4.4. Photolithography 45

1.4.5. Multiphoton Lithography 46
1.4.6. Soft Lithography 53
1.5. Thesis Outline 55
Chapter 2: Replication of Biocompatible, Nanotopographic Surfaces 58
2.1. Introduction 58
2.2. Results 60
2.3. Discussion 71
2.4. Conclusions 75
2.5. Materials and Methods 76
2.5.1. Fabrication of Master Nanotopographic Surfaces. 76
2.5.2. Solvent-Assisted Nanotransfer Molding. 77
2.5.3. Uniform Coating of Proteins. 78
2.5.4. Surface Characterization. 78
2.5.5. Cell Culture, Fixing, and Staining. 79
2.5.6. Evaluation of Cytotoxicity. 80
2.5.7. Image Analysis. 80
2.6. Acknowledgments 81
Chapter 3: Actin Cytoskeleton and Focal Adhesions Regulate the Biased Migration of Breast Cancer Cells on Nanoscale Asymmetric Sawteeth 82
3.1. Introduction 82
3.2. Results and Discussion 85
3.2.1. Nanoridges Provide Bidirectional Guidance for Both Benign and Metastatic Breast Cancer Cells 85
3.2.2. Asymmetric Sawteeth Bias the Movement of Breast Cancer Cells in a Cell-Type-Dependent Manner 88
3.2.3. Degree of Bias in Cell Migration Is Related to Cell Speed and Long-Term Persistence 94
3.2.4. Unidirectional Actin Polymerization Drives Biased Cell Migration 99
3.2.5. Distinct FA Patterns and Cortical Plasticity Promote Biased Cell Migration 105
3.3. Conclusions 113
3.4. Materials and Methods 113
3.4.1. Surface Fabrication and Replication 113
3.4.2. Cell Culture 115
3.4.3. Individual Cell Migration and Time-Lapse Imaging 116
3.4.4. Live-Cell Actin Fluorescent Imaging 116
3.4.5. Immunostaining 116
3.4.6. Quantitative Analysis of Cell Migration 117
3.4.7. Averaged Actin Kymograph Analysis 118
3.4.8. Scanning Electron Microscopy Imaging 120
3.4.9. The Principle of the Optical-Flow Algorithm 120

3.5. Acknowledgments 121
Chapter 4: Quantifying Topography-Guided Actin Dynamics across Scales Using Optical Flow 122
4.1. Introduction 122
4.2. Results 124
4.3. Discussion 138
4.4. Materials and Methods 145
4.4.1. Cell Culture and Imaging 145
4.4.2. Surface Fabrication 146
4.4.3. Kymographs 148
4.4.4. Optical Flow 148
4.4.5. von Mises Model of Flow Distribution 151
4.4.6. Cluster-Tracking Analysis 151
4.4.7. Statistical Methods 153
4.4.8. Data and Software Availability 153
4.5. Acknowledgments 153
Chapter 5: Guided Actin Dynamics Regulate Directed Cell Motion along Nanoridges Regardless of the Availability of Collagen IV 154
5.1. Introduction 154
5.2. Results 161
5.2.1. Collagen IV Facilitates Cell Spreading on Nanoridges 161
5.2.2. Availability of Collagen IV Is Not a Strong Determinant of Cell Alignment with Nanoridges 164
5.2.3. Cell Migration Is Guided Well by Nanoridges Regardless of Collagen Density 164
5.2.4. Surface Density of Collagen IV Has Limited Influence on Esotaxis 168
5.2.5. The Cell-Trajectory Phenotype Is Not Linked to the Actin-Flow Direction 173
5.3. Discussion 175
5.4. Methods 183
5.4.1. MAP 183
5.4.2. Functionalization and Molding of the MAP-Fabricated Pattern 183
5.4.3. Replication via Nanoimprint Lithography 184
5.4.4. Coating Nanoridge Substrates with Collagen IV 185
5.4.5. Cell Culture 185
5.4.6. Imaging 186
5.4.7. Analysis 186
5.5. Acknowledgements 187
Chapter 6: Conclusion: A Perspective on Esotaxis 188
6.1. Introduction 188
6.2. Fabrication of Nanotopographic Substrates 191
6.3. Nanotopography-Based Directed Cell Migration, Microthigmotaxis 193

6.4. Esotaxis Is Ubiquitous 195
6.5. Quantification of Contact Guidance and Esotaxis 196
6.6. Guidance of Cytoskeletal Dynamics and Wave-Like Motion 203
6.7. Response of Other Cellular Molecules to Nanotopography 204
6.8. Immune cells 206
6.9. Different Topographical Cues 223
6.9.1. Sawteeth 223
6.9.2. Wavy Ridges 228
6.9.3. EMPs 231
6.10. Dimensions Matter 231
6.11. Esotactic Response Varies by Cell Type 241
6.12. Modulation of Other Cues with Nanotopography 249
6.12.1. Surface Chemistry 249
6.12.2. Electric Fields/Electrotaxis 252
6.13. Summary and Outlook 256
Bibliography 263

List of Tables

Table 2.1. MCF10A cell viability averaged over three experiments on nanoridge surfaces replicated with various photoinitiators …… 70
Table 3.1. Fitting parameters for persistence time *versus* instantaneous speed plots …. 98

List of Figures

Figure 2.1. Schematic of the replication processes for nanoridges and nanogrooves …. 62
Figure 2.2. Characterization of the fidelity of the solvent-assisted nanotransfer molding ……..…. 63
Figure 2.3 AFMs of 1-μm-spaced master and replica ridges, and 1.5-μm-spaced replica ridges and grooves ……... 64
Figure 2.4. Replication of nanograss ……... 66
Figure 2.5. Functionalization of nanoridges with collagen IV …… 66
Figure 2.6. Functionalization of nanoridges with fluorescently labeled fibronectin …... 67
Figure 2.7. Cytoskeletal alignment and focal adhesion distribution on nanoridges and nanogrooves ……. 68
Figure 2.8. Percentages of live cells 48 h after plating on nanoridges replicated with various photoinitiators ……. 71
Figure 3.1. Nanotopographies used in this study …… 87
Figure 3.2. Nanoridges provide bidirectional guidance for benign and metastatic breast cancer cells ……. 88-89
Figure 3.3. Asymmetric sawteeth bias the movement of various breast-cancer cell lines …….. 91
Figure 3.4. Level of biased cell motion increases with cell speed and long-term persistence …….. 96-97
Figure 3.5. Persistence time *versus* mean instantaneous speed plots for MDA-MB-231, HS578T, M1, BT549 and M4 cells ……. 98
Figure 3.6. Sawteeth trigger unidirectional actin polymerization in the same direction as the cell motion in a cell-type-dependent manner …… 100-101
Figure 3.7. Influence of sawteeth on microtubules in MDA-MB-231 cells and M4 cells ……. 104
Figure 3.8. MDA-MB-231 and M4 cells exhibit distinct cortical plasticity and focal adhesion patterns …… 108-109
Figure 3.9. Cortical plasticity of M1 cells on sawteeth ……. 110
Figure 4.1. Surface topography prompts distinct actin morphology ……. 126
Figure 4.2. Surface topography leads to distinct actin morphodynamics ……... 126-127
Figure 4.3. Optical-flow calculations capture the dynamics in movies of actin fluorescence ……... 130-131
Figure 4.4. Using optical flow to measure pixel-scale guidance ……... 133-134
Figure 4.5. Clustering of optical-flow vectors to measure micron-scale dynamics ……. 135-136

Figure 4.6. Actin-wave speeds ……... 139
Figure 4.7. Cluster-finding workflow …… 142
Figure 5.1. Collagen promotes cell spreading and nanoridges cause cells to elongate along the ridge axis ……. 162-163
Figure 5.2. Cell migration on nanoridges is modulated by the surface density of collagen IV ……... 166
Figure 5.3. Nanotopography can guide actin polymerization even in the absence of added ECM coating, although collagen IV coating can limit actin-polymerization oscillations perpendicular to the ridge axis ……... 171
Figure 5.4. Actin distribution at the ventral surface of MCF10A cells migrating on nanoridges …….. 172
Figure 5.5. Cells with different trajectory phenotypes have similar actin OF distributions ……. 174
Figure 5.6. Various morphologies during epithelial cell migration on nanoridges ….. 178

List of Abbreviations

ABP	Actin-binding protein
ADF	Actin-depolymerizing factor
ADF-H	Actin-depolymerizing factor homology
ADP	Adenosine diphosphate
AFM	Atomic force microscopy
Akt	Protein kinase B (also known as PKB)
APC	Antigen-presenting cell
Arp2/3	Actin-related protein 2/3
ARPC#	Actin-related protein 2/3 complex subunit followed by number
ATP	Adenosine triphosphate
BCR	B-cell receptor
BM	Basement membrane
BSA	Bovine serum albumin
CAP	Cyclase-associated protein
CD	Cluster of differentiation
CD4	$CD4^+$ T helper cell
CD8	$CD8^+$ cytotoxic T cells
Cdc42	Cell division control protein 42
CMSC	Cortical microtubule stabilization complex
CP	Capping protein
CV	Coefficient of variation
CVD	Chemical vapor deposition
DAPI	4’,6-diamidino-2-phenylindole
DC	Dendritic cell
DMD	Digital micromirror device
DNA	Deoxyribonucleic acid
ECM	Extracellular matrix
EF	Electric field
EGF	Epidermal growth factor
eGFP	Enhanced green fluorescent protein
EMP	Elongate mineral particle
EMT	Epithelial-to-mesenchymal transition
FA	Focal adhesion
$F(ab')_2$	Divalent fragment antigen-binding region
F-actin	Filamentous actin

FAK	Focal adhesion kinase
fMLF	N-formylmethionine-leucyl-phenylalanine
FsLDW	Femtosecond laser direct writing
GAG	Glycosaminoglycan
GDP	Guanosine diphosphate
GEF	Guanine nucleotide exchange factor
Gly	Glycine
GTP	Guanosine triphosphate
HBSS	Hank's balanced salt solution
hMSC	Human mesenchymal stem cell
h-PDMS	Hard-polydimethylsiloxane
HSC	Hematopoietic stem cell
Hyp	Hydroxyproline
Ig	Immunoglobulin
IgM+G	Immunoglobulin M+G
ITAM	Immunoreceptor tyrosine-based activation motif
Kank	Kidney ankyrin-repeat domain-containing protein
LPA	Lysophosphatidic acid
M1	Nontumorigenic epithelial cell line in a breast cancer progression model (most often referred to as MCF10A)
M4	Highly malignant, metastatic cell line in a breast cancer progression model originating from the M1 cell line following HRAS transformation and xenografting of the derived cell line (most often referred to as MCF10CA1)
MA-μTM	Membrane-assisted microtransfer molding
MAP	Multiphoton absorption polymerization
MCF10A	Spontaneously immortalized nontumorigenic human breast epithelial cell line established at the Michigan Cancer Foundation from an adult female patient with benign fibrocystic disease that grow as attached (A) cells (referred to as M1 within the progression model)
MCF10CA1	Highly malignant, metastatic cell line in a breast cancer progression model originating from the MCF10A cell line (established at the Michigan Cancer Foundation) established from a carcinoma (CA) formed from a xenograft of the HRAS-transformed derivative cell line (referred to as M4 within the progression model)
MHC	Major histocompatibility complex
MLCK	Myosin light-chain kinase
MMP	Matrix metalloproteinase

MNA	Mean-normalized autocovariance
MPA	Multiphoton absorption
MSD	Mean squared displacement
MT	Microtubule
MTOC	Microtubule-organizing center
μCP	Microcontact printing
NA	Numerical aperture
NBC	Nucleotide-binding cleft
NC	Neural crest
NET	Neutrophil extracellular trap
N-WASP	Neuronal Wiskott-Aldrich syndrome protein
OF	Optical flow
Pak1	p21-activated kinase 1 (activated by specific proteins (P) with molecular masses of approximately 21 kDa)
PBS	Phosphate-buffered saline
PDMS	Polydimethylsiloxane
PH	Pleckstrin homology
PKB	Protein kinase B (also known as Akt)
PLL	Poly-L-lysine (amino acid enantiomer which can potentially be synthesized from L-glyceraldehyde)
PIP2	Phosphatidylinositol-4,5-bisphosphate
PIP3	Phosphatidylinositol-3,4,5-trisphosphate
PIV	Particle image velocimetry
Pro	Proline
Rac	Rat-sarcoma-virus (Ras)-related C3 botulinum toxin substrate
Ras	From rat sarcoma virus; family of small guanosine triphosphate hydrolases or binding proteins (GTPases)
Rho	Ras homolog; family of small guanosine triphosphate hydrolases (GTPases) within the Ras superfamily
RIE	Reactive ion etching
ROCK	Rho-associated protein kinase
ROS	Reactive oxygen species
SAM	Self-assembled monolayer
SEM	Scanning electron microscopy
SH2	Src-homology 2 (domain resembling the proto-oncogene tyrosine-protein kinase Src; pronounced sarc, which is short for sarcoma)
SLM	Spatial light modulator
TAF	Tumor-associated fibroblast
TAM	Tumor-associated macrophage
TCR	T-cell receptor

TF	Transcription factor
TFM	Traction force microscopy
TGF-β	Transforming growth factor-β
TMBP	Tandem monomer-binding protein
TME	Tumor microenvironment
TPIP	Two-photon-induced or -initiated (photo)polymerization
TPP	Two-photon photopolymerization
TRITC	Tetramethylrhodamine isothiocyanate
UCSP	Universal coupling between cell speed and cell persistence
UV	Ultraviolet
VASP	Vasodilator-stimulated phosphoprotein
WASP	Wiskott-Aldrich syndrome protein
WAVE	WASP-family verprolin-homologous protein
WH2	WASP homology 2
WIP	WASP interacting protein
ZAP-70	Zeta-chain-associated protein kinase-70

List of Publications

Publications are sorted chronologically. Works relevant to this dissertation are underlined and set in a larger font.

Wang, L.; Liu, Y.; He, J.; Hourwitz, M. J.; Yang, Y.; Fourkas, J. T.; Han, X.; Nie, Z. Continuous Microfluidic Self-Assembly of Hybrid Janus-Like Vesicular Motors: Autonomous Propulsion and Controlled Release. *Small* **2015**, *11* (31), 3762-3767.

Sun, X.; Hourwitz, M. J.; Baker, E. M.; Schmidt, B. U. S.; Losert, W.; Fourkas, J. T. Replication of biocompatible, nanotopographic surfaces. *Sci Rep* **2018**, *8* (1), 564.

Chen, S.; Hourwitz, M. J.; Campanello, L.; Fourkas, J. T.; Losert, W.; Parent, C. A. Actin cytoskeleton and focal adhesions regulate the biased migration of breast cancer cells on nanoscale asymmetric sawteeth. *ACS Nano* **2019**, *13* (2), 1454-1468.

Sun, X.; Hourwitz, M. J.; Das, S.; Fourkas, J.; Losert, W. Cell motility and nanolithography. In *Three-Dimensional Microfabrication Using Two-Photon Polymerization*, Second ed.; Baldacchini, T. Ed.; Micro and Nano Technologies, William Andrew Publishing, 2020; pp 527-540.

Lee, R. M.; Campanello, L.; Hourwitz, M. J.; Alvarez, P.; Omidvar, A.; Fourkas, J. T.; Losert, W. Quantifying topography-guided actin dynamics across scales using optical flow. *Mol Biol Cell* **2020**, *31* (16), 1753-1764.

Cao, L.; Li, D.; Pollard, T.; Deng, T.; Zhang, B.; Yang, C.; Chen, L.; Vatamanu, J.; Hu, E.; Hourwitz, M. J.; Ma, L.; Ding, M.; Li, Q.; Hou, S.; Gaskell, K.; Fourkas, J. T.; Yang, X. Q.; Xu, K.; Borodin, O.; Wang, C. Fluorinated interphase enables reversible aqueous zinc battery chemistries. *Nat Nanotechnol* **2021**, *16* (8), 902-910.

Fischer, R. S.; Sun, X.; Baird, M. A.; Hourwitz, M. J.; Seo, B. R.; Pasapera, A. M.; Mehta, S. B.; Losert, W.; Fischbach, C.; Fourkas, J. T.; Waterman, C. M. Contractility, focal adhesion orientation, and stress fiber orientation drive cancer cell polarity and migration along wavy ECM substrates. *Proc Natl Acad Sci U S A* **2021**, *118* (22), e2021135118.

Yang, Q.; Miao, Y.; Campanello, L. J.; Hourwitz, M. J.; Abubaker-Sharif, B.; Bull, A. L.; Devreotes, P. N.; Fourkas, J. T.; Losert, W. Cortical waves mediate the cellular response to electric fields. *Elife* **2022**, *11*, e73198.

Ma, L.; Pollard, T. P.; Zhang, Y.; Schroeder, M. A.; Ren, X.; Han, K. S.; Ding, M. S.; Cresce, A. V.; Atwater, T. B.; Mars, J.; Cao, L.; Steinrück, H.-G.; Mueller, K. T.; Toney, M. F.; Hourwitz, M.; Fourkas, J. T.; Maginn, E. J.; Wang, C.; Borodin, O.; Xu, K. Ammonium enables reversible aqueous Zn battery chemistries by tailoring the interphase. *One Earth* **2022**, *5* (4), 413-421.

Bull, A. L.; Campanello, L.; Hourwitz, M. J.; Yang, Q.; Zhao, M.; Fourkas, J. T.; Losert, W. Actin dynamics as a multiscale integrator of cellular guidance cues. *Front Cell Dev Biol* **2022**, *10*, 873567.

Wheatley, B. A.; Rey-Suarez, I.; Hourwitz, M. J.; Kerr, S.; Shroff, H.; Fourkas, J. T.; Upadhyaya, A. Nanotopography modulates cytoskeletal organization and dynamics during T cell activation. *Mol Biol Cell* **2022**, *33* (10), ar88.

Gu, S.; Bull, A.; Perry, J. K.; Huang, A.; Hourwitz, M. J.; Abostate, M.; Fourkas, J. T.; Korchevskiy, A. A.; Wylie, A. G.; Losert, W. Excitable systems: A new perspective on the cellular impact of elongate mineral particles. *Environ Res* **2023**, *230*, 115353.

Yang, Q.; Miao, Y.; Banerjee, P.; Hourwitz, M. J.; Hu, M.; Qing, Q.; Iglesias, P. A.; Fourkas, J. T.; Losert, W.; Devreotes, P. N. Nanotopography modulates intracellular excitable systems through cytoskeleton actuation. *Proc Natl Acad Sci U S A* **2023**, *120* (19), e2218906120.

Chapter 1: Introduction

Healthy physiology often requires cells to move to fulfill their normal functions. These motility-based processes can have far-reaching consequences throughout an organism during the course of its lifespan. Errors in cell migration or the unwanted motion of specific cells can lead to disease or exacerbate its outcome. Cell motion depends on the dynamic architecture of the cytoskeleton to drive and support the shape changes necessary to exert force on the cell's surroundings and achieve displacement. Adaptor proteins, adhesion complexes, and signaling molecules modulate the activity of the actin cytoskeleton, myosin motors, and microtubules and translate interactions with the extracellular environment into structural changes and the exertion of force toward the cell membrane. The properties of the extracellular matrix (ECM) that constitutes the extracellular environment surrounding cells in most tissues influences cell migration and other actions. Composed mostly of proteins and glycoproteins, its chemical composition, as well as stiffness and fiber alignment, can be an indicator of tissue health. In this introduction, I will describe the importance of cell migration for organismal health and disease and the mechanisms of cell motion. I will then provide a description of the actin cytoskeleton and how it coordinates with actin-binding proteins (ABPs), signaling molecules, adhesion complexes, and other molecules within the cell. Subsequently, I will review the ECM and how it influences cell motion and behavior. A lot of fabrication techniques have been applied to simulate properties of the ECM in order to study the cell response as well as to develop biomedical and implantable devices. A section of this introduction will be devoted to describing some of these techniques, with a focus on photolithography and soft-lithography-based

replication methods. Finally, I will provide a layout of the subsequent chapters of this dissertation.

1.1. Cell Migration

The ability of cells to move permits the fulfillment of vital functions, both on the cellular and organismal levels. In the simplest case, shape changes occur to allow the separation of daughter cells during cell division.[1] Many physiological processes require actual displacement of cells over relatively large distances. How cells migrate can vary across cell type. In fact, even cells of a single type or cell line can exhibit different migrational properties, and can alter their manner of migration at different times.[2] The underlying molecular machinery and mechanisms differ somewhat for these different migrational phenotypes. However, the factors that drive cells to move are generally similar.

1.1.1. Physiological Relevance

Cell migration contributes to physiological processes throughout the life cycle, from the formation of organisms to important daily functions. For many animals, during most stages of embryogenesis and development cells must migrate to target locations to advance properly through the process. For example, during neurulation, neural crest (NC) cells undergo delamination (detachment or separation) from the neural plate or tube, depending on the species.[3] NC cells subsequently travel to different regions of the embryo, at which point the cells differentiate into a variety of cells throughout the body and comprise tissues and organs that are vital to properly functioning organisms.[3] The exact mechanism and timing of neurulation and NC cell migration vary slightly across vertebrate species,[3] yet this process always involves migration

of cells to other parts of the embryo. Distinct migration routes are favored by different classes of interneurons during development of the cerebral cortex.[4] Defective migration of neurons during development can lead to abnormal formation of the cortical circuit, which can, in turn, result in developmental and psychiatric disorders.[5]

During wound healing, a variety of cells coordinate to stop bleeding (hemostasis), prevent infection and remove foreign bodies, recruit and produce more cells, and generate and reorganize tissue.[6] When fibroblasts travel from nearby connective tissue and enter the wound, they produce the ECM proteins and other biomolecules necessary to help repair the wounded tissue.[7]

The various types of dendritic cells (DCs) have distinct travel routes and target locations in the body, and their migratory properties and inflammatory responsibilities differ accordingly.[8] Inhibition of DC migration likely limits the efficacy of T-cell response to SARS-CoV-2.[8] Malignant processes, such as cancer or other disease formation, can also involve cell migration. Cancer cells can migrate to invade neighboring tissue; later, these cells can enter the bloodstream, eventually to metastasize in other organs or tissues. The important role of cell migration in many physiological and disease processes has driven research into understanding how and why cells move.

1.1.2. Single and Collective Cell Migration

Cell migration can occur individually or collectively. Whether a cell travels alone or in a group adhered to other cells can depend on the type of cell and on other intracellular and extracellular conditions. Fibroblasts have been shown to enter wounds as individual cells in

scratch assay tests.[7] Epithelial cells, which form a thin layer outside of organs and vasculature, migrate collectively.[9] Under the right set of conditions, some cells are capable of changing their mode of migration from individual to collective, or vice versa. Cancer cells are known to be capable of highly adaptive behavior. For instance, hypoxia can induce these cells to migrate individually, allowing the cancer to spread to other regions of the body.[10] A broad array of physical and biochemical properties have been observed in migrating cells. Although many of these characteristics can appear in various combinations, and although many cells can exhibit different properties at different times or under alternative conditions,[11] there are some categorizations of migrational modes that are generally accepted, while maintaining awareness of the aforementioned caveats.

1.1.3. Modes of Migration

Shape is the most common observable used to describe differences in migrating cells. This practice has been employed for over 70 years, since Weiss and Garber emphasized the dynamic nature of cell morphology.[12] Despite the transience of cell shapes, several features are frequently observed and are used to characterize cell migratory behavior. Cells that spread on substrates and push out flat protrusions at their leading edge are categorized as mesenchymal.[11,13] Lamellipodia are broad and flat (~200 nm high) protrusions, whereas filopodia are flat and finger-like.[11] The cells employ these protrusions for driving migration and for sensing the extracellular environment. Migratory behavior and the associated morphologies can change as a result of the complexity of the environment. Mesenchymal cells often become elongated in three-dimensional (3D) environments.[13] The protrusions of these cells may then become 3D pseudopodia (round, but not spherical).[11] Leader cells at the front of collectively migrating cells

often display mesenchymal characteristics, including the protrusion of lamellipodia and filopodia at their leading edge, and less adhesivity to other cells in the group.[7] Follower cells, often exhibit epithelial traits; these cells have tight junctions with their neighbors and their membrane is somewhat polygonal in shape and exhibits polarity towards the apical surface.[7] Aside from the leader-follower migrational mode, cells that migrate collectively can employ an organization in which all cells exhibit some mesenchymal characteristics while maintaining adhesions to neighboring cells in the group.[14] Whereas mesenchymal cells can often be described as having a polarized morphology,[15] with the cell front and back clearly distinguishable, amoeboid migration is associated with a round cell body.[13] Amoeboid cells also push out protrusions at the leading edge. Round blebs are the protrusions most commonly associated with amoeboid migration. Protrusions in amoeboid cells can lead to frequent shape changes and deformations.[14] Looking more closely at the mechanisms involved in protrusion formation and cell motility gives a better understanding of why categorizing migration as amoeboid or mesenchymal can be problematic.

1.1.4. Mechanical Forces

As with any object, cells must apply a force, or have a force applied onto them, to move. Cellular environments can be characterized as having a low Reynolds number (the ratio of inertial to viscous forces),[11] which means that force must be continuously applied to sustain motion. The protrusions that cells extend at the leading edge require internal mechanisms for the membrane to achieve this forward push. For filopodia and lamellipodia, actin polymerization pushes on the membrane, resulting in protrusions. Blebs, on the other hand, result from cytosolic pressure. The differences in these protrusions extend further, so to speak. Mesenchymal cell migration is characterized as an adhesive migratory mode.[16] Integrins, and potentially other

transmembrane receptors, as well as the more organized focal adhesions adhere to binding sites on the ECM.[16] These focal adhesions develop in the lamellipodium and adhere tightly to the underlying substrate. Adhesion to the ECM via integrin receptors stabilizes the protrusions.[15] The intracellular portion of these adhesions is connected to the cytoskeleton.[15] Through these transmembrane adhesive structures, actin can apply forces on the ECM, with stronger forces applied with more dense actin networks and more organized adhesion complexes.[16] Actin flow then proceeds toward the rear of the cell. This traction force is transmitted to the ECM as a pulling or frictional force through the adhesion assemblies.[11,14] Adhesions toward the back of the cell are broken down and the actin cytoskeleton at the rear contracts.[14] A gradient of force magnitude applied on the substrate from the front to the rear of the cell (strong to weak, respectively; and of force duration in the opposite direction: stable to transient, respectively) results from the contractile activity of myosin on the cytoskeleton, maintaining cell migration.[17] Contraction of the actomyosin cortex can contribute to hydrostatic pressure within the cell, which can, in turn, facilitate the formation of protrusions, actin- or pressure-driven, at the front of the cell.[16] The cyclic process of protrusion generation, actin retrograde flow, focal adhesion maturation and degradation (at the front and back, respectively), and rear contraction repeats as the cell continues to migrate. Cells that form these strong adhesions to the substratum tend to migrate more slowly. In amoeboid migration, blebs are formed as a result of hydrostatic pressure in the cytoplasm, which applies force on the cell membrane. This force results in displacement of the membrane at a location or locations at which the cortical actin is temporarily weakly connected.[11] Amoeboid cells tend not to form strong adhesions with the underlying surface, which allows cells that use this method of migration to travel more quickly. Force generation for amoeboid, non-adhesive migration is believed to result from friction with the underlying

substrate due to retrograde actin flow; the force is transmitted to the substrate surface via weakly interactive transmembrane molecules.[11] Although bleb protrusions are most often associated with amoeboid migration, amoeboid cells can extend filopodia and lamellipodia. Cells can also simultaneously exhibit adhesions, which are characteristic of mesenchymal migration, and pressure-driven protrusions, which are characteristic of amoeboid migration. These protrusions are usually less spherical, and blunter, than blebs.[11] These cells pull on the ECM and generate pressure by pushing the nucleus forward like a piston.[14] This type of migration has been labeled as lobopodial.[14] Force generation in some collectively migrating cells results from a coordinated band of contractile actomyosin spanning across multiple cells at the rear of the cell cluster. This contractile force can push cells from the side boundaries of the collective toward the center, resulting in the forward flow of cells and displacement of the group.[14] Because many cells can simultaneously exhibit characteristics associated with both of the classical categories of migration, amoeboid and mesenchymal, or alter their migratory behavior and employ different mechanisms based on external or internal cues,[13] it can be beneficial to avoid assigning cell types to sharply defined migration categories.

1.1.5. Extracellular Cues

A variety of external cues can affect the migratory behavior of cells. Exposure to specific biomolecules can turn on the migration machinery in cells. For instance, lipids produced by cancer-associated adipocytes can stimulate migration in cancer cells.[18] Contact with neighboring cells can influence the direction of cell motion. Contact inhibition of locomotion involves the formation of cell–cell adhesions and restricts the direction of protrusions away from site of contact.[19] This phenomenon has been shown to occur in collective cell migration during

development.[3] Directional guidance of cell motion is often referred to as directed cell migration. The stimulus-driven guidance of cells can be classified into one of the following categories: chemotaxis, durotaxis, haptotaxis, electrotaxis (or galvanotaxis), and topotaxis.[13] Chemotaxis is the guided motion in response to a chemical gradient.[20] Durotaxis refers to migration that follows a stiffness gradient.[21] Cells have been shown to preferentially migrate toward stiffer substrates.[22] Haptotaxis is the term used to describe directed motion that follows substrate-bound chemical cues.[23] Electrotaxis describes the guidance of cell migration due to sensing of an electric field.[24] Finally, cells can migrate with a directional preference in response to topographic cues, which is referred to as topotaxis when there is a topographic gradient.[25] In addition to stimuli outside the cell, internal processes can determine whether cells will migrate. Activation of transcription factors[18] and regulation of post-translational modifications[26] can bias cellular migratory behavior. Study of the cell-specific response to the array of external cues provides a deeper understanding of physiological processes that involve cell migration. Furthermore, these studies have the potential to identify targets for therapeutic treatments for disease.

1.2. Actin Cytoskeleton and Other Cellular Components Involved in Migration

Actin is a cytoskeletal protein found in practically all eukaryotic cells.[27] Additionally, bacteria and archaea also have actin or proteins that are structurally and functionally similar to actin.[27] The first eukaryotic organism is believed to have gained the gene for actin when it hosted the bacterial symbiont that became the mitochondria.[27] Actin is the most abundant protein in most organisms.[27] Dynamic assembly of actin is required for all forms of cell motion and also plays a role in many other vital cellular processes. For example, the mechanisms of mitochondrial fission—the process by which the mitochondrion divides into two daughter

organelles—depend on the polymerization of actin and the activity of three different classes of ABPs: actin-related protein 2/3 complex (Arp2/3), tandem monomer-binding proteins (TMBPs), and formins.[28] Mitochondrial fission also depends on the recruitment of dynamic myosin II.[28] Regulation of these proteins can dictate the prevailing mechanism of mitochondrial fission.[28] Transport of material (often in the form of vesicles) between the endoplasmic reticulum and the Golgi apparatus is also facilitated by actin.[29]

Actin is involved in all modes of cell migration. Lamellipodia and filopodia are protrusions that result from forces applied on the membrane by actin polymerization. In filopodia, actin filaments are arranged as linear bundles. In lamellipodia, polymerized actin forms a branched network (and linear bundles). Pseudopodia share similarities with lamellipodia, in that both are protrusions containing branched actin. However, pseudopodia are usually 3D instead of sheet-like, and are not supported by strong adhesions to the substrate. Blebs, which are pressure-driven protrusions, can form from rupture of the actomyosin cortex.[13] Additionally, the contraction of the cortex itself can cause an increase in hydrostatic pressure, which can, in some cases, lead to the formation of blebs.[14]

1.2.1. Structure of Actin and Mechanism of Polymerization

Actin actually refers to a family of proteins that are isoforms, some of which perform specialized functions or are expressed in specific types of cells.[30] These isoforms generally differ by just a few amino acids, even across species,[27] in which changes occur during synthesis or upon subsequent posttranslational modifications on amino acid side-chains.[30] Individual molecules of actin are often referred to as G-actin, due to their globular shape. G-actin is flattened in one dimension and is mapped into two domains and four subdomains, with

specialized functions localized in or between these regions, including, but not limited to: a nucleotide-binding cleft (NBC), phosphate binding loops, and a hydrophobic cleft.[31] The structure of an actin molecule is often delineated as having a barbed end and a pointed end, based on the appearance of an actin filament bound to myosin heads in electron micrographs.[27] The NBC, as the name suggests, is responsible for binding the adenine nucleotide in its various states of phosphorylation, along with its associated Mg^{2+} ion.[30,31] The NBC exists near the middle of the actin molecule and interacts with all four subdomains, although the cleft is inclined toward the pointed end.[27] Molecules of G-actin exist in pools throughout the cell, available as monomers for the construction of polymerized actin filaments (F-actin) with variable architecture. In its F-actin (polymerized) state, the NBC and phosphate-binding loops of an actin protomer execute their function as an ATPase. One phosphate-binding loop modifies the nucleotide through dephosphorylation of adenosine triphosphate (ATP) or, alternatively, stabilizes the bound ATP molecule with other intermolecular interactions.[30] Depending on the activity of this phosphate-binding loop, the reactions lead to conformational changes initialized by the other phosphate-binding loop and the NBC, which influence the actin-protomer binding affinity for ABPs and interactions with other protomers within the actin filament. Actin protomers can interact with neighbors within the filament through another hydrophobic region known as the H-plug.[31] Determination of rate constants for the assembly and disassembly of actin filaments has shown that there is an order that dictates the location at which each step occurs, as well as the degree of phosphorylation of the associated nucleotides within the actin monomers. ATP-actin monomers are added at the barbed end of the filament, whereas adenosine diphosphate (ADP)-actin dissociates at the pointed end.[32] The addition of G-actin at the barbed end of a filament and release of G-actin at the pointed end creates a treadmilling effect.[32] The conformational changes

that result from hydrolysis of ATP signify that F-actin subunits should be disassembled from the filament.[32] Many other proteins participate in constructing and deconstructing these cytoskeletal networks, including ABPs and signaling molecules, so that this treadmilling process can enable cytoskeletal dynamics and effective execution of cellular functions. These ABPs often bind to the hydrophobic cleft[31] (also known as the target-binding cleft)[30] of actin subunits, by insertion of an amphiphilic helix into this cleft.[30] The orientation of the polypeptide chains with respect to the target-binding cleft varies among ABPs.[30]

1.2.2. Actin-Binding Proteins

Numerous proteins are involved in regulating actin polymerization. There are several classes of ABPs that serve various roles in the mechanisms by which actin polymerizes, depolymerizes, and otherwise organizes. Polymerized actin forms filaments (filamentous (F)-actin) that can be organized into linear bundles or branched networks. ABPs help to determine the types of structures that form. Actin monomers are added to the barbed ends of growing polymerized actin structures. The formation of new actin filaments is an unfavorable process, due to the instability of actin dimers and trimers.[32] To overcome this problem, ABPs that nucleate F-actin resemble the structure of trimeric or tetrameric actin.[33] Several classes of ABPs are responsible for nucleating filaments. The Arp2/3 actin-related protein 2/3 complex is composed of seven subunits: Arp2, Arp3, actin-related protein 2/3 complex subunit 1 (ARPC1), ARPC2, ARPC3, ARPC4, and ARPC5.[34] Arp2 and Arp3 belong to a group of eleven Arps that serve distinct cellular functions.[27] The genes that encode the Arp proteins evolved from actin genes, and these proteins often share a large proportion of their amino-acid sequence with actins.[27] Arp2/3 binds to pre-existing actin filaments and promotes the formation of new

branches of actin along the filament, adding actin monomers at the barbed end.[15] Formins nucleate F-actin bundles[35] to produce linear filaments,[34] as opposed to the dendritic network created by Arp2/3.

In addition to the actin nucleators, a group of ABPs is responsible for growing existing filaments. Formins (including the protein diaphanous homologs (mDias)) also regulate filament growth at the barbed ends, and can work in collaboration with other actin nucleators.[29] In a process referred to as processive elongation, formins regulate filament growth by adding actin monomers one at a time to the barbed end (when performing this function, formins act as capping agents on filament barbed ends, as discussed below).[36] Ena/VASP (vasodilator-stimulated phosphoprotein) bundle and elongate actin.[33] Fascin is another protein that bundles actin filaments.[15]

Other ABPs restrict actin polymerization, which can be achieved by various means. Some ABPs control the amount of G-actin available for polymerization by binding to monomers and controlling the state of the bound nucleotide within the NBC. However, while serving in this role, these ABPs also assist with the polymerization and growth of F-actin by bringing ATP-G-actin to the ABPs responsible for elongating the filaments.

Profilin prevents the nucleation of new actin filaments and promotes the addition of actin monomers to the barbed ends of existing filaments.[15,35] Profilin is often present when formins perform their role of growing filaments.[33] To execute these functions, profilin facilitates the nucleotide exchange of ADP-actin monomers to ATP-G-actin, and interacts with other actin-monomer-binding proteins to target the barbed ends of existing actin filaments.[35]

Like profilin, thymosin β4 binds to actin monomers to restrict polymerization.[33] Twinfilin sequesters G-actin, preferentially in its hydrolyzed state (ADP-actin versus ATP-actin), using its actin-depolymerizing factor (ADF) homology (ADF-H) domains, and prevents actin from polymerizing.[37] The sequestration of ADP-G-actin by twinfilin can drive the formation of ATP-G-actin, which can, in turn, be bound by profilin to grow actin filaments rapidly (in the absence of capping proteins).[37]

Alternatively, filament growth can be halted by sequestration of filament barbed ends. Two ADF-H domains allow twinfilin to cap the barbed ends of actin filaments in mammalian cells.[37] As the name suggests, the role of capping protein (CP) is to cap the barbed ends of actin filaments to prevent further growth and to optimize size and stiffness.[34] In addition to elongating F-actin, Ena/VASP binds to the barbed ends of actin filaments and inhibits capping and branching.[15]

Yet other ABPs disassemble F-actin into actin monomers. ADF/cofilin, under certain circumstances, can sever actin filaments at barbed ends and, more importantly, promote the depolymerization of actin.[15,35] The ability of ADF/cofilin to depolymerize pointed ends of actin filaments increases cytoskeletal dynamics, and is vital for cell viability and the formation of effective actin structures.[35] By binding G-actin, cofilin can increase the rate of depolymerization at the pointed ends of filaments.[36] In addition to monomer sequestration, twinfilin can drive disassembly of actin filaments at both ends.[33]

Gelsolin is a member of a family of proteins that perform both capping and severing functions.[30] Binding of calcium promotes conformational changes to an active state in which two of gelsolin's six homologous domains bind to the sides of an actin filament.[30] Further

conformational changes cause these domains to grasp subunits on each strand and then sever the actin filament.[30]

Some ABPs liaise among actin, ABPs, and signaling molecules. Wiskott-Aldrich syndrome protein (WASP)/WASP-family verprolin-homologous protein (WAVE) activates the Arp2/3 complex near the membrane.[15] WASP-family proteins serve as a connection between signaling pathways and cytoskeletal dynamics.[35] Verprolin/WASP interacting protein (WIP) similarly interacts with signaling proteins, ABPs (including WASP), and actin monomers and filaments to regulate actin polymerization.[35]

Srv2, or cyclase-associated proteins (CAPs) in higher-order eukaryotes, serve to promote both actin polymerization and depolymerization by recycling actin monomers and ADF/cofilins, respectively.[35] WASP/WAVE, verprolin/WIP, Srv2/CAP, and other actin-regulating proteins, such as β-thymosins, share a WASP homology 2 (WH2) domain, which binds with high affinity to actin in its ATP (adenosine triphosphate) state.[35]

Cortactin stabilizes filament branches formed by Arp2/3.[15] These branches are metastable, and cortactin prevents debranching and the breakdown of the actin network.[34] To support the network branches, cortactin engages directly with both F-actin and Arp2/3.[34] Cortactin also interacts with WASP family proteins in a collaborative way to promote branched actin formation by activating each other under different circumstances to enhance Arp2/3 nucleation of actin.[34]

WASP/WAVE, verprolin/WIP, Srv2/CAP, profilin, ADF/cofilin, and twinfilin all participate in Arp2/3-related actin polymerization at the cortex. Filamin A and α-actinin stabilize

the actin network by crosslinking filaments.[15] All of these proteins play a vital role in cell function. Knockout of the genes used to synthesize the actin nucleators (Arps, formin, and Spire/cordon bleu/leiomodin families) or their regulators (WASP family) are often lethal.[38]

1.2.3. Rho GTPases

Rho GTPases (also known as guanosine triphosphate (GTP)-binding proteins, G proteins, or GTP hydrolases), including cell division control protein 42 (Cdc42), Ras-related C3 botulinum toxin substrate (Rac), and the Ras homolog (Rho) proteins, are signaling proteins. Among other cellular responsibilities, these proteins modulate actin polymerization, often through regulation of proteins more directly involved in the process.[15] Rho proteins regulate the actomyosin contractile forces exerted on the cell.[39] Rac and Cdc42 activate various ABPs to perform their roles in actin polymerization. For example, binding of Cdc42 deactivates the autoinhibitory state of WASP, allowing this protein to bind Arp2/3 and actin monomers, and thereby augment actin filaments at their barbed ends.[35] Rac1 behaves in a similar manner to Cdc42 in the regulation of WAVE.[36] RhoA and Cdc42 activate the capping and filament growth functions of formins.[36] RhoA also activates profilin.[36] Mutations in the genes that encode the Rho GTPases can cause defects in cytoskeletal and receptor organization and motility-related functions such as chemotaxis and homing.[38] These defects can lead to immunodeficiency syndromes and persistent infections.[38] Rho GTPase activity is regulated by several families of proteins. Guanine nucleotide dissociation inhibitors release or sequester GTPases to control their availability for activation.[40,41] Guanine nucleotide exchange factors (GEFs) exchange GDP for GTP to activate the GTPases.[40,41] GTPase-activating proteins inactivate GTPases by hydrolysis of GTP.[40,41]

1.2.4. Myosin

Myosins are dynamic proteins that can prompt changes in cell shape and can serve as a source of force generation within the cell. In addition to modulating cell shape and motility, these proteins also play a role in Golgi apparatus structure and function, as well as short-range transport in the endoplasmic reticulum.[29] The family of myosins is diverse, with 12 different classes occurring in mammals, and each having its own specialized functions.[42]

Myosins contain three key structural regions—the motor domain, the lever arm, and the tail—that are present and serve the similar functions in each class, although structural differences allow for specialization in function or target molecules.[42] The motor head groups of myosin can bind to actin filaments, whereas the tail motif can attach to the membrane.[29] For most forms of myosin, this structure allows the motors to move along actin filaments and translocate materials along the membrane to other regions of the cell.[29] The motor domain is also the region that binds to, and hydrolyzes, ATP.[42] The motor head has four subdomains, including a region referred to as the converter that links to the rest of the myosin structure.[42] Special connectors attach the separate subdomains to their neighbors. The affinity of regions within the cleft formed between subdomains for the binding of actin or hydrolysis of ATP is modulated by conformational changes in the motor head.[42] The lever arm is connected to the motor domain. The lever arm varies in length between classes of myosin.[42] As in the case of the dynamics of actin filaments, myosin force generation is achieved by the hydrolysis of ATP. Release of the hydrolysis products, an inorganic phosphate and ADP, is linked with binding of myosin to actin and with conformational changes within myosin.[43] These changes include the swinging of the lever arm (powerstroke), a region of the myosin molecule that channels the conformational changes that

result from hydrolysis of ATP, and release of the products into functional motion.[43] The lever arm amplifies the conformational changes driven by ATP hydrolysis in the motor domain.[42] The lever arm includes a converter subdomain that connects to the motor head and contributes motility to the swinging of the lever arm during force generation.[42]

Myosin classes vary in the mechanism through which they process ATP and bind targets, as well as their associated morphology, conformations, and motor properties.[42] The lengths of actin-binding loops also differ.[42] These variations explain the distinct functions of the different types of myosin. In addition to binding to the membrane, the tail region, which also varies in length and structure among myosin classes, recruits and assembles motors.[42] Specific signaling molecules or cargo-recognition mechanisms prevent myosins from operating at the wrong place or time.[42] Myosins use actin filaments as tracks, with all but the myosin VI class moving toward the barbed end of actin filaments (+ end, or fast-growing end).[42]

Several classes of myosins, including myosin II, are dimers that contain two head domains. Dimeric myosins contain coiled coils in their tails that hold the two filaments together.[42] The bipolar filaments of myosin II can grasp multiple actin filaments.[29] As the head groups travel towards the barbed end of F-actin, which is tethered to the membrane through certain ABPs, the myosin motors can cause the membrane to contract.[29] This process is a source of force-generation within the cell on the membrane, as well as on the ECM. Myosin II activity is coordinated with actin polymerization at the leading edge of the cell.[36] The contractile forces exerted by myosin can pull polymerized actin away from the leading edge in a process referred to as retrograde flow, thereby potentially modulating protrusions by limiting the amount of actin filaments present at the front of the cell.[36]

1.2.5. Focal Adhesions

Focal adhesions (FAs) provide a connection between the ECM and the interior of the cell. FAs are comprised of many protein components, including transmembrane proteins that interact directly with both ECM molecules and structural proteins within cytoplasmic face of the membrane. These protein components form complexes that change in conformation over time due to mechanical tension and allosteric binding.[44] Governed by Rac and Cdc42, focal complexes tend to form at the cell periphery and grow to become FAs,[45] which are regulated by Rho.[46] Other terms have been coined to classify FAs based on the distinct properties of the FAs such as size, location, and dimensionality, as well as on the molecules that participate in the formation.[45] Growth of FAs and the necessary recruitment of the additional molecular components depends on the tensile properties of myosin.[47] Interaction of FAs with the ECM is mediated by integrins, a family of heterodimeric proteins that bind to specific polypeptide regions within ECM proteins.

Integrins are categorized into α and β subunits, of which 18 and 8 different isoforms are found in vertebrates, respectively, and that interact noncovalently to form 24 different possible heterodimers.[48] Excess β integrins are present in the cell, and the amount of α integrins determines how many heterodimers are assembled and delivered to the membrane.[48] The α integrins have a seven-bladed propeller structure that contains a binding site for Ca^{2+} to regulate ECM ligand binding through allosteric conformational changes.[48] Many α integrins also feature an αI domain that facilitates binding to collagens with coordinated adhesion to a Mg^{2+} ion.[48] β integrins interact with the actin cytoskeleton through adaptor proteins or ABPs.[48] The βI domain of β integrins responds to ion binding to drive conformational changes in neighboring domains.[44]

In integrin heterodimers that contain α subunits lacking an αI domain (present in only half of the α integrins), the βI domain in the β subunit facilitates ECM ligand binding.[48] A Ca^{2+} binding site regulates inhibition of β-integrin activity.[48] These rearrangements expose ECM ligand-binding sites.[44]

Variations in activation exist among integrins. Some isoforms require contact with intracellular or extracellular molecules, such as ECM proteins or the cytoskeleton, to transition to an active conformation.[44] Integrins are transmembrane proteins, and their cytoplasmic tails are restricted to the region within a few tens of nanometers from the plasma membrane.[49] This same region has few actin molecules, and the actin density does not increase for another few tens of nanometers away from the membrane,[49] indicating that integrins do not interact with actin directly. Integrins can cluster on the membrane at the sites of actin-rich protrusions to form nascent adhesions.[44] These immature adhesions do not require cytoskeletal contractile forces to develop, but their further growth and maturation—which are not guaranteed and depend on the intracellular and extracellular conditions experienced by an individual cell—determine whether these sites of adhesion can sense and reciprocate mechanical forces.[44]

Maturation of FAs depends on actin crosslinking.[44] VASP and α-actinin are actin-regulatory proteins, or ABPs, that participate in actin bundling or crosslinking. α-actinin also organizes into actin stress fibers. These actin structures are then linked to integrins and focal adhesions through a network of proteins that serve distinct roles in FA structure and function. Each group of proteins that fulfills a specific role in the formation of FAs occupies a distinct region in the space between the integrins and the actin structures.[49]

Some of the key protein components of focal adhesions include focal adhesion kinase (FAK), paxillin, talin, vinculin, and zyxin. FAK is a tyrosine kinase that participates in signal transduction and whose activity depends on integrins and localizes with paxillin to the same region as the integrin cytoplasmic tails.[49] FAK regulates other signaling molecules via phosphorylation, including paxillin and Rho GTPases (through phosphorylation of their GEFs), although FAK is also believed to serve as a scaffolding component to FAs.[45] Binding to FAK and/or the cytoplasmic domains of β integrins also activates Src, another tyrosine kinase, which then phosphorylates tyrosine residues on other FA components, and also regulates FA disassembly.[45] Phosphorylation of different tyrosine residues on FAK controls its participation in signaling at the sites of focal adhesions.[45]

Paxillin, p130Cas, and Crk are signaling scaffolds, also known as adaptor proteins, that bind to kinases, structural proteins, Rho GTPases or their regulators, and other adaptor proteins and signaling molecules to facilitate activation and morphological changes at FAs.[45] Paxillin can also bind to the membrane and the cytoplasmic tails of certain integrins, with this latter capability contributing to the regulation of cell migration.[45] Talin binds to integrins and actin, and is associated with vinculin, which binds actin.[50] By binding to the membrane proximal motif of the β integrin at the membrane, talin can separate the cytoplasmic tails of the α and β integrins, and drive their rearrangement to an extended open conformation that promotes high-affinity binding to the ECM ligand.[44,51] By binding to F-actin, talin remains in an activated state and exposes cryptic vinculin binding sites.[44] As talin is responsible for binding to both integrins and actin stress fibers in FAs, talin acts as a tether and spans the different FA protein strata within the cytosol, with its N terminus near the integrin tail, FAK, and paxillin and its C terminus neighboring zyxin, α-actinin, and actin.[49] Vinculin is an actin crosslinker and membrane

anchor.[52] Vinculin can also bind to talin and several other ABPs.[53] Vinculin and talin perform the function of force transduction in the region between those in which integrin-based signaling and cytoskeletal regulation occur.[49]

Zyxin is another cytoskeletal adaptor.[49] Zyxin links the actin cytoskeleton to the membrane at the sites of adhesion and regulates the filament growth by binding Ena/VASP family ABPs and other proteins, including vinculin.[52] Phosphatidylinositol-4,5-bisphosphate (PIP2) is a phospholipid that contributes to the regulation of multiple FA proteins of different classes through similar mechanisms. PIP2 activates FAK from its auto-inhibitory state.[44] Talin activation is also promoted by PIP2, similarly releasing talin from its auto-inhibitory state and leading to the disentanglement of talin's head and tail domains.[44] PIP2 can also contribute to the activation of vinculin by binding to its tail domain, which causes unfurling of its head domain, which can bind to talin.[44] Interactions among talin, vinculin, and PIP2 can modulate cellular response to mechanical forces and the size of focal adhesions.[44]

Focal adhesions and their components are dynamic. Different proteins have distinct exchange rates from within FAs, and the FAs themselves can be displaced on the membrane as a result of traction forces and cell motion.[44] Signaling molecules or proteases regulate FA disassembly to allow for cell motion and for the recycling of protein components,[44] often through an endocytic pathway.[54]

1.2.6. Stress Fibers

Stress fibers are bundles of actin filaments that are crosslinked by α-actinin and myosin, and are often bound to focal adhesions.[50,55] Myosin II molecules are incorporated into stress

fibers, lending the contractile nature of the fibers.[46] In addition to its involvement in crosslinking actin filaments, myosin tension draws the filaments together to facilitate stress-fiber formation.[46] The formation of stress fibers often depends on the stiffness or compressive strength of the substrate that the cell encounters.[47] There are several types of stress fibers that are distinct in structure, location, and function. The same holds for some of the molecules with which stress fibers interact. Dorsal stress fibers are long and linear, and are bound to FAs at one end on the ventral surface of the cell.[56] These stress fibers are non-contractile.[56] Dorsal stress fibers form from formin-mediated actin polymerization around focal complexes and α-actinin crosslinking of filaments, with myosin performing this role in regions with limited α-actinin.[50]

Transverse arcs, the second type of stress fiber, are not attached to focal adhesions.[56] Transverse arcs are formed from the crosslinking of Arp2/3-polymerized actin bundles, some of which include α-actinin and others myosin.[50] Alternating bands of α-actinin and myosin on transverse arcs manage the motion of these curved fibers on the dorsal stress fibers that serve as tracks.[56] Transverse arcs fuse near the center of the cell to form contractile actomyosin bundles.[56]

Ventral stress fibers span the length of the cell, and each end is attached to focal adhesions.[50] In the center, however, ventral stress fibers have similar bands of α-actinin and myosin II.[56] The combination of the structural properties of dorsal stress fibers and transverse arcs enables ventral stress fibers to link contractility with interactions with the ECM. The reason for the similarity of ventral stress fibers to both dorsal stress fibers and transverse arcs is because the latter are the precursors of, and develop into, ventral stress fibers.[50] Both dorsal stress fibers and transverse arcs form near the leading edge of migrating cells, and the arcs move away from the front during migration.[50] A transverse arc fuses with two dorsal stress fibers, one on each side

of the cell, to form the ventral stress fiber, which explains why this type of stress fiber is linked to two FAs.[50] A fourth type of stress fiber is known as the perinuclear actin cap.[47]

Palladin belongs to a family of proteins, including numerous isoforms, that support proper actin organization within cells.[57] Palladin crosslinks actin into bundles.[57] This protein supports stress fibers and localizes to stress fiber puncta and ends.[58] Palladin is found in dorsal stress fibers, along with VASP.[56] Stress fibers can elongate by additional actin polymerization localized at focal adhesions. As the stress fibers grow, they can collide with other stress fibers, and the nascent arcs condense into long, mature arcs. These arcs then combine with other stress fibers, all still attached to focal adhesions, to form a stress-fiber network.[55]

The stabilities of focal adhesions and stress fibers are interdependent,[56] in that disassembly of one impacts the other. Forces exerted by stress fibers are often directed to the extracellular matrix through focal adhesions. Additionally, components of FAs can help reinforce stress fibers and prevent overgrowth and breakage. It has been found that zyxin can travel from FAs to vulnerable sites on stress fibers and can recruit α-actinin and VASP to thicken and strengthen stress fibers at these locations.[47]

1.2.7. Microtubules

Microtubules are composed of heterodimers formed from the stable, noncovalent interaction of α- and β-tubulin molecules,[59] which are similar in size and amino-acid sequence.[60] Distinct isotypes of tubulin exist within vertebrate species, with each isotype having a distinct, characteristic, negatively charged amino-acid sequence at the C-terminal (and sometimes at the N-terminal).[59] Like G-actin, tubulin monomers bind a nucleotide, although the specific

nucleotide is guanosine triphosphate (GTP).[60] Microtubules are polymerized structures that assemble in a manner similar to actin filaments. Nucleation of microtubules is performed by another isotype of tubulin, γ-tubulin, which also stabilizes growing tubules during assembly in the microtubule organizing center.[59] However, tubulin is added to growing microtubules as dimers. The GTP in β-tubulin becomes hydrolyzed upon polymerization, and guanosine diphosphate (GDP) remains bound to β-tubulin while the dimer remains within the microtubule.[60] GTP in α-tubulin is not exchanged,[60] meaning that only β-tubulin has GTPase activity.[59]

Heterodimers of tubulin assemble end-to-end to form linear protofilaments (arranged so that α-tubulin only has β-tubulins as neighbors, and vice versa).[60] The protofilaments (usually 13) are then arranged so that the starting point of each is offset by 0.9 nm to form hollow, cylindrically shaped microtubules with a diameter of 25 nm and with the appearance of a helical pattern of a given tubulin monomer due to the offset.[60] When heterodimers of tubulin are added directly to an existing microtubule, the dimers are preferentially added to the end with β-tubulin exposed (the plus end), based on the rate of addition.[60]

Studies indicate that GTP hydrolysis is involved in the conformational change from a sheet to a cylinder during microtubule formation, but is not necessary for addition of tubulin dimers for microtubule growth.[59] The hydrolysis of GTP to form GDP-tubulin also seems to increase the propensity for microtubule disassembly.[59] Dynamic instability refers to the sudden shrinkage of a microtubule, referred to as a catastrophe.[59] Rapid addition of tubulin dimers can regrow the microtubule and rescue it from shrinkage.[59] One of the roles of microtubules is the transport of material between the ER, the Golgi apparatus, and the rest of the cell; another related

role is the movement of the ER itself within the cell.[29] Microtubules also move chromosomes during cell division (microtubules are a major component of mitotic spindles).[61] Furthermore, microtubules provide structural support for cell shape and participate in signal transduction, both of which affect cell migration.[61] Microtubules can also drive FA disassembly through a process that depends on clathrin,[54] a protein that is a major component of coated vesicles.

1.2.8. Forces and the Cytoskeleton

The actin cytoskeleton, including actin filaments, myosin II, and the proteins responsible for constructing the polymerized actin network, serves as a sensor for mechanical forces applied on the cell. Cortical actin is connected to the plasma membrane through anchoring proteins. External forces applied on the cell are transmitted directly to the cytoskeleton through these anchors, as opposed to occurring through signaling mechanisms.[62] Similar mechanosensing occurs during cell adhesion, although signaling molecules participate in that process despite molecular links between the extracellular matrix and the cytoskeleton. Integrins can potentially strengthen their binding to ECM proteins upon exposure to mechanical tension.[47] RhoA is necessary for focal adhesion growth, as this protein mediates mechanisms of actin polymerization and the response to mechanical tension.[47] The formation of ventral stress fibers and FAs relies on myosin contractile action, as well as the actin-filament assembly by formins, both of which are controlled by RhoA.[46] Focal adhesion area increases with the magnitude of force applied across the FA.[47,63] The growth of FAs is accompanied by recruitment of additional component molecules, which can be accomplished through the exposure of cryptic binding sites on proteins already present within the FA by applied force.[47]

Binding to actin is necessary for myosin II accumulation at the site of an applied force, but actin alone cannot mount a buildup in the region of external pressure in the absence of myosin.[62] All components of the cytoskeleton share the force burden to varying degrees, and, in some instances, the presence of certain proteins can influence the accumulation of others.[62] The process of polymerization and depolymerization is a source of force generation.

Motor proteins—myosins for actin and dyneins for microtubules—can exert forces on the membranes.[29] In addition to the interactions among cytoskeletal proteins, the nature and magnitude of the external force, and its effect on the cortex, can determine specific protein responses.[62] When the cytoskeleton exerts force on the membrane, these forces can be transmitted directly to the extracellular environment by deformation of the membrane and by the motion of transmembrane proteins that interact with molecules of the ECM.

1.2.9. Examples of Other Molecules that Can Affect the Cytoskeleton

Many other proteins and biomolecules have been shown to modulate actin polymerization through interactions with proteins or other biomolecules that are known to regulate actin. For example, Kank (kidney or KN motif and ankyrin-repeat domain-containing) proteins interact with talin and microtubules, and help organize the cortical microtubule stabilization complex (CMSC).[64] Through these interactions, Kank supports the connection between microtubules, integrins, and actin. Kinases activate actin nucleators, and also participate in other processes of cytoskeletal dynamics, often through direct or indirect activation of ABPs. LIM-kinases phosphorylate and inactivate cofilin,[65] thereby regulating the depolymerization of actin filaments. p21-activated kinase 1 (Pak1) activates LIM-kinase to perform its regulatory function of cofilin activity.[65] Pak1 interacts directly with actin to cause cytoskeletal

rearrangements, and also binds the Rho GTPases Cdc42 and Rac.[65] The Rho GTPases, Pak1, and LIM-kinases function together to regulate multiple aspects the actin cytoskeleton, including filament disassembly and membrane motions (such as ruffling). Protein kinase B (PKB, also known as Akt) phosphorylates a specific amino acid on palladin, which activates the latter's actin-crosslinking function.[66] Myosin light-chain kinase (MLCK), Rho-associated protein kinase (ROCK), and myosin phosphatase can regulate myosin II activity by switching the presence of a phosphate group on the light chain.[36] Further upstream, lysophosphatidic acid (LPA) activates Rho, which, in turn, can activate ROCK.[46] As a result, LPA signals can modulate myosin activity and actomyosin contractility and stress fiber formation.[46] The activation of LIM-kinase by ROCK also causes the phosphorylation of cofilin, which inhibits filament severing/depolymerizing activity, thereby stabilizing existing filaments.[47] Control of contractility and actin depolymerization regulates the morphology and composition of stress fibers in migrating cells.[50] These are just a few of the many molecules that influence or are influenced by one or more the proteins described here. There is still much to discover about the relationships among other intracellular (and extracellular) molecules and their effects on kinases, Rho GTPases, other signaling molecules, ABPs, and cytoskeletal and adhesion components.

1.2.10. Roles of ABPs and Signaling Molecules in Cell Migration

Actin-binding proteins and signaling molecules directly impact steps in cell-migration mechanisms. The extension of actin filaments through actin nucleators, and the molecules that regulate them, exert force on the membrane and push forward regions of the leading edge of the cell.[29] The branched actin network formed through activation of Arp2/3 can push on the membrane, leading to the extension of lamellipodia. The capping function of twinfilin (and other

proteins with this ability), as well as the sequestration function, aid in the organization of actin filament structures that support motility.[37] Actin crosslinking by palladin reduces the migratory behavior of cancer cells.[66]

Just as important as protrusive actions at the leading edge are in cell motion, the function of myosin at the cell rear also plays a crucial role. Myosin II can exert contractile forces on the cytoskeleton, and is necessary for cell retraction.[62] In mesenchymal migration, a polarity exists between opposing GTPases at the front and rear of the cell, which directs cell motion. Rac is present in higher amounts at the leading edge.[33] Meanwhile, for contraction of the cell boundary to occur, Rho proteins must signal to the region and activate the motion of the myosin motors, through several other signaling molecules.[33] Rho proteins are therefore concentrated at the cell rear during mesenchymal migration.[33] The contractile forces of myosin II are also applied onto the actin cortex to create protrusions in amoeboid-like migratory modes.[33] The hydrostatic pressure created by the contractile force deforms the actin cortex and pushes on the plasma membrane to form protrusions[33] (as described in the previous section). Under amoeboid migration, therefore, the presence of Rac would be limited and concentrated Rho would promote myosin contractility.[33]

1.3. Extracellular Matrix

1.3.1. General Characteristics and Composition

The extracellular environment of practically all organisms generally includes neighboring cells and macromolecules of varying density and organization. The characteristics and complexity of this environment can differ across species, as well as within distinct anatomical

regions of many organisms. The macromolecular network of the cells' surroundings is referred to as the ECM. Many of the molecules that comprise the ECM are proteins or glycoproteins. Glycoproteins contain oligosaccharides bonded to the side-chains of amino acids in some regions of the protein. Polysaccharides are another component of the ECM. Glycosaminoglycans (GAGs), such as hyaluronic acid, can be present on their own or as groups attached to amino acid side-chains in proteoglycans (a subgroup of glycoproteins).[67] The physical and chemical properties of the ECM impact, and are impacted by, the cells situated within it. Characteristics that negatively influence cell function, whether caused by aberrant cell behavior or otherwise, can lead to negative health outcomes.

Anatomical components vary considerably in stiffness as well as in the order and organization of molecules, fibers, and networks. The properties of the ECM often indicate the mechanical functions and requirements of that anatomical region.[16] For example, chondroitin sulfate (another GAG) is more prevalent on proteoglycans found in connective tissue, and provides improved support to those structures.[67] Common classes of ECM glycoproteins include collagen, fibronectin, tenascins, elastins, and laminins.[68] Elastins, as the name suggests, provide elasticity to specific tissues.[68] Laminins offer distinct adhesive ligands for integrin binding than those available on collagens and fibronectins.[68] All of these proteins exist in different forms or types, which often vary in structural, mechanical, and adhesive properties and, consequently, where they are found within the (human) body.[68]

1.3.2. Structure

Some cell types must traverse multiple distinct extracellular environments with varied physical properties, whereas others remain in the same surroundings for most of the organism's

existence (excluding the period of development). The ECM serves as a protective barrier that separates cells and organs.[67] The organization of the macromolecular network effectively serves to produce a confined space for the cells, with barriers and pores that can restrict or limit passage.[14] ECM fibers can serve as tracks on which to travel or climb, or as obstacles that should be pulled apart, broken down, or circumvented for cells to reach the intended destination.

Anatomical components with highly ordered ECM often function as regions of mechanical support for the organism.[16] More loosely organized fibrillar or sheet-like ECM often serves as a substrate to allow cell motion or migration.[16] The interstitial matrix is the portion of the ECM that is constructed as an interwoven mesh; this component of the ECM provides structure and support for tissues, and protects tissues against potentially damaging external compression forces.[67] To achieve this mechanical strength, the interstitial matrix is often largely composed of fibrillar glycoproteins collagen I and fibronectin.[67] The other section of the ECM is known as the basement membrane (BM). This region is sheet-like in structure, and is composed primarily of collagen IV, laminins, and nidogens.[67] Other collagen types are also present, and together with collagen IV make up 50% of the total protein composition of the BM.[69] Additionally, heparan sulfate is a common GAG linked to these glycoproteins.[67] A high degree of crosslinking and limited solubility make BMs resistant to proteolysis.[69] Basement membranes interact with both the epithelial and endothelial cell layers.[67] The thin layers of BM are formed in many tissues and other anatomical components throughout the body, including blood vessels, skin, organs, glands, and muscles.[69]

The density, organization, homogeneity, and porosity of ECM proteins often varies by anatomical location. For example, fibrillar collagens that surround bone are aligned and spaced

less than 10 μm apart, whereas gaps between the fibers in breast tissue are variable in width, but can be as large as 20 μm.[70]

1.3.3. Cellular Interaction with the Extracellular Matrix

Attachment to the ECM is vital for a variety of cell types, and detachment of these cells can result in abnormal cellular processes, including defective metabolic pathways, anoikis, autophagy, and entosis.[71] Each of these processes can lead to cell death.[71] The interaction of cells with the ECM depends on the properties of both the ECM and the cells, the latter of which can vary due to, e.g., gene expression. The ability of cells to navigate the ECM impacts the efficacy with which the cells perform their functions and can contribute to overall organismal health.

The cell–ECM relationship is reciprocal in nature. Properties of the ECM impact cell behavior and function, and can determine actions taken by the cell onto the ECM. For example, properties of the BM orient epithelial cells to execute distinct processes (which leads to different properties) at the upper and lower regions of the cell with respect to the position of the tissue/organ surface (a phenomenon known as apicobasal polarity), and can also influence cell differentiation.[67] Any changes incurred by the ECM will alter future cell behavior and processes. Functional groups present on peptide regions of ECM proteins have been observed to alter gene expression and influence differentiation in MC3T3-E1 cells.[72] The ECM is capable of sequestering growth factors and cytokines for later release when the need arises, such as to expedite wound healing.[67]

Specific amino acid sequences in many proteins and glycoproteins of the ECM facilitate cell adhesion.[73] In fact, these characteristic adhesion sequences on distinct classes of ECM

proteins promote the organization and binding of specific integrins.[68] The types, as well as the density and organization, of integrins can affect cytoskeletal dynamics and signaling pathways, which, in turn, can influence cell proliferation and differentiation. For these reasons, the precise organization of ECM molecules is vital.[67] Several cellular functions require adhesion to the substratum for proper execution, including cell division[74] and migration (for some cell types and under certain conditions). Changes to the ECM, such as through protease degradation, can alter mechanical that can lead to the disassembly of FAs.[44]

In addition to chemical cues, cells can also respond to the stiffness of the ECM. Some cells are able to sense the mechanical response of the substrate in the range of hundreds to thousands of Pa.[16] Stiffening of tissues can be an indicator of disease.[22] Changes in stiffness can influence many cell properties, such as morphology, motility, and proliferation.[22] Some cell types are capable of synthesizing ECM proteins or rearranging the existing architecture of the ECM. These modifications can alter the mechanical properties of the matrix, as it has been found that aligned collagen fibers have lower microscale stiffness than do randomly oriented fibers.[75] The porosity of the matrix is another factor; the organization and density of proteins varies by location, and can restrict cell motion without specialized skills such as nuclear deformation and proteolysis.[16]

1.3.4. Fibronectin

Fibronectins are a group of glycoproteins that consist of a dimer of two nearly identical monomers bonded through a disulfide linkage,[73] forming a V-shape.[68] Variations in the sequence, composition, and structure of fibronectin exist due to alternative splicing of mRNA that can differ across species or anatomical component.[76] The monomers contain three types of

repeating units. The number of repeats differs between types. Type I has 12 repeats, Type II has two repeats, and Type III has 15-17 repeats.[76] Type I and II repeats each have two intrachain disulfide bonds.[76] Fibronectin molecules are synthesized in a globular conformation, but get rearranged into a fibrillar form when integrated into the ECM.[68] Although fibronectin facilitates cell adhesion to the ECM, with binding sites for many different integrins,[76] its ligand binding sites also enable adhesion to other ECM proteins.[68] Amino-acid sequences within the repeating units fibronectin are also found in other ECM proteins and GAGs, as well as other proteins.[76]

1.3.5. Collagen

Each collagen molecule consists of a triple helix of three α-chains consisting of a repeating amino-acid sequence that always includes glycine and two other amino acids (Gly-X-Y).[77] Often, proline (Pro) and hydroxyproline (Hyp) are the other amino acids in this sequence[77] (not necessarily simultaneously). Glycine has a hydrogen atom rather than a side chain, and its small size allows Gly to fit perfectly within each turn of the α-chain helix that faces the center of the collagen monomer.[77] The bulky pyrrolidine rings of Pro and Hyp face away from the center of the molecule.[77] Hydrogen bonds formed between the amino end of Gly in one α-chain and the carbonyl end of Pro in another α-chain stabilize the secondary structure of the triple helix in collagen.[77] The estimated Gibbs free energy of formation of the amide-amide hydrogen bonds in native collagen is approximately -6 kJ/mol, assuming negligible entropy change.[78-80] Similar stabilization can be achieved between a hydrogen on the α-C of Gly or Hyp and the carbonyl oxygen of Pro or Gly, respectively.[78] One hydrogen bond exists per triplet of amino acids across the three strands, and the configuration of amino acids across the three α-chains tends to repeat every 28.6 Å.[78]

There are 28 known types of collagen in humans, which differ in their composition (amino acid sequences) of α-chains and their secondary, tertiary, and quaternary structures.[81] Even within a given collagen type, there can be distinct α-chains and supramolecular assemblies of the collagen molecules.[81] Some collagen types require that triple helices are composed of homotrimeric α-chains, whereas others are always heterotrimeric.[82] The collagen types are classified into separate categories of structural organization based on the nature of the supramolecular structure they form. These categories include the fibril-forming collagens, fibril-associated collagens with interrupted triple helices, network-forming collagens, and membrane collagens.[81] In fibril-forming collagens, tropocollagen molecules (the triple helix formed from three α-chains) bind to each other in a quarter-stagger pattern (a positional offset), which creates a banding pattern.[68] Collagen I is the most abundant collagen, and forms fibrils.[68] Collagen IV, which will be discussed in more detail below, is a network-forming collagen.[81] Many cells express multiple collagen types.[82]

The organization of collagen within a tissue often depends on the function and physical requirements of that tissue. Collagen fibril linearity and uniformity depend on the mechanical load requirements of the tendons from which they are derived.[83] Collagen I—found in such distinct anatomical components as bone, skin, and blood vessels—can pack together into fibrillar structures of varying density and of diameters that range from tens of nanometers to hundreds of microns.[68] Collagen II, another fibril-forming collagen, organizes at different densities and orientations based on its depth within a tissue.[68]

1.3.6. Collagen IV

Collagen IV networks are constructed from a triple helix of three α-chains that constitute a heterotrimeric collagen IV molecule. Each α-chain features a region of a repeating amino-acid sequence featuring Gly and two other amino acids that persists for ~1400 residues.[84] Variations in amino-acid sequences result in distinct α-chains. The number of available combinations for the selection of three α-chains with which to form a triple helix leads to many possible isoforms of collagen IV.[84] For example, in mammals, there are six genetically distinct α-chains.[82] As with isoforms of laminins, collagen IV isoforms can vary by as much as 30-50% in their amino-acid sequences.[69]

Non-collagenous domains occur at various regions throughout the α-chain, including the amino and carboxyl termini of the polypeptide, as well as brief interruptions in the Gly-X-Y repeat domain.[84] The interruptions of these triple repeats provide structural flexibility for supramolecular organization and also serve as ligands for the binding of integrins.[82] The N-termini of α-chains are glycosylated with an oligosaccharide, and contain a region with multiple cysteines and lysines.[82] Properties of the non-collagenous domains of α-chains can influence and limit the α-chain partners with which to form the triple helix of the collagen IV molecule.[84] Perhaps for this reason, only three combinations of α-chains have been found *in vivo* out of 76 possibilities (including six homotrimers).[82] Several of the six collagen IV α-chains have a higher affinity for associating with other α-chain isoforms than for forming homotrimers, and these chains regulate assembly of the triple helices.[82] The non-collagenous domains at the C-termini mark the location at which the triple helix begins to form among the three compatible α-chains.[82] The formation of the triple helix from three α-chains includes the exchange of β-hairpin

structures from the non-collagenous domains at the C-termini between the α-chains.[82] The non-collagenous domains of carboxyl termini of α-chains offer functional reactivity and molecular flexibility that facilitate interactions between molecules and stabilize their proximal organization to form dimers.[84] These dimers are formed from molecules with identical heterotrimeric α-chains, and are stabilized through hydrophobic and hydrophilic interactions.[82]

Covalent bonds between methionine residues and hydroxylated lysine residues can crosslink and further stabilize α-chains at the C-termini,[82] through unusual sulfilimine bonds that require a protonation step,[85] although the extent of covalent bonding varies based on anatomical location and the availability of specific enzymes.[82] Additionally, the cysteine- and lysine-rich region at the N-termini of α-chains supports disulfide linkages within or across molecules, leading to the formation of tetramers[82,84] and lysine-hydroxylysine crosslinks.[82] Glycosylation protects against collagenase activity.[82] Molecules that are already linked as dimers or tetramers can also intertwine/twist with other molecules to form supercoiled structures[84] or align their collagenous domains to form additional associations through noncovalent interactions.[82] These various interactions among molecules enable the formation of complex supramolecular structures of collagen IV. Collagen IV genetic expression and synthesis occurs throughout the body to various degrees. The different α-chains vary in their distribution, with some being more widespread than others.[84]

1.3.7. The Extracellular Matrix and Its Relation to Health and Disease

The presence or absence of ECM molecules can be an indicator of the current state of tissue health. For example, the mRNA needed to produce one of the three α-chains of the heterotrimeric collagen VI molecule is not expressed in many cells derived from mesenchymal

tumors.[86] Collagen VI is a protein that provides structural and functional support in muscular and connective tissue and stroma throughout the body. The absence of collagen VI, therefore, is detrimental to proper function of these tissues, and potentially indicates and facilitates the presence of cancer.[86] On the other hand, collagen VI is absent from, or present at low density in, healthy synovium that lines many joints throughout the body.[87] In contrast, collagen VI is strongly expressed throughout rheumatoid synovial membranes.[87] As mentioned earlier, the composition of the ECM is anatomically dependent. A large proportion of a protein in a specific tissue can be healthy or normal, whereas the presence of the same protein in another tissue is indicative of disease. However, the composition of the ECM is dynamic, and external or internal changes in conditions can lead to increased synthesis and incorporation of ECM components. For example, exercise can improve joint health by initiating the production of glycoproteins to compensate for a deficit caused by atrophy and immobility.[67]

Extracellular matrix molecules can participate in the development or progression of disease in a variety of ways. Proteins in the ECM can be targeted and broken down, leading to the degradation of tissue. In the case of Goodpasture syndrome—an autoimmune disease that results in kidney and lung damage—autoantibodies target the non-collagenous domains of a specific α-chain in collagen IV molecules.[84] The sites of antigen binding on these collagen molecules are exposed upon protein denaturation as a result of infection or exposure to organic solvent.[84] Alternatively, genetic mutations or deletions can cause defects in protein synthesis that can similarly degrade the ECM. Depending on the amino acid and the location within the protein, the mistaken insertion of an incorrect amino acid in a collagen α-chain can cause defects in protein folding and posttranslational modifications that lead to the damage of organs or tissues and the development of disease.[78] Alport syndrome is a hereditary disease in which genetic

alterations in the genes that encode collagen IV synthesis lead to degradation of the basement membrane in the kidneys, eyes, and inner ear, with renal failure a common prognosis.[84] These defects lead to errors during production of collagen IV that can affect molecular length or stability of supramolecular organization.[84] The irregularities that are built into the collagen IV network in the case of this disease cause thickening and splitting of the glomerular basement membrane (in the case of renal disease) and the formation of lesions in the kidneys.[84] The amount of ECM molecules deposited can cause organ dysfunction in fibrotic and degenerative diseases.[67]

In cancers, cells often alter the ECM to promote disease progression. Tumor-associated macrophages (TAMs), for instance, express matrix metalloproteinases (MMPs) that can break down the ECM around tumors, which allows tumor cells to escape and invade neighboring tissue.[88] Dense tissue is often associated with excess ECM protein deposition and increased stiffness.[89] These properties cause an influx of inflammatory signals, as well as of soluble fibronectin and fibrinogen, that heightens the immune response, exacerbates inflammation, and fosters the growth of tumors and cancer progression.[89] TAMs have been shown to promote the deposition of aligned collagen fibers,[89] which guide tumor cells to invade neighboring tissue. Both *in vitro* and *in vivo* studies have found that TAMs can guide tumor cells along collagen fibers, through the release of chemokines, toward vasculature.[89]

1.4. Development of Nano- and Micro-Scale Patterned Surfaces for Biological and Biomedical Applications

1.4.1. Devices/Systems

The complexity of human physiology has led to the continuous expansion of research and development efforts to identify and address the minutia of both the physiological systems and of the devices produced for their understanding, diagnostics, preservation, and therapeutics. Many of these applications are being scaled down so that they may be wearable—and perhaps partially or entirely embedded beneath one or multiple layers of skin or tissue—or delivered directly to a region of the body through means of ingestion, inhalation, or injection. Additional chemical and/or physical properties can ensure that the object can target a specific location. Drug-delivery systems are biomedical devices that can vary in their intended lifetimes, ranging from hours to months. Implantable devices, including prostheses, can serve as replacements or possibly growth stimulants for missing or damaged anatomical components. The development of effective devices for biomedical applications requires understanding of cell behavior in the complex, three-dimensional environments that cells encounter *in vivo*, which are full of many competing stimuli. Additionally, before adoption as an approved device, researchers must study how cells interact with the device through *in vitro* studies. Many cell biology studies have involved examining cells on flat substrates. However, in recent years, a lot of effort has been focused on simulating properties of the natural cellular environment, with artificial ECMs of different degrees of dimensionality. Cells exhibit characteristics that more resemble *in vivo* behavior when plated on linear, fibril-like, topographical arrays than when placed on flat substrates.[14]

1.4.2. Materials

When selecting materials for applications, there are several factors that must be considered. First, the material must possess properties that enable the device to execute the desired function. Perhaps just as importantly, one must consider the ease with which a device can be produced with a specific material using the selected fabrication technique. Complicating matters is the reality that biomedical systems often must execute multiple functions, and must comprise several materials to perform these functions. Optimizing the devices requires iterative changes and tests to determine the properties of these combinations of materials, as well as their response to physiological conditions. For example, the manner by which a drug delivery system is produced, the properties of the drug, and the device material all contribute to the efficacy and efficiency of the system performance.[90] The properties of a material can vary depending on synthesis and processing,[91] which must also be considered during the design stage and before production. Physical characteristics of mixtures or blends of materials can also change in response to heat treatment or annealing steps that might be required in manufacturing. Each material contributes to the bulk properties of the mixture, and heat can drive phase separation and lead to changes in these properties.[92] This phenomenon has been exploited to produce substrates with topographical cues forming due to morphological changes from the annealing process.[93]

Several categories of materials are frequently employed for the manufacturing of topographical substrates that can be used to study cellular responses. Metal oxides are often used to synthesize nanoparticle arrays that serve as substrates or vehicles, or as sacrificial layers for patterning.[93] Concerns about adverse health effects of particles produced from this class of

materials might limit their popularity in some applications. Polymers can similarly be used as vehicles for drugs and can also serve as scaffolds for tissue and bone growth. Studies have found that several polymers are biocompatible and biodegradable, and they are suitable for therapeutic devices designed for use in the human body. Similarly, polydimethylsiloxane (PDMS), a silicone elastomer, is frequently used in cell studies due, in part, to its chemical inertness and biocompatibility. Proteins, including those comprising the ECM, as well as growth factors,[94] can be used to construct complex cellular environments. Fluorescent labels are frequently attached to the different materials to visualize changes that occur as a result of cellular response to the substrates. In many cases, biotechnology combines different classes of materials in a single device.

1.4.3. Fabrication Techniques

The method of production of biotechnological devices in research settings always depends on cost, and frequently on the availability and ease of use of instruments and equipment. Additionally, the properties of the desired material(s) might also contribute to the selection of specific fabrication techniques. One approach to test the properties of the combination of drugs and delivery vehicles is through the fabrication of thin films by spin coating. Techniques have also been developed whereby films have been heat-sealed to create a reservoir to house drugs for gradual release into the system.[90]

A popular focus of biotechnology research is the production of substrates with unique chemical or physical properties for *in vitro* and *in vivo* (and possibly *ex vivo*) studies, which can provide insight on biochemical and biophysical processes and test surface properties that can be

fabricated on implantable devices. Numerous techniques have been developed for the fabrication of such substrates.

Electrospinning uses polymer solution that can be extruded and deposited to form a complex, 3D network of random or oriented polymer fibers resembling the natural ECM. This technique can produce fibers with diameters below 1 μm.[95] Control of the properties of the fibers can be achieved by tuning the voltage applied by the machine, as well as by tuning the solution properties.[93] It is possible to incorporate ECM proteins into the polymer fibers by creating a blend that contains both the protein and the polymer and adding this mixture to the electrospinning machine.[95] Alternatively, ECM proteins can be incorporated into a preexisting electrospun substrate by plasma treating the mesh-like film and adding the protein solution, thereby altering the surface chemistry of the polymer fibers to enable the proteins to penetrate the pores of the film and be incorporated completely within the polymer matrix.[96]

Surface coating or functionalization is commonly employed in biological studies on flat substrates or in combination with techniques described in this section that create topographical features. The techniques can vary in complexity or ease of use, but they can be as simple as depositing a solution of ECM proteins onto a glass or plastic substrate. Consideration must be given to the interaction of the substrate and coating materials, because adhesion can vary depending on the chosen protein and polymer (for example).[97] Additional processing steps can be performed on the substrate surface—e.g., plasma treatment or surface modification or coating with another chemical—to improve the adhesion of the desired ECM protein. Characterization methods that can confirm the successful coating of the surface and changes in coating density must be identified. Self-assembled monolayers (SAMs) with distinct functional groups have been

coated onto substrates to study their effects on gene expression and cell proliferation and differentiation.[72] Additionally, a substantial amount of research has been invested into identifying peptides or amino-acid sequences that promote cell adhesion and can be used instead of proteins for biomaterial applications,[73] such as implantable devices and tissue engineering. Use of peptides instead of entire proteins for surface coatings can avoid problems with denaturation under unfavorable conditions, such as small changes in pH and temperature, and peptide synthesis allows for the precise control of the amino-acid sequence.[73]

Gelation protocols can produce 2D and 3D networks composed of polymers or proteins. The hydrogel viscoelasticity can be tuned by adjusting its chemical composition, which can be useful for simulating *in vivo* environments with different stiffness values.

Etching methods can be used to pattern substrates to produce topographical surfaces. The equipment available determines the intricacy of the design. Colloidal lithography, for instance, which involves the deposition of a film of nanoparticles and subsequent etching to pattern the underlying substrate,[93] is limited in terms of resolution by the degree of control one has over the self-assembly of the particles. However, this technique can be used to etch surfaces that create pattern features with dimensions between 100-250 nm.[98] Reactive ion etching (RIE) is a technique that exposes substrates to reactive ionic species. Although the resolution of surface roughness can be controlled down to the nanometer scale, the location of individual peaks and valleys of the resultant topographical features depends on localized material properties and other factors that lead to random patterning.[93]

Nanoparticle synthesis also has many biomaterial applications, with various classes of materials employed to elicit different cellular responses based on the chemical and physical

properties of the particles, including the geometrical influence on phagocytosis.[99,100] In many cases, the nanoparticles are incorporated into substrates fabricated by other techniques. Fluorescent particles embedded within hydrogels allows for the detection and quantification of the cellular force applied on the hydrogel through techniques such as traction force microscopy (TFM).[101] Although protocols have been developed to yield precise control of nanoparticle shape and dimensions, it is often difficult to deposit or place individual particles selectively in a desired location and orientation without applying other technologies. Electrochemical methods have also been employed to synthesize metal-containing nanoparticle arrays[93,102] and to pattern substrates with distinct metallic regions[93] that also serve as unique topographical cues. In electrochemical anodization, the reactivity of metals can be exploited and the appropriate salt selected to control formation of the metal oxide (or another insoluble salt) on the metal substrate. Manipulation of the electrolyte (for example, via aging) and prior topographical patterning of the substrate empowers electrochemical anodization to control topographical cues on multiple scales.[102]

Chemical vapor deposition (CVD) is a technique to deposit thin layers of a material on a substrate. Tuning the CVD protocol and selecting appropriate starting materials makes it possible to achieve chemical reactions during subsequent processing steps that alter the composition of the deposited film.[94] Other surface-modification or functionalization techniques can be employed to prepare a substrate for patterning steps.

Microfluidic devices are used to simulate *in vivo* fluid flow conditions experienced by cells. Additionally, topographical cues can be incorporated into the device or the microchannels can be patterned with discrete regions of specific protein coatings and gradients or distinct layers of cells embedded within hydrogel precursors.[93,103] Inkjet printers designed to print proteins are

capable of creating patterned substrates, though with feature sizes on the scale of hundreds of microns.[103] Dip-pen nanolithography is a high-precision, direct-write technique that applies material via an atomic force microscope cantilever. This technique can apply a range of materials to a substrate in arbitrary three-dimensional designs.[103]

Surfaces produced by methods with limited patterning precision frequently provide new insights in the targeted biological systems, as well as new tools to study cellular processes while guiding further innovation in biomedical device design. However, when used in combination with fabrication techniques capable of high resolution, such as soft lithography and photolithography, it is possible to achieve precise control of local chemical and physical surface properties.[93]

1.4.4. Photolithography

Photolithography generally refers to the patterning of a material using light. Photolithography is most frequently associated with integrated circuits and the electronics industry, though it has been applied to other fields such as microfluidics, optics, and bioengineering. There are a variety of techniques of varying complexity that can be categorized as photolithography. However, the term is most often used to describe the exposure of material to ultraviolet light transmitted through a photomask. Although most applications use polymers, photolithography can be applied to any material or combination of materials reactive to and/or patternable upon exposure to light. The process of photolithography includes the following general steps: deposition of material on a substrate (and possible pre-exposure processing); light exposure; and post-exposure processing and development (often referring to the treatment of the patterned material with solvents). Using the terminology associated with polymer films,

photoresists are categorized as positive-ton or negative-tone. These terms describe whether the material exposed to or not exposed to light is removed from the substrate, respectively, due to decreased substrate adhesion and/or increased solubility in the selected solvent(s). Depending on the application and material, additional steps might be incorporated after development of the patterned substrate. A photoinitiator is generally incorporated as a photoactive species in negative-tone photoresists. Often, the selected photoinitiator undergoes radical formation, which then leads to polymerization that undergoes a radical chain reaction. However, cationic photoiniators can also be used. Some experimental systems have been developed in which UV light or a laser can dynamically and selectively etch, oxidize, or crosslink material *in situ* to change the biochemical or physical environment encountered by cells.[93]

1.4.5. Multiphoton Lithography

Nonlinear optical processes have been applied to many different research and industrial fields, including microscopy, spectroscopy, lasers, medicine, telecommunications, information transmission and storage, electronics, and manufacturing.[104] Multiphoton lithography has achieved advances in many of these, as well as other (e.g., optical devices, microfluidics, biotechnology) technological areas of study.[105-107] Multiphoton lithography involves (in most cases) the time-coincident absorption of multiple photons of light (sometimes referred to as multiphoton absorption (MPA)); i.e., the photons must interact with the material at approximately the same location and time. For the electronic transition to an excited energy level to occur, the absorbed photons must convey enough energy to surmount the gap between levels. For single-photon excitation, the quantized energy must equal the difference between electronic

levels, whereas for two- and three-photon absorption, each photon would contribute one-half or one-third of requisite energy, respectively, and so on.

Simultaneous absorption of multiple photons by an individual molecule is an unlikely process, and multiphoton lithography has been referred to as femtosecond laser direct writing (FsLDW) to indicate the need for ultrafast laser pulses with high peak power. A commonly used excitation source is a Ti:sapphire oscillator. The photons must be concentrated spatially, too, so the laser beam is often passed through a high-numerical-aperture objective before impinging on the photoactive material. Despite these efforts to increase the likelihood of simultaneous absorption of two or more photons by an individual molecule, the process is still improbable throughout the exposed material, and only occurs within the focal region of the microscope objective (i.e., power loss due to absorption deep within the material is limited).[105] As a result, multiphoton lithography enables three-dimensional control of the fabricated patterns. Modulation of the laser power can reduce the voxel size, and thus the feature dimensions, of fabricated structures.[107] 2D and 3D control of the design can be achieved by a computer-controlled microscope stage used to change the position of laser exposure within the substrate material, although other approaches have also been employed for this purpose. A computer-operated optical shutter allows for further control over the location and time of laser exposure. A computer interface is necessary to transmit instructions to the stage, mirrors, shutters, and other equipment that requires real-time adjustment during patterning. Computer software of varying complexity is usually employed to design patterns and implement coordinates and instructions to be performed by the dynamic components of the setup. If the substrate is transparent, and the material is also somewhat transparent, fabrication can potentially be monitored by including a camera in the optical path of the microscope.

Multiphoton lithography, like standard photolithography, is based on the excitation of electrons to higher orbitals or levels through the absorption of photons that match the energy gap. For the material to be useful, the excited state must lead to a change in reactivity or in the physical properties of the system. The use of multiple photons for excitation means the application of light from less energetic and more accessible regions of the electromagnetic spectrum is a standard benefit of multiphoton lithography.

Patterning with multiphoton lithography has been demonstrated with many different classes of materials. A popular focus of reports in this field is the fabrication of patterned substrates made of polymers, and the technique is referred to as multiphoton absorption polymerization (MAP)[107] (or two-photon-induced polymerization, TPIP, or two-photon photopolymerization, TPP). Much of the research in MAP has been focused on producing photonic structures or other optical components, including lenses, waveguides, and photonic crystals.[107] Creativity in terms of device design and the incorporation of diverse materials is often necessary to maximize the refractive index difference or to optimize other optical properties.[107] Nano- or micro-scale polymer structures fabricated using MAP can have different mechanical properties than those produced from the same material using standard (UV) photolithography, or with macroscopic dimensions, likely due to reduced crosslinking of the material during multiphoton fabrication.[106] Acrylates are an especially popular class of polymers for MAP, due to their appealing properties that include the availability of a variety of functional groups and molecular weights, as well as rapid polymerization, and transparency in the visible range of the electromagnetic spectrum.[106] Acrylic resins are often liquid at room temperature, and crosslinking forms solid structures. As is the case with standard photolithography, a photoresist or photopolymerizable material usually includes a radical, or cationic, photoinitiator

and occasionally a co-initiator. However, selection of the photoinitiator must be carefully considered, because not all photoinitiators have a sufficiently large two-photon absorption cross section to efficiently absorb multiple photons to produce radicals. Radical photoinitiators from a variety of families of molecules have been successfully applied to MAP, and have been combined to form hybrid photoinitiators with improved power thresholds and efficiency of radical formation.[108] Another application that uses polymers for patterning exploits the solubility of stereoisomers,[105] in which laser exposure converts the polymer to an isomer with greater intermolecular interactions and lower susceptibility to solvation.

3D protein structures, including hydrogels composed of biomolecules, have also been prepared using multiphoton lithography.[105] The patterning of trypsin microreactors in a microfluidic channel allows for the cleavage of proteins as they flow past the enzymatic structures in a solution.[109]

Nano- and micro-scale devices can be produced that are partially or entirely composed of metal.[106] These devices can then be applied to electronic applications. Noble metal nano- or microstructures can be fabricated by reducing the metal present as a salt or acid.[110,111] A polymer matrix is often used to stabilize the formation of the metal structures, and a reducing agent (the polymer, in some designs) is activated by multiphoton excitation.[110,111] The polymer can be removed by developing the fabricated structure in an appropriate solvent.[110,111] Conductivity can be enhanced through electroless plating.[110] Metal oxides have similarly been patterned through this general technique by chemical modification of metal alkoxides to a photoactive species. Laser exposure is believed to break down organic bonds and reduce the solubility of the reacted material,[105] similar to the application with stereoisomeric polymers.

The 3D control over pattern features that is offered by multiphoton lithography allows for the fabrication of structures that many other lithographic techniques are incapable of producing easily. Many of these difficult patterns contain features that are not continuous within a plane normal to that of the substrate, for example structures containing voids. Structures that contain closed loops are especially problematic, as molding or replication material used to copy the original structure will fill the empty space and the pattern will rip upon peeling. Incorporating membranes—2D planes of patterned material of approximately 1-μm thickness (in the third dimension)—into the structural voids during fabrication makes it possible to mold and replicate these complex patterns, through a technique referred to as membrane-assisted microtransfer molding (MA-μTM);[112] these patterns would otherwise be destroyed during the replica molding process.

The resolution of features produced using multiphoton lithography is often near or below the diffraction limit. Material properties, equipment details, and protocol adaptations can improve resolution and reduce feature size, in some cases to well below the diffraction limit. The nonlinear optical effect of the multiphoton absorption process contributes to resolution below the diffraction limit through a reduced square light intensity distribution and a smaller volume of material impacted by the incident light.[105] Controlling the exposure duration at any location within a material also impacts feature size.[105] Simply increasing the laser scan speed (e.g., by adjusting the motion of the microscope stage) can also decrease the thickness of a fabricated line due to fewer photoactive molecules being excited during exposure in each spot.[113] These factors emphasize the importance of the equipment used for multiphoton lithography, as the rate at which a shutter can respond or a stage or mirror can alter direction or position (and the precision with which motion can be controlled) affects feature size and resolution. Precise overlap of

voxels (individual volume elements) controlled by a piezo stage or mirrors with similar precision enables features to be shaped at the nanometer scale. Photoinitiator selection is one factor that determines the threshold power necessary for polymerization. A photoinitiator that efficiently initiates polymerization in the resin or photoresist requires a lower threshold power, which, in turn, can provide better spatial resolution.[113] Quenchers have been added to resins or photoresists to limit further the region in which radical polymerization—and, therefore, lithography—occurs.[105] The physical properties of the patterned material also contribute to sub-diffraction-limited resolution. When exposed to air or to solvent changes, the surface tension can smooth regions between voxels, thereby reducing surface roughness and feature size.[105]

Exposure with additional laser beams can also improve resolution. Studies have found that coincident irradiation with a second laser beam of appropriate wavelength and power can inhibit MPA-induced polymerization in specific materials.[114] The mechanisms through which this process—now often referred to as multicolor lithography—works depend on the material, and the setup must be adjusted accordingly. However, in general, this approach exploits the presence of unreactive excited states within the photoreactive molecules, and these additional laser beams are used to transfer some or all of these electrons to unreactive states. The extent of inhibition can be adjusted by offsetting the excitation and deactivation beams, adjusting the power output of the lasers, and/or incorporating phase masks into the beam path (which can affect the spatial distribution of laser intensity).[114]

Multiphoton fabrication is generally performed by allowing the beam to encounter different locations within the material sequentially, either by moving the position of the beam relative to the substrate (scanning mirrors) or vice versa.[106] This approach limits the rate of

fabrication and the scalability of the process. Several adaptations allow for faster patterning.[106] Use of a microlens array can simultaneously fabricate tens of copies of a patterned structure on the same substrate (discussed in several reviews).[108 105,106] Researchers are now seeking to independently, simultaneously control multiple fabrication designs on the same substrate, using devices such as a spatial light modulator (SLM).[108] Methods that are capable of fabricating multiple patterns simultaneously must be paired with an experimental setup that ensures the alignment of the substrate in the *z* dimension; otherwise, some of the structures produced will differ in height or will be incomplete or absent due to variations in the position of the voxels from the focused laser beam with respect to the surface of the substrate.[108] Holographic patterning of a mode-locked beam with an SLM can be achieved with control of the beam phase and polarization.[115] Software processes the desired intensity distribution and uses an iterative Fourier transform algorithm to construct the necessary phase hologram.[115] Additional optical elements are usually incorporated to control the beam properties before and after incidence on the SLM.[115] Creative techniques can facilitate spatiotemporal patterning of large areas without an SLM. Directing the beam into the objective using a digital micromirror device (DMD) provides spatial patterning and temporal patterning through angular dispersion.[116,117] The DMD is often programmable to allow easy control of patterning the dispersed light.[117] Coordinating stage motion with the projected image from the DMD provides 3D control over pattern printing.[116] Use of angular dispersion to spatiotemporally control the projected multiphoton beam can be further controlled with beam-shapers and even an SLM.[116,117]

1.4.6. Soft Lithography

Soft lithography refers to the process of creating a pattern design and then producing copies of the original through replica molding or related processes. The initial pattern is often fabricated with photolithography, although other techniques have been demonstrated, including the deposition and immobilization of diatoms.[118] A mold of the original is then produced using an elastomeric material (often PDMS). The elasticity of PDMS makes this material an excellent choice for molding 3D structures, such as those produced using multiphoton lithography, without damaging complex features.[107] Several soft-lithographic techniques have been developed to stamp replicas of the original pattern design. Microcontact printing (μCP) usually involves depositing a material in solution (proteins are a common choice) on a stamp and allowing it to dry. The material is then transferred to a substrate whose surface promotes adhesion or reaction.[93] The pattern of the elastomeric stamp determines the distribution of transferred material on the substrate, and can be used, e.g., to create protein gradients for haptotaxis studies.[103] Imprint lithography is another method derived from soft lithography, which will be discussed in greater detail later. These techniques can produce distinct patterns on a substrate from a single mold/stamp. Some adaptations of these approaches have strategically separated the stamping process from the step in which the patterned material is attached to the substrate, thereby making it possible to produce scaffolds with embedded microchannels.[93]

The replica-molding process entails the production of a negative relief of the original pattern, i.e., the creation of a copy in which the solid regions become voids and the voids become solid. Replica-molding techniques that offer fast replication times can improve the scalability of serial techniques such as MAP. Structures containing features with open regions or unfilled

spaces within a *z*-plane are prone to damage or destruction during molding, which can limit the applicability of this method to less complex patterns. However, incorporating membranes into the original design (MA-μTM)[112] is one solution that has been demonstrated to increase the applicability of replica molding, and to facilitate replication of 3D patterns or features. Generally, at the beginning of the process the molding material is liquid, and so can conform to the shape of the pattern. To maintain its shape, the properties of the material must change such that when molding is complete, the mold is solid. PDMS is often chosen for this technique across the many applications and fields of study. PDMS is a silicone polymer with repeating siloxane units. Due to a list of attractive properties, including optical transparency, gas permeability, limited reactivity, and viscoelasticity, PDMS is also a popular material choice for microfluidics and biological applications. The most common approach to producing PDMS molds is through the mixing of the components of the Dow Corning Sylgard 184 Elastomer Kit, which is composed of an elastomer base and curing agent, usually mixed in a 10:1 ratio. However, adjustment of the composition has also been explored to change the properties of the mold, either through altering the ratio of these components or using entirely different starting materials (including those with different functional or terminal groups). Using precursors with vinyl and hydrosilane functional groups produces what are often referred to as hard-PDMS (*h*-PDMS) molds, which improve the resolution attainable. Adding a solvent that matches the hydrophilicity of the substrate material (by gauging dipole moment) and reduces the solution viscosity (while also supporting the solubility of the components) of the prepolymer mixture can produce high-fidelity, composite molds (combined with a thick slab of soft PDMS made from Sylgard 184) that effectively replicate dense patterns with features and spacings on the scale of tens of

nanometers.[119] The elastomeric molds exhibit viscoelastic properties that allow the molds to conform to and detach from substrates without damaging the features of either.

1.5. Thesis Outline

The migratory behavior of cells depends on the coordination of the cytoskeleton, signaling pathways, and other molecules that contribute to the structure and dynamics of the cell and that regulate or otherwise affect the cytoskeletal and signaling networks. Interactions with extracellular cues can alter intracellular processes. Properties of the ECM, including stiffness and surface chemistry, affect transmembrane proteins, as well as components of the cytoskeleton and signaling pathways that interact with these proteins. Nano- and micro-scale topographical cues in the extracellular environment also influence the organization and dynamics of intracellular molecules, a phenomenon we refer to as *esotaxis*, from the Greek for inner guidance. This guidance by nanotopography can drive directed cell motion, which we term *microthigmotaxis*, signifying guidance by texture on a subcellular level.

In Chapter two, a technique that facilitates the production of nanotopographic substrates on a relatively large scale is described. This method is based on soft lithography and replica molding techniques. Structures that were originally fabricated using MAP were replicated using solvent-assisted nanotransfer molding. This process, which can incorporate ultraviolet photolithography, is applicable to photoresists produced using a variety of photoinitiators that support cell viability during a 48-h incubation period. The molding technique is capable of reproducing patterns with many different geometries, and reproduces nanoscale topographical features with high fidelity. The acrylic photoresists used in this study form replicas that can be

coated with ECM proteins. These replicas also have high optical transparency that permits the use of various imaging modalities and fluorescent labels across the much of the visible spectrum.

The examination of an array of breast-cancer cell lines plated on an asymmetric sawtooth nanotopography revealed distinct migratory characteristics, which is discussed in Chapter three. The directional bias of cell motion, as well as cell speed and persistence and morphologies of migrating cells, vary across cell lines. Actin localization and dynamics on individual sawteeth contribute to the differences in guided motion among cell lines. Scanning electron micrographs and super-resolution confocal images of stained focal adhesions further elucidate how cell lines vary in their perception of and interaction with nanotopographic cues.

Chapter four explores how the organization and dynamics of actin depend on the topography encountered by the cell. Additionally, actin response to nanotopographic cues is not uniform across cell types. In this chapter, an analysis method is presented that calculates the optical flow of actin based on time-lapse images of cells with fluorescently labeled F-actin. The calculations are performed based on fluorescence intensity gradients (spatial gradients) and changes in the position of actin structures between frames (difference images, or temporal gradients). The optical-flow data for actin are compared between an epithelial cell line and neutrophil cell line on flat and nanoridged substrates. The clustering of optical-flow vectors adjusts the scale of actin dynamics being analyzed up to the micron scale, which can allow for the characterization of actin waves and the motion of actin structures that span multiple ridges.

Cells respond to multiple properties of the ECM. These properties affect the cell simultaneously; e.g., when a cell comes in contact with a collagen fibril, the cell senses both the shape and the stiffness of the fibril. In Chapter five, the effect of surface chemistry on the

cellular response to nanotopography is explored. Cells were plated on either uncoated nanoridges or on ridged surfaces that varied in collagen IV coating density. The effect of collagen coating on cell morphological and migrational response to nanoridges is explored. Whether incubation time has an effect on the cellular response is also investigated. Cell orientation and contact guidance are not dramatically different on ridges with different coatings. Actin dynamics are well guided by the nanoridges, and this guidance increases with incubation time. The actin guidance is compared across different migratory phenotypes.

Chapter six concludes this thesis with a review of esotaxis based on results described in earlier chapters, as well as other recent reports based on or related to studies of cellular and cytoskeletal responses to nanotopography fabricated using solvent-assisted nanotransfer molding. This summary will touch on the ubiquity of esotaxis and how nanotopography influences immune cells. The organization and dynamics of other cellular components are also discussed. Different topographic cues can elicit distinct cellular and esotactic responses. Cytoskeletal organization depends on the dimensions of the nanotopographic substrate. However, the same topography can elicit distinct cytoskeletal responses in different cell types.

Chapter 2: Replication of Biocompatible, Nanotopographic Surfaces

This chapter is adapted from Sun, X.; Hourwitz, M. J.; Baker, E. M.; Schmidt, B. U. S.; Losert, W.; Fourkas, J. T. Replication of biocompatible, nanotopographic surfaces. *Sci. Rep.* **2018**, *8*, 564. It is adapted with permission through the Creative Commons Attribution 4.0 International License. Sun fabricated the master nanotopographic surfaces, performed solvent-assisted nanotransfer molding, coated the surfaces with proteins, characterized the surfaces, cultured, fixed, and stained the cells, evaluated cytotoxicity for different photoinitiators, and wrote the manuscript. Hourwitz performed solvent-assisted nanotransfer molding, coated surfaces with proteins, cultured, fixed, and stained the cells, evaluated cytotoxicity for different photoinitiators, and wrote the manuscript. Baker performed solvent-assisted nanotransfer molding and evaluated cytotoxicity for different photoinitiators. Schmidt analyzed images. Losert and Fourkas wrote the manuscript.

2.1. Introduction

In physiological environments, cells are not only subjected to chemical signals, but also to physical interfaces that present various geometries and topographies. For instance, the phagocytosis of microparticles by macrophages depends on the shape and the orientation of the particles.[99,100] The activation of T cells can be initiated by contacting antigen-presenting dendritic cells, which are characterized by complex surface topographies such as filopodial protrusions, membrane ruffles, and invaginations.[120] The extracellular matrix (ECM), which is replete with collagen fibers that are hundreds of nanometers wide, has been demonstrated to be

crucial in physiological processes, such as cell differentiation,[121] embryonic development,[122] immune response,[123] and wound healing.[124] In contrast, an aberrant ECM contributes to pathological conditions, such as rheumatoid arthritis[125] and cancer metastasis.[126,127] Although certain proteins, such as actin and integrins, have been identified as playing a role in these processes, the effect of physical cues on the dynamics of these proteins and the mechanism of their mechanosensing remain elusive. Compared with commonly-used 2D chemical micropatterns on flat surfaces,[128,129] nanotopographies that resemble the physical features *in vivo* provide a more physiologically-relevant tool for studying cellular behaviors and intracellular dynamics, as well as for dissecting the mechanism of mechanosensing. For example, nanoridges[130] and asymmetric microsawteeth[131] have been demonstrated to guide cytoskeletal dynamics (esotaxis) and cell migration (microthigmotaxis). Micro- and submicro-pillars have been found to affect cellular rigidity sensing via biasing the localization of myosin filaments and focal adhesions.[132] Disordered nanodots[133] have been shown to induce cell differentiation. With growing interest in the effect of physical cues, such as topography and curvature, on cell behavior and intracellular dynamics, methods for generating nanotopographic biomaterials are highly desirable.

A number of techniques have been developed for the generation of nanotopographic materials for biomedical applications. One such method is the replica molding of photolithographically-fabricated master surfaces using photocurable hydrogels.[134] However, some of the photoinitiators involved in the hydrogel photopolymerization have been found to be cytotoxic,[135,136] and the underlying topography can deform under the nanoNewton cellular traction force due to the compliance of the hydrogels.[137] Although the ECM and other biological microenvironments are compliant on the mesoscale, they are rigid at the nanoscale. It has been

suggested that both convex- and concave-curvature-sensing proteins can stimulate actin polymerization,[138] so nanotopography that retains its original geometry is desirable for comparing how topography comparable to that of the ECM affects cytoskeletal dynamics. Injection molding has been used for the rapid creation of rigid, polymeric nanotopographic substrates.[139] However, the method is limited to molding low-aspect-ratio nanostructures, and the thick flash layer formed in the injection cavity presents a challenge for the use of the replicas in high-magnification cell imaging.

Here we report a method for the rapid generation of rigid, biocompatible nanotopographic materials that can be chemically functionalized with ease. By adding solvent to the polydimethylsiloxane (PDMS) prepolymer, we are able to mold complex nanotopographies with resolution as fine as ~25 nm. The resulting PDMS mold can also serve as a master for the replication of complementary nanotopographies. The acrylic resin used in the replica molding provides a platform for the subsequent surface functionalization for cell experiments. Resin formulations and processing conditions that prevent cytotoxicity in the replica surfaces are also examined. The molding resolution, versatility of surface functionalization, and potential applications of the nanotopographic surfaces are discussed.

2.2. Results

In our method, a master surface is fabricated using multiphoton absorption polymerization (MAP).[140] The master surface is then functionalized with a perfluorocarbon to reduce the surface energy and to facilitate the subsequent release of the PDMS mold. In the solvent-assisted nanotransfer molding, hexane-containing hard PDMS prepolymer[141] is cast on the perfluorocarbon-passivated master surface containing the desired nanotopography. Hexane

serves as a solvent to reduce the viscosity and the surface tension of the hard PDMS prepolymer, and thus to assist the prepolymer's penetration into gaps and voids. After precuring at 60 °C, a thick layer of soft PDMS prepolymer is poured on top of the hard PDMS and cured again at 60 °C. Next, a drop of acrylic resin is sandwiched between the PDMS mold and the acrylate-functionalized cover glass, and then is photocured for 5 min. The resulting replica has nanotopography that is identical to that on the master surface (Fig. 2.1A). The complementary (negative) nanotopography can be produced by using the negative PDMS mold as a master for a new round of molding (Fig. 2.1B).

We examined the fidelity of the molding process by comparing the nanotopography of master and replica substrates using scanning electron microscopy (SEM) and atomic force microscopy (AFM). The widths of the master ridges (Fig. 2.2A), replica ridges (Fig. 2.2B), and replica grooves (Fig. 2.2C) are all ~350 nm, with no discernible difference between master and replica. AFM profiles show that the ridge heights and groove depths are also replicated accurately (Fig. 2.2D, Fig. 2.3A,B, 400-nm-tall master and replica ridges; Fig. 2.2E, Fig. 2.3C,D, 470-nm-tall replica ridges and 470-nm-deep replica grooves). Using this method, we are able to replicate a diverse range of topographies, representative examples of which are shown in Fig. 2.2F-I. Asymmetric microsawteeth (Fig. 2.2F) have been demonstrated to induce unidirectional cell migration through esotaxis.[131] Nanoposts with a diameter of ~500 nm (Fig. 2.2G) are on the same size scale as many bacteria, rendering these structures a useful tool for studying cytoskeletal dynamics involved in frustrated endocytosis and invagination. Curved (Fig. 2.2H) and kinked (Fig. 2.2I) nanoridges mimic collagen fibers and nodes in the branched collagen network *in vivo*, respectively, providing a platform for the systematic study of how curvature and branching angles affect intracellular dynamics.

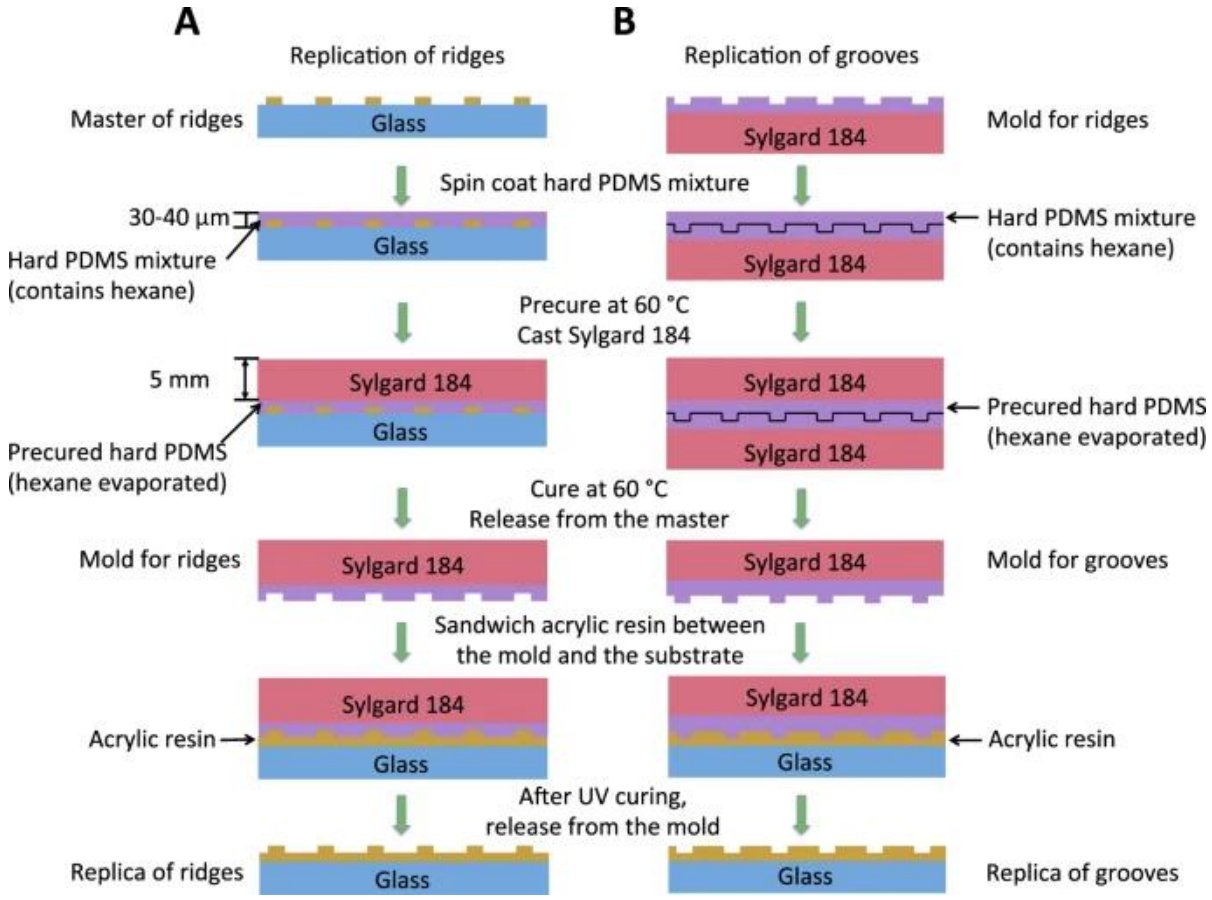

Figure 2.1. Schematic of the replication processes for nanoridges (A) and nanogrooves (B). Reprinted with permission from reference 142.

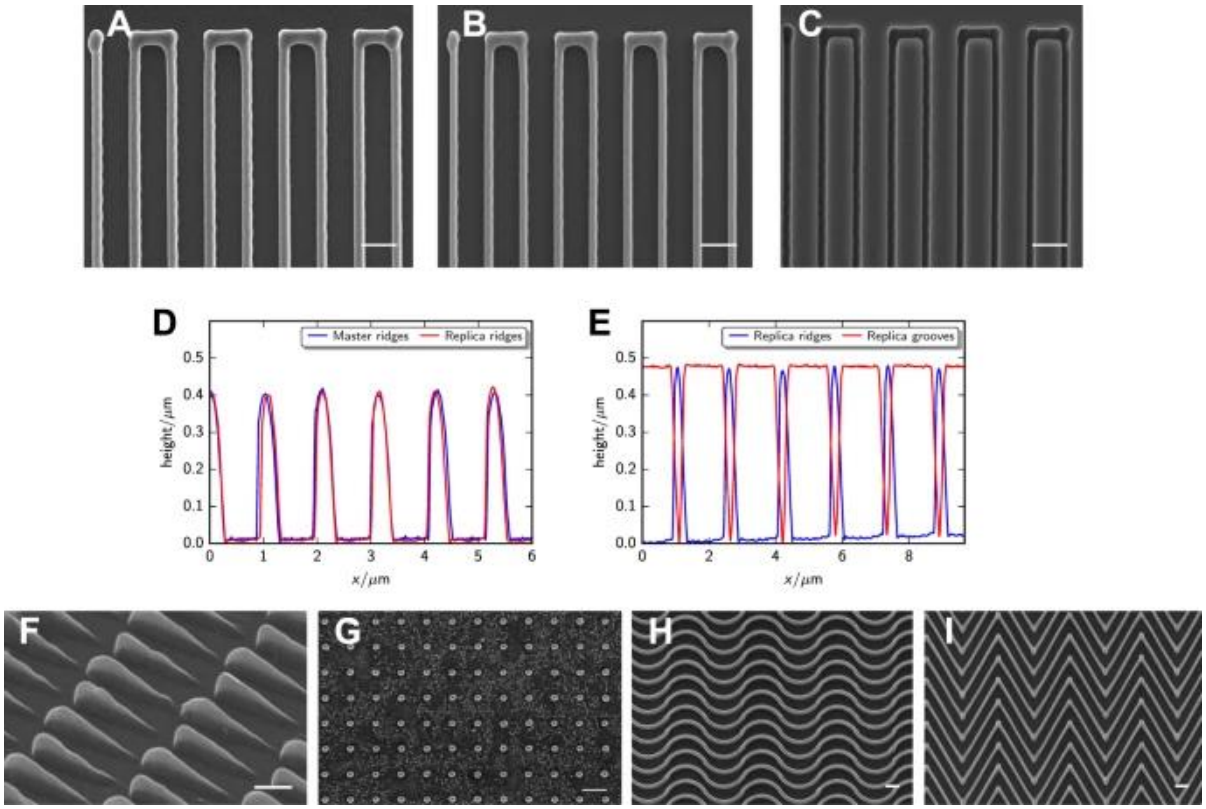

Figure 2.2. Characterization of the fidelity of the solvent-assisted nanotransfer molding. (A–C) SEM images of master ridges (A), replica ridges (B), and replica grooves (C). The negative topography C in the juxtaposition has been flipped horizontally for consistency. (D,E) Sectional AFMs of 1-μm-spaced master (blue) and replica (red) ridges (D), and 1.5-μm-spaced replica ridges (blue) and grooves (red) (E). (F–I) SEM images of asymmetric sawteeth (F), nanoposts (G), curved ridges (H), and kinked ridges (I). Scale bars, 1.5 μm (A–C), 1 μm (F), and 2 μm (G–I). Reprinted with permission from reference 142.

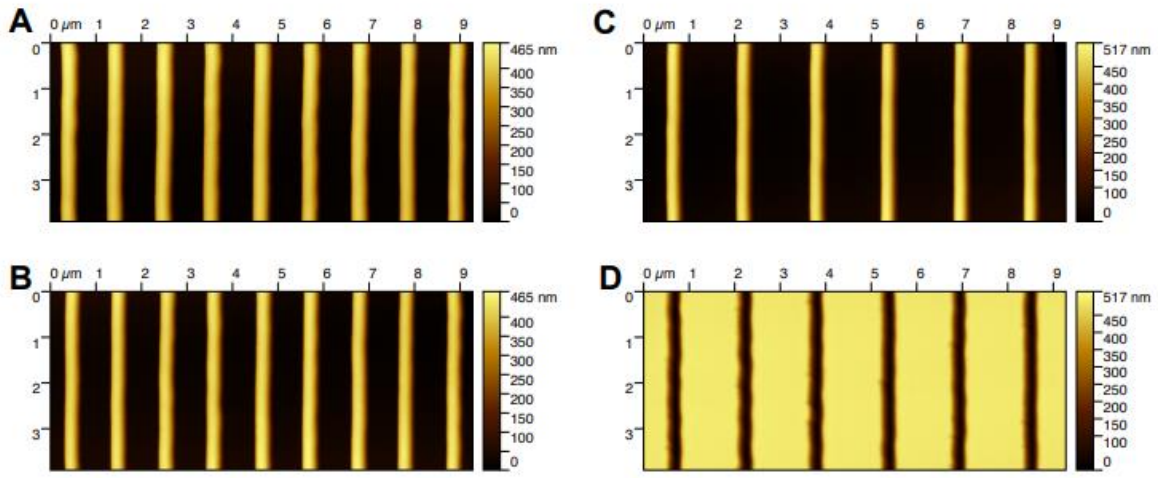

Figure 2.3 AFMs of 1-µm-spaced master (A) and replica (B) ridges, and 1.5-µm-spaced replica ridges (C) and grooves (D). Reprinted with permission from reference 142.

To assess the resolution of the solvent-assisted nanotransfer molding, it would be desirable to mold nanostructures that are smaller and more closely-packed than the aforementioned nanotopographies. However, the typical width of a MAP-fabricated voxel is ~300 nm. To test whether our method is capable of molding features smaller than 300 nm, an alternative master nanotopography was needed. Therefore, nanograss with a thickness and spacing of ~25 nm (Fig. 2.4A,B) was used to investigate the resolution. This nanograss was created by subjecting the nanoridges to reactive ion etching (RIE). As shown in Fig. 2.4, the replica nanograss (Fig. 2.4C,D) exhibits thickness and spacing that are similar to those of the master nanograss (Fig. 2.4A,B), suggesting that the resolution of the molding is at least as fine as 25 nm.

We coated the nanoridges with collagen IV to render the surfaces adherent to mammalian cells such as MCF10A human breast epithelial cells and HL60 neutrophil-like cells. It is also

possible to functionalize the surface of the nanotopograhical substrate with other ECM proteins. The exposed amine groups on collagen can react naturally with surface acrylate groups through Michael addition.[143] The collagen IV used in our studies, however, is stabilized in a solution of 0.05 N HCl. Michael addition reactions require basic (or nearly basic) conditions. Although it is possible to transition the solution to basic conditions through the addition of certain salts to stabilize and prevent denaturation of the protein, this is not necessary for our purposes, as the collagen IV remains adsorbed on the surface of the acrylic substrate even after multiple rinses and changes of the cell medium.

To characterize the collagen coating, we treated the collagen-IV-coated nanoridges with NHS Alexa 594, which fluorescently labels the protein but not the acrylic polymer (Fig. 2.5). Figure 2.5A shows the average cross section reconstructed from confocal z-stack images, which starts below the bottom surface and ends above the tops of the nanoridges. The uniform fluorescence delineates the contour of the nanoridges, whereas the bulk polymer region remains dark. This phenomenon indicates that the nanoridges are coated conformally with collagen. The fluorescence along the sides of the ridges and the middles of the trenches further confirms the conformal nature of the collagen coating (Fig. 2.5B,C). [Note that the thickness of the coating is exaggerated in the axial direction due to the elongated point-spread function of the microscope.] Similar results were obtained on nanoridges coated with fluorescently labeled fibronectin (Fig. 2.6), indicating the functionalization of nanotopographies replicated in acrylic resin is not protein-specific. Any protein/peptide with surface amine and/or thiol groups is expected to exhibit good adhesion. The curing time of the replica can also be tuned to adjust the density of residual acrylate groups on the polymer surface available for the subsequent protein coating.[143]

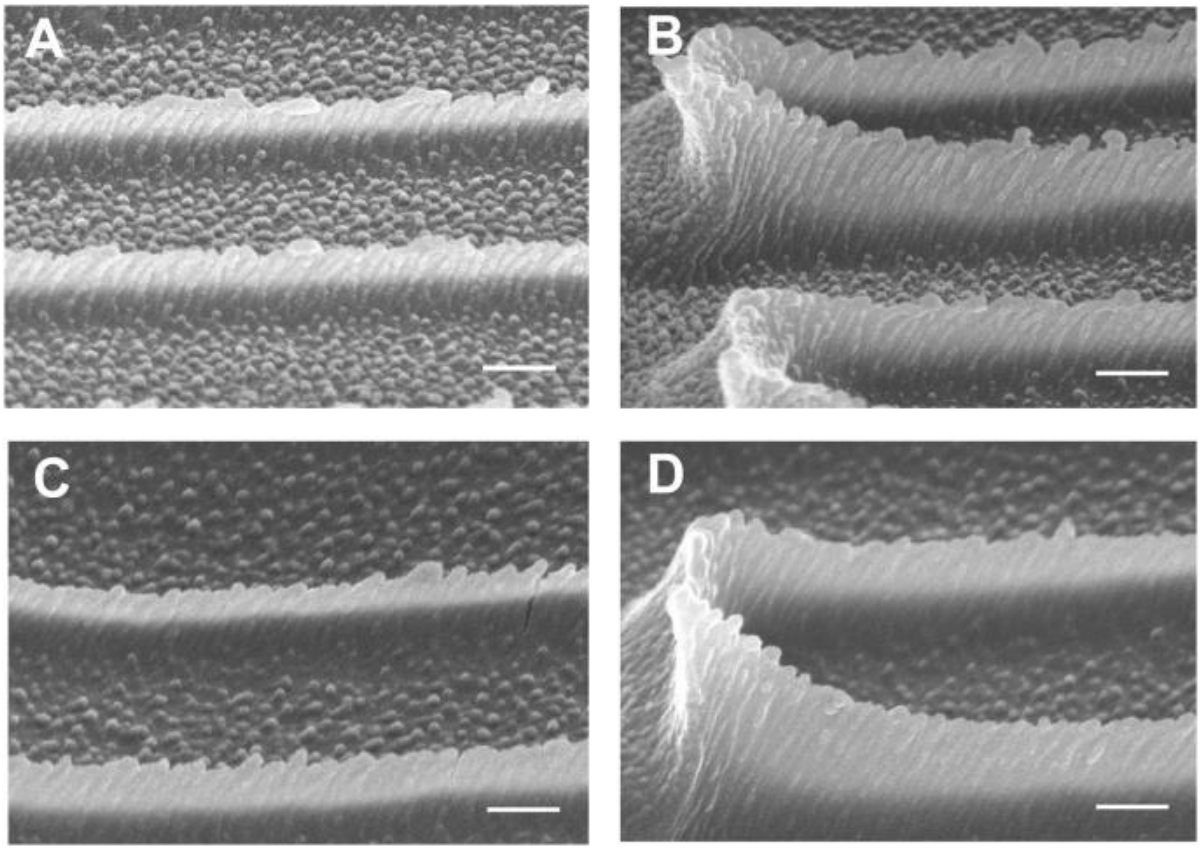

Figure 2.4. Replication of nanograss. SEM images of the master (A,B) and replica (C,D) nanograss. Scale bars, 200 nm. Reprinted with permission from reference 142.

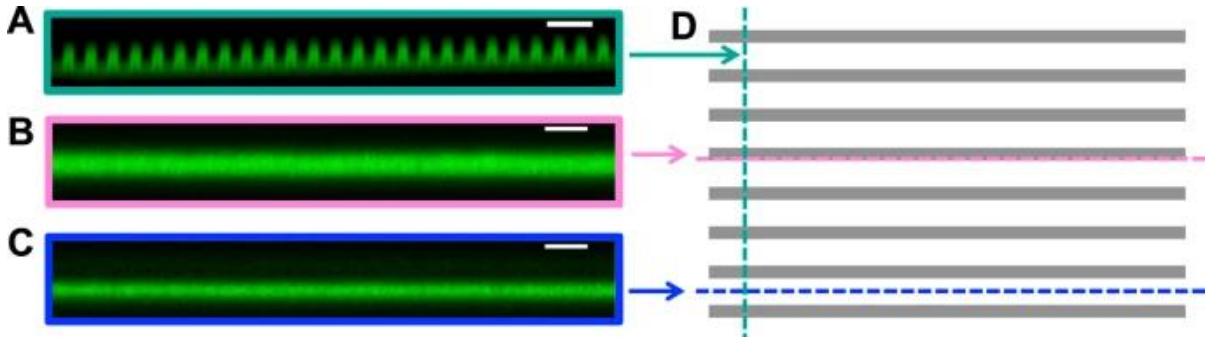

Figure 2.5. Functionalization of nanoridges with collagen IV. (A–C) Side-view images of the fluorescent-collagen-coated nanoridges reconstructed from z-stack confocal images. The planes are perpendicular to the surface in the position of the dashed lines in (D) of the color of the image borders. (D) Top-view schematic of nanoridges with grey representing the ridges. Scale bars, 3 μm. Reprinted with permission from reference 142.

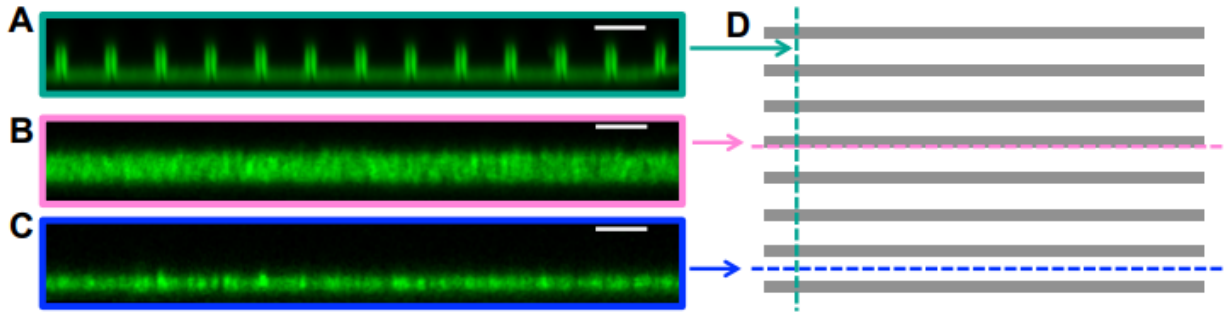

Figure 2.6. Functionalization of nanoridges with fluorescently labeled fibronectin. (A-C) Side-view images of the fluorescent-fibronectin-coated nanoridges reconstructed from z-stack confocal images. The planes are perpendicular to the surface in the position of the dashed lines in (D) of the color of the image borders. Scale bars, 3 μm. Reprinted with permission from reference 142.

To investigate how replicated nanotopography affects cytoskeletal alignment and the distribution of focal adhesions, we plated individual MCF10A cells on collagen-IV-coated nanoridges and nanogrooves, and fixed the cells after 12 h. Cells tend to elongate along the 1.5-μm- and 2-μm-spaced ridges and grooves (Fig. 2.7A–F). Both F-actin (Fig. 2.7A) and microtubules (MTs) (Fig. 2.7B) form long fibers that align along the ridges. We observed strong alignment of MTs but not of F-actin near the trailing edge of the same cell (cf. the right part of the cell in Fig. 2.7A,B), indicating that MTs align naturally along the ridges, rather than being dragged into alignment by F-actin. Inside the grooves, however, F-actin primarily forms long streaks (Fig. 2.7C), whereas MTs barely appear (Fig. 2.7D). Differences in the localization of focal adhesions (FAs) are also observed between cells on the ridges and cells on the grooves, although FAs form on both types of nanotopography (Fig. 2.7E–H). FAs prefer to localize on most of the ridge area covered by the cell, especially near the cell periphery (Fig. 2.7E,G).

However, FAs either only localize in limited numbers inside the grooves that are near the cell periphery (Fig. 2.7F), or barely appear inside the grooves (Fig. 2.7H). Even though F-actin forms streaks in the grooves covered by the interior cellular region, FAs still avoid those groove areas (Fig. 2.7H).

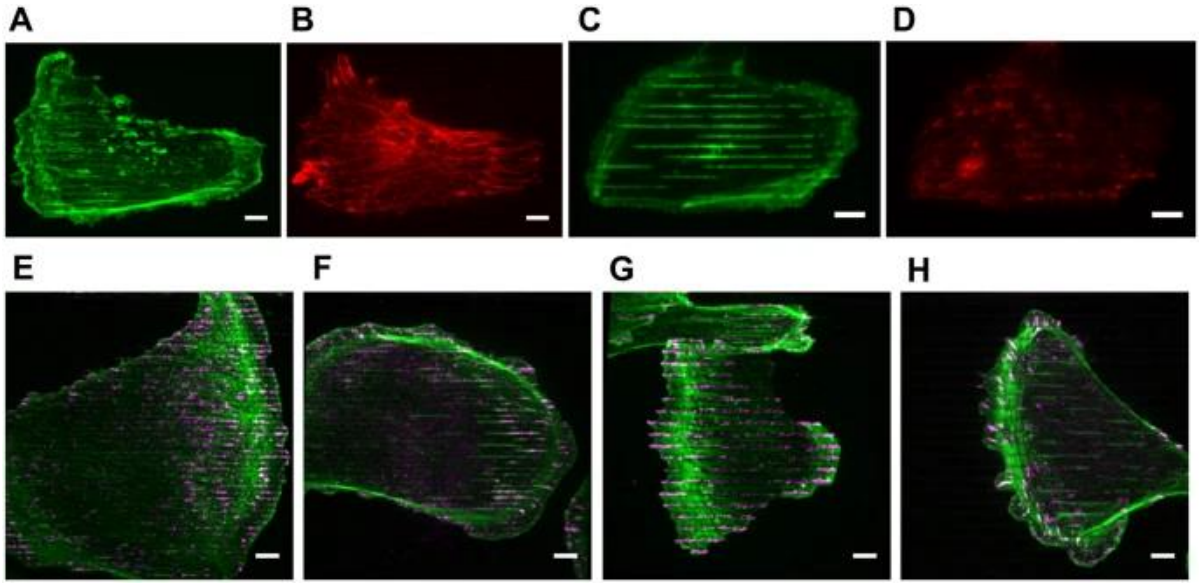

Figure 2.7. Cytoskeletal alignment and focal adhesion distribution on nanoridges and nanogrooves. (A–H) Maximum intensity projection of confocal z-stacks that go through the entire ridge/groove volume. The nanoridges/grooves are horizontally oriented. (A–D) Actin (A,C) and tubulin (B,D) stain of one cell on 2-μm-spaced nanoridges (A,B) and another cell on 2-μm-spaced nanogrooves (C,D). (E–H) Actin (green) and paxillin (magenta) stain of cells on nanoridges (E, 1.5-μm-spaced; (G) 3-μm-spaced) and nanogrooves (F, 1.5-μm-spaced; (H) 3-μm-spaced). Scale bars, 6 μm. Reprinted with permission from reference 142.

The use of photoinitiators, which are incorporated into the polymer upon reaction and are then no longer photoactive, is advantageous over the use of photosensitizers such as Rose

Bengal,[144,145] which retain their ability to generate radicals after polymerization. To ensure the creation of non-cytotoxic replicas of nanotopographies, we molded 6.4-μm-spaced nanoridges using acrylic resins prepared with a range of different photoinitiators. To remove potentially toxic unreacted photoinitiator molecules and byproducts of polymerization, the surfaces were soaked in ethanol and water before being coated with collagen IV and plated with MCF10A cells. Table 2.1 lists the photoinitiators that were tested, with the corresponding minimum concentrations required for the faithful replication of nanoridges, along with the average viability of MCF10A cells 48 hours after being plated. Collagen-IV-coated glass and tissue-culture-treated culture dishes served as controls. Also included as a reference is a collagen-IV-coated, nanoridge substrate replicated with 2 wt% TPO-L, the same photoinitiator/concentration used to replicate the topographies shown in Figures 2.1 and 2.2. We found that cell viabilities were above 95% on almost all the surfaces, except for ones replicated with benzoin methyl ether as the photoinitiator (Table 2.1, Fig. 2.8). On some of the surfaces, the cell viabilities were even higher than those on the control surfaces. It is worth noting, however, that these data were not obtained under imaging conditions. Free radicals could be created during imaging by any residual photoinitiators, which may render the surface toxic to the cells. We have never observed this phenomenon, but in the event of any cytotoxicity during imaging the replication process should be optimized for the specific imaging conditions required for any given application.

Table 2.1. MCF10A cell viability averaged over three experiments on nanoridge surfaces replicated with various photoinitiators. Reprinted with permission from reference 142.

Photoinitiator/Control	Concentration (wt%)	Viability (%)
Irgacure 184	1.12	95
Irgacure 369	0.92	98
Irgacure 651	1.19	96
Irgacure 819	0.59	97
Irgacure TPO-L	2.01	96
Benzoin methyl ether	1.32	68
Collagen-coated glass	NA	96
Tissue culture plate	NA	96

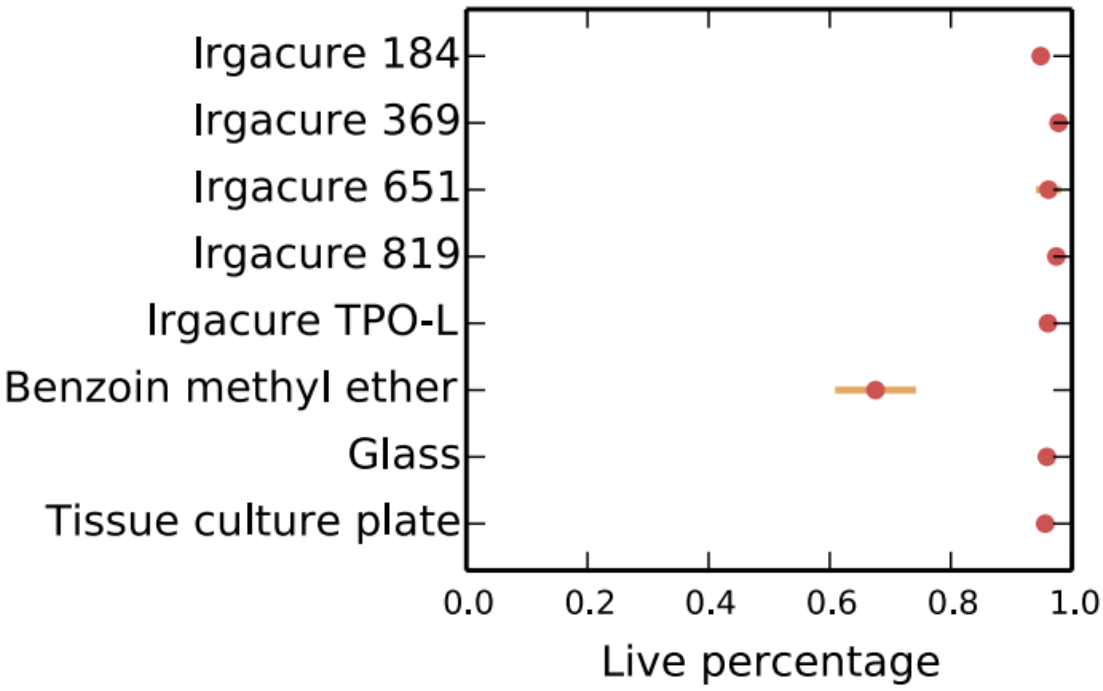

Figure 2.8. Percentages of live cells 48 h after plating on nanoridges replicated with various photoinitiators. Error bars represent the standard error of the mean. Reprinted with permission from reference 142.

2.3. Discussion

We have demonstrated a method for the mass production of biocompatible, nanotopographic surfaces. The method is also capable of replicating complementary nanotopographies. The acrylic resin employed in the replica molding not only facilitates the subsequent surface functionalization for biological and biomedical applications, but also results in a rigid and highly transparent nanotopographic coating that can be used for high-resolution, live-cell imaging. We have previously found that the Young's modulus of this acrylic polymer that was cured with UV light is 2 GPa.[146] Cells typically deform substrates that have a stiffness

in the range of tens of kiloPascals or less,[147] so our replica surfaces are rigid enough to resist the cellular traction forces and to maintain the original topographies. 2 GPa is comparable to the rigidity of collagen fibers,[148] making the nanotopographic surfaces relevant to *in vivo* processes. The method is also applicable to replicating nanotopography that covers a large area, allowing specific proteins involved in mechanosensing and mechanotransduction pathways to be analyzed by techniques such as SDS-PAGE and enzyme-linked immunosorbent assays. In the work reported here the master is created using either MAP or RIE, but our replication technique is compatible with a wide variety of methods for the production of masters. Each master can be molded numerous times, and the resulting PDMS mold can be used more than 30 times without discernible damage. Each replica can also serve as a master and be molded repeatedly through the same process, allowing the production of a virtually unlimited number of replicas. In addition to acrylic resins, a broad range of other materials can be used for replication, although other materials require different surface-functionalization chemistries.

The theoretical resolution limit of nanotransfer molding is determined by the average chemical bond length and distance between crosslinks in hard PDMS,[149] as well as by the interaction between the master and the hard PDMS surfaces.[150] The increased wettability of hard PDMS prepolymer on the master surface and the increased crosslink density of the cured hard PDMS result in an improved molding resolution. The formulation and curing temperature of the hard PDMS prepolymer could be further tuned towards an even higher crosslink density. To increase the wettability of the hard PDMS, the molecular composition and the roughness of the hard PDMS and master surfaces need to be considered. In all the molding experiments we performed, the master surfaces were coated with a fluorocarbon to reduce the surface energy, facilitating the release of the PDMS mold. However, a low-energy surface is associated with a

low wettability, which prevents the hard PDMS prepolymer from conforming perfectly to the nanotopography. On a low-energy surface, the cosine of the contact angle increases linearly as the surface tension of the liquid decreases.[151] Therefore, adding a solvent to the hard PDMS prepolymer may reduce the surface tension and improve the conformability. Hexane possesses low surface tension (γ = 18.4 mN/m at 20 °C) and low viscosity (0.67 cp at 25 °C). The fact that hexane is miscible with the PDMS prepolymer[152] prevents phase separation of the mixture, thus making this solvent an ideal candidate for improving the molding resolution. Limited by the available smallest features on the master nanotopography, we demonstrated a molding resolution of ~25 nm with nanograss (Fig. 2.4). However, the actual resolution could be even finer. When the features to be molded approach the molecular scale, the thickness of the anti-adhesion coating needs to be considered, as this coating will influence the geometry of the underlying nanotopography. Fluorocarbon molecules with a shorter chain length can be used, provided that the resultant surface energy is low enough to release the PDMS mold. Additionally, in our attempts to mold nanotopographies with high-curvature features, such as concentric rings and sinusoidal waves, the PDMS mold tended to stick to the high-curvature features. Separating the mold from the master while the two are immersed in a solvent that does not swell PDMS (such as methanol) substantially alleviates the sticking phenomenon, presumably due to a reduction in surface adhesion[153] and roughness.[154]

An important advantage of using acrylic resin as the replica-molding material lies in the unreacted acrylate groups on the polymer surface, which can react readily with the amine and/or thiol groups exposed on a protein/peptide, allowing the nanotopographies to be functionalized with various biomolecules for cell experiments (Fig. 2.5, Fig. 2.6). Because most mammalian cells require a substrate that is chemically similar to the ECM to form integrin-mediated FAs,

substrates that are compatible with surface functionalization would be beneficial for studies of the effects of physical cues on mammalian cells. For instance, we have functionalized nanoridges with fibronectin and B-cell receptor ligand to study the contact guidance of human tumor-associated fibroblasts (TAFs)[155] and the activation of B cells,[156] respectively. We found that the TAFs and their actin stress fibers align along the nanoridges, and that the actin-wave dynamics and calcium signaling in B cells are modulated by the ridge spacing. In the present study, we demonstrate that MCF10A epithelial cells adhere to, and align along, the nanoridges/grooves (Fig. 2.7A–F). The paxillin stain indicates that the FAs form microdomains preferentially on the nanoridges (Fig. 2.7E,G). The fact that paxillin is a downstream component of the integrin-mediated signaling pathways suggests that the same localization may be observed with integrins. Because integrin activation is related to it unfolding, it would be interesting to investigate how nanotopography affects the conformational change of integrin, as well as how it affects downstream processes such as calcium signaling. Rather than coating the surface with collagen/fibronectin to enhance cell–substrate adhesion, coating the nanotopographic surface with bovine serum albumin or concanavalin A can decouple the influence of physical cues from that of substrate-adherent ligand on the activation of integrin. Furthermore, the unreacted acrylate groups on the polymer surface also allow the nanotopography to be functionalized with other molecules, such as perfluorocarbons and polyethylene glycol, to study non-integrin-mediated cell adhesion or migration. For instance, the collective migration of *Dictyosteliuim discoideum* cells has been found to be affected substantially by surface adhesivity.[157] Because the nanotopography fosters reproducibly controlled cytoskeletal dynamics (esotaxis),[130,131] coupling nanotopography with different surface adhesivity may reveal how the actomyosin cortex

coordinates with the weak adhesion molecules to regulate the cell–substrate and cell–cell adhesion.

The replicated nanotopographic surfaces may find use in an even broader range of fields. For instance, as shown in Fig. 2.7B, MTs naturally align along the nanoridges. Therefore, nanotopographic surfaces can be used to study activities related to MT alignment, such as cell division and intracellular trafficking. Additionally, given that our method possesses a molding resolution of ~25 nm or even better, surfaces coated with nanoparticles and nanowires can be replica-molded with acrylic resin, providing nanotopography with features that approach molecular scale. These small features can be exploited to study the dynamics of curvature-sensing proteins such as the BAR-domain proteins. Although we only demonstrate single-cell studies on the nanotopographic surfaces, these surfaces can also be applied to study the effects of physical cues on cell sheets, tissues or even organoids, to elucidate the mechanisms of mechanosensing in processes such as embryonic development, immune responses, wound healing, and cancer metastasis.

2.4. Conclusions

In conclusion, we have demonstrated a method for the replication of biocompatible, complementary nanotopographies and for the functionalization of the topographies with adhesion-promoting molecules. This approach may be an attractive alternative to other methods in terms of simplicity, low cost, the range of materials that can be used, and the ease of surface functionalization. As such, this approach should facilitate the investigation of phenomena such as the effects of physical cues on the dynamics of intracellular proteins and the role of mechanosensing in processes such as cell migration, phagocytosis, division, and differentiation.

These nanotopographic surfaces can be applied to studies on single cells, as well as cell sheets, tissues and organoids, to help elucidate mechanisms in pathology and provide diagnostics for diseases.

2.5. Materials and Methods

2.5.1. Fabrication of Master Nanotopographic Surfaces.

To improve the adhesion of nanostructures, glass slides were treated with an oxygen plasma (Harrick plasma cleaner, PDC-32G) at 200 mTorr for 3 min, and immersed overnight in a solution composed of 4 mL of (3-acryloxypropyl)trimethoxysilane (SIA0200.0, Gelest), 10 mL of deionized water, and 196 mL of ethanol. The acrylate-functionalized slides were then rinsed in ethanol for 1 h and baked at 90°C for 1 h. The acrylic resin was composed of 49 wt% tris (2-hydroxyethyl) isocyanurate triacrylate (SR368, Sartomer), 49 wt% dipentaerythritol pentaacrylate (SR399, Sartomer), and 2 wt% Lucirin TPO-L (Ciba). The resin was mixed overnight to ensure homogeneity. A drop of resin was applied to the acrylate-functionalized glass slide and the slide was mounted on a piezoelectric stage (Physik Instrumente). Master nanotopographic surfaces were fabricated via MAP[106] using a commercial Ti:sapphire laser (Coherent Mira 900-F, 200 fs pulsed, 800 nm). The beam was focused on the sample through a 100× objective (NA 1.4). The power was 4 mW as measured at the sample. Upon completion of fabrication, the sample was developed in N,N-dimethylformamide and ethanol to remove the unpolymerized resin. Master nanograss[158] was created by subjecting nanoridges to RIE in a gas mixture of O_2 (5 sccm) and CHF_3 (15 sccm) at 150 W and 50 mTorr for 10 min.

2.5.2. Solvent-Assisted Nanotransfer Molding.

The method of molding the nanotopographies is adapted from prior work.[119] Briefly, the master surface was functionalized with ethylenediamine (E26266, Sigma-Aldrich) and then reacted with perfluorooctadecanoic acid (L16837, Alfa Aesar) to reduce the surface energy and facilitate the release of cured PDMS. The hard PDMS mixture was composed of 1.7 g of vinyl PDMS prepolymer (VDT-731, Gelest), 9 μL of Pt catalyst (SIP6831.2, Gelest), 0.05 g of modulator (87927, Sigma-Aldrich), 0.5 g of hydrosilane (HMS-301, Gelest), and 1 g of hexane. The mixture was spin-coated on the master surface (1000 rpm, 40 s), allowed to sit at room temperature for 2 h, and prebaked at 60 °C for 1 h. Soft PDMS was prepared by mixing the base and curing agent (Sylgard 184, Dow Corning) in a 10:1 mass ratio. After degassing, the uncured soft PDMS prepolymer was poured onto the precured hard PDMS to form a layer of roughly 5 mm thick, and was then baked at 60 °C for 1 h. After curing, the composite PDMS was peeled off of the master surface. In the double-molding process, the first mold served as a master. The mold was treated with an oxygen plasma at 200 mTorr for 30 s. The mold was then transferred into a desiccator and was exposed to the vapor of (tridecafuoro-1,1,2,2,-tetrahydrooctyl)methyldichlorosilane (SIT8172.0, Gelest) for 1 h. The master was molded in the same manner as described above. Unless otherwise noted, the acrylic resin for replicating the nanotopographic surfaces was made by mixing 49 wt% tris (2-hydroxyethyl) isocyanurate triacrylate (SR368, Sartomer), 49 wt% ethoxylated trimethylolpropane triacrylate (SR499, Sartomer), and 2 wt% Lucirin TPO-L (Ciba). Replicas of nanotopographic surfaces were created by sandwiching a drop of acrylic resin between the mold and an acrylate-functionalized coverslip and then UV curing for 5 min (Blak-Ray, B-100AP, 100 W, 365 nm; samples were cured 254 mm from the source).

2.5.3. Uniform Coating of Proteins.

Replicas were soaked in ethanol and then in ultrapure water for 12 h each to allow the unreacted photoinitiator and byproducts of polymerization to diffuse out. For collagen IV coating, replicas were immersed in 25 μg/mL collagen (354233, Corning) in 0.05 M HCl atop ice for 1 h, and then rinsed two times by aspirating in and out ultrapure water. To image the coating using a confocal fluorescence microscope, the surfaces were treated with 0.5 mg/mL Alexa Fluor 594 NHS ester (A37572, Thermo Fisher Scientific) in 0.1 M $NaHCO_3$ for 1 h, and then rinsed three times by aspirating in and out phosphate buffered saline (PBS). For fluorescent fibronectin coating, replicas were coated with 10 μg/mL HiLyte Fluor 488 fibronectin (FNR02-A, Cytoskeleton) in Hank's balanced salt solution (HBSS) at 37 °C for 1 h and rinsed three times by aspirating in and out HBSS.

2.5.4. Surface Characterization.

Master and replica surfaces were imaged using a Hitachi S-4700 SEM. The surfaces were sputter-coated with Pt/Pd in argon plasma at 20 mA for 25 s (Cressington sputter coater 108). The height/depth of the structures was characterized by a Veeco Multimode AFM in tapping mode using aluminum-coated silicon probes (TAP300AL-G, Ted Pella).

A collagen-coated surface treated with Alexa Fluor 594 NHS ester was imaged in PBS using a Leica SP5 X confocal microscope with a 100× objective (NA 1.4) and a scanner zoom factor of 4. Images were obtained in a 512 × 512 pixel format. The fluorescent-fibronectin-coated surface was imaged in HBSS in the same manner. The orthogonal view is a single slice reconstructed from z-stack images.

2.5.5. Cell Culture, Fixing, and Staining.

MCF10A cells were cultured in DMEM/F-12 medium (11330-057, Thermo Fisher Scientific) supplemented with 5% horse serum (26050-088, Invitrogen), 10 μg/mL insulin (12585-014, Thermo Fisher Scientific), 10 ng/mL EGF (AF-100-15, PeproTech), 0.5 μg/mL hydrocortisone (H0888, Sigma-Aldrich) and 100 ng/mL cholera toxin (C8052, Sigma-Aldrich). 2 mL of MCF10A cells with a density of 1×10^4 cells/mL were plated on collagen-IV-coated 1.5-μm-spaced ridges and were incubated at 37 °C overnight. To stain tubulin and actin, the cells were fixed with 4% paraformaldehyde in DMEM/F-12 containing 50 mM PIPES for 10 min and permeabilized with 1% Saponin for 10 min. The samples were blocked in 1% bovine serum albumin (BSA) for 1 h, incubated with 1:400 anti-tubulin primary antibody (MAB1864, rat host, EMD Millipore) at 4 °C overnight, and washed three times in PBS for 5 min each. Next, the samples were incubated at room temperature for 1 h with 1:250 goat anti-rat IgG secondary antibody conjugated to Alexa Fluor 568 (A-11077, Thermo Fisher Scientific), and 1:200 phalloidin conjugated to Alexa Fluor 488 (A12379, Thermo Fisher Scientific), and then incubated at room temperature for another 15 min with 1:40000 DAPI (4’,6-diamidino-2-phenylindole, D1306, Thermo Fisher Scientific). Finally, the samples were washed three times in PBS for 5 min each. A standard protocol was adopted to stain paxillin and actin. Briefly, the cells were fixed with 4% paraformaldehyde in PBS and permeabilized with 0.2% Triton X-100 in PBS. The samples were blocked in 1% BSA for 1 h, incubated at 4 °C overnight with 1:500 phospho-paxillin pTyr118 primary antibody (44–722G, rabbit host, Thermo Fisher Scientific), and then incubated at room temperature for 1 h with 1:250 goat anti-rabbit IgG secondary antibody conjugated to Alexa Fluor 568 (A-11011, Thermo Fisher Scientific) and 1:200 phalloidin conjugated to Alexa Fluor 488 (A12379, Thermo Fisher Scientific). Finally, the

samples were imaged using a Perkin Elmer spinning-disk confocal microscope with a 100× objective (NA 1.49).

2.5.6. Evaluation of Cytotoxicity.

Resins were made by mixing SR368, SR499, and photoinitiators at the weight percentages listed in Table 2.1. The systematic names of the listed photoinitiators are (going from the top to the bottom of Table 2.1): 1-hydroxycyclohexyl-phenyl-ketone, 2-benzyl-2-(dimethylamino)-4′-morpholinobutyrophenone, 2,2-dimethoxy-2-phenylacetophenone, phenylbis(2,4,6-trimethylbenzoyl) phosphineoxide, 2,4,6-trimethylbenzoylphenyl phosphinate. 6.4-μm-spaced ridges were replicated on acrylate-functionalized coverslips and coated with collagen IV. Collagen-coated glass and tissue-culture-treated culture dish (CLS430165, Corning) served as control surfaces. MCF10A cells were plated in four separated 18-μL drops on each surface at a density of 1.67×10^6 cells/mL and were given 1 h to adhere to the surfaces in the incubator. Non-adherent cells were then washed off and fresh medium was added to the plate. The cells were cultured on the surfaces for 48 h before being washed with PBS and incubated in 0.25% trypsin (25200056, Invitrogen) at 37 °C for 10 min. The culture medium, washing buffer, and cell-enriched trypsin were collected and centrifuged at 200 g for 4 min. Cells were then resuspended in 50 μL of PBS and incubated with 50 μL of 0.4% Trypan Blue (15250–061, Thermo Fisher Scientific) at room temperature for 5 min. Finally, cells were loaded into a hemocytometer. The numbers of dead (blue) and live cells were counted under a microscope.

2.5.7. Image Analysis.

A custom MATLAB (MathWorks) script was used to determine the angle between the ridges and the horizontal axis from maximum intensity projection of the z-stack images. The 3D

stack was then rotated by this angle using ImageJ[159] plugin VolumeViewer to create an average image of the cross section along the ridges using the fluorescence intensity as weight for the voxels.

2.6. Acknowledgments

This work was supported by National Institutes of Health (R01GM085574) and the Air Force Office of Scientific Research (FA9550-16-1-0052). We thank C. A. Parent (National Cancer Institute, National Institutes of Health) for sharing the MCF10A epithelial cell line with us, and D. Park (Laboratory for Physical Science, University of Maryland, College Park) for his help with the reactive ion etching.

Chapter 3: Actin Cytoskeleton and Focal Adhesions Regulate the Biased Migration of Breast Cancer Cells on Nanoscale Asymmetric Sawteeth

This chapter is adapted with permission from Chen, S.; Hourwitz, M. J.; Campanello, L.; Fourkas, J. T.; Losert, W.; Parent, C. A. Actin cytoskeleton and focal adhesions regulate the biased migration of breast cancer cells on nanoscale asymmetric sawteeth. *ACS Nano* **2019**, *13*, 1454-1468. Copyright 2019 American Chemical Society. Chen cultured the cells, imaged cell migration and live-cell actin fluorescence, immunostained the cells, and analyzed cell migration and actin kymographs. Hourwitz fabricated and replicated surfaces. Campanello analyzed actin kymographs. Everyone contributed to writing and editing the manuscript.

3.1. Introduction

The ability to migrate is conserved in a wide variety of cell types throughout the phylogeny, and plays a pivotal role in many cellular processes.[123,160-162] Cells typically undergo directional migration with a relatively high persistence[163] rather than moving randomly.[164] However, the biological and physical mechanisms governing directed cell migration in many physiological and pathological processes are still poorly understood. In addition to the intrinsic characteristics of cells, the extracellular environment plays an important role in the guidance of cell movement. Cells can be guided by single or multiple extracellular cues, including chemoattractant gradients (chemotaxis),[20,165] stiffness gradients of the underlying substrate (durotaxis),[166] electric fields (electrotaxis),[167] and topographic structures on the surfaces (contact guidance).[168,169]

Cancer invasion and metastasis, processes in which active primary tumor cells migrate to adjacent tissues and eventually colonize distant organs, are major life-threatening events in cancer patients. Contact guidance is known to regulate cell adhesion, intracellular signaling, and directed migration,[126,170,171] and as such is a key component of cancer invasion. The role of the extracellular matrix (ECM) in guiding the three-dimensional (3D) migration of cancer cells *in vivo* has been studied extensively.[126,171-174] For example, the directional migration of carcinoma cells can be enhanced by aligned collagen fibers, especially for breast cancer stem-cell populations.[173] Furthermore, Alexander *et al.* suggested that cancer-cell dissemination patterns, including individual cell invasion, diffusively collective invasion, and strand-like invasion, are governed by the ECM structures that tumor cells encounter.[172] However, the topographic features dictating the invasion pattern remain unknown, as do the mechanisms by which tumor cells sense topographic features on a subcellular level. Nanofabrication techniques have inspired the rapid growth of materials that mimic natural *in vivo* topographies or 3D environments.[175] Recent studies have shown that engineered nanotopographies can not only cause cells to recapitulate *in vivo* migrational behaviors[176-178] but also influence various cell functions.[179-181] Thus, nanopatterned substrates have the potential to provide insight into the physical and molecular mechanisms that regulate contact guidance during cancer progression.

The ability of patterned topographies to induce directional cell migration is a complex process that requires coordination between distinct cellular machineries, such as the assembly and disassembly of focal adhesions (FAs), the polymerization and depolymerization of actin filaments, and even the reorganization of organelles.[182] The formation of a FA is initiated by the engagement of integrins with their corresponding ligands on the substrate, followed with the recruitment of FAK, paxillin, vinculin, and other associated proteins.[183] The FA-associated

proteins not only link the integrin receptors with the actin cytoskeleton[49] but also regulate actin polymerization and contractility through Rho GTPase signaling.[36] Furthermore, the actin cytoskeleton controls the protrusive activity of migrating cells, which in turn mediates the formation of adhesions. Recent studies from our group on *Dictyostelium discoideum* (*D. discoideum*) cells and neutrophils have shown that actin polymerization occurs preferentially near nanoridges, leading to guided traveling waves that can bias cellular movement bidirectionally.[130] In the case of asymmetric nanotopographies this motion can be biased unidirectionally.[131] It is also well established that various cell types elongate and exhibit aligned stress fibers when placed on ridges or grooves with widths and repeat distances on a subcellular scale.[184-186] Ray *et al.* reported that the anisotropic force originating from local FAs and the concomitant alignment of actin fibers induces the polarization and migration of carcinoma cells along ridges, and that the guidance response varies considerably among different types of carcinoma cells.[178] However, the link between the intrinsic heterogeneity of cancer cell lines and its influence on FA and actin dynamics during contact guidance is poorly understood.

Here, we study the migrational phenotypes of multiple breast-cancer cell lines plated on aligned ridges and asymmetric sawtooth architectures. Data from long-term live-cell imaging enable us to perform extensive analysis of cell migration, actin polymerization dynamics, and FA distributions. Our findings elucidate the connection between the overall cell motility phenotype of breast-cancer cells and their intracellular scaffolding architectures, adhesion complexes, and actin cytoskeleton, and also provide insights into the biophysical mechanisms underlying contact guidance during cancer metastasis.

3.2. Results and Discussion

3.2.1. Nanoridges Provide Bidirectional Guidance for Both Benign and Metastatic Breast Cancer Cells

We compare the migration phenotypes of two cell lines belonging to the MCF10A cell series, a breast-cancer progression model,[187-189] to explore contact guidance in cell lines sharing a similar genetic background but with distinct metastatic abilities. MCF10A (also referred to as M1), a benign epithelial human cell line, and its metastatic mutant cell line counterpart MCF10CA1 (also referred to as M4) were studied on flat surfaces and on nanoridges composed of the same material. The M1 and M4 cells are negative for receptors for estrogen, progesterone, and HER2 (*i.e.*, triple negative).[190] Compared to immortalized epithelial M1 cells, the invasive M4 cells form tumors in the lungs of immunocompromised mice after tail-vein injection.[189,191]

Arrays of parallel nanoridges or nanogrooves (where nano implies that their widths are on the nanoscale) have been used in previous contact guidance studies.[176,192,193] Here, we use nanotopographies composed of an acrylic resin.[142] Each nanoridge has a width of ~250 nm and a height of ~1 μm, and the spacing between the centers of adjacent nanoridges is 1.5 μm (Figure 3.1A). By tracing cell boundaries over time and generating spider plots of the cell tracks, we found that both M1 and M4 cells move in a random manner on a flat acrylic surface (Figure 3.2Ai,ii,Ci,ii). Polar histograms of the directions of both M1 and M4 cells demonstrate that there is no preferred direction of motion, as expected for a microenvironment in which no chemoattractant gradient nor other guidance cue is present (Figure 3.2Aiii,Ciii). However, M1 and M4 cells migrating on nanoridges move preferentially parallel to the nanoridges (Figure 3.2Bi,ii,Di,ii), as is also seen in polar histograms (Figure 3.2Biii,Diii). This finding is consistent

with previous results showing that parallel micro- or nanoscale grooves and ridges induce bidirectional guidance in a variety of cell types.[130,192-195] M1 cells exhibit a notably stronger guidance response to the nanoridges than do M4 cells (Figure 3.2Biii,Diii), suggesting that the ability of cells to follow guidance cues is cell-type-dependent. We also found that although the nanoridges provide guidance for cell migration, they do not increase the mean cell speed compared to the flat resin surface and, in the case of M4 cells, actually decrease the mean speed (Figure 3.2E). To explore this behavior in more detail, we measured the mean value of all velocities within a given angle range relative to the orientation of the nanoridges. We define the angle of motion as ranging from −180 to +180°, with the ridge direction along the *x* axis. Because the ridges are aligned horizontally in our images of ridges, on flat surfaces, the horizontal direction in images was also defined as the *x* axis. We found that on flat surfaces, the mean velocity value is independent of angle for both cell types, within our experimental uncertainty (Figure 3.2F). However, on nanoridges, both M1 and M4 cells exhibit a mean velocity when migrating along the ridge orientation that is higher than the mean velocity when migrating perpendicular to it (Figure 3.2F). To confirm the significance of this trend, we fitted the experimental results with a horizontal line model and a one-phase decay model, and compared the robustness of two models for each curve. We found that for M1 and M4 cells on flat surfaces, the fit of the horizontal line model is preferred; however, the fit of the one-phase decay model is preferred for the two cell lines on nanoridges ($P < 0.0001$ and $P = 0.001$ for M1 and M4 cells, respectively). Together, these findings show that cells not only migrate preferentially along nanoridges, but also migrate faster along nanoridges than perpendicular to nanoridges.

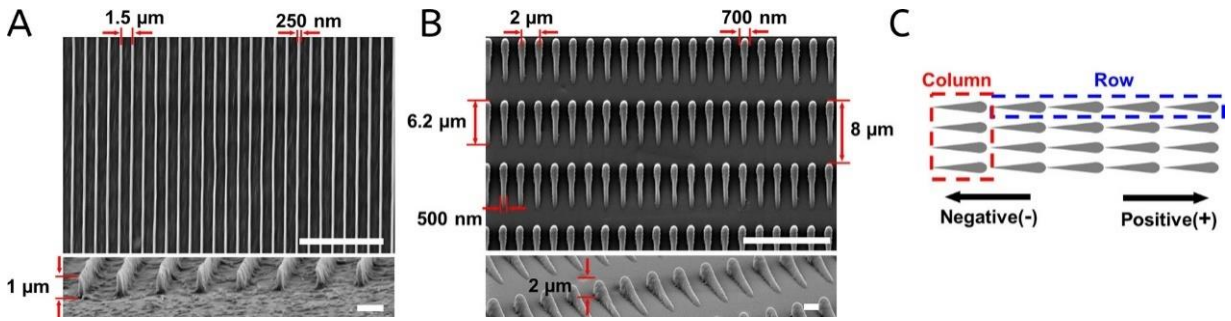

Figure 3.1. Nanotopographies used in this study. Top-view and side-view SEM images of (A) nanoridges and (B) asymmetric sawteeth used in this study. The scale bars in the top- and side-view images are 10 µm and 1 µm, respectively. (C) Schematic depicting a sawtooth row (blue box) and a sawtooth column (red box), as well as the direction defined as positive. Reprinted with permission from reference 196, © 2019 American Chemical Society.

Scanning electron microscopy (SEM) provides further insights into how cells interact with the nanoridges. On nanoridges, the lamellipodia of M1 cells form along nanoridges on both sides of the cell and are anchored on top of the nanoridges, without much penetration into the regions between nanoridges (Figure 3.2G). One possible explanation for this phenomenon is that the nanoridges guide M1 cells bidirectionally because lamellipodium formation is promoted along the ridge direction and/or is suppressed perpendicular to the ridge direction. In contrast, M4 cells form lamellipodia that curve over nanoridges and into the bottom of the regions between nanoridges, and typically span several nanoridges (Figure 3.2G, white arrows). Because contact guidance relies upon the spatial control of cell protrusions,[177] the behavior of the lamellipodia of M4 cells likely contributes to their lower contact guidance as compared to M1 cells.

3.2.2. Asymmetric Sawteeth Bias the Movement of Breast Cancer Cells in a Cell-Type-Dependent Manner

We next consider the ability of breast-cancer cells to respond to asymmetries in texture using sawtooth-shaped asymmetric nanotopographies. Each sawtooth has a maximum height of ∼2 μm, a length of ∼6.2 μm, and a width of ∼700 nm at the head and ∼500 nm in the center (Figure 3.1B). The height of an individual sawtooth increases gradually from its tail to its head and then drops rapidly. The pitch of the sawteeth is 8 μm along the sawtooth direction and 2 μm perpendicular to the sawtooth direction. We define a line of sawteeth along the sawtooth direction as a row. As all of the rows are in registry, we define a line of sawteeth perpendicular to the rows as a column (Figure 3.1C). We define the direction from the tail of a sawtooth to its head (up the slope) as the positive direction along the *x* axis.

Figure 3.2 (next page). Nanoridges provide bidirectional guidance for benign and metastatic breast cancer cells. (A–Di) Bright-field images of M1 or M4 cells on a flat surface (A,C) and on nanoridges (B,D). The colored outlines depict how the cell morphology changes over time, which increases from blue to red. The scale bar is 10 μm. (A–Dii) Centroid motion tracks of M1 and M4 cells, respectively, on a flat surface (A,C) and on nanoridges (B,D); n = 56 tracks (Aii); 94 tracks (Bii); 49 tracks (Cii); 68 tracks (Dii). The scale bar is 60 μm. (A–Diii) Probability distributions of cell motion directionality. The scale at the bottom corresponds to the horizontal axis in each rose plot. (E) Average cell speed of M1 and M4 cells on flat surfaces and on nanoridges. The middle solid line in each column is the mean value, and the bar is standard error of the mean; ***$p < 0.001$ (unpaired t test). (F) Average instantaneous speed of M1 and M4 cells relative to the orientation of ridges (0° along ridges, 90° perpendicular to ridges). Squares and triangles are experimental results, and solid lines are the fits to the experimental results. Blue solid line was fitted to a horizontal line, and the pink solid line was fitted to a one-phase decay model. (G) Representative SEM images of M1 (top) and M4 (bottom) cells on nanoridges. The magnified image highlights the anchoring of M1 cell lamellipodia on top of the nanoridges. White arrows indicate sites where M4 cell lamellipodia curve over the nanoridges. The scale bar is 10 μm. Reprinted with permission from reference 196, © 2019 American Chemical Society.

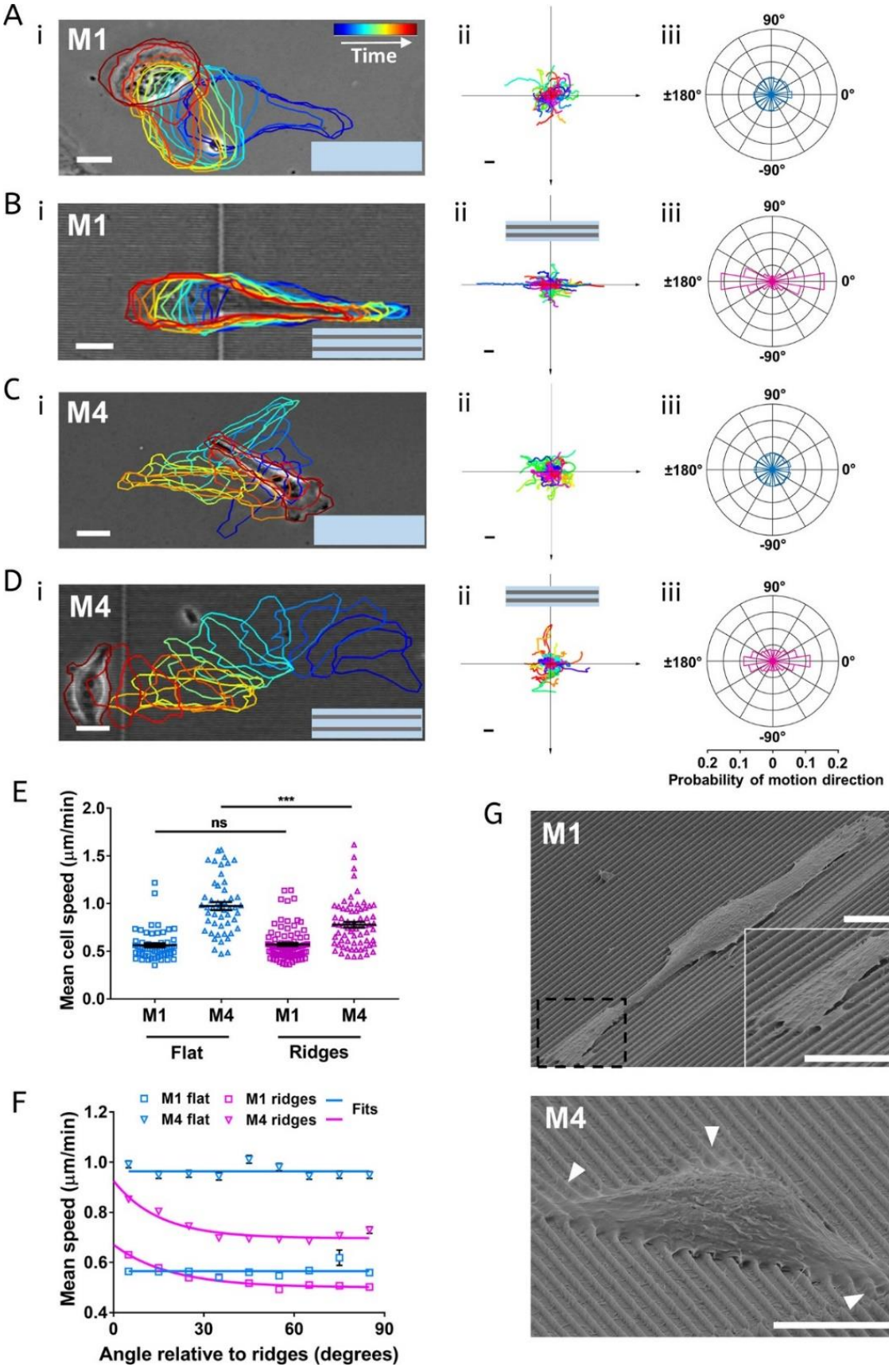
A
i
M1
Time
ii
iii
90°
±180°
0°
-90°
B
i
M1
ii
iii
90°
±180°
0°
-90°
C
i
M4
ii
iii
90°
±180°
0°
-90°
D
i
M4
ii
iii
90°
±180°
0°
-90°
0.2 0.1 0 0.1 0.2
Probability of motion direction
E
Mean cell speed (μm/min)
2.0
1.5
1.0
0.5
0.0
ns
***
M1
M4
M1
M4
Flat
Ridges
F
M1 flat
M1 ridges
Fits
M4 flat
M4 ridges
Mean speed (μm/min)
1.2
1.0
0.8
0.6
0.4
0
30
60
90
Angle relative to ridges (degrees)
G
M1
M4

We found that M1 cells plated on the sawteeth move preferentially in the positive direction with an anterior lamellipodium (Figure 3.3Ci,ii). A polar histogram of directionalities shows a higher percentage of orientation angles around 0 than 180° (Figure 3.3.Ciii). In contrast, M4 cells exhibit amoeboid-like migration, with ellipsoidal cell shapes and multiple pseudopods (Figure 3.3Ei).[197,198] Furthermore, the majority of the M4 cell tracks face in the negative direction (Figure 3.3Eii), as do the cell velocities (Figure 3.3Eiii). The preference of the M4 cells to move in the negative direction is considerably stronger than that of the M1 cells to move in the positive direction. Unlike M1 cells, M4 cells are more likely to move perpendicular to the sawteeth than to move in the positive direction.

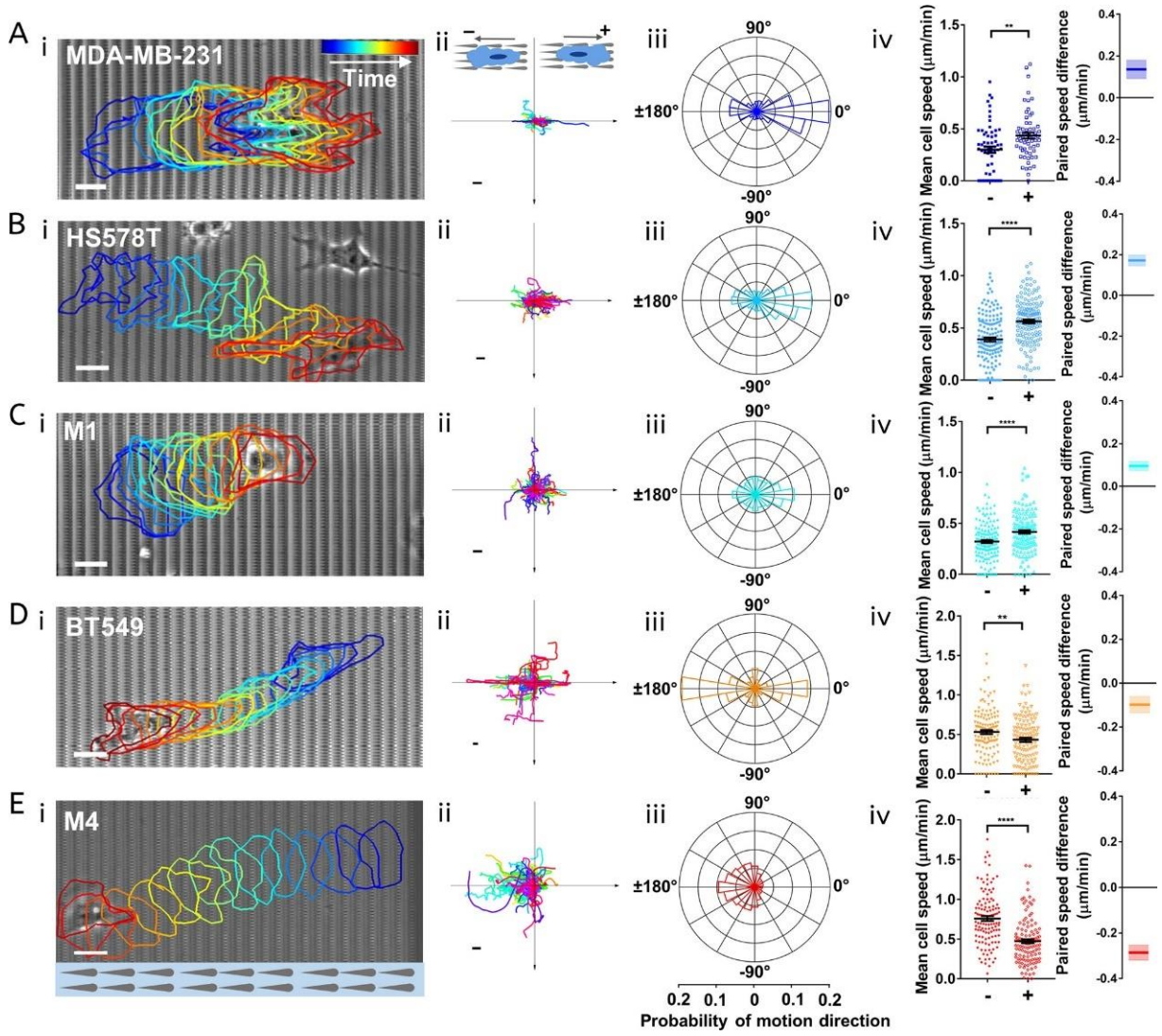

Figure 3.3. Asymmetric sawteeth bias the movement of various breast-cancer cell lines. (A–Ei) Bright-field images of (A) MDA-MB-231, (B) HS578T, (C) M1, (D) BT549, and (E) M4 cells migrating on sawteeth. The colored outlines illustrate how the cell morphology changes over time, which increases from blue to red. The scale bar is 10 μm. (A–Eii) Centroid motion tracks of (A) MDA-MB-231, 62 tracks, (B) HS578T, 151 tracks, (C) M1, 143 tracks, (D) BT549, 126 tracks, and (E) M4, 122 tracks cells on sawteeth. The scale bar is 60 μm. (A–Eiii) Probability distributions of cell motion directionality. The scale at the bottom corresponds to the horizontal axis in each rose plot. (A–Eiv) Average cell velocity components of the cell lines along the positive direction (+) and the negative direction (−) and paired speed difference for each cell. The middle solid line is the mean value, and the bar is standard error of the mean. The shaded areas represent standard errors in paired speed difference plots; *$p < 0.05$, **$p < 0.01$, ****$p < 0.0001$. Reprinted with permission from reference 196, © 2019 American Chemical Society.

We also measured the behavior of three other triple-negative human breast cancer cell lines, HS578T, MDA-MB-231, and BT549. HS578T and BT549 are carcinoma cell lines derived from primary tumors. MDA-MB-231 is a metastatic carcinoma cell line from pleural effusion.[199] We found that MDA-MB-231 and HS578T cells exhibit a mesenchymal migration mode on the sawteeth, with multiple competing protrusions (Figure 3.3Ai,Bi).[198,200] Spider plots of cell tracks and polar histograms indicate that these cells tend to move in the positive direction (Figure 3.3Aii,iii,Bii,iii). In contrast, BT549 cells migrate in a blebby (and slightly elongated) manner on the sawteeth (Figure 3.3Di). The BT549 cells preferentially move along the sawteeth, with a somewhat greater probability of moving in the negative direction than in the positive direction (Figure 3.3Dii,iii). We also found some motion of BT549 cells perpendicular to the sawteeth (Figure 3.3Diii), as was the case for M4 cells. To assess the behavior of the cells on the sawteeth further, we grouped the velocity component along the sawtooth axis into motion in the positive and negative directions, + and −, respectively. The velocities in each group were then averaged separately for each cell, and a paired speed difference for each cell was determined. We found that MDA-MB-231, HS578T, and M1 cells have higher mean speeds in the positive direction than in the negative direction, but the difference is smaller for M1 cells than for the other two cell lines (Figure 3.3Aiv,Biv,Civ). For the BT549 and M4 cells, the mean speeds in the positive direction are lower than those in the negative direction (Figure 3.3Div,Eiv). BT549 cells exhibit less paired speed difference and less unidirectional contact guidance than do M4 cells. Together, these results show that the sawteeth provide both contact guidance and unidirectional bias in migration and speed for the breast cancer cell lines studied here. Both of these phenotypes are dependent on the cell type.

We previously reported that *D. discoideum* cells and neutrophils exhibit biased directional migration when plated on asymmetric sawteeth.[131] This unidirectional topographic guidance, which is achieved by an asymmetric textures on a subcellular scale, is termed microthigmotaxis.[201] Topographic gradients represent another way to guide cell migration unidirectionally—a phenomenon called topotaxis.[25] Kim *et al.* reported that individual fibroblasts are able to sense the anisotropic gradient of ridged patterns and modify their morphology and migration in response to the local pattern density.[184] On a 2D-gradient-lattice-patterned substrate, the fibroblasts preferentially migrated toward the denser area, and ultimately accumulated at the denser zones.[202] Anisotropic variation of the density of nanoposts along one direction has also been reported to lead to the biased migration of melanoma cells.[203] Recent work from Comelles *et al.* showed that large asymmetric ratchet-like structures (at the scale of single cells) biased the motion of fibroblasts toward the positive direction of the ratchet pattern, and that this ratchet guidance was improved by superimposing a fibronectin gradient.[204] Interestingly, even without the topographic ratchet pattern, aligned ratchet-shaped adhesive fibronectin patches were able to induce a biased long-term motion that was determined by asymmetric protrusion formation.[205,206] In contrast with ratchet-like topography, the asymmetry induced by the nanoscale sawteeth in our study is at the subcellular level, suggesting that directed migration can stem from the accumulation of small biases in intracellular elements. Furthermore, we show that breast-cancer cells exhibit microthigmotactic behavior that depends strongly on cell type. Although the underlying mechanism remains to be determined, it is likely that the distinct mutation patterns and intrinsic heterogeneities of the different cell lines are reflected in the cells' contact guidance and directional bias behaviors. We speculate that such

significant differences may be related to the metastatic potential of the different cancer cell lines *in vivo*.

3.2.3. Degree of Bias in Cell Migration Is Related to Cell Speed and Long-Term Persistence

Cell migration is a heterogeneous process, in which different cells move with distinct velocity and persistence. Indeed, the direction and speed of any given cell also vary over time. To study how cell speeds influence unidirectional guidance on sawteeth, we divided histograms of the cell speeds into four quartiles (see insets of Figure 3.4Ai–Ei). We also plotted the normalized probabilities of the angle of cell motion relative to the sawtooth positive direction for each quartile (Figure 3.4Ai–Ei). For HS578T and MDA-MB-231 cells, there is no observable directional preference at low speeds, but migrational bias increases with increasing cell speed (Figure 3.4A,Bi). This trend is similarly robust for these two cell lines. In contrast, the level of directional preference of M1 cells remains low even at higher speeds, suggesting that speed and contact guidance are not strongly coupled in these cells (Figure 3.4Ci). BT549 and M4 cells behave like HS578T and MDA-MB-231 cells: unidirectional guidance increases with increasing speed (Figure 3.4Di,Ei). The trend is less evident for BT549 cells because the probability curves are considerably overlapping. Nevertheless, the probability of BT549 cells migrating along the sawtooth negative direction (~180°) keeps increasing with speed, whereas the probability for migration along intermediate angles decreases.

Using a similar segmentation approach, we investigated the effect of long-term persistence of cell motion on the unidirectional guidance of migration. We define the long-term persistence of cell motion as the ratio of the total displacement of the cell to the total length of the cell track for a chosen time interval. A cell moving in a straight line has a long-term

persistence of 1. In the case of random motion, each step of an N-step 1D random walk increases the expected value of the mean squared displacement (MSD) by 1, resulting in a root-mean-squared distance of $\sqrt{N}$. Based on this approximation, the long-term persistence of a cell moving randomly is proportional to $1/\sqrt{N}$. In this case, the long-term persistence approaches zero as *N* approaches infinity. Cells were separated into three equal fractions based on their distributions of cell persistence (see insets of Figure 3.4Aii–Eii). The normalized probabilities of the cell motion direction were then calculated by using all velocities from the cells in each of the three fractions. We found that cells with the greatest long-term persistence show the strongest contact guidance and bias toward the preferred direction of each cell line (Figure 3.4Aii–Eii). However, the directional preference is similarly vague for cells with low and intermediate long-term persistence across all cell lines (Figure 3.4Aii–Eii). For BT549 cells, the probability curves from all three fractions greatly overlap within the estimated uncertainty, suggesting that the correlation between contact guidance and cell persistence is weak in these cells. Together, we conclude that the propensity of cells to migrate in a biased fashion increases when the cells move with higher speeds or with higher directional persistence. Recently, a universal coupling between cell speed and cell persistence (UCSP) was discovered, and proved to be valid across a variety of cells and dimensional settings.[207] To test whether this UCSP law can be applied to our system, we plotted the persistence time *versus* mean instantaneous speed for all cell lines by following the definition of persistence time and the quantification method in Maiuri *et al.*[207] We also found a correlation between the persistence time and mean instantaneous speed at low speeds and a rapid saturation at high speeds for all of the breast-cancer cell lines studied here except for M4 cells, for which we observed a second rising phase at high speeds (Figure 3.5). We speculate that the rapid saturation has several causes. First, in our experimental setup, the cell density is higher and cell

trajectories are not long compared with the plating conditions of Maiuri *et al.* Second, the UCSP law assumes a linear coupling between cell speed and actin flow, which may not be valid in our setup due to the complexity induced by the sawteeth. Nevertheless, it will be interesting to examine further whether the UCSP law holds for microthigmotaxis.

Figure 3.4 (next page). Level of biased cell motion increases with cell speed and long-term persistence. Column (i) shows the probability of the direction of motion based on speed for (A) HS578T, (B) MDA-MB-231, (C) M1, (D) BT549, and (E) M4 cells. The insets show the speed distributions of the cell lines and the ranges of four sections which were equally divided based on the total counts of cell speeds. The cell speed increases from light red to dark red in both the plots and the insets. Column (ii) shows the probability of the direction of motion based on migrational persistence for the same cell lines. The insets show the long-term persistence distributions of the cell lines and the ranges of tertiles based on the total counts of cells. The long-term persistence increases from light blue to dark blue in both the plots and the insets. All error bars represent the standard error of the mean. Reprinted with permission from reference 196, © 2019 American Chemical Society.

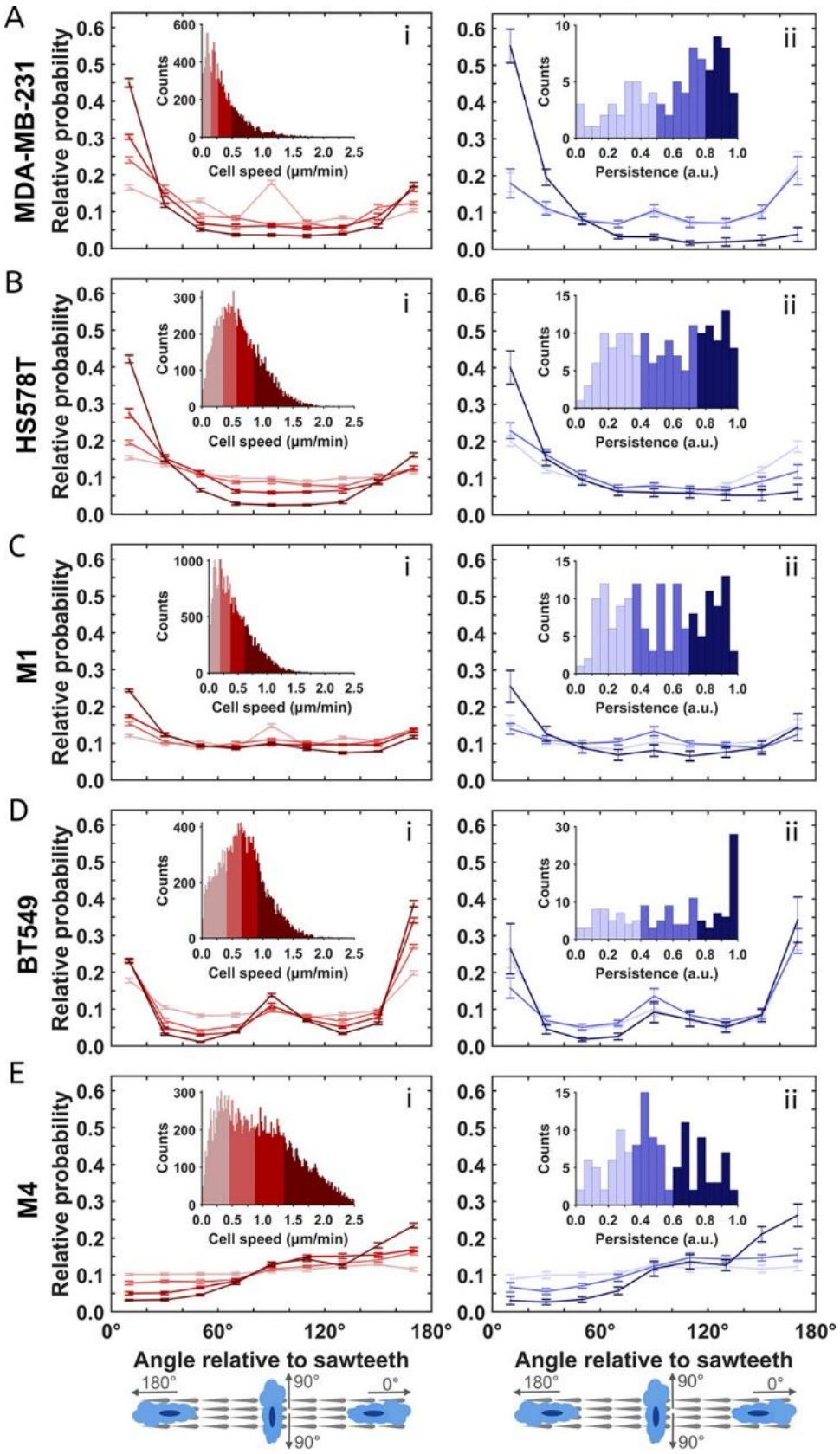
A
MDA-MB-231
B
HS578T
C
M1
D
BT549
E
M4
Relative probability
i
ii
Counts
Cell speed (μm/min)
Persistence (a.u.)
0°
60°
120°
180°
Angle relative to sawteeth
180°
90°
0°
90°

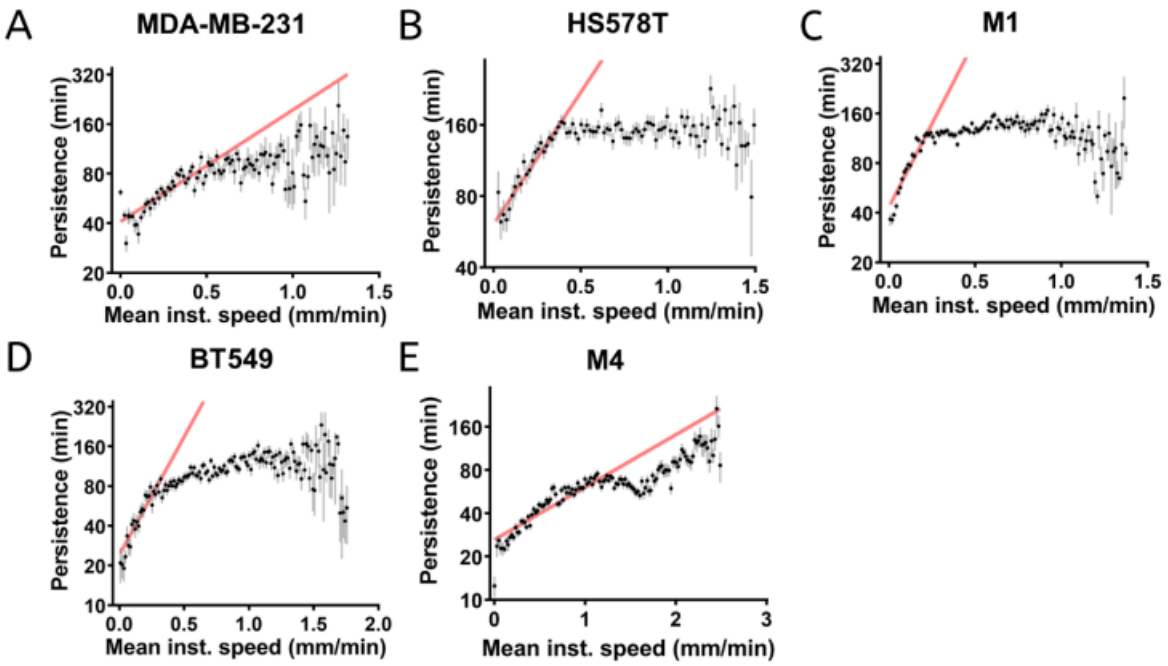

Figure 3.5. Persistence time *versus* mean instantaneous speed plots for MDA-MB-231 (A), HS578T (B), M1 (C), BT549 (D) and M4 (E) cells. The definition of persistence time in 2D geometry and the calculation method have been described previously.[207] The black dots are the mean for the data in each bin and the shaded gray lines are standard error of the mean. The shaded red lines are fits following an exponential equation $\tau = Ae^{\lambda v}$.[207] The fitting parameters are listed in Table 3.1. Reprinted with permission from reference 196, © 2019 American Chemical Society.

Table 3.1. Fitting parameters for persistence time *versus* instantaneous speed plots. Adapted with permission from reference 196, © 2019 American Chemical Society.

	MDA-MB-231	**HS578T**	**M1**	**BT549**	**M4**
A (min)	41 ± 2	61 ± 3	43 ± 3	24 ± 2	27 ± 1
λ (min · μm^{-1})	1.6 ± 0.2	2.6 ± 0.2	4.7 ± 0.4	4.1 ± 0.3	0.84 ± 0.04

3.2.4. Unidirectional Actin Polymerization Drives Biased Cell Migration

During migration and metastasis, each cancer cell dynamically reorganizes its cytoskeleton, including actin structures and microtubules, to maneuver and to adapt to complex and changing environments. Filopodia and lamellipodia are actin-rich structures that act as dynamic sensors with which cells detect their surrounding microenvironment.[177,192,208] The formation of filopodia and lamellipodia requires extensive rearrangement of cytoskeletal elements. Driscoll *et al.* found that actin polymerization in *D. discoideum* migrating on nanoridges is nucleated near the nanoridges, after which actin polymerization proceeds in a wave-like manner along the ridges (a process called esotaxis).[130] Further, it has been established previously that the unidirectionally guided motion of *D. discoideum* cells on lines of sawteeth is a consequence of esotaxis, which shares the same direction as cell motion.[131] We therefore explored the correlation between the directional bias in actin polymerization and cell motion for the MDA-MB-231 and M4 cell lines, as these cells represent two opposite extremes of contact guidance and bias. To assess actin dynamics, we used cells infected with a fluorescence-tagged protein (Lifeact-eGFP), which associates with polymerizing F-actin. Time-lapse recordings of Lifeact-eGFP/MDA-MB-231 cells reveal that these cells preferentially form distinct F-actin structures surrounding the nanosawteeth at the leading edges of cell protrusions. Actin polymerization bursts occur occasionally in the middle of migrating cells and then diffuse across the nanosawteeth. We used an optical-flow algorithm that will be described in detail elsewhere (see chapter 4) to examine the local direction of the actin polymerization flux. Zooming in on one representative sawtooth (Figure 3.6A,B), we see that actin polymerization was initiated at the tail of the sawtooth and propagated toward the head on both sides of the sawtooth in a wave-

like manner. The black arrows in Figure 3.6B represent optical-flow vectors, which are related to the local directionality of the actin waves. The optical-flow analysis indicates that actin polymerization is nucleated at the back of the sawtooth, after which the polymerization front moves forward on both sides of the sawtooth. Finally, the waves terminate at the front of the sawtooth (Figure 3.6B), which is consistent with our previous findings in *D. discoideum*.[131]

Figure 3.6 (next page). Sawteeth trigger unidirectional actin polymerization in the same direction as the cell motion in a cell-type-dependent manner. (A,E) Fluorescence images of Lifeact-eGFP/MDA-MB-231 (A) or Lifeact-eGFP/M4 (E) cells on sawteeth. The colors indicate the intensity of fluorescence. The scale bar is 20 μm. (B,F) Actin flux at different time points around a single sawtooth highlighted by the boxes in (A) and (E), respectively. The boundary of the sawtooth was generated based on the corresponding bright-field image and, due to diffractive effects, does not correspond to the actual shape of the sawtooth. The different colors represent different fluorescence intensities. The black arrows illustrate the direction of actin polymerization flux. The scale bar is 5 μm. (C,G) Averaged kymograph of actin intensity along one sawtooth boundary over time for (C) Lifeact-eGFP/MDA-MB-231 and (G) Lifeact-eGFP/M4 cells. The *x* axis is the relative time difference from defined time point, t_w, when the actin polymerization wave initiates or reaches the sawtooth position 0. The length of the *x* axis is 71 frames (11.83 min). The *y* axis is the scaled position along one sawtooth boundary, for which 0 represents the front and ±25 represents two symmetric points near the tail. The different colors represent different fluorescence intensities. (D,H) Space/time plots of actin polymerization along two adjacent sawteeth in a sawtooth row for (D) Lifeact-eGFP/MDA-MB-231 and (H) Lifeact-eGFP/M4 cells. Reprinted with permission from reference 196, © 2019 American Chemical Society.

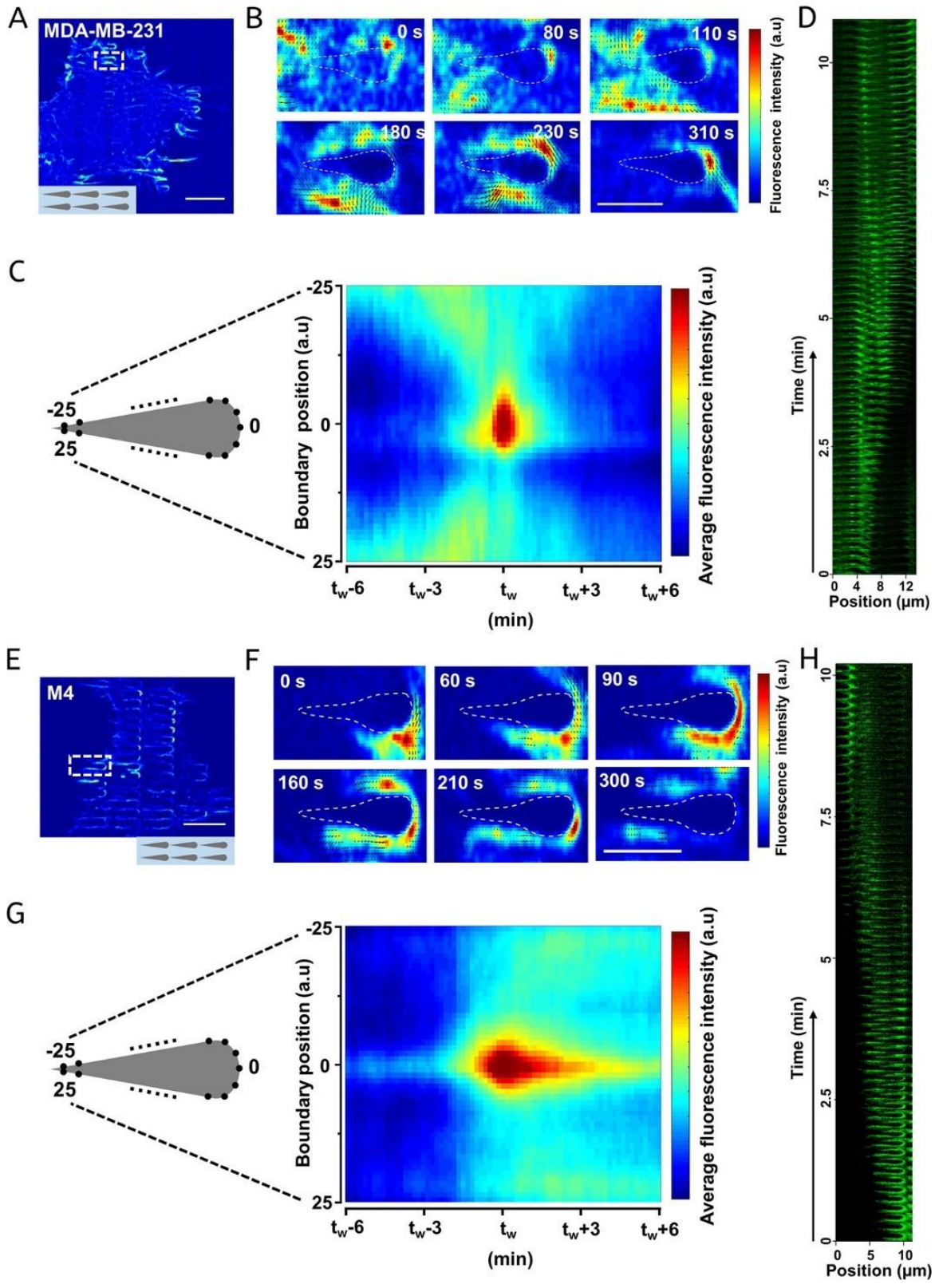
A
MDA-MB-231
B
0 s
80 s
110 s
180 s
230 s
310 s
Fluorescence intensity (a.u)
D
Time (min)
Position (μm)
C
-25
25
0
Boundary position (a.u)
Average fluorescence intensity (a.u)
t_w-6
t_w-3
t_w
t_w+3
t_w+6
(min)
E
M4
F
0 s
60 s
90 s
160 s
210 s
300 s
H
G

To assess the average actin flow around a sawtooth, we extracted the boundary of every sawtooth from the bright-field images, measured the average intensity at each of the 51 boundary points of each sawtooth, and generated a kymograph representing all boundary points (on the *y* axis, −25 to +25) over time (on the *x* axis). The average kymograph for all of the sawteeth shows that the average fluorescence intensity is higher at the tails of the sawteeth (position ± 25) at time t_w – 6, suggesting that the initiation of actin polymerization occurs there. After time t_w – 6, the average actin fluorescence slowly increases at the sides of the sawteeth, peaking at position 0 around time t_w. These findings support the conclusion that actin polymerization is nucleated at the tails of the sawteeth and moves toward the heads (Figure 3.6C). A space–time plot also shows that the actin waves propagate from one sawtooth to the adjacent one in the positive direction with a speed of ∼1 μm/min (Figure 3.6D). Thus, the unidirectional guidance of actin polymerization is in the same direction as that of the cell motion.

In Lifeact-eGFP/M4 cells, actin polymerization structures form not only at the cell protrusions but also in the middle of each cell. The actin polymerization intensity is always higher at the front of the sawteeth (Figure 3.6E). Data from a representative sawtooth reveal that actin polymerization is nucleated at the head of the sawtooth, after which the wavefront flows toward the tail of the sawtooth (Figure 3.6F). The average kymograph of actin polymerization activity around the sawteeth confirms that actin polymerization is nucleated at the heads of sawteeth and flows toward the tails along both sides (Figure 3.6G). The average kymograph also shows that the sawteeth heads maintain a relatively higher level of actin fluorescence intensity compared to other locations on the sawteeth after time t_w. This observation may indicate that the

curvature of the sawteeth heads promotes actin polymerization. The actin waves also are observed to travel from one sawtooth to the adjacent one in the negative direction (Figure 3.6H).

Microtubules are another essential cytoskeletal component of cells. Microtubules have been shown to be the first cytoskeletal element to be aligned by micron-scale grooves during the spreading of fibroblasts.[209] This process is followed by the alignment of focal contacts, actin filaments, and finally cells.[209] Microtubules were found to align with ridges on ridged substrates.[142] Because microtubules regulate FA disassembly through integrin recycling and trafficking,[54,210] it is natural to consider that microtubules play an important role in cell polarization and migration during contact guidance. To investigate this idea, we fixed MDA-MB-231 and M4 cells migrating on sawteeth and stained for microtubules using an antibody against tubulin. We found that the microtubules of MDA-MB-231 cells align with the sawtooth patterns. This alignment is particularly evident at the cell protrusions, where microtubules coil around the sawteeth (Figure 3.7A, arrows). This phenomenon was not observed in M4 cells (Figure 3.7B), suggesting that the mechanisms that regulate microtubule dynamics differ in cells that respond differently to a specific nanotopographic surface.

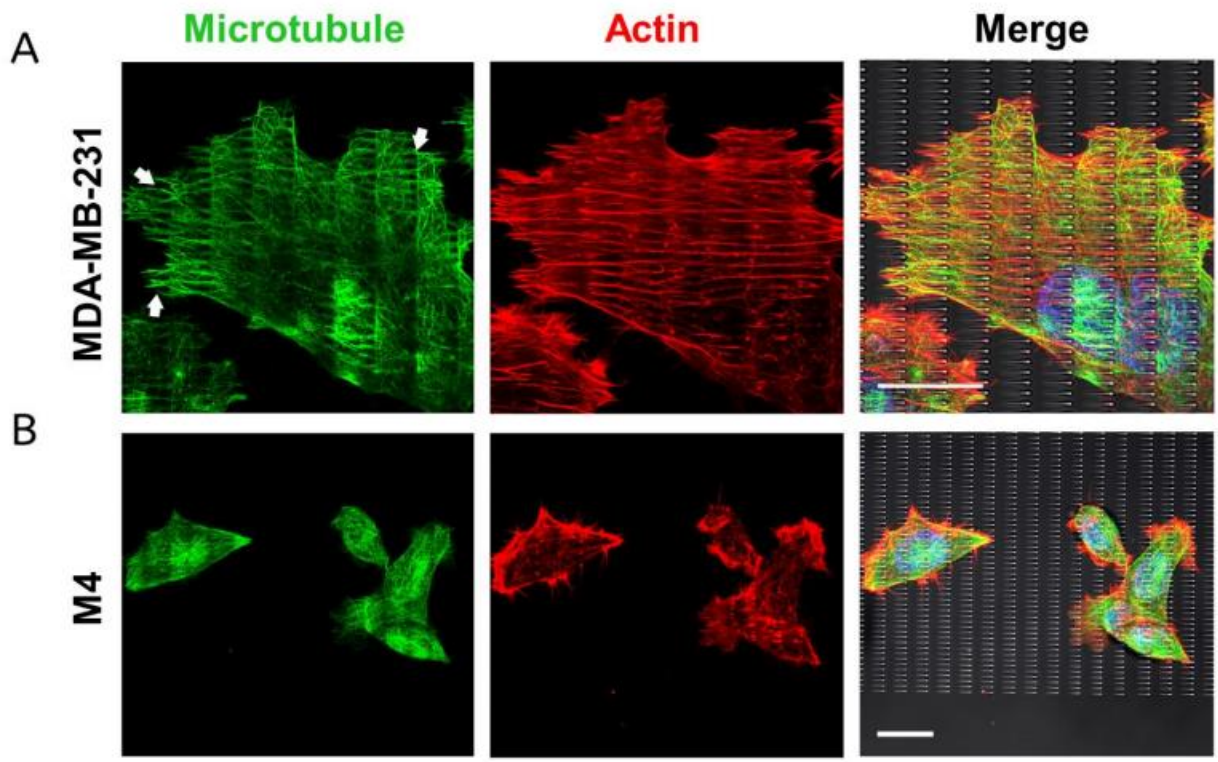

Figure 3.7. Influence of sawteeth on microtubules in MDA-MB-231 cells and M4 cells. (A, B) From left to right, fluorescence images of microtubules, actin, and merge of these two with the bright-field image and DAPI labeling for MDA-MB-231 (A) cells and M4 (B) on sawteeth. The arrows highlight the locations where microtubules coil around nanosawteeth. The scale bar is 10 μm. Reprinted with permission from reference 196, © 2019 American Chemical Society.

These findings show, as previously observed for *D. discoideum* and neutrophils,[131] that there is a direct connection between the migrational response to sawteeth and the underlying cytoskeletal dynamics. In other words, the esotactic guidance of the actin cytoskeleton plays an important role in microthigmotaxis. Actin waves are known to be important in cell-membrane dynamics and motility. It has previously been shown that actin polymerization drives the wave-like movement of its upstream nucleator through an autoinhibitory mechanism,[211] which can further generate the directional motion of cells.[212,213] By using asymmetric sawtooth surfaces, we expand this concept to show that an asymmetric topography can induce esotactic (actin) and

microthigmotactic (migrational) behaviors in a cell-type-dependent manner. This dependence of the direction of these phenomena on cell type suggests that multiple regulatory nodes contribute to the fine control of actin dynamics. Some of these nodes may be intrinsic, including the antagonistic interplay between GTPase signaling and the activation of different actin nucleators,[211,214] whereas others may be extrinsic, such as the use of integrin-based complexes to interact with the underlying topographic guidance cues.

3.2.5. Distinct FA Patterns and Cortical Plasticity Promote Biased Cell Migration

In addition to the actin and microtubule cytoskeletal networks, FAs are key components in contact guidance. FAs transduce extracellular forces from the ECM and induce a wide range of biochemical signals that go on to regulate cell adhesion and motility.[36] In this context, Ohara and Buck first proposed that the polarization and alignment of cells on ridges results from the need to maximize the area of focal contacts.[215] Several studies have now suggested that FA formation represents one plausible mechanism by which contact guidance is regulated.[178,185,186,216,217] We examined the distribution pattern of FAs for both MDA-MB-231 and M4 cells on sawteeth using high-resolution fluorescence imaging of actin and paxillin, the latter of which is an important scaffold protein of FAs that recruits and integrates numerous structural and signaling proteins for the transduction of ECM signals.[218]

To capture the paxillin fluorescence signal around each sawtooth on the *z* axis (*i.e.*, along the surface normal), we imaged cells at *z* positions ranging from below the bottom of the surface to above the top of each sawtooth, resulting in each sawtooth falling into a range of 1.2 to 3.2 μm on the *z* axis. A montage of paxillin and/or actin labeling of a MDA-MB-231 cell is presented in Figure 3.8A. The paxillin signal is first observed at a *z* of approximately 1.2 μm, which is at

the bottom of the cell. The majority of the FAs are located around the cell periphery, at the tips of filopodia (Figure 3.8A; paxillin and merge channels). FA complexes are also seen in the gaps between adjacent sawtooth columns that connect with stress fibers (Figure 3.8A; see white arrows in merge channel). Above $z = 2.0$ μm, no obvious FAs are observed. The actin filament network starts to show up in cell lamellipodia and becomes obvious at $z = 2.8$ μm (Figure 3.8A; see white arrow in actin channel). Surprisingly, above $z = 2.8$ μm, the FA punctae are well organized, with a spacing similar to that of adjacent rows of sawteeth (Figure 3.8A; paxillin channel). To show the spatial positions of the FAs precisely in different *z* slices, we selected FA complexes from either the bottom layer (Figure 3.8A,B; 1–3, blue arrows) or the tips of the sawteeth (Figure 3.8A,B; 4–6, red arrows) and generated *x*–*z* and *y*–*z* projections (Figure 3.8B). The FAs from the bottom layer reach a peak intensity at a *z* of approximately 1.3 μm (Figure 3.8B; blue dashed lines and Figure 3.9B; top panel). In contrast, the ordered FA complexes from the top layer are located near the tips of the sawteeth and exhibit a maximum intensity at a *z* of approximately 2.9 μm (Figure 3.8B; red dashed lines and Figure 3.9B; bottom panel). Notably, strong fluorescence signals are not observed in the gaps between two adjacent FAs on the top of the sawteeth, suggesting that there is little membrane penetration into the grooves of the structures (Figure 3.8B; 4–6 *y*–*z* view). Because FA complexes are indicators of the cell–ECM interfaces, we speculate that the MDA-MB-231 cells primarily interact with the tips of the nanosawteeth and that the FAs and stress fibers sustain most of the cortex above the grooves.

Indeed, SEM images of MDA-MB-231 cells on sawteeth show that the entire cell body remains on top of sawteeth like a “floating rigid blanket” (Figure 3.8C). The leading lamellipodia spread across multiple sawteeth in the same column, whereas the membrane rests on the top of the sawteeth with no penetration into the grooves between rows of sawteeth. This behavior is

further highlighted by zooming in at the front of the cell lamellipodium (Figure 3.8C; zoomed-in image). This bridging behavior is in agreement with our results on M1 cells on nanoridges (Figure 3.2G; top panel), as well as with many previous reports.[176,186,215,217] Bridging is thought to promote cellular alignment and anisotropic traction forces because of confined FA growth.[178] In fact, this bridging effect may provide an explanation for our previous observation that M1 cells preferentially form FAs on ridges.[142] At the front of a sawtooth, the cell membrane curves somewhat and wraps around the head (Figure 3.8C; white arrow heads). M1 cells, whose migration bias is in the same direction as that of MDA-MB-231 cells, exhibit a similar phenotype (Figure 3.9A). When the cell lamellipodia extend from one sawtooth column to another, the membrane can either bridge the gap (Figure 3.8C; see cross-hatch symbol) or droop down to the bottom surface (Figure 3.8C; see asterisk). We envision that cell areas in which the cell interacts with the bottom ECM (marked by $*$) provide support for the cell body, as observed by fluorescence imaging of actin and paxillin (Figure 3.8A).

Figure 3.8 (next page). MDA-MB-231 and M4 cells exhibit distinct cortical plasticity and focal adhesion patterns. (A,E) Fluorescence image montage of paxillin (top), actin (middle), and the merge of the two (bottom) at different *z* positions for (A) MDA-MB-231and (E) M4 cells. Blue and red arrows highlight the focal adhesions chosen for further analysis in (B) and (F). The white arrows in the actin channel of (A) highlight the actin filament network. The white arrows in merge channel of (A) indicate focal adhesions located between two sawtooth columns. The scale bar is 10 μm. (B,F) The *x*–*z* and *y*–*z* views of representative FAs from the lowest and highest *z* positions in (A) and (E), respectively. The white stars indicate the representative FAs in the images in the *x*–*z* and *y*–*z* views. The single red and blue dashed lines in (B) mark the center *z* positions of the chosen FAs and the double red dashed lines in (F) indicate the expansion ranges of the chosen FAs. The scale bar is 2 μm. (C,G) Representative SEM images of (C) MDA-MB-231 and (G) M4 cells migrating on sawteeth. Magnified images of the areas are highlighted by the boxes with black dashed lines. White arrows point out the places showing distinct cell cortical plasticity of MDA-MB-231 and M4 (G). The scale bars are 10 μm in the zoomed-out images and 1 μm in the magnified images. (D,H) Schematic representation of the biased contact guidance for (D) MDA-MB-231 and (H) M4 cells on sawteeth. The purple arrow represents the direction of motion. Reprinted with permission from reference 196, © 2019 American Chemical Society.

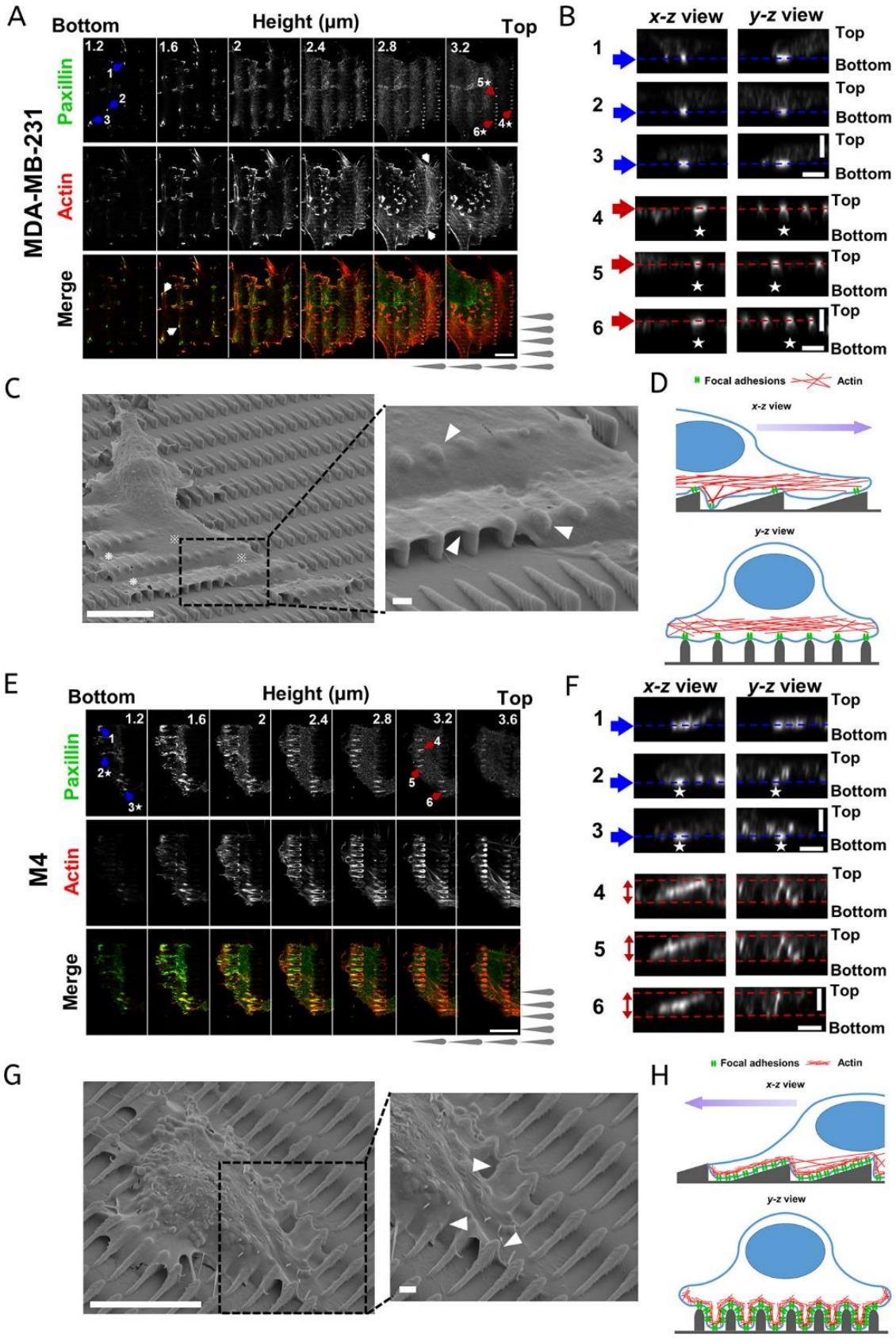
A
Bottom
Height (μm)
Top
MDA-MB-231
Paxillin
Actin
Merge
1.2
1.6
2
2.4
2.8
3.2
B
x-z view
y-z view
Top
Bottom
C
D
Focal adhesions
Actin
x-z view
y-z view
E
M4
3.6
F
G
H

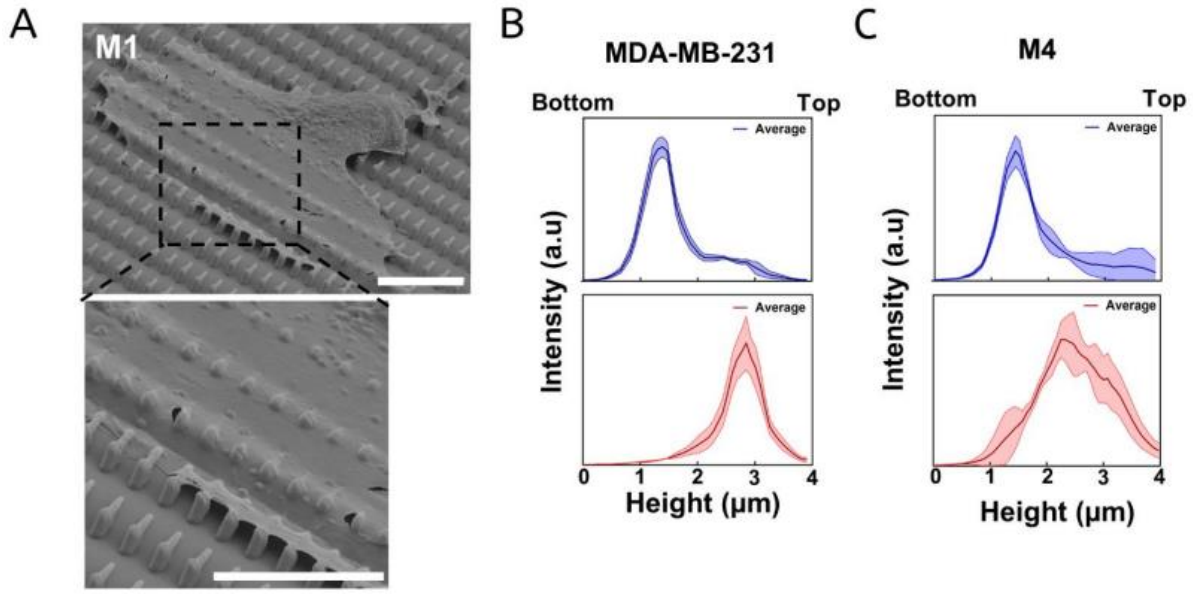

Figure 3.9. Cortical plasticity of M1 cells on sawteeth. (A) A representative SEM image of an M1 cell on sawteeth (top) and a zoomed-in image of the area in the box (bottom). The scale bar is 10 μm. Fluorescence intensity of *x*-*z* projections of FAs in Figure 3.8B,F for MDA-MB-231 (B) and M4 (C) cells. The top panels in (B) and (C) are for FAs 1-3 and bottom panels are for FAs 4-6. The solid line is the average intensity of three FAs and the shaded area represents the standard errors. Reprinted with permission from reference 196, © 2019 American Chemical Society.

Profoundly different FA patterns are observed for M4 cells than for MDA-MB-231 cells. At the interface between an M4 cell and the bottom ECM, large FA complexes are formed at the front of the cell protrusions and also in the grooves between adjacent rows of sawteeth (Figure 3.8E; paxillin channel). These FAs display a maximum intensity at a *z* of approximately 1.4 μm (Figure 3.8F, 1–3 blue dashed lines, and Figure 3.9C, top panel). Above $z = 2.0$ μm, the M4 cells exhibit organized FA patterns surrounding each sawtooth, resulting in brighter outlines of the sawteeth (Figure 3.8E; paxillin channel). Furthermore, thick actin structures are seen around the sawteeth through the entire *z* section (Figure 3.8E; actin channel). This phenomenon is visible in a 3D reconstruction, which clearly shows the outlines of sawteeth.[196] In contrast to FAs in MDA-

MB-231 cells, FAs of M4 cells interact with the ECM on the side walls of the sawteeth (Figure 3.8F; 1–3 *y*–*z* view). Furthermore, the FA complexes are located along the slopes of the sawteeth, extend from the bottoms to the tops of the sawteeth (Figure 3.8F, 4–6 *x*–*z* view). This finding is further substantiated by the quantification of fluorescence intensity, which shows a broad distribution over the entire *z* depth (Figure 3.9C; bottom panel). The *y*–*z* view of FAs 4–6 further illustrates that FA complexes are assembled on the side walls of the sawteeth for a range of *z* values. SEM images provide further evidence that the cortical plasticity of M4 cells is distinct from that of MDA-MB-231 cells (Figure 3.8G). Multiple protrusions are formed around M4 cells, compared with only one lamellipodium for MDA-MB-231 cells (Figure 3.8C,G). The cell boundary of M4 cells is also highly dynamic, with extensive membrane ruffling and blebbing (Figure 3.8G). Zooming in on one dominant protrusion indicates that the cell boundary, especially at the front of the protrusion, is able to wrap around individual sawteeth (Figure 3.8G; see white arrows in the zoomed-in image). This observation is consistent with the ability of M4 cells to assemble FA complexes surrounding sawteeth. Based on these experimental results, we summarize the primary differences in actin cytoskeleton and FA patterns between MDA-MB-231 and M4 cells on sawteeth in a schematic (Figure 3.8D,H). For MDA-MB-231 cells, the high cortical rigidity limits the contact of membranes to the sawtooth structures. As a result, the majority of the FAs are located on the top of the sawteeth (Figure 3.8D). In contrast, the distinct cortical plasticity of M4 cells allows maximum contact with the sawteeth structures and FA formation throughout the sawteeth (Figure 3.8H).

Although it has been shown that the application of cytoskeletal force generated by cells on the ECM directly affects FA assembly,[63,219] the overall cell shape or distortion of the cell shape are also known to modulate the size and distribution of FAs.[220] Here, we found that

various cell types exhibit both distinct cell-boundary deformability and FA organization. It has been suggested that FA size and distribution determine the adhesion strength[221] and FA composition,[222] spatially control the activation of downstream messengers,[223] and determine the balance among ECM-activated signaling pathways.[203] Thus, the distinct FA organization patterns we observed in breast-cancer cells migrating on sawteeth may play an important regulatory role. Topography-induced membrane curvature could represent another critical factor. Indeed, instead of being passively determined by the actin cytoskeleton, membrane shape and deformation have been shown to drive the active regulation of the recruitment of curvature-sensitive proteins and activators of actin polymerization.[224,225] The recruited curvature-sensitive proteins can further promote membrane deformation; however, the triggered actin polymerization limits this positive feedback process by stiffening the cortex.[224,225] This antagonistic interplay generates propagating waves of both curvature-sensing proteins and actin polymerization with changes in local membrane curvature.[224-226] In addition, it has been determined that out-of-plane curvature provided by microscale wires or tubules also regulates the collective behavior of epithelial cell monolayer.[227,228] This observation raises the possibility that the different membrane deformability we observed in MDA-MB-231 and M4 cells results in the distinct recruitment of curvature-sensing proteins and actin nucleators, thereby leading to the generation of actin-polymerization waves in opposite directions. We hypothesize that differences in the balance between cortex deformation and FA formation ability in MDA-MB-231 and M4 cells promote distinct cytoskeletal dynamics and migration behaviors.

3.3. Conclusions

Contact guidance plays a critical role in cancer invasion and metastatic processes. Using multiple breast-cancer cell lines and symmetric and asymmetric nanotopographic designs, we examined the biophysical and molecular mechanisms behind contact guidance and directional bias. We showed that all of the breast-cancer cell lines we studied are able to sense and respond to physical guidance cues, yet do so in distinct ways. We envision that this behavior is dependent on distinct intrinsic characteristics of the cancer cell lines. Consistent with prior findings, the bias in cell migration we measured is in the same direction as, and likely arises from, asymmetries in the direction of actin polymerization. Furthermore, we identified distinct local cell cortical plasticity and heterogeneity in FA patterns as key differences between breast-cancer cell types. We hypothesize that this difference in FA patterns, and the associated difference in the deformation ability of cell boundaries into the valleys of the textures, are both driven by, and ultimately regulate, the bias in actin polymerization and cell migration. Because we can average observations over identical nanotopographic elements (Figure 3.6), our approach is well suited for in-depth investigations of intracellular signaling to identify the molecular mechanisms underlying the distinct FA patterns, actin dynamics, and cell-boundary shapes.

3.4. Materials and Methods

3.4.1. Surface Fabrication and Replication

The nanoridge and sawtooth topographies that were employed to study migratory and cytoskeletal responses were designed and fabricated using MAP. More details regarding this method can be found elsewhere.[106,229] Briefly, the output of an ultrafast Ti:sapphire laser (Coherent Mira 900) tuned to 800 nm was passed through a high-numerical-aperture objective

(Zeiss alpha-Plan Fluar 100×; numerical aperture 1.45) and focused onto a photopolymerizable resin ((1:1 w/w tris (2-hydroxy ethyl) isocyanurate triacrylate (SR368)/ethoxylated (6) trimethylolpropane triacrylate (SR499) (both from Sartomer), 3 wt % Lucirin TPO-L (BASF)) that was sandwiched between a glass coverslip and a microscope slide. Based on the experimental conditions, the photoinitiator undergoes efficient two-photon absorption only in the focal region of the objective, allowing for the fabrication of three-dimensional structures with arbitrary shape. The sample was mounted on a motorized stage that can be controlled by a computer. A LabVIEW program (National Instruments) was used to control the stage movement to fabricate the desired patterns. The same program controlled a shutter to dictate when and where polymerization should occur. After fabrication was completed, the sample was soaked in two containers of ethanol for 3 min each to remove the unreacted monomer resin. The MAP-fabricated "master" structure was then baked/dried in oven at 110 °C for at least 1 h.

To reproduce nanotopographic surfaces, we used solvent-assisted nanotransfer molding[142] to make a negative-relief mold of the master structure fabricated with MAP. A film of hard PDMS[119,142] was spin-coated onto the original pattern. This PDMS mixture included hexanes to decrease viscosity to allow the film to conform optimally onto the structures being coated, thereby improving the resolution of the mold. After sitting at room temperature for 2 h, the patterned microscope slide and coated film were baked at 60 °C for 1 h. Sylgard 184 (10:1 w/w elastomer base/curing agent; Dow Corning) was poured on top of the baked sample to form a layer approximately 1 cm thick. The sample was then returned to the oven for 70 min. Once baking was completed, the mold was peeled from the master in the direction parallel to the ridges. For the sawteeth mold, peeling should occur from the tail to the head of the sawteeth to prevent damage to the pattern.

Molds can be used to make replicas of the original MAP structure. A drop of the same resin used for MAP was sandwiched between a functionalized coverslip and the mold, and the sandwich was exposed to UV light for 5 min. Using this process, many replicas of an original pattern can be produced in a short amount of time.

3.4.2. Cell Culture

Benign epithelial cell line MCF10A (M1) and its corresponding metastatic mutant cell line MCF10CA1 (M4) from the MCF10A cell series were used (Barbara Ann Karmanos Cancer Institute, Detroit, MI). Cells were cultured in DMEM/F12 (Invitrogen, Carlsbad, CA) supplemented with 5% horse serum (Invitrogen) at 5% CO_2 in humidified culture incubators, as previously described. The medium for M1 cells was additionally supplemented with 10 μg/mL insulin (Invitrogen), 10 ng/mL EGF (Peprotech, Rocky Hill, NJ), 0.5 μg/mL hydrocortisone, and 100 ng/mL cholera toxin (both from Sigma, St. Louis, MO). HS578T and BT549 cells, kind gifts from Dr. Stanley Lipkowitz, were cultured in RPMI supplemented with 10% fetal bovine serum (both from Invitrogen). MDA-MB-231 cells were cultured in DMEM/high glucose supplemented with 10% fetal bovine serum.

The pTK92_Lifeact-GFP plasmid was a gift from Iain Cheeseman (Addgene plasmid #46356). To generate M1 and MDA-MB-231 cells stably expressing Lifeact-eGFP, phoenix cells (human kidney epithelial) were transfected with the plasmid with Lipofectamine 2000 (Thermo Fisher Scientific) according to the manufacturer's protocol, then the cell-culture medium containing retroviral particles was collected at 48 h after transfection. After the collected medium was filtered with 0.22-μm filters, viral particles were added to M1 and MDA-MB-231 cells. Stably infected cells were selected and maintained in puromycin-containing media (2.5 μg/mL).

3.4.3. Individual Cell Migration and Time-Lapse Imaging

Prior to cell seeding, nanoridges or nanosawteeth surfaces were coated with 20 μg/mL collagen IV (BD Biosciences) at 4 °C for about 1 h and then mounted back to a homemade 6-well plate. Cells were trypsinized and resuspended to 1×10^4 cell/mL each in their own growth medium, and then 2 mL of cell suspension was added to each well. After the cells were allowed to adhere for approximately 1 h, nonadherent cells were washed off and each well was refilled with 2 mL of fresh medium. The cells were then cultured overnight. Two h before imaging, fresh growth medium was replaced for each cell line. For time-lapse imaging, the plate was placed in the incubator chamber (37 °C, 5% CO_2) of a Zeiss Observer 2.1 microscope with an automated stage. Phase-contrast images were collected every 3 min for approximately 20 h.

3.4.4. Live-Cell Actin Fluorescent Imaging

Similar to the protocol for individual cell migration experiments, a nanosawtooth surface was coated with 20 μg/mL collagen IV at 4 °C for about 1 h, then mounted in a homemade 35 mm Petri dish. Lifeact-eGFP/MDA-MB-231 and Lifeact-eGFP/M4 cells were harvested following the same protocol as in the individual cell migration experiments. On the second day, cells were imaged with a Zeiss LSM 880 laser-scanning confocal microscope. Both fluorescent and bright-field images were collected every 10 s using an oil-immersion, 63× objective and a zoom-in factor of 2.5.

3.4.5. Immunostaining

Cells were fixed in 4% formaldehyde without (paxillin) or with (tubulin) 2 mM EGTA (bioWORLD, Dublin, OH) and 2 mM $MgCl_2$ (Quality Biological Inc., Gaithersburg, MD) for 15

min, followed by permeabilization in 0.1% Triton X-100 for 15 min and blocking of unspecific antibody binding with 1% bovine serum albumin (BSA) for 1 h. Targets were labeled with either antitubulin (1:200, MAB1864, Millipore) or antipaxillin (1:200, 612405, BD) primary antibody in 0.1% BSA at 4 °C overnight. On the second day, the primary antibodies were detected by secondary, fluorescently labeled antibodies (1:200, Invitrogen). Meanwhile, F-actin was labeled with phalloidin-TRITC (1:200, Invitrogen), and nuclei were labeled with DAPI (Invitrogen). Super-resolution images of the specimens were obtained with a Zeiss LSM 880 confocal microscope in Airyscan mode, and 3D reconstruction movies were generated using ZEN software (Zeiss, Germany). Further image analysis, such as generating *x*–*z*/*y*–*z* view images, was performed in ImageJ (NIH, Bethesda, MD).

3.4.6. Quantitative Analysis of Cell Migration

After time-lapse images were postprocessed, cell tracking was performed using Manual Tracking in ImageJ, and cells were outlined manually in MATLAB (Mathworks). The files containing all cell tracks were imported into MATLAB for further analysis. Cell tracks were smoothed with a 10-frame (30 min) unweighted sliding window. This period is sufficient to allow cells to move about one nuclear diameter. Using the smoothed center positions, cell velocities were determined by calculating the displacement between two frames: $\overrightarrow{v_i}(t) = \overrightarrow{x_i}(t) - \overrightarrow{x_i}(t - \Delta t)$, where Δt is the interval between the frames. Assuming the uncertainty in finding the cell center is 1 pixel (0.625 μm) for both the *x* and *y* directions, a velocity was only counted if the net displacement between two frames was above 1.4 pixels. The direction of the motion at each frame was determined by the angle between $\overrightarrow{v_i}(t)$ and the *x* axis, based on which histograms of direction of motion were created. All cell instantaneous velocities within a certain angle range relative to ridges were averaged to plot the velocity profile with respect to

orientation. To calculate the mean velocity components relative to the nanosawtooth orientation for each cell, the velocity components along the *x* axis were separated based on their signs, with positive being the same as the nanosawtooth orientation and negative being the opposite orientation.

The velocity direction distribution was also plotted for each speed quartile and each long-term persistence tertile. The angles were determined relative to the sawtooth orientation, meaning that angles that are left–right symmetric about the sawtooth orientation are considered to be the same. This process transforms the original range of velocity direction from −180–180° to 0–180°. To estimate the variations in our distributions, we adapted a random resampling Bootstrap method.[230,231] First, we randomly divided all velocities into ten groups for each speed quartile or persistence tertile. To distribute the velocities randomly, we then selected a random seed between 2^0 and 2^{32} for each of the five cell lines. The seeds are 418932850, 1196140743, 2348838240, 4112460544, and 4144164703 for MDA-MB-231, HS578T, M1, BT549, and M4 cells, respectively. The velocities whose speed values are zero were discarded because their directionality cannot be determined. The velocity direction distribution was then calculated for each of the groups. We considered the measurement from each of the groups as independent and calculated the average velocity direction distribution and standard error of the mean from the measurements of the groups.

3.4.7. Averaged Actin Kymograph Analysis

We measured the mean actin fluorescence and actin dynamic around one sawtooth by averaging across all sawteeth in either a single movie or multiple movies. First, the images with both bright-field and fluorescence channels were rotated in ImageJ such that all sawteeth were

aligned horizontally with their positive direction (tail to head) facing right, and the image edges were discarded. The sawtooth regions and boundaries were subtracted from the bright-field channel. Because the light aberration caused by cells resulted in the inability to recognize some sawteeth, sawteeth that appeared to be connected with others or smaller than a certain threshold were excluded from the analysis. After subtraction, the sawtooth outlines were superimposed on the actin fluorescent channel, and 51 points were placed evenly about the circumference of each outline. For each sawtooth, the sawtooth centroid was used as the origin point, and the horizontal row passing the centroid was used as the *x* axis with its positive direction facing right (same as the sawtooth positive direction). Then, the angle of each of the 51 points was calculated relative to the axis positive direction, and the position 0, which is the head of the sawtooth, was identified as the point with the smallest angle. The 25 points from position 0 in the clockwise direction were assigned indices 1 to 25 with position 1 near the sawtooth head and position 25 near the sawtooth tail. Similarly, the 25 points from position 0 in the counterclockwise direction were given indices −1 to −25. As the 51 points were evenly placed, positions ±1 are nearly symmetric to the sawtooth head and positions ±25 are nearly symmetric to the sawtooth tail. The actin-fluorescence intensity within a constant radius around each point was averaged. Then, we aligned the 51 points linearly so that position 0 was in the middle and positions ±25 were in the two sides. To quantify the actin dynamics for two cell lines in an unbiased way, we first calculated averaged intensity for position 0 for all frames and then made a plot of intensity *versus* time. The time point t_w was determined as the frame of the first peak, which has the average intensity above 90% of the maximum intensity in the plot. A kymograph showing the actin dynamic around one sawtooth was then generated by measuring the actin intensity profile

as mentioned for 6 min before and after time point t_w. The kymographs from different sawteeth were averaged by using the position 0 and time t_w as the center.

3.4.8. Scanning Electron Microscopy Imaging

For SEM imaging, cells were washed with 0.1 M Sorensen's sodium phosphate buffer three times to remove any growth medium, and then were fixed with 2.5% glutaraldehyde in the same buffer at 4 °C overnight. After rinsing, the cells were postfixed with 1% osmium tetroxide for 1 h. Then, the cells were dehydrated through a series of 35, 50, 85, 95, and 100% ethanol solutions for 10 min each, followed by chemically drying with hexamethyldisilazane (Sigma-Aldrich) for 5 min. The samples were then sputter-coated with gold and imaged using an AMRAY 1910 microscope.

3.4.9. The Principle of the Optical-Flow Algorithm

Optical-flow algorithms of florescence images capture translational motion on a frame-by-frame basis. For each pixel in a fluorescence image, the algorithm assumes that the pixel undergoes a translation from its initial coordinate (x, y) to a new coordinate $(x + \Delta x, y + \Delta y)$.[232] Therefore, each two-dimensional frame in an image series is denoted by:

$$I_t(x, y) = I_{(t + \Delta t)}(x + \Delta x, y + \Delta y) \tag{3.1}$$

In other words, the objective is to find the translations Δx and Δy that map the intensity profile in I_t to what is observed in $I_{t+\Delta t}$.

Expanding the right side of this equation assuming small Δx, Δy, and Δt, and neglecting second-order and higher order terms, yields the master optical-flow equation.

$$I_t(x,y) = I_t(x,y) + \frac{\partial I_t}{\partial x}\Delta x + \frac{\partial I_t}{\partial y}\Delta y + \frac{\partial I_t}{\partial t}\Delta t \quad (3.2)$$

$$0 = \frac{\partial I_t}{\partial x}\Delta x + \frac{\partial I_t}{\partial y}\Delta y + \frac{\partial I_t}{\partial t}\Delta t \quad (3.3)$$

$$-\frac{\partial I_t}{\partial t}\Delta t = \vec{\nabla} \cdot \left(\frac{\Delta x}{\Delta t}, \frac{\Delta y}{\Delta t}\right) \quad (3.4)$$

$$-\frac{\partial I_t}{\partial t} = \vec{\nabla} \cdot \vec{v} \quad (3.5)$$

Equation (3.4) is underdetermined (one equation and two unknown variables) so the Lucas-Kanade technique was used to apply an additional constraint.[233]

3.5. Acknowledgments

We thank S. Lipkowitz and the Parent, Losert, and Fourkas laboratory members for valuable discussions and suggestions. We also thank C.H. Stuelten and R. Lee for their help with the experimental setup and quantification of cell migration. We thank S. Garfield, L. Lim, and P. Mannan in the confocal microscopy core in CCR for their assistance with imaging. We thank J. Harrison and P. Blakely in the microscopy and image analysis laboratory at University of Michigan for the assistance with scanning electron microscopy. This work was supported by the Intramural Research Program of the Center for Cancer Research, NCI, National Institutes of Health (C.A.P.), by the NCI-UMD Partnership for Integrative Cancer Research (S.C.), by funds from the University of Michigan (S.C. and C.A.P.) and by AFOSR Grant FA9550-16-1-0052 (J.T.F. and W.L.).

Chapter 4: Quantifying Topography-Guided Actin Dynamics across Scales Using Optical Flow

 Lee, Campanello, Fourkas, and Losert analyzed the data; Campanello developed the optical flow-based analysis code; Hourwitz fabricated the nanoridge surfaces and optimized conditions for surface coating and cell viability; Omidvar and Alvarez collected the time-lapse images; and all authors contributed to interpreting the data and writing and editing the manuscript.

4.1. Introduction

Understanding the rearrangements of the cytoskeleton is essential to developing a complete picture of the dynamic forces involved in cellular processes such as migration, division, and differentiation. Cytoskeletal dynamics, and in particular actin dynamics, have been shown to be important for the growth of cell junctions and focal adhesions[234] and for immune-cell activation.[235] The formation of actin waves through directional polymerization and depolymerization of filaments drives many types of cell migration,[236] and has been associated with the establishment of polarity in a variety of cell types.[237]

Forces from the extracellular environment are an important modulator of actin dynamics. Physical and chemical characteristics of the extracellular environment, such as rigidity, biochemical composition, and topography, have been shown to influence actin dynamics and associated cell behavior.[238-241] One mechanism for this modulation is mechanosensing via focal adhesions.[156] In addition, actin waves respond when cells encounter obstacles.[211] It has been established that ridges of width comparable to fibers in the extracellular matrix (ECM) can alter actin dynamics significantly[130,131,156] and bias the localization of focal adhesions.[142,186] Thus, *in vivo*, the topography of the ECM, such as collagen networks,[242,243] is likely to modulate actin dynamics.

Periodic nanotopographic surfaces provide the opportunity to obtain systematic data on the modulation of such intracellular dynamics. In prior work, we have shown that actin waves can be nucleated near, and guided along, periodic nanotopography, in a phenomenon termed esotaxis. Actin-wave guidance has been observed in cell types that exhibit distinct physiological functions and migration phenotypes, including *Dictyostelium discoideum*,[130,131] neutrophil-like HL60 cells,[131] B cells,[156] and breast-cancer cell lines.[196] However, there are clear differences in the responses of each of these cell types to nanotopography. For example, although both *D. discoideum* and HL60 cells exhibit esotaxis, these two types of cells have been found to move preferentially in different directions on specific nanoscale asymmetric sawtooth textures.[131] Furthermore, different breast-cancer cell lines preferentially move in different directions on asymmetric sawtooth nanotopography.[196]

Here we introduce a method for performing quantitative measurements of the influence of nanotopography on intracellular dynamics at both the submicron and the micron scales. This

approach enables the detection of subtle differences in cytoskeletal dynamics, and allows for in-depth analysis of both the differences and the similarities of these dynamics across cell types and phyla. Our method of quantification of actin dynamics across scales is based on optical flow, an image-analysis technique developed in the fields of robotics and navigation control that uses changes in pixel intensities to detect motion in image sequences.[232,233] Because of the popularity of particle image velocimetry (PIV), optical flow has seen limited use on biological images. However, PIV is poorly suited for the variety of features that can be exhibited in fluorescence images of amorphous concentration fields. Indeed, a recent study indicated that optical flow may be better suited for analysis of fluorescence images, as this technique provides a more accurate estimate of ground-truth flow fields.[244] Here, we use optical flow to measure the dynamics of actin polymerization with submicron precision, and we further expand the utility of optical flow by introducing modeling and fitting approaches to the analysis of optical-flow vector fields. Clustering of the optical-flow data further allows us to quantify actin dynamics on the micron scale. Thus, this optical–flow-based analysis enables the identification of similarities and differences between esotaxis in neutrophil-like HL60 cells and human breast epithelial MCF10A cells across length scales.

4.2. Results

Esotaxis has been observed in a wide range of cell types that are known to respond to their *in vivo* microenvironment through processes such as directed migration or immune-system activation.[130,131,156] More recently, esotaxis has also been observed in epithelial cells, which are less motile.[196] Here we contrast the actin dynamics of epithelial MCF10A cells with those of neutrophil-like HL60 cells.

LifeAct–GFP-labeled epithelial MCF10A cells were plated on a 900 μm × 900 μm region patterned with parallel nanoridges with a spacing of 1.5 μm, as well as on the surrounding flat region. Confocal imaging near the surface revealed distinct actin morphologies on nanoridges as compared with the flat region (Figure 4.1). On the flat region the phenotype is a common one for these cells on such surfaces, with a broad lamellipodium at the cell front and stress fibers throughout the cell body (Figure 4.1A). In contrast, MCF10A cells on nanoridges exhibit actin streaks aligned with the ridges throughout the cell area (Figure 4.1B). The local nature of the response of actin to surface texture is illustrated in Figure 4.1C, which shows a cell that is partially on the nanoridges and partially on the flat region. On the nanoridged region, the cell shows the same actin streaks as a cell that lies fully on a ridged surface, whereas the same cell maintains a broad lamellipodium on the flat region.

Ridged and flat regions also engender distinct actin dynamics. Kymographs can be used to visualize dynamics in a region of interest in one spatial direction over time. The left side of Figure 4.2A compares an MCF10A cell on a flat region with one on a nanoridged region. The cell on the nanoridged region shows actin streaks that are characteristic of esotaxis. Actin kymographs from two perpendicular regions (Figure 4.2A) in an MCF10A cell on a flat surface show oscillatory dynamics in all directions at the cell boundary. These oscillations in the kymographs indicate the presence of fanlike protrusions and retractions across each region over 30 min (Figure 4.2B). In contrast, on the nanoridged region, the actin dynamics parallel and perpendicular to the ridges are different (Figure 4.2C). Parallel to the nanoridges, MCF10A cells show oscillatory actin dynamics. As shown in the bottom left of Figure 4.2C, a representative kymograph of a region perpendicular to the ridges shows actin structures that persist for tens of minutes and do not move perpendicular to the ridges. This behavior is typical for kymographs

perpendicular to the ridges, although perpendicular motion is observed in some cases as discussed below.

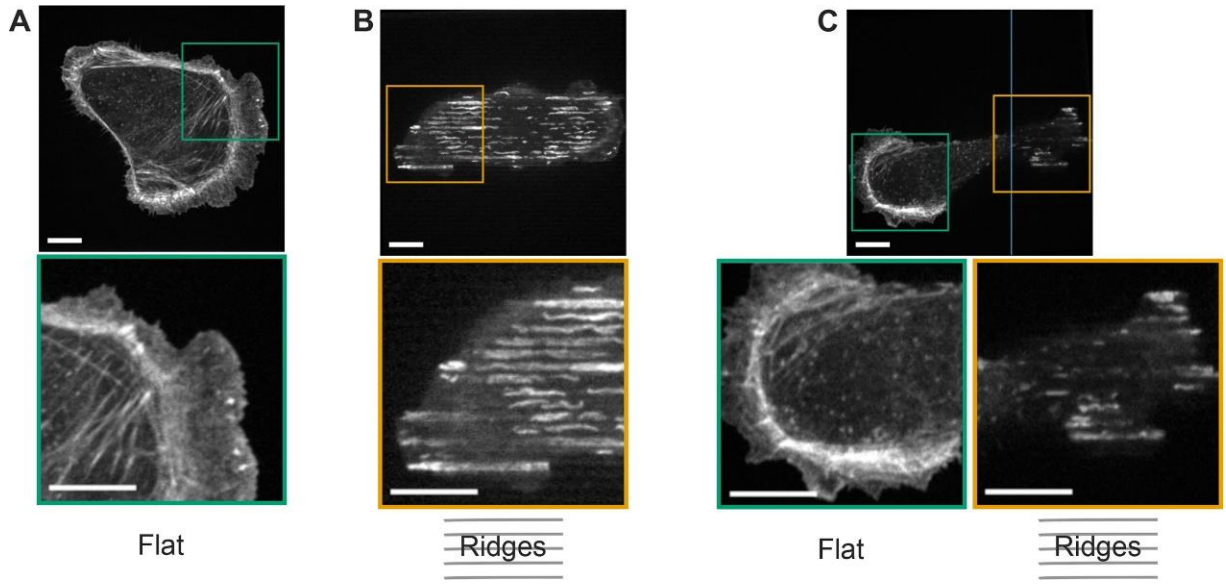

Figure 4.1. Surface topography prompts distinct actin morphology. The actin cytoskeleton of an epithelial MCF10A cell on (A) a flat surface has an actin morphology that is distinct from that of a cell on (B) a nanoridged surface. (C) A cell that is partially on a nanoridged region and partially on a flat region exhibits local actin morphologies that are driven by the underlying topography. The blue line in C indicates the boundary between the flat region and the nanoridged region. All scale bars are 10 μm. Reprinted with permission from reference 245.

Figure 4.2 (next page). Surface topography leads to distinct actin morphodynamics. (A) Optical micrographs of MCF10A cells in (left) bright-field and (right) fluorescence on (top) a flat region and (bottom) a nanoridged region. All scale bars are 10 μm. Kymographs for the areas denoted in A are shown in B for the flat region and in C for the nanoridges. D–F are the same as A–C, respectively, but for HL60 cells. Reprinted with permission from reference 245.

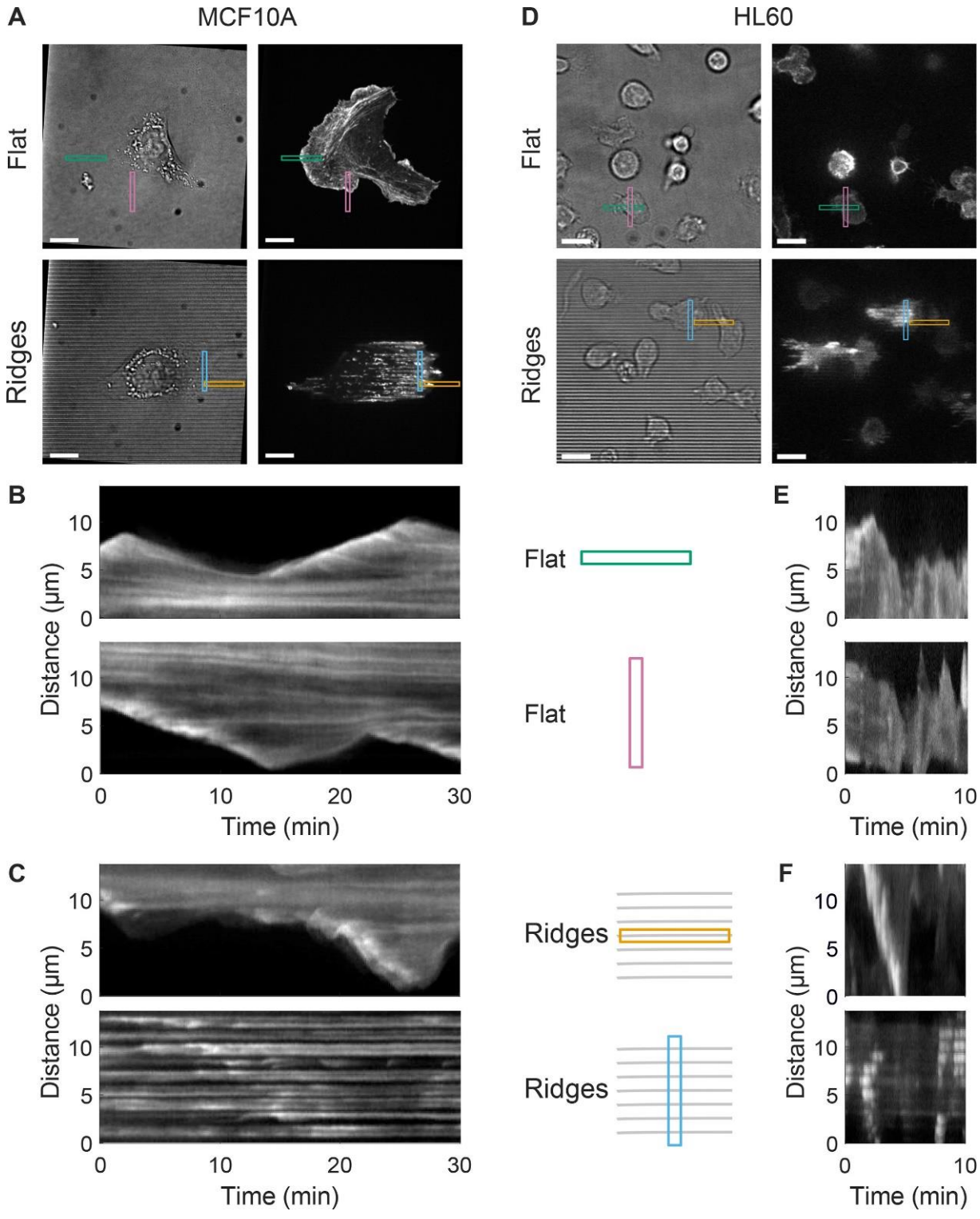
A
MCF10A
D
HL60
Flat
Ridges
B
C
E
F
Distance (μm)
Time (min)
Flat
Ridges
0
5
10
20
30

The behavior of motile, neutrophil-like HL60 cells on flat and nanoridged regions is illustrated in Figure 4.2D-F. Figure 4.2D illustrates the regions from which kymographs were generated. In HL60 cells on flat regions, actin is concentrated near the cell front. This localization is largely preserved on the ridged surfaces, although the morphology of the actin changes such that streaks of actin are aligned with the ridges. On flat surfaces, the HL60 cells show regions of protrusions and retractions (Figure 4.2E) similar to the actin dynamics seen in MCF10A cells (Figure 4.2B). We note that protrusions occur on the scale of seconds in HL60 cells and on a scale of minutes in MCF10A cells. Kymographs of the HL60 cells in the direction parallel to the nanoridges show protrusive dynamics, although often in the form of a single persistent wave (Figure 4.2F, top), in contrast to the oscillatory behavior seen on flat surfaces (Figure 4.2E). A representative kymograph of an HL60 cell in the direction perpendicular to the nanoridges shows streaks (Figure 4.2F, bottom) that indicate that actin waves do not move perpendicular to the ridges, but the streaks are shorter in duration than those in a typical MCF10A cell (Figure 4.2C). This behavior is typical for kymographs of actin in HL60 perpendicular to the ridges. Unlike in MCF10A cells, in which actin streaks on the ridges localize throughout the cell (Figure 4.2C, bottom), in the HL60 cells the streaks occur near the cell front (Figure 4.2F, bottom). Groups of actin streaks propagate together at the front of the HL60 cells, suggesting that there may be large-scale organization of actin dynamics (spanning many ridges) in these cells. It is unclear whether there is large-scale organization of actin dynamics in the MCF10A cells.

The full range of actin dynamics is more complex than is revealed by kymographs. MCF10A cells on the ridged regions exhibit actin dynamics throughout the substrate contact

area, whereas actin dynamics on flat surfaces are largely confined to the cell boundary. In both cell types, nanoridges stimulate reproducible, dynamic, linear actin structures.

Time-lapse fluorescence images of actin waves are difficult to interpret by visual inspection or kymographs alone, because the observed dynamics arise from a complex spatio-temporal concentration field. To measure these wavelike dynamics quantitatively, we must first define a wave (size and shape) and then capture its propagation (splitting, recombination, and changes in direction). Here, we address these challenges by introducing an automated approach to quantify actin-wave dynamics across length scales for unbiased comparison in different cell types and extracellular environments.

Our method is based on a computer-vision algorithm from robotics and navigation control called optical flow,[232,233] which provides pixel-based information about the direction and magnitude of intensity flux in a series of time-lapse images. Fields of optical-flow vectors are calculated by integrating changes of intensity in space and time, as shown schematically in Figure 4.3. For example, two images of a migrating HL60 cell taken 8 s apart are shown with changes in time highlighted by a green-to-magenta montage (Figure 4.3A). The magenta region indicates growth of the actin front (which, as expected, occurs at the leading edge of the cell), and the green region indicates a decrease in actin intensity.

The general objective of calculating optical flow is to solve for the unknowns Δx and Δy in

$$I(x, y, t) = I(x + \Delta x, y + \Delta y, t + \Delta t) \tag{4.1}$$

where $I(x,y,t)$ represents the actin fluorescence intensity at frame t. The intensity I that exists at point (x,y) at time t translates to a new point $(x + \Delta x, y + \Delta y)$ at some future time $t + \Delta t$. Expanding about small Δx and Δy and neglecting second-order derivatives yields the master optical-flow equation

$$-\vec{\nabla} I \cdot \vec{v} = \frac{\partial I}{\partial t} \tag{4.2}$$

Figure 4.3 (next page). Optical-flow calculations capture the dynamics in movies of actin fluorescence. (A) Two frames of a representative HL60 cell obtained 8 s apart and a merged image show the dynamics of the cell's behavior over time. The schematic in B illustrates how the procedure used to carry out optical-flow calculations combines the spatial gradient of an image (left) and the difference image/temporal gradient (right) to yield the optical-flow vector field (center). These calculations are applied to the images in A and shown in the images of C. The spatial gradient field (left) and temporal gradient (right) result in the output optical-flow vector field (center). Blue pixels in the right panel of C indicate a positive change (increase) in the pixel brightness from the first frame to the second frame, and red pixels in the right panel indicate a negative change (decrease) in the pixel brightness from the first frame to the second frame. All scale bars are 5 μm. Reprinted with permission from reference 245.

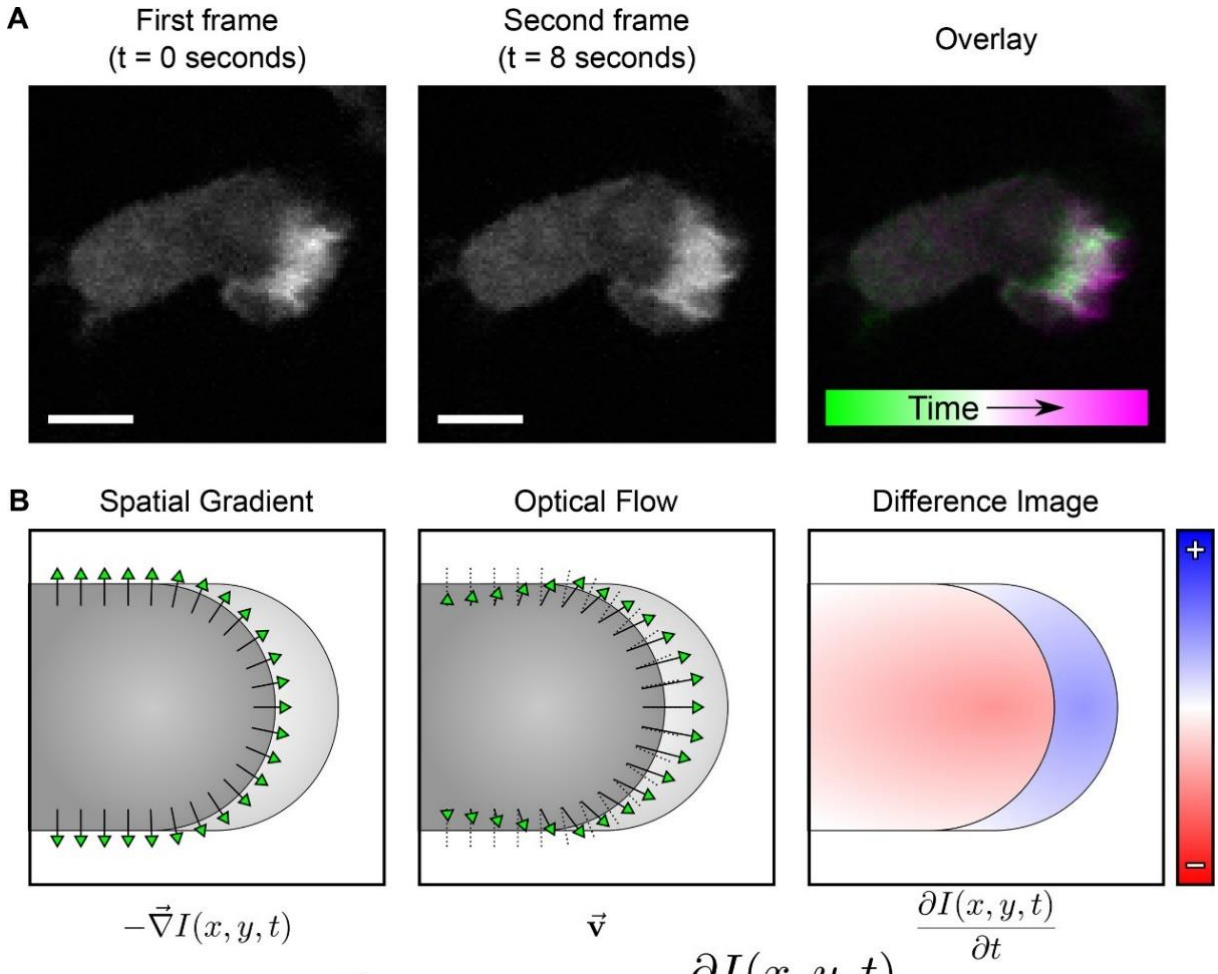
A
First frame
(t = 0 seconds)
Second frame
(t = 8 seconds)
Overlay
Time
B
Spatial Gradient
Optical Flow
Difference Image
+
−
$-\vec{\nabla} I(x,y,t)$
$\vec{\mathbf{v}}$
$\frac{\partial I(x,y,t)}{\partial t}$
$-\vec{\nabla} I(x,y,t) \cdot \vec{\mathbf{v}} = \frac{\partial I(x,y,t)}{\partial t}$
C
Spatial Gradient
Optical Flow
Difference Image
+
−
$-\vec{\nabla} I(x,y,t)$
$\vec{\mathbf{v}}$
$\frac{\partial I(x,y,t)}{\partial t}$

This governing equation is underdetermined, and so the Lucas–Kanade optical-flow constraint[233] was applied to calculate flow fields. This constraint prescribes that all pixels in a small window centered at (*x*,*y*) each have the same translational optical-flow vector. The equation can then be solved using the least-squares criterion (an explicit derivation is given below) to yield the intensity flow, $\vec{v}$ (Figure 4.3B, center panel). Solving for $\vec{v}$ requires use of the negative spatial gradient, $-\vec{\nabla}I$ (Figure 4.3B, left panel), which forms a vector field oriented away from regions of highest local intensity, and the time derivative, $\partial I/\partial t$ (Figure 4.3B, right panel) as shown in Eq. 4.2. Using the pair of images from Figure 4.3A as a representative example, the spatial and temporal gradients are used to calculate the optical-flow vector field, which approximates the flow of actin between the two frames. In this example, the vector field captures the translational motion on the leading edge of the cell (Figure 4.3C).

Optical-flow measurements of actin intensity translation enable the quantification of the pixel-scale response of actin dynamics to nanoridge topographies (Figure 4.4). The green-to-magenta montages of representative HL60 and MCF10A cells show dynamic and protrusive actin behavior at the leading edge of the cell (Figure 4.4A). Coloring the calculated flow fields based on direction relative to the nanoridges (Figure 4.4B) reveals the clear bias of actin wave guidance in the direction parallel to the ridges, which is consistent with the qualitative features of the montage images in Figure 4.4A. Measurements of the optical-flow directions on all HL60 and MCF10A cells on both flat and ridged surface topographies are shown in the histograms of Figure 4.4C. In both cell types, the cumulative distribution of flow in cells on flat surfaces shows no appreciable bias in any direction. However, cells on ridges exhibit a clear preference for flow along the ridge direction.

For further quantification, we fit the distribution of flow directions from each cell to a bimodal von Mises model with a constant offset. The distribution used consists of a uniform component and two peaked components that are 180° apart. The five parameters of the bimodal model are illustrated in Figure 4.4D. The angle θ_μ indicates the direction of the main component, and $1/\kappa$ is proportional to the width of the distribution. The values of κ on ridged regions are significantly higher than those than on flat regions for both the MCF10A and the HL60 cells (Figure 4.4E, $p = 0.0001583$ and $p = 0.0040$), indicating that the ridges strongly guide the actin flows in a bidirectional manner. A comparison of κ and θ_μ shows that cells with a bidirectional actin flow (i.e., high κ values) are more likely to be guided along the ridge direction (Figure 4.4F).

Figure 4.4 (next page). Using optical flow to measure pixel-scale guidance. (A) Representative merged time-lapse images of an MCF10A cell (top, 100 s apart) and an HL60 cell (bottom, 8 s apart). (B) Optical-flow vector fields colored by direction relative to the horizontal ridges. Blue indicates motion aligned with the ridges and yellow indicates motion perpendicular to the ridges. All scale bars are 5 μm. (C) Cumulative distributions of the directions of optical-flow vectors for multiple HL60 and MCF10A cells on flat and ridged surfaces; all cells are weighted equally in the distribution. ($N = 4$ MCF10A cells on flat surfaces from three independent experiments, $N = 19$ MCF10A cells on ridges from four independent experiments, $N = 14$ HL60 cells on flat surfaces from two independent experiments, and $N = 17$ HL60 cells on ridges from three independent experiments.) (D) The distribution of angles can be fit to a mixture of two von Mises distributions with five fitting parameters: θ_μ (primary direction of motion), κ (inversely related to distribution width), and three coefficients indicating the component of motion in the θ_μ direction, the component in the $\theta_\mu + 180°$ direction, and the component that is uniform. (E) In both MCF10A and HL60 cells, the distribution width, parameterized by κ, shows significant differences ($p = 0.0001583$ and $p = 0.0040$) on flat versus ridged surfaces. (F) For each cell, the mean direction of motion (angular axis) is plotted vs. κ (radial axis). Values of κ less than 2 (indicated by the dashed line) indicate cells with direction distributions that are statistically indistinguishable from a uniform distribution. We note $\kappa = 19.6$ for one HL60 cell, and this point is not visible in this figure. Reprinted with permission from reference 245.

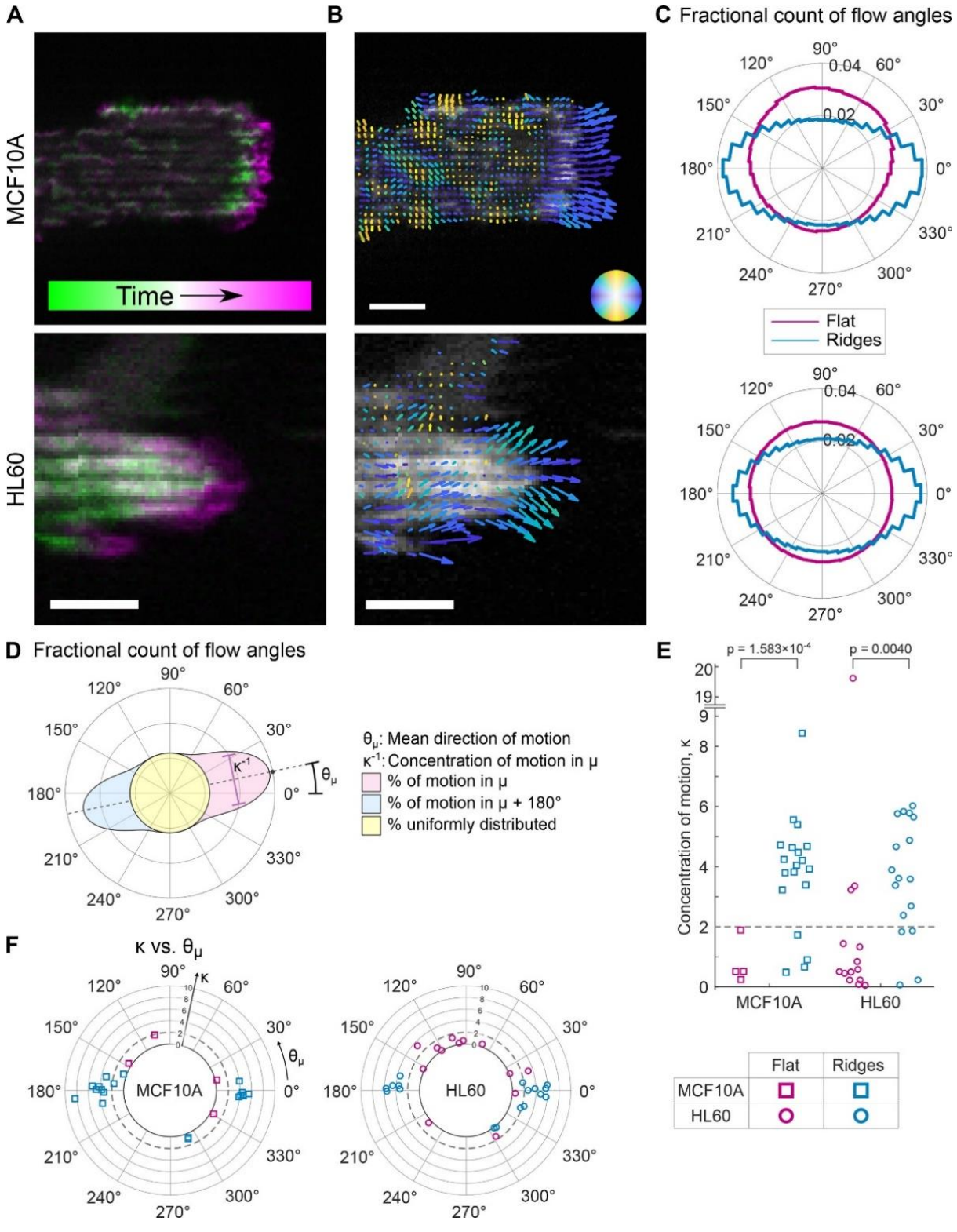
A
B
C Fractional count of flow angles
MCF10A
HL60
Time
90°
120°
60°
150°
30°
180°
0°
210°
330°
240°
300°
270°
0.04
0.02
Flat
Ridges
D Fractional count of flow angles
θμ: Mean direction of motion
κ-1: Concentration of motion in μ
% of motion in μ
% of motion in μ + 180°
% uniformly distributed
E
p = 1.583×10-4
p = 0.0040
Concentration of motion, κ
MCF10A
HL60
F
κ vs. θμ
Flat
Ridges

Although the optical-flow vector field indicates preferred directions of actin flow, it does not yield propagation speeds of actin polymerization waves directly. The magnitude of an optical-flow vector incorporates both the shift of actin in space and the change in actin intensity over time. This submicron-scale (i.e., pixel-scale) flux of intensity does not translate directly into characteristics of the dynamics that are notable on the micron scale (i.e., tens of pixels), such as the organization of waves across ridges seen in neutrophils in Figure 4.2F or the speed of wave propagation. To quantify these micron-scale characteristics, we combined similarly oriented optical-flow vectors into clusters (Figure 4.5A), which were then tracked over time. To ensure that we tracked robust clusters, we applied additional constraints, such as requiring sufficiently large intensity changes. The result of this clustering was the identification of broad regions of actin that moved collectively (Figure 4.5B).

Figure 4.5 (next page). Clustering of optical-flow vectors to measure micron-scale dynamics. (A) Similar flow vectors are grouped into clusters. (B) Clusters contain optical-flow vectors with a wide array of orientations, resulting in micron-scale structures. All scale bars are 5 μm. (C, D) Particle-tracking algorithms are applied to the tracked clusters. The cluster tracks are consistent with the motion at the leading edge of the actin waves seen in the kymographs in both HL60 (C, left) and MCF10A (D, left). Panels to the right of each kymograph show the same track in the 2D context of the cells; clusters found throughout the cell over time are indicated by colored regions. (E) The cluster tracks are used to determine speed distributions of actin waves on the ridges in the MCF10A and HL60 cells, which show no significant difference ($p = 0.5529$ and $p = 0.0586$) between flat surfaces and ridges. (F) Cumulative angle distribution of cluster track directions for multiple HL60 and MCF10A cells on flat and ridged surfaces; all cells are weighted equally in the distribution. ($N = 4$ MCF10A cells on flat surfaces from three independent experiments, $N = 17$ MCF10A cells on ridges from four independent experiments, $N = 9$ HL60 cells on flat surfaces from two independent experiments, and $N = 16$ HL60 cells on ridges from three independent experiments.) Reprinted with permission from reference 245.

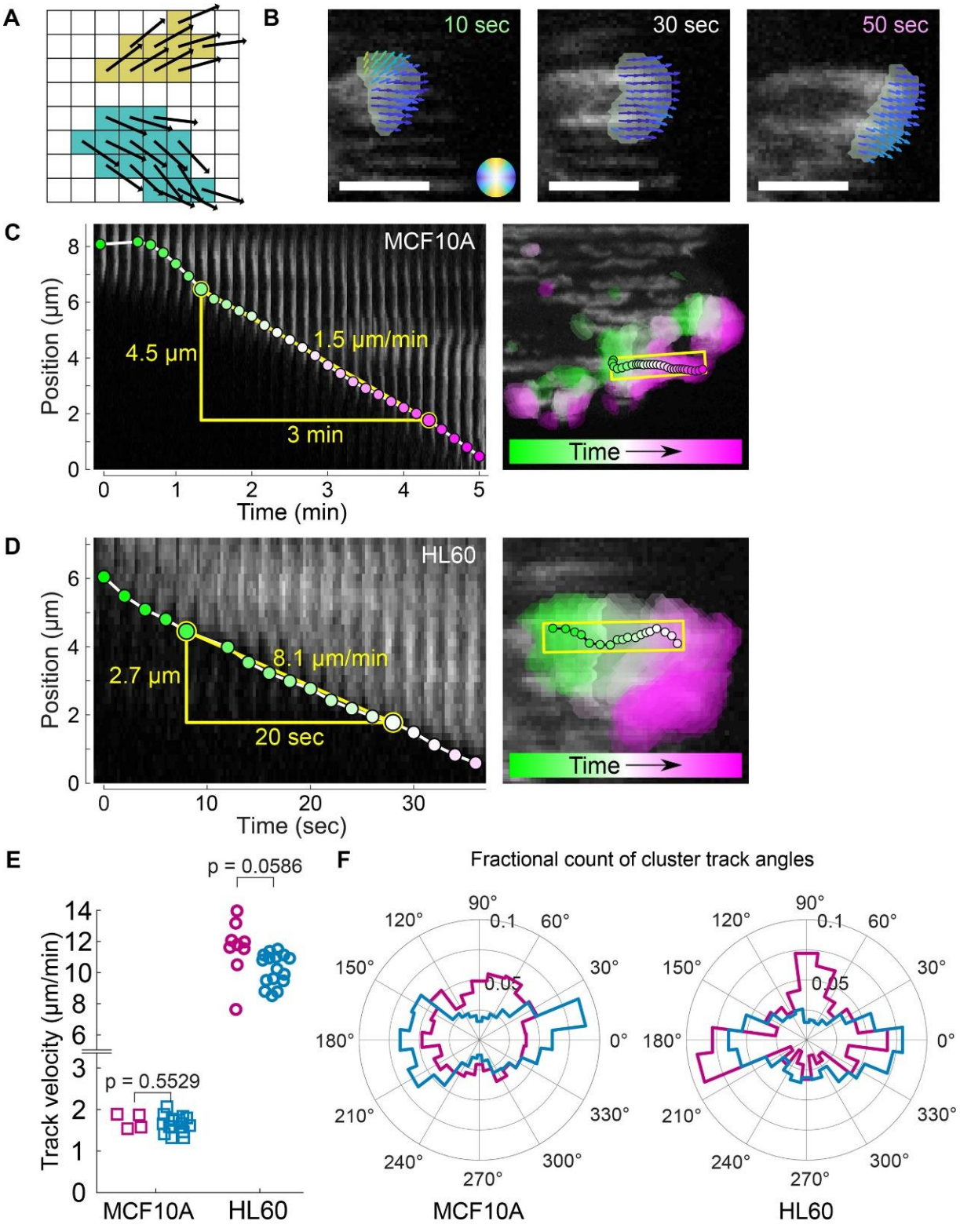
A
B
10 sec
30 sec
50 sec
C
MCF10A
Position (μm)
4.5 μm
1.5 μm/min
3 min
Time (min)
Time
D
HL60
Position (μm)
2.7 μm
8.1 μm/min
20 sec
Time (sec)
Time
E
p = 0.0586
p = 0.5529
Track velocity (μm/min)
MCF10A
HL60
F
Fractional count of cluster track angles
MCF10A
HL60

We applied peak-finding and tracking algorithms[246] to follow the locations of maximum alignment of these optical-flow clusters on the micron scale. Although the optical-flow results shown in Figure 4.4 follow motion on the pixel scale, by following the peak alignment of the optical flow, we are able to track larger coordinated clusters of actin. Our tracking is consistent with the actin dynamics seen in kymographs, as shown by representative kymographs of MCF10A (Figure 4.5C) and HL60 (Figure 4.5D) cells overlaid with the tracked location of actin waves. Unlike kymographs, which are sensitive to motion along a chosen direction, tracks of clustered flow vectors reveal the micron-scale motion of actin in two dimensions. The benefits of our approach are illustrated in Figure 4.5C for an MCF10A cell. For the initial frames, the kymograph indicates a stationary actin structure (Figure 4.5C, left), but when the actin dynamics are viewed in two dimensions (Figure 4.5C, right), it is evident that in the early frames this wave is moving perpendicular to the ridges, a motion that cannot be captured in this one-dimensional kymograph. Thus, the combination of optical flow, clustering, and tracking allows us to follow actin waves without being limited to tracking only motion that occurs along a straight line.

The speeds of the tracked actin clusters (Figure 4.5E) are similar to speeds derived from actin kymographs (Figure 4.5C and D, and Figure 4.6), despite an approximately order-of-magnitude difference in speed between the two cell types that is consistent with their distinct *in vivo* functions and with previously reported cell-migration speeds.[247,248] For both cell types we find no significant difference ($p = 0.5529$ and $p = 0.0586$) between actin-wave speeds on flat and ridged surfaces (Figure 4.5E), implying that nanoridges steer actin dynamics but do not alter wave speeds in these two cell types. On flat surfaces, the directions of the clusters are distributed

uniformly for MCF10A cells but show distinct peaks in multiple directions for HL60 cells (Figure 4.5F). This observation is consistent with the polarized character of actin in several of the HL60 cells on flat surfaces, corresponding to κ values greater than 2 in Figure 4.4E,F.

4.3. Discussion

Extracellular texture, which is an important component of the 3D, *in vivo* environment, is capable of spatially patterning actin and modulating actin dynamics. Using nanoridge structures in conjunction with optical-flow approaches, we are able to probe and quantify this intracellular response to extracellular textures in a systematic manner.

Previous studies of *D. discoideum*,[130,131] B cells,[156] and tumor-associated fibroblasts[155] showed similarity in actin response to texture, which suggests that guidance of actin driven by texture (esotaxis) is broadly conserved across cell types. Controlled textures are thus a useful model microenvironment for the systematic, reproducible, and quantitative study of intracellular dynamics and force regulation. Here we demonstrated the analysis of time-lapse images of two cell types that have distinct physiological function. Neutrophil-like HL60 cells are polarized and highly motile, and respond to a variety of cues as they fulfill their role in the immune system. Epithelial MCF10A cells, however, have a nonmotile physiological function. Nevertheless, both cell types show clear, and quantitatively similar, actin dynamics in response to surface textures. Consistent with our prior results,[130,155] we find that nanoridges lead to persistent streaks of actin that are not seen on flat surfaces.

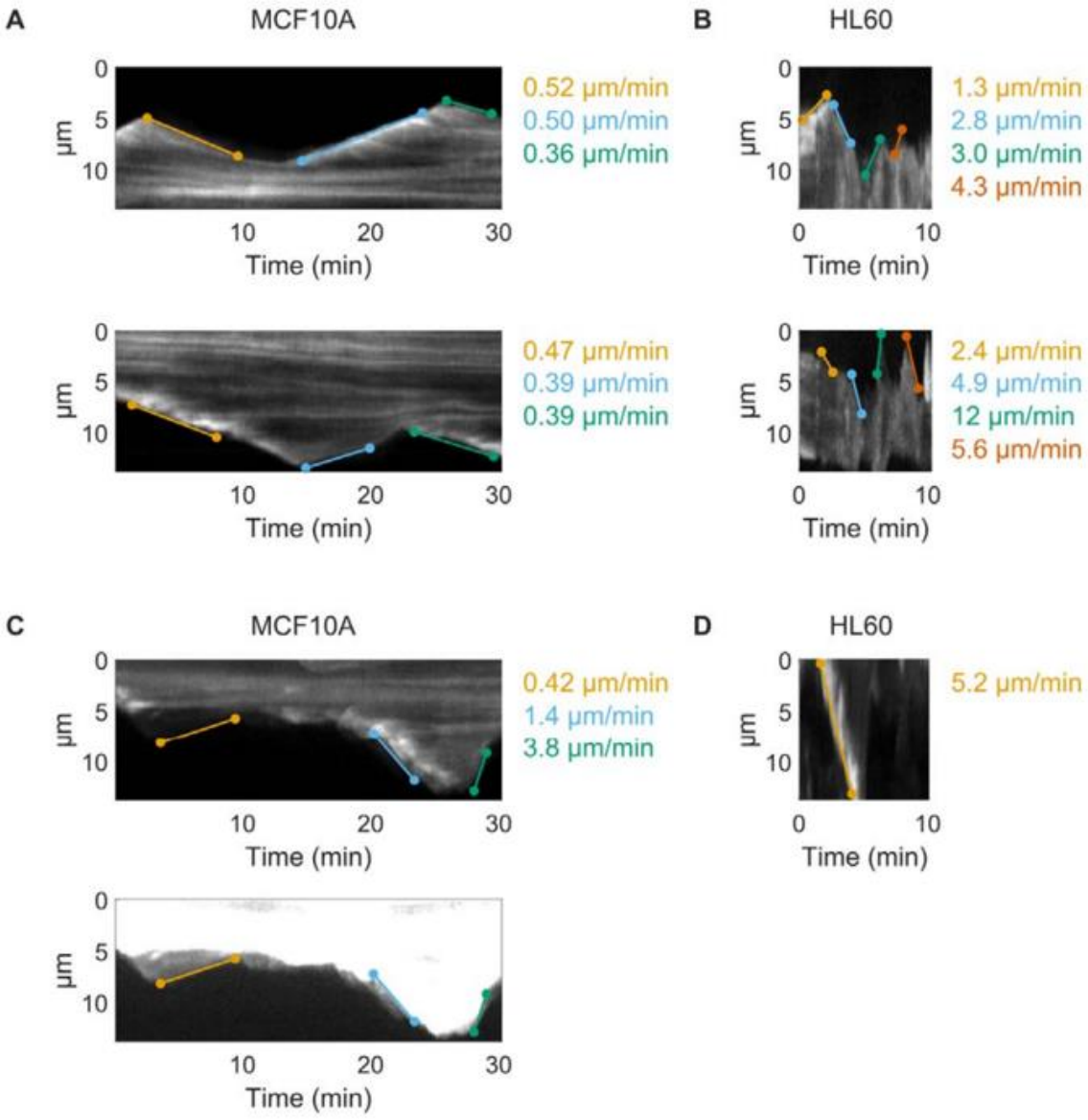

Figure 4.6. Actin-wave speeds. Actin-wave speeds were calculated from the kymographs shown in Figure 4.2 by manually selecting two points on the kymograph (using the ginput function in MATLAB) and calculating the slope between them. The speeds shown here agree with the distribution of speeds found using optical-flow-based tracking (Figure 4.5) for a MCF10A on a flat surface (A), an HL60 cell on a flat surface (B), a MCF10A cell on a ridged surface (C), and an HL60 cell on a ridged surface (D).The bottom panel of (C) shows a saturated version of the underlying kymograph to emphasize the protrusions being tracked. Reprinted with permission from reference 245.

Optical flow enables the quantification of both the reproducible streaks of actin seen on nanoridged surfaces and the more chaotic actin waves seen on flat surfaces. The latter waves are typically much wider than guided actin waves. On flat surfaces the waves often change direction and can also grow wider and split. Such motion phenotypes are not easily captured with standard techniques such as kymographs. Optical flow enables us to follow these dynamics and thus yields insights beyond those derived from kymograph-based techniques.

We note that optical flow is suitable for comparisons of systems imaged under different conditions (e.g., 60× vs. 100× objectives), enabling comparisons of widely varying cell sizes and migration speeds. The use of varying acquisition rates (i.e., 2 and 10 s) in this work was based on the differences in cell migration speeds of the two cell lines studied. In general, optical flow requires using a frame rate such that changes in fluorescence intensity between frames are small, but larger than noise. Our use of the Lucas–Kanade optical-flow constraint also makes the assumption that there is a smoothness to the flow field over a certain neighborhood, which is a length-scale parameter in the optical-flow analysis. This assumption is met by a wide variety of biological imaging data sets, and thus the use of our optical-flow approach is not limited to actin dynamics. Optical flow could provide insights into the motion of other cytoskeletal proteins, such as tubulin, or into the dynamics of other fluorescent markers that exhibit a spatially and temporally changing intensity field. Our use of clustering to study larger-scale actin dynamics could similarly be adapted to other fluorescent markers under the assumption that there are larger-scale dynamics that move together in similar directions. In this work, we used a spinning-disk confocal microscope for image acquisition, but our analysis pipeline would also be appropriate for other imaging techniques, such as epifluorescence. When working with other imaging modalities or fluorescent markers, the size of the Lucas–Kanade neighborhood and the

threshold for vector reproducibility (Figure 4.7) can be adapted to only include robust results in further analysis.

Using submicron-scale optical flow and associated micron-scale analysis, we have shown that both MCF10A and HL60 cells have actin flows that are biased along nanoridges. By clustering similarly oriented optical-flow vectors, we are able to measure the speed of actin waves within the cell. The measured speeds are comparable to speeds calculated from actin kymographs. Optical-flow analysis allows us to determine that the speeds do not differ significantly on flat versus ridged regions. This finding indicates that nanoridges guide, but do not fundamentally alter, the speed of actin dynamics in these two cell types. We measure actin-wave speeds on the order of 1 μm/min in the MCF10A cells, consistent with previously reported cell migration speeds of approximately 0.5 μm/min.[248] In the HL60 cells we find actin speeds ranging from approximately 8 to 14 μm/min, consistent with the 8 μm/min speed for cell migration previously reported.[247]

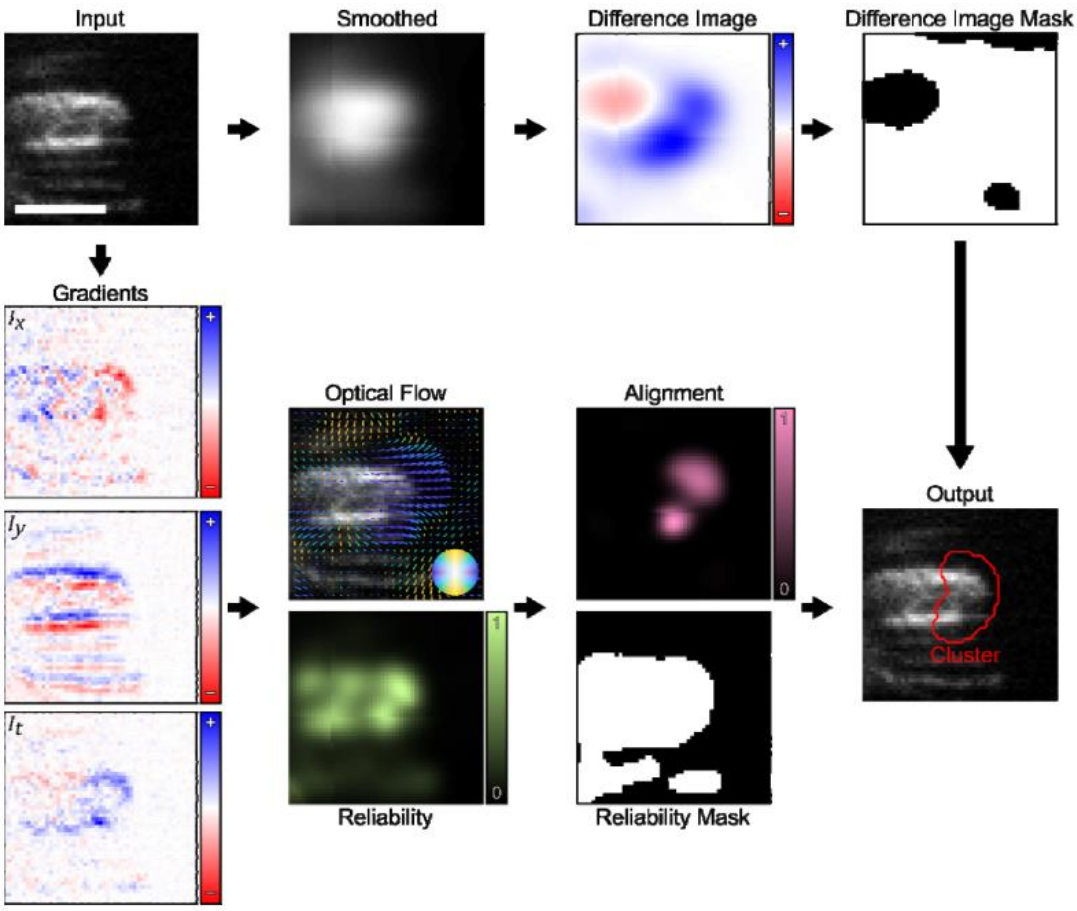

Figure 4.7. Cluster-finding workflow. Input time-lapse images (upper left) are used to generate a series of masks along two independent workflows: 1) To generate the difference image mask, images are smoothed and then subtracted from adjacent frames. The difference image mask is calculated by applying a threshold (in this work, the threshold is set to 0). 2) To generate the alignment and reliability mask, spatiotemporal intensity gradients are calculated and used to calculate optical flow and reliability. Alignment is calculated by taking the dot product between vectors and their local neighborhood (in this work, the neighborhood is a Gaussian with a standard deviation of 0.63 μm). The reliability mask is calculated by applying a threshold (in this work, the threshold is set to 10× the median of the reliability distribution. Taken together, the difference image mask, alignment, and reliability mask are multiplied in an elementwise fashion to generate the final cluster image. In this work, the cluster image is used as an input to peak finding and tracking algorithms. Scale bar is 5 μm. Reprinted with permission from reference 245.

Fitting the optical-flow vectors to a bimodal von Mises distribution enables quantification of the differences in the directionality of actin flows on flat and ridged surfaces in both cell lines.

The fit parameters also show differences in actin polarization in these two cell lines. HL60 cells occasionally exhibit coordinated and directed actin flows even on flat surfaces, whereas MCF10A cells on flat surfaces show uniform direction distributions of actin waves. On the micron scale, actin-wave tracks from individual HL60 cells on flat surfaces generally polarize and have a preferred direction, consistent with the behavior of immune cells, which tend to polarize and migrate in a directed manner. Tracks from MCF10A cells on a flat surface, on the other hand, are more directionally uniform for each cell. In both cell types, ridges guide actin waves in a bidirectional manner.

The quantitative actin responses in MCF10A and HL60 cells support a model in which surface texture provides a symmetry-breaking cue that leads to nucleation of actin polymerization. Under flat tissue-culture conditions, which lack symmetry-breaking cues, actin polymerization relies on spontaneous nucleation or edge effects.[249] Edge effects may lead to morphological features such as the lamellipodia seen in HL60 cells on flat surfaces in Figure 4.2B. By changing the landscape on which nucleation occurs, surface texture can lead to actin polymerization in other locations of the cell, such as the persistent streaks seen in the center of MCF10A cells on ridges in Figure 4.2A.

There are multiple mechanisms by which cells may respond to local forces and geometry,[250] including sensing mechanisms that can respond to membrane curvature on a variety of scales.[251] Our finding that nanoridges change the direction, rather than the speed, of actin waves suggests that growth of existing actin filaments away from the surface is the rate-limiting step in actin polymerization wave propagation. In some cases, sensing mechanisms may rely on the preferential formation of focal adhesions. This hypothesis is consistent with previous results

on focal-adhesion localization and orientation in response to surface texture.[142,186] Although MCF10A cells form strong focal adhesions that may align with texture cues,[142] the HL60 cells form weaker adhesions, and the previously studied *D. discoideum* cells[130,131] are not known to form integrin-mediated focal adhesions. Thus, the dominant mechanism of surface texture response likely depends on both the cell type and the extracellular environment.

Known surface-sensing mechanisms also include cytoskeletal components such as septins, which respond to micron-scale curvatures,[252] and BAR domains, which sense nanoscale curvature.[253] Proteins with BAR domains have been linked to actin assembly[254] as well as to key components of actin-regulating pathways, such as WAVE and Rac.[255,256] Recent work has suggested that nucleation of new actin filaments is enhanced by nanotopography. Specifically, curved nanopillars activate the nucleation-promoting factors Arp2/3 and N-WASP through enhanced binding of an F-BAR domain containing protein.[257] Additionally, evidence suggests that topography is capable of shifting multiple gene-expression pathways,[98] which implies that longer-term exposure to topography may mediate additional surface-sensing pathways. As *in vivo* microenvironments contain a variety of textures, it is likely that multiple mechanisms respond to distinct features of extracellular texture, and future work on the response of actin regulators to controlled topographies such as those investigated here will help elucidate the contributions of distinct signaling pathways in esotaxis.

Although the systematic modulation and interrogation of all possible molecular factors of esotaxis is beyond the scope of this chapter, our analysis yields two remarkable constraints on the molecular sources of esotaxis. First, the speed of actin waves is not altered by esotaxis in these two cell types. Second, the directional guidance provided by nanotopography is

comparable in the two cell types investigated, despite their disparate functions and migratory phenotypes. Quantitative analysis of esotaxis as a physical phenotype could yield crucial prognostic disease insights, especially in the case of cancer, in which changes in the texture of the microenvironment correlate with disease progression.

4.4. Materials and Methods

4.4.1. Cell Culture and Imaging

HL60 YFP-actin cells were a gift from Orion Weiner of the University of California, San Francisco. The cells were cultured in RPMI 1640 medium, Glutamax (Life Technologies) supplemented with 10% heat-inactivated fetal bovine serum (Gemini Bio). Cells were passaged every 2–3 d and kept between 3×10^5 and 1×10^6 cells/ml. For differentiation, cell media was additionally supplemented with 1.3% dimethyl sulfoxide Hybri-Max (Sigma Aldrich) for 5 d before imaging. Actin dynamics of HL-60 YFP-actin cells were observed by confocal fluorescence and bright-field time-lapse imaging using a PerkinElmer spinning-disk confocal microscope with a water immersion 60× objective (0.21 μm/pixel). Images were recorded every 2 s. We note that this method of plating resulted in the imaging of some multicellular clusters of HL60 cells; these clusters were not considered further.

Preparation for imaging included a 10 μg/ml coating of fibronectin on the substrates. Cells were plated and allowed to settle. After approximately 30 min, N-Formyl-Met-Leu-Phe (fMLF; Sigma Aldrich) was added to 1 μM. HL-60 cells were imaged on flat resin and ridged

nanotopographies beginning between 10 and 15 s after fMLF stimulation. All images analyzed in this work were obtained after fMLF stimulation.

MCF10A LifeAct-EGFP cells were a gift from Carole A. Parent (National Cancer Institute, Bethesda, MD). These cells were cultured in DMEM/F12 media supplemented with 5% horse serum, 10 μg/ml insulin (ThermoFisher Scientific), 10 ng/ml EGF (Peprotech, Rocky Hill, NJ), 0.5 μg/ml hydrocortisone, and 100 ng/ml cholera toxin (both Sigma, St. Louis, MO). The media were additionally supplemented with 2 μg/ml puromycin dihydrochloride (ThermoFisher Scientific) to select for EGFP-positive cells. Before imaging, cells were plated on a nanoridged surface coated with collagen IV and were allowed to adhere to the surface overnight. Actin dynamics were studied by confocal fluorescence and bright-field, time-lapse imaging using a PerkinElmer spinning-disk confocal microscope with a 100× objective (0.14 μm/pixel). Images were recorded every 10 s.

For both cell types, data were collected using PerkinElmer's Volocity software (version 6.4.0). The spinning-disk confocal microscope was equipped with a Hamamatsu ImagEM X2 EM-CCD camera (C9100-23B), which recorded 12-bit images. Cells used in this study tested mycoplasma negative using the MycoAlert (Lonza) testing system.

4.4.2. Surface Fabrication

The nanotopographies were designed and fabricated using MAP, as described previously.[142] A drop of prepolymer resin (1:1 wt/wt Tris [2-hydroxy ethyl] isocyanurate triacrylate [SR368]: ethoxylated (6) trimethylolpropane triacrylate [SR499], both from Sartomer; 3% Lucirin TPO-L [BASF]) was sandwiched between a coverslip and a plasma-treated

microscope slide that had been functionalized with acrylate groups.[106,107,142] The coverslip was mounted onto the stage of an inverted microscope (Zeiss Axiovert 135). A beam of 150-fs pulses centered at 800 nm from a Ti:sapphire oscillator (Coherent Mira 900) was directed into the microscope and through a high-numerical-aperture objective (Zeiss alpha-Plan Fluar 100×; NA 1.45). The stage motion and shutter were controlled using a program written in LabVIEW (National Instruments). Once the pattern was fabricated, the sample was developed in ethanol and baked at 110°C for 1 h.

A replica molding approach was then used to mold the chemically functionalized pattern.[142] This step included the initial casting of a hard-poly(dimethylsiloxane) (*h*-PDMS) layer (1000 rpm, 40 s) to better resolve nanoscale features of the topographical pattern. This layer was allowed to sit on the pattern at room temperature for 2 h and was then baked at 60 °C for an additional 1 h. Finally, Sylgard 184 was mixed (10:1 elastomer base:curing agent) and poured onto the initial *h*-PDMS layer. The PDMS was cured at 60 °C for 1 h 10 min.

The MAP-fabricated structure was then reproduced through a soft-lithographic technique. A drop of the aforementioned resin was sandwiched between the PDMS mold and an acrylate-functionalized coverslip and was then exposed to UV radiation from a lamp for a desired amount of time. After the resin cured, the coverslip was peeled off the mold. This process was repeated many times to produce enough replicas to perform the necessary experiments. The replicas were soaked in ethanol for at least 4 h and subsequently baked/dried in an oven at 110 °C for 1 h. Samples used to study MCF10A cells were also soaked in UltraPure water (ThermoFisher) for approximately 12 h.

4.4.3. Kymographs

Kymographs were created in MATLAB by manually selecting a rectangular region in an actin image. Fluorescence intensities inside the region were averaged across the short axis of the region; this process was repeated for each image in the time-lapse sequence, and the resulting intensity data were combined into the kymographs shown in Figure 4.2 and Figure 4.6.

4.4.4. Optical Flow

The Lucas–Kanade optical-flow method[233] was used to capture the direction and strength of intensity flow of fluorescent actin and to produce vector fields indicating actin motion. The optical-flow vector field of an image series is the field of apparent translation in the image plane, as is shown schematically in Figure 4.3B. Calculating the optical flow for two adjacent 2D images in an image series requires solving for the unknowns Δx and Δy in Eq. 4.1, as described above. The Lucas–Kanade method uses a least-squares regression approach to solve for the best optical-flow vector on a pixel-by-pixel basis under the assumption that all pixels within a "neighborhood" move in a similar direction.[233] If solving for the optical-flow vector of some point p with coordinate (x_p,y_p,τ), the master optical-flow equation requires that the optical flow vector of point p and all points in the neighborhood about p (points 1,2,…,p,…, N) follow the underdetermined relation

$$-\begin{bmatrix} I_{x_1}v_{x_1} & I_{y_1}v_{y_1} \\ I_{x_2}v_{x_2} & I_{y_2}v_{y_2} \\ \vdots & \vdots \\ I_{x_{p-1}}v_{x_{p-1}} & I_{y_{p-1}}v_{y_{p-1}} \\ I_{x_p}v_{x_p} & I_{y_p}v_{y_p} \\ I_{x_{p+1}}v_{x_{p+1}} & I_{y_{p+1}}v_{y_{p+1}} \\ \vdots & \vdots \\ I_{x_N}v_{x_N} & I_{y_N}v_{y_N} \end{bmatrix} = \begin{bmatrix} I_{t_1} \\ I_{t_2} \\ \vdots \\ I_{t_{p-1}} \\ I_{t_p} \\ I_{t_{p+1}} \\ \vdots \\ I_{t_N} \end{bmatrix} \tag{4.3}$$

Under the Lucas–Kanade assumption, the vector for point *p* is assigned to all points in the neighborhood

$$-\begin{bmatrix} I_{x_1} & I_{y_1} \\ I_{x_2} & I_{y_2} \\ \vdots & \vdots \\ I_{x_{p-1}} & I_{y_{p-1}} \\ I_{x_p} & I_{y_p} \\ I_{x_{p+1}} & I_{y_{p+1}} \\ \vdots & \vdots \\ I_{x_N} & I_{y_N} \end{bmatrix} \begin{bmatrix} v_{x_p} \\ v_{y_p} \end{bmatrix} = \begin{bmatrix} I_{t_1} \\ I_{t_2} \\ \vdots \\ I_{t_{p-1}} \\ I_{t_p} \\ I_{t_{p+1}} \\ \vdots \\ I_{t_N} \end{bmatrix} \tag{4.4}$$

The least-squares solution to equations of this form, $A\vec{x} = \vec{b}$, is $\vec{x} = (A^T A)^{-1} A^T \vec{b}$. Furthermore, we implement a scheme using a Gaussian weight matrix centered at point *p* to ensure that pixels near *p* have more influence over the result. The equation then becomes

$$\begin{bmatrix} \sqrt{w_1} & & & & & & 0 \\ & \sqrt{w_2} & & & & & \\ & & \ddots & & & & \\ & & & \sqrt{w_{p-1}} & & & \\ & & & & \sqrt{w_p} & & \\ & & & & & \sqrt{w_{p+1}} & \\ 0 & & & & & & \ddots \\ & & & & & & & \sqrt{w_N} \end{bmatrix} \begin{bmatrix} I_{x_1} & I_{y_1} \\ I_{x_2} & I_{y_2} \\ \vdots & \vdots \\ I_{x_{p-1}} & I_{y_{p-1}} \\ I_{x_p} & I_{y_p} \\ I_{x_{p+1}} & I_{y_{p+1}} \\ \vdots & \vdots \\ I_{x_N} & I_{y_N} \end{bmatrix} \begin{bmatrix} v_{x_p} \\ v_{y_p} \end{bmatrix}$$

$$= \begin{bmatrix} \sqrt{w_1} & & & & & & 0 \\ & \sqrt{w_2} & & & & & \\ & & \ddots & & & & \\ & & & \sqrt{w_{p-1}} & & & \\ & & & & \sqrt{w_p} & & \\ & & & & & \sqrt{w_{p+1}} & \\ 0 & & & & & & \ddots \\ & & & & & & & \sqrt{w_N} \end{bmatrix} \begin{bmatrix} I_{t_1} \\ I_{t_2} \\ \vdots \\ I_{t_{p-1}} \\ I_{t_p} \\ I_{t_{p+1}} \\ \vdots \\ I_{t_N} \end{bmatrix} \tag{4.5}$$

where w is a $\sqrt{N} \times \sqrt{N}$ centered Gaussian matrix. The equation then takes the form $\sqrt{w}A\vec{x} = \sqrt{w}\vec{b}$ and has solution

$$\vec{x} = \left(A^T\sqrt{w}^T\sqrt{w}A\right)^{-1} A^T\sqrt{w}^T\sqrt{w}\vec{b} = (A^T wA)^{-1}A^T w\vec{b}. \tag{4.6}$$

Optical-flow reliability is defined as the smallest eigenvalue of the $A^T wA$ matrix,[258,259] and was used to remove flow vectors that were created by noise or an ill-defined least-squares calculation. The threshold used can be adapted to best suit the experimental data and scientific questions of interest by only keeping the most reliable vectors while measuring the motion of more regions of the cell. The optical-flow weight matrix for MCF10A cells was a 27 × 27 pixel Gaussian with a SD of 4.5 pixels (0.63 μm). The optical-flow weight matrix for HL60 cells was

19 × 19 pixel Gaussian with a SD of 3 pixels (0.63 μm). With other imaging modalities, magnifications, or fluorescent markers, it may be appropriate to change the size of this weight matrix based on the size of features of interest and noise in the image.

4.4.5. von Mises Model of Flow Distribution

Optical-flow distributions were modeled with a modified bimodal von Mises distribution (von Mises distributions are a continuous and differentiable analogue of normal distributions on a circle with similar statistical properties). The model was defined as

$$f(\theta|\theta_{\mu,\kappa}) = p_1 * VM(\theta|\theta_{\mu,\kappa}) + p_2 * VM(\theta + \pi|\theta_{\mu,\kappa}) + (1 - p_1 - p_2) * \frac{1}{2\pi} \quad (4.7)$$

where $VM(\theta \mid \theta_{\mu,k})$ is the von Mises distribution

$$VM(\theta|\theta_{\mu,\kappa}) = \frac{e^{\kappa \cos(\theta - \theta_\mu)}}{2\pi I_0(\kappa)} \quad (4.8)$$

and $I_0(\kappa)$ is the modified Bessel function of the first kind. The maximum likelihood estimates of the parameter k were used for statistical analyses.

4.4.6. Cluster-Tracking Analysis

Regions of actin fluorescence were clustered using the direction of optical-flow vectors together with an optical-flow reliability threshold and by requiring that actin intensity change over time (see Figure 4.7 for a visualization of this workflow). The dot products between optical-flow vectors around a point p (i.e., vectors $v_1, v_2, \ldots, v_{p-1}, v_{p+1}, \ldots, v_N$) were calculated and accumulated using a Gaussian weighting scheme to a single scalar alignment metric. The alignment metric is defined as

$$a_p = \sum_{i=1}^{N} w_i * \left(\vec{v}_p \cdot \vec{v}_i\right) \quad (4.9)$$

where *w* is a renormalized $\sqrt{N} \times \sqrt{N}$ centered Gaussian matrix with a center manually set to 0. This calculation was carried out for each pixel.

To require that the actin intensity change over time, a mask of the thresholded difference image between subsequent frames was calculated. For every pair of adjacent frames, I_t and $I_{t+\Delta t}$, the resulting mask took value *I* where $I_{t+\Delta t} > I_t$ and 0 otherwise. For our analysis, Δt = 30 s for MCF10A and 6 s for HL60.

To calculate the final clustered regions, the alignment metric a_p, optical-flow reliability λ_p, and difference-image mask were multiplied in an element-wise manner to create a final cluster image. The cluster image was inputted into a peak-finding algorithm to locate peaks in the resulting intensity profile, and the Crocker-Grier particle-tracking algorithm[246,260] was used to track coordinates of the resulting peaks over time.

The clustering weight matrix for MCF10A was a 27 × 27 pixel Gaussian with a SD of 4.5 pixels (0.63 μm). The clustering weight matrix for HL60 cells was 19 × 19 pixel Gaussian with a SD of 3 pixels (0.63 μm). The diameter of the peaks used in pkfnd.m[246] was 15 pixels (2.1 μm) for MCF10A cells and 10 pixels (2.1 μm) for HL60 cells. The maximum displacement used in track.m[246] was 11.5 pixels (1.54 μm) for MCF10A cells and 7 pixels (1.47 μm) for HL60 cells. Tracks measured in the movies of MCF10A cells were considered only if they were tracked for more than three frames (30 s) and tracks measured in movies of HL60 cells were only considered if they were tracked for more than three frames (6 s).

4.4.7. Statistical Methods

Measurements of κ for MCF10A cells (Figure 4.4E) and actin-wave speeds for both cell types (Figure 4.5E) were compared on flat versus nanoridged surfaces using two-sample *t* tests with unequal variances. A two-tailed *t* distribution was used to calculate the reported *p* values. As the measurements of κ for HL60 cells violated the normality assumption for a *t* test, we used a nonparametric Wilcoxon rank sum test to compare these values. A full description of the statistical parameters involved in these tests is available.[245]

4.4.8. Data and Software Availability

Our optical-flow analysis code is available on GitHub at https://github.com/losertlab/flowclustertracking. Imaging data from this study is available in a Mendeley Data repository on publication.[261]

4.5. Acknowledgments

We thank the University of Maryland Imaging Incubator Core Facility for use of their systems in collecting images for this work. We appreciate Ema Smith's work on the optical-flow code. This work was supported by AFOSR grant number FA9550-16-1-0052. R.M.L was supported by National Cancer Institute/National Institutes of Health (NIH) award number T32CA154274. L.C. was supported by COMBINE NRT award number 1632976 and NIH 1U01GM109887.

Chapter 5: Guided Actin Dynamics Regulate Directed Cell Motion along Nanoridges Regardless of the Availability of Collagen IV

5.1. Introduction

The ability to control cell migration with cell-type specificity is a focus of research and development for disease treatments,[262] but such control requires profound knowledge of the target cell, as well as its environment. Cell motion may be controlled by any of its governing internal components and processes, such as the cytoskeletal network,[263,264] molecular signaling pathways,[265-271] gene expression,[265,272,273] protein synthesis,[274,275] and post-translational modifications,[26,276-278] all of which coordinate to regulate cell migration.[17] In some cases, the influence of specific genes and proteins on cell migration varies across cell types.[64] Many of these internal components can be impacted by external factors, including chemical and physical stimuli.[13] In natural environments, these cues are generated by neighboring cells and the extracellular matrix (ECM), and can be strong enough to influence disease progression, including cancer metastasis.[18] Thus the characteristics of cell motility can be changed in response to external factors.[7,13,14] Such control is found in nature, e.g., in neural crest cells that undergo the epithelial-to-mesenchymal transition (EMT),[3] a process that entails changes in expression of cell–cell adhesion, as well as molecules capable of digesting proteins in the ECM and the cell surface. At the same time, an EMT can also facilitate the progression of cancer, by similarly altering the adhesion and motility characteristics of cancer cells[3] and increasing ECM detachment.[71] Controlled changes in migration state also often involve additional feedback: for

example, the transcription factors (TFs) produced during the EMT program promote DNA repair[279] and inhibit apoptosis.[279,280] Therefore, treatments that involve external stimuli impacting cellular pathways can be developed to promote healthy cell migration, or to inhibit deleterious cell migration.

Cells perpetually sense their physical environment to determine whether to maintain or adapt their behavior and to execute necessary functions. Differentiation, for example, can be induced through sensing of topography.[180,281-284] Changes in the physical interactions with the environment or the ability of cells to sense their physical can have dramatic implications for cell health. For instance, detachment from the ECM induces anoikis in endothelial and epithelial cells, with some physiologically relevant exceptions. This sensing of the physical environment is altered in cancer cells, which often have altered signaling networks that inhibit anoikis driven by the physical environment.[71,285-288] Cells can sense a variety of facets of their physical environment, including substrate stiffness,[238,289,290] and topography,[291-298] primarily through the detection of gradients.[13,299] Physical stimuli are often sensed by inducing changes in the conformation and distribution of biomolecules near the plasma membrane, which then initiate signaling.[300,301] Protrusions, such as filopodia, can provide information about the physical surroundings, including the presence (and location) of neighboring cells and nearby changes in topography.[302,303] Sensing of the physical environment can also enable chemical signals. Cancer cells have demonstrated the ability to exploit physical stimuli to create chemical gradients.[300] Similarly, nanoscale topographical organization of membrane protrusions, invaginations, receptors, or channels on the cell surface enables efficient antigen recognition and immune response.[156,304-308]

The ability to sense a given physical cue depends on molecules at or near the surface of the cell, as well as on the properties of the cue. A cell must be able to orient itself such that sensitive molecules can detect changes in the physical landscape. Integrins often serve as sensors on the membrane surface. Depending on the biomolecular nature of the ECM, specific integrins can sense stretching of the substrate or shear stress from blood flow[309] (as can other membrane proteins[310]), and allow activation of transcription factors and molecular pathways that result in changes in cell function and behavior.[73,309] Other proteins, especially membrane-bound or membrane-associated proteins, e.g., those in BAR domains, can sense curvature.[311-313] Curvature can also influence myosin contractility[314] and stress-fiber organization.[315]

Our recent work has shown that the dynamic architecture of the cell, the actin cytoskeleton, also acts as a primary sensor of the physical environment, specifically electric fields and nanotopography. Although the involvement of the actin cytoskeleton in sensing has often been considered as part of the transduction network attached to transmembrane sensors such as integrins[316] (and other adhesion molecules), it has recently been suggested to have a more active role in force detection.[317] We discovered that the sensitivity of actin dynamics to both electric and nanotopographic cues can be modulated by tuning the properties of these combined cues, generating distinct actin wave behavior in response.[318,319] We have found that the dynamic response of F-actin to nanotopographic cues can vary by cell line,[196] and many studies have shown that changes in the dimensions of nanotopography prompt distinct cytoskeletal organization.[130,131,142,155,156,320-322] Cytoskeletal dynamics drive shape changes involved in processes such as motion and migration[33] and cell division,[323-325] and can also impact DNA repair and replication,[326,327] and protein transport.[328] The organization of the dynamic actin network is achieved by a multitude of other proteins that are responsible for further

polymerization/filament formation, branching, anchoring/tethering, contraction, and depolymerization.[16] Luo *et al.* found that different forces applied on cells can prompt specific actin-associated proteins to respond, thereby influencing the cytoskeletal change resulting from the applied force.[62] Additionally, it remains unclear which proteins near the membranes must be guided to accomplish directed migration.

Many of the transmembrane proteins involved in extracellular sensing are responsible for (or are involved with those responsible for) adhesion. Although integrins are the membrane proteins most often discussed with regard to matrix adhesion, others, such as polycystins, are capable of binding to ECM proteins[329] and are important for pressure sensing.[330] The spatial density and organization of integrins on the membrane control the strength and duration of adhesion to the ECM.[16] Integrins that cluster into focal adhesions form sites of strong adhesion.[15] The organization of integrins and the formation of adhesions are modulated by actin and actin-binding proteins, myosin, microtubules, GTPases, and kinases.[17,34,35] Similar relationships have been observed between GTPases and actin-binding proteins and other sensory and adhesion proteins.[331]

The nature of the cellular environment can determine how strongly a cell adheres to the ECM. Cells respond to changes in substrate stiffness, with the organization, size, and strength of adhesions generally increasing on stiffer substrates,[22] although not all cells follow this trend.[332] The ECM can also promote distinct adhesion characteristics depending on its molecular composition,[68] due to the organization of protein components and the presence of ligands to which specific integrins preferentially bind.[332,333] Adjusting the ECM protein concentration can change the substrate stiffness without modifying the biomolecular composition, and this selective

tuning of environmental properties has been shown to modify epithelial cell behaviors, such as the degree of proliferation, migration, adhesion, and signaling pathway activation.[67] Structural characteristics of ECM components can vary depending on anatomical location,[83] and topographical properties have been shown to influence the localization of adhesion complexes.[142,196,334] However, the state of the cell can also dictate its adhesion, as well as alter the properties of the surroundings, such as by producing matrix metalloproteinases to degrade the ECM. Cancer cells with lower expression of collagen genes (and thus lower production of collagen) exhibit less adhesion to the ECM and more tumorigenicity.[335] Even cells without integrin-modulated focal adhesions, such as the ameoboid *Dictyostelium discoideum*, can sense and respond to nanotopography.[130] The local characteristics of the ECM and the unique properties of the various cells encountering the environment determine the nature of adhesion to the substrate, which, in turn, affects cell function and behavior,[336] such as migration.

Adhesivity is a property that is often used to classify cellular migratory behavior. Cell types are frequently categorized as employing either amoeboid or mesenchymal migration, with adhesion as one of the primary characteristics used for distinction.[337,338] Amoeboid migration features a more rounded morphology, non-adhesive protrusions, and fast motion.[339] Cells exhibiting mesenchymal migration have a more elongated morphology, extend lamellipodia stabilized by focal adhesions, and move slowly.[14] However, these properties are really part of a continuum.[340] It has been determined that cells can simultaneously exhibit characteristics of both categories, and can also switch between migratory behaviors either with or without encountering changes in the extracellular environment.[13,341] Cancer cells can undergo transitions between amoeboid and mesenchymal modes, as determined by the contractility of the actomyosin network, the availability of signaling molecules, and the expression of membrane proteins and

proteases.[342-347] Switching between migratory phenotypes serves to promote disease progression when cancer cells encounter three-dimensional ECM environments with distinct properties, some of which might better suit the compact shape of a round cell or the ability to grasp or break down individual ECM fibers.[342,348] The properties of the ECM itself can also induce the change between mesenchymal and amoeboid modes.[339,344,346,349,350] Confinement of the cell within the ECM promotes the transition from elongated to round morphology that is often used to demarcate migratory categorization,[344,349,350] and the nucleus provides guidance through the close quarters.[351] Adjusting the surface chemistry of nanotopographic substrates offers another mechanism to modulate the migratory behavior of cells.

How strongly is directed migration that is induced by topographic cues dependent on actin and adhesion guidance? Topographical cues can elicit a morphological response, based on how actin senses, that is uncharacteristic of directed motion on flat substrates *in vitro* and still achieve guided migration due to texture sensing from integrins. For example, small-amplitude wavy ridges influence lamellipodial actin to organize at the wave peaks away from the leading edge of the cell, yet focal adhesions form in the direction of the nanoridges.[334] Although adhesions are often necessary for accurately directed migration,[352] some of the actin-binding proteins are also required for guidance.[65] Previous studies of T cells indicated that both actin polymerization and adhesion are necessary for cells to follow the guidance cues of nanoridges.[353,354] The conditions and limitations of actin sensing must continue to be probed.

In this study, we examine how F-actin can sense a combination of cues on the substrate, as determined through changes in the actin organization and dynamics, and the ability of F-actin to influence cell guidance in a complex extracellular environment. Specifically, we studied how

the cellular response to a specific nanotopographic cue is affected by surface chemistry. A pattern of aligned nanoridges was fabricated using a technique known as multiphoton absorption polymerization (MAP),[107] which allows for three-dimensional control over pattern features and dimensions. The nanoridges contained individual features with dimensions on the scale of collagen fibers. The substrates were coated with varying amounts of collagen IV to determine how chemical cues on the artificial matrix modulate cellular response to the ridges. MCF10A cells, a human breast epithelial cell line, labeled with LifeAct-GFP, were plated on these substrates. We then imaged the migration behavior of these cells over three distinct time periods: shortly after plating, 18 to 30 hours later, and another 20 to 30 hours after that. After each migration imaging session, individual cells were selected for imaging of the dynamics of their fluorescently labeled actin. Collecting data at the different time points enabled the determination of the temporal dependence of the migratory behavior and characteristic actin dynamics.

A shape-detection algorithm was used to quantify cell spreading on the nanoridges as a function of collagen IV coating density. Tracks of cell motion were also collected. To quantify the motion of actin, we employed a computer vision algorithm known as optical flow (OF),[232] which detects gradients of fluorescence intensity within a given image frame and compares changes in the distribution in consecutive frames to determine the flux of actin polymerization. The algorithm identifies and groups small regions of fluorescence intensity and maps the magnitude and direction of motion of actin polymerization within the cell. The actin dynamics were compared across the different collagen coatings on the nanoridges. The shape detection, cell-tracking, and OF data also provide information on how well the cells aligned with the orientation of the ridges.

We found that cells on collagen-coated ridges were more likely to spread and migrate. The amount of collagen did not affect these tendencies dramatically, though any difference decreased as time elapsed during the experiments. Cells that spread and migrated on uncoated ridges were also relatively well guided, and, again, this guidance improved over the course of the experiment. In general, the nanoridges provided strong guidance for migrating cells, with many cells maintaining alignment with the ridge axis while traveling over tens or even hundreds of microns. The preferred orientation of actin polymerization was also along the ridges, although some actin flux swept out nearly perpendicular to this direction. More densely coated ridges and the passage of time both increased the likelihood of aligned actin. The ability of polymerizing actin to sense the topography and orient accordingly did not influence the migratory behavior of cells. Persistent, turning, and random motion all exhibit similar actin kymographs.

5.2. Results

5.2.1. Collagen IV Facilitates Cell Spreading on Nanoridges

We examined cell shape and motion to develop a better understanding of how the availability of ECM ligands for integrins and adhesion affects guidance by topography. We first quantified the morphological response of the MCF10A cells. Based on a description of the mechanism of fibroblast cells spreading on fibronectin, the organization of adhesion proteins initiates spreading.[355] Therefore, we varied the surface coating density of collagen IV to observe the effect on the rate and extent of cell spreading. The cell shape was monitored, and the eccentricity was calculated to determine the degree of spreading and provide a measure of the ability of the cells to sense and respond to the topographic cues of the nanoridges. Specifically, we measured the eccentricity of the cells on the ridges, and how the eccentricity changed when

different amounts of collagen were coated onto the surface (Fig. 5.1A-D). We found that the expected cell eccentricity was higher on collagen-coated surfaces than on uncoated surfaces at each experimental timepoint (Fig. 5.1E). The majority of cells on uncoated ridges remained round throughout the period of observation. Despite this preponderance of round cells, the proportion of cells that elongated or spread (eccentricity > 0.5) on uncoated ridges increased after approximately 24 h. A similar, although greater, increase in the fraction of elongated cells with time was observed on ridges that were coated with collagen. MCF10A cells are known to deposit their own ECM proteins,[356] which likely explains why the average cell eccentricity on uncoated nanoridges increased over time. The population of eccentric cells did not differ greatly on nanoridges coated with distinct densities of collagen IV. Cell spreading on the nanoridges was dependent on the presence of the ECM protein coating, but could be achieved across a range of coating densities.

Figure 5.1 (next page). Collagen promotes cell spreading and nanoridges cause cells to elongate along the ridge axis. A. Schematic showing eccentricities for different ellipses. B-D. Histograms of the eccentricities of cells on nanoridges with approximate collagen IV coating densities of 0 (0%), 0.65 (20%), and 3.25 μg/cm^2 (100%) at different experimental timepoints. The green plots are the probability densities for the time window with an approximate midpoint of 2.75 h after plating (early), the orange plots are probability densities for the window centered at approximately 21.5 h after plating (middle), and the blue plots are probability densities for the time window centered at approximately 40.5 h after plating (late). E. The proportion of cells exhibiting an eccentricity greater than 0.5 on ridge surfaces for different collagen coating densities as a function of experimental timepoint for no collagen (blue), 20% collagen (orange), and 100% collagen (purple) F-H. Rose plots of the proportion of cells oriented at angles with respect to the ridge axis at different times after plating. The ridges are aligned with 0°/180° line. The color coding is the same as in panel E.

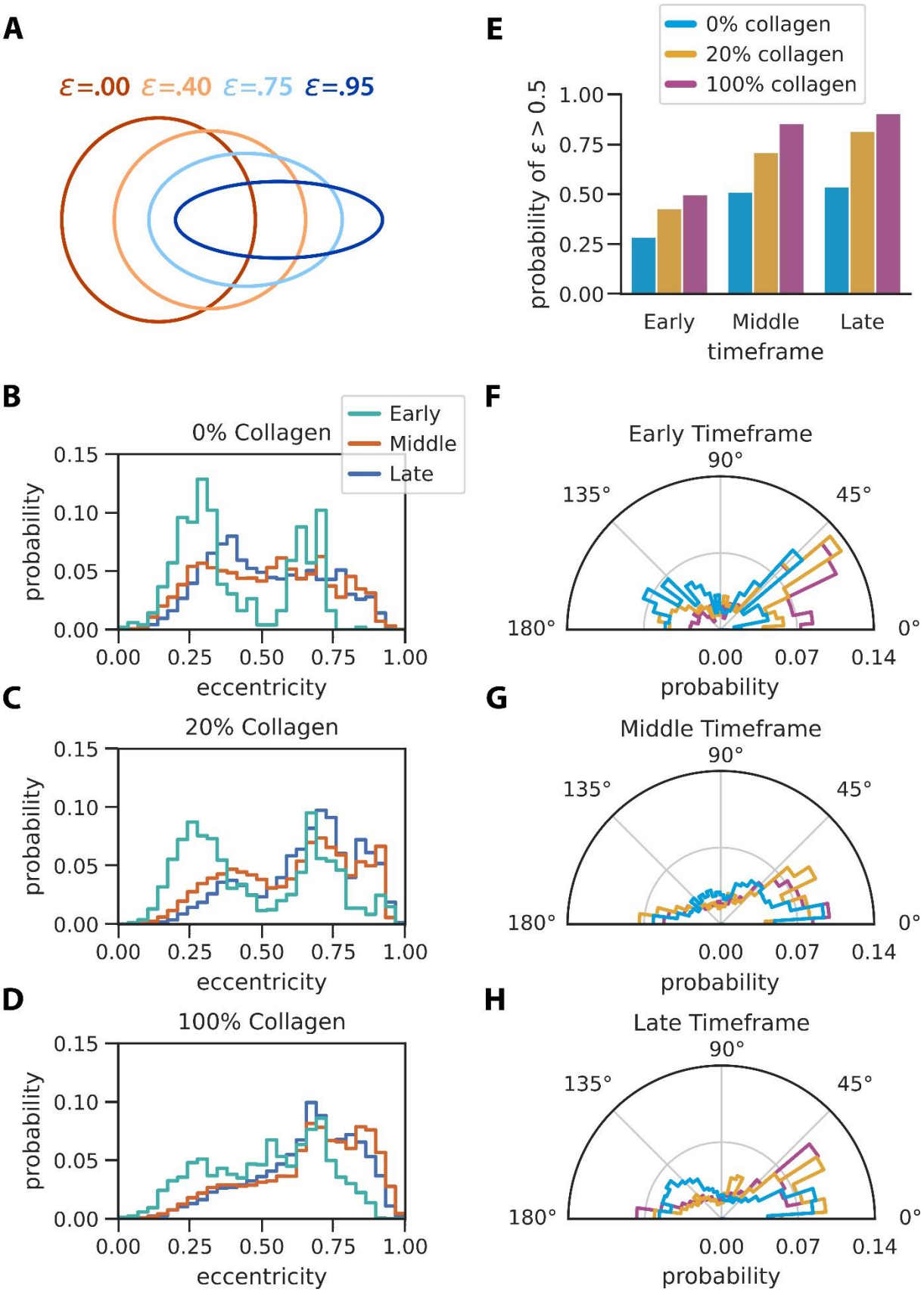
A
ε=.00 ε=.40 ε=.75 ε=.95
B
0% Collagen
Early
Middle
Late
probability
eccentricity
C
20% Collagen
D
100% Collagen
E
0% collagen
20% collagen
100% collagen
probability of ε > 0.5
timeframe
Early
Middle
Late
F
Early Timeframe
G
Middle Timeframe
H
Late Timeframe
90°
135°
45°
180°
0°
0.00
0.07
0.14

5.2.2. Availability of Collagen IV Is Not a Strong Determinant of Cell Alignment with Nanoridges

We next examined how cell shape responds to nanoridges when different amounts of adhesive cues are available for the cell to sense by analyzing the distribution of cell alignment with respect to the ridge direction (Fig. 5.1F-H). Our goal was to determine whether ridges orient spreading, and whether collagen influences the extent of any such alignment. We denote the first time window with an approximate midpoint of 2.75 h after plating the "early" timeframe in our experiments. Cells on uncoated nanoridges did not respond to the topographic cues within this time window (Fig. 5.11F). However, the discrepancy in alignment with the ridge axis between cells on uncoated and collagen-coated surfaces is smaller than might be expected. Indeed, in the early timeframe, the density of collagen does not seem to influence the distribution of cell alignment. After approximately 24 h after plating (the "middle" timeframe), the cells exhibit a significant degree of alignment with the ridges, but there is little distinction in the degree of alignment among the different coating conditions (Fig. 5.1G). Similar results were observed in the "late" timeframe, nearly 2 days after plating (Fig. 5.1H).

5.2.3. Cell Migration Is Guided Well by Nanoridges Regardless of Collagen Density

Although most of the cells that we observed spread on collagen-coated substrates, few of the cells migrated. The limited number of migrating cells might be a result of the stiffness or adhesive nature of the combination of collagen IV and the acrylic ridge material. On ridges coated with collagen, cells can take on an exaggerated, spindly mesenchymal shape, which is indicative of stable and well-organized adhesions that are induced by both surface chemistry and

nanotopography. Indeed, on surfaces with a high enough coating of collagen, some cells can stretch to a length of hundreds of microns and tear themselves apart (data not shown).

Migration was observed more frequently on coated substrates than on uncoated substrates (Fig. 5.2A). For cells whose displacement reached a minimum threshold over the course of observation, we used a tracking algorithm to trace the cell trajectory. As shown in Fig. 5.2B, the motion of most of the cells follows the ridges, which are oriented along the horizontal axis. Migrating cells were guided by the ridges over tens of microns. Although there are a few exceptions, most cells that migrate on the nanoridges travel along the ridge direction. Previous studies have shown the role of focal adhesion organization in the ability of cells to sense and follow nanotopographic cues during migration.[196,334] In analogy to our results for cell spreading on the ridges, in which the surface density of ECM ligands for adhesion influenced cell eccentricity (Fig. 5.1A-E), but had a limited impact on alignment with the nanotopography over the course of the experiments (Fig. 5.1F-H), we found that adhesive cues affect the likelihood of migration (Fig. 5.2A), but do not appear to be predominantly responsible for directed migration, as shown in the histograms of the direction of motion with respect to the ridges (Fig. 5.2D-F). The exception, in both the case of cell spreading and guided motion, occurred within a few hours after plating the cells. Across all coating densities, there were more occurrences of instantaneous motion away from the ridge axis (more aligned with the normal) during this time period (Fig. 5.2D-F, green curves). However, the frequency of these unaligned movements was higher on the uncoated substrates, with several peaks oriented perpendicular to the ridges on the polar histogram (Fig. 5.2D, green curve). Cells that are motile on the uncoated ridges exhibit instantaneous motion at all angles relative to ridge direction. However, in the middle timeframe, it became difficult to distinguish the prevalence of aligned motion for cells on surfaces that were

uncoated and surfaces with 20% collagen coating (Fig. 5.2D,E, orange curves). The guidance on the nanoridges with 100% collagen coating was slightly stronger, based on the greater prominence and narrower width in the polar histogram (Fig. 5.2F, orange curve). The strength of directed migration became even less distinct during the late timeframe (Fig. 5.2D-F, blue curves).

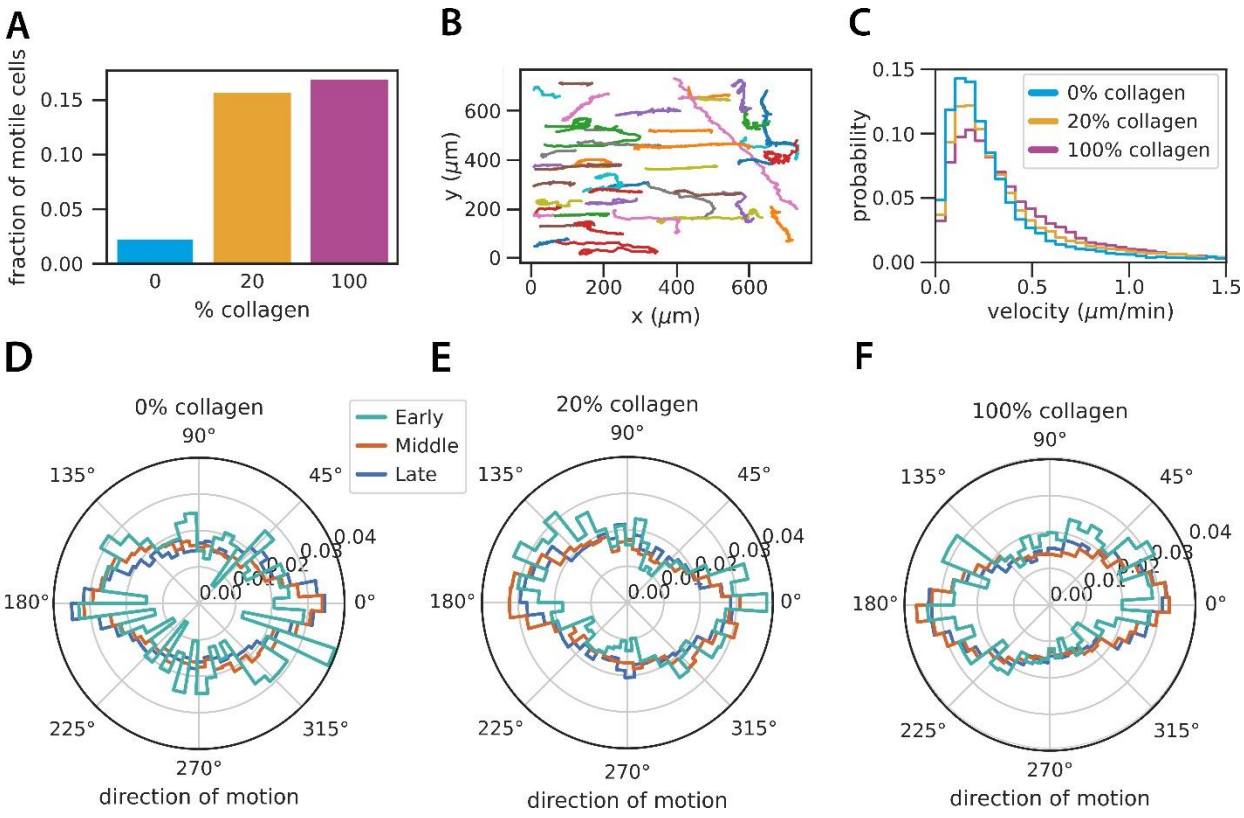

Figure 5.2. Cell migration on nanoridges is modulated by the surface density of collagen IV. A. Fraction of cells that are motile on the nanoridges as a function of collagen coating density. B. Tracks of cells migrating on, or adjacent to, the nanoridges. C. Distributions of populations of cells as a function of migration velocity on nanoridges with different coatings. D-F. Instantaneous orientation of cells migrating on nanoridges at different experimental times with no collagen, 20% collagen, and 100% collagen, respectively.

Overall, the nanoridges were capable of guiding cell motion, regardless of the availability of adhesive cues. There were, nevertheless, many moments at which cells on collagen-coated nanoridges appeared to be oriented away from the ridge direction, although this phenomenon became somewhat rarer with increasing time following plating. The relatively large occurrence of instantaneous motions at angles deviating from the ridge axis on all nanoridge surfaces makes the overall fidelity of the cell tracks to the ridge axis even more remarkable.

5.2.4. Collagen Promotes Faster Migration on Nanoridges

We next examined how adhesion to collagen affected the velocity at which cells migrated on the ridges. An early study by DiMilla *et al.* surmised that the maximum speed of smooth muscle cells occurred within an optimal range of ECM-ligand surface density, and thus is related to the adhesion strength between the cell and ECM.[357] If adhesion to the substrate is too strong, there will be fewer motile cells, and those cells that do migrate will move more slowly. A more recent study by Keely and coworkers investigated how fiber alignment, ligand density, and stiffness combine to impact how rapidly breast-cancer cells travel in collagen gels and collagen-coated polyacrylamide gels.[358] This group found that cells moved more slowly if the ligand density surpassed a threshold, yet fiber alignment did not influence cell speed.[358] Interestingly, a report by Wang *et al.* determined that aligned haptotactic cues of fibronectin induced fibroblasts to migrate faster than on non-aligned patterns of fibronectin, regardless of ECM ligand density.[359]

We found that on surfaces both with and without collagen, most of the motile cells migrating on the ridges travelled at speeds below 0.5 μm/min (Fig. 5.2C). We note that this relatively low average velocity is, in all likelihood, influenced by the material composition of the

nanoridges. The velocity distributions broaden with increasing coating density, such that a larger proportion of the population has a speed between 0.5 and 1 μm/min. All of the surfaces were essentially equally unlikely to promote cell speeds beyond 1.25 μm/min.

5.2.4. Surface Density of Collagen IV Has Limited Influence on Esotaxis

Considering the essential role of actin in cell motion, we studied how actin dynamics varied on ridges with different surface coating densities of collagen IV. Nanoridges have been shown to lead to enhanced nucleation of actin polymerization[130,156,321] and to guide the waves of polymerization,[130,245,321] in a process called esotaxis.[131,142] To quantify esotaxis, fluorescence movies of MCF10A LifeAct-GFP cells were analyzed using OF (Fig. 5.3A-B). Images were generally collected at a *z* plane near the basal membrane of the cells, where the cytoskeleton has its strongest interaction with the nanotopography. In the representative image in Fig. 5.3A, actin streaks can be seen to have a spacing that is approximately equal to that of the ridges, and align with and propagate along the ridge axis. The flow vectors determined for the representative image in Fig. 5.3A are shown in Fig. 5.3B. The orientations of the flow vectors relative to the ridge axis were collected for cells on the different coatings in the different experimental timeframes (Fig. 5.3C-E). Cells on ridges with 100% collagen coating exhibited the best guidance of actin polymerization throughout the experiments, as well as the lowest occurrence of polymerization perpendicular to the ridges. However, a majority of the actin polymerization flux was parallel or nearly parallel to the nanoridges, and was least likely to be perpendicular to the ridge direction, in all experimental timeframes, regardless of coating. Even cells that were recently plated on substrates without collagen exhibited esotaxis. Additionally, the fraction of flow vectors aligned with the ridges for cells on the uncoated nanoridges and the nanoridges with

20% collagen were consistently similar throughout the experiment. In Fig. 5.3F we plot the fraction of actin flux that propagated along the ridge axis (the “mean prominence”) for the different coatings and experimental timeframes. In Fig. 5.3G we plot the amount of actin polymerization that significantly deviated from the ridges (the “mean width”) for the different coatings and timeframes. Both of these plots reinforce the point that there is not a strong difference in esotaxis on the various coatings.

Although the majority of OF vectors are aligned within 30° of the ridge axis on all coatings and in all experimental timeframes (Fig. 5.3C-E), there is a quantifiable difference in the distribution of OF orientations between cells on the nanoridges with 100% collagen coating and the nanoridges under other coating conditions. These histograms provide only a limited visualization of how the orientational dynamics of actin polymerization and organization might differ in cells on topography with the various coating densities. We therefore examined how the angle of actin flux throughout a representative cell varied with time on nanoridges with a given collagen coating density. From kymographs of the direction of actin flux with respect to the ridge axis and the actin fluorescence intensity as a function of time (Fig. 5.3Hi-iv), the influence that collagen coating has on actin guidance is evident. Based on a comparison of actin dynamics in a cell on uncoated nanoridges in the early timeframe (Fig. 5.3Hi) with a cell on nanoridges with 100% collagen coating in the same timeframe (Fig. 5.3Hiii), collagen IV appears to promote a consistent sense of, and response to, nanotopographic cues. The cell on uncoated ridges experienced intense, unidirectional actin flux (appearing as horizontal bands in the kymograph in Fig. 5.3Hi) along the ridges that was interrupted periodically by probing motion at other angles, followed by reversal of direction. The cell on the nanoridges with 100% collagen maintained intense actin dynamics in both directions along the ridge axis with few fluctuations in intensity

and limited probing of other orientations. During the late timeframe, less actin propagated perpendicularly to the ridge axis for each coating condition (Figure 5.3Hii,iv) than was observed in the early timeframe. In both timeframes, actin polymerization is more confined along the nanoridges with 100% collagen coating than on the uncoated nanoridges. These results suggest that esotaxis can occur in these cells even without a large supply of ECM ligands available for adhesion, but that the adhesive cues help to sustain esotaxis.

Images of the fluorescently labeled F-actin provide information regarding how the dynamic organization of the actin cytoskeleton near the basal surface (the plane of interest in our study) responds to the nanoridges (Fig. 5.4A-E). There is a slight decrease in the fluorescence intensity at the rear of each cell in this figure. It is evident from these images that the majority of actin polymerization occurs at or near the ridges, and takes the form of streaks that extend along the ridge axis. Comparing individual frames of actin movies enables visualization of changes in the cytoskeleton that occur during motion, including the formation of protrusions. Fig. 5.4E shows a cell sensing an approximately 1-μm gap between adjacent nanoridges. We also observed one cell that rapidly altered its morphology and took on less common shapes (Fig. 5.4D). These results suggest that esotaxis is tied to microthigmotaxis, the preferential migration of cells parallel to the nanoridges, as has been observed previously for MCF10A cells.[130,131,155,196,321,334]

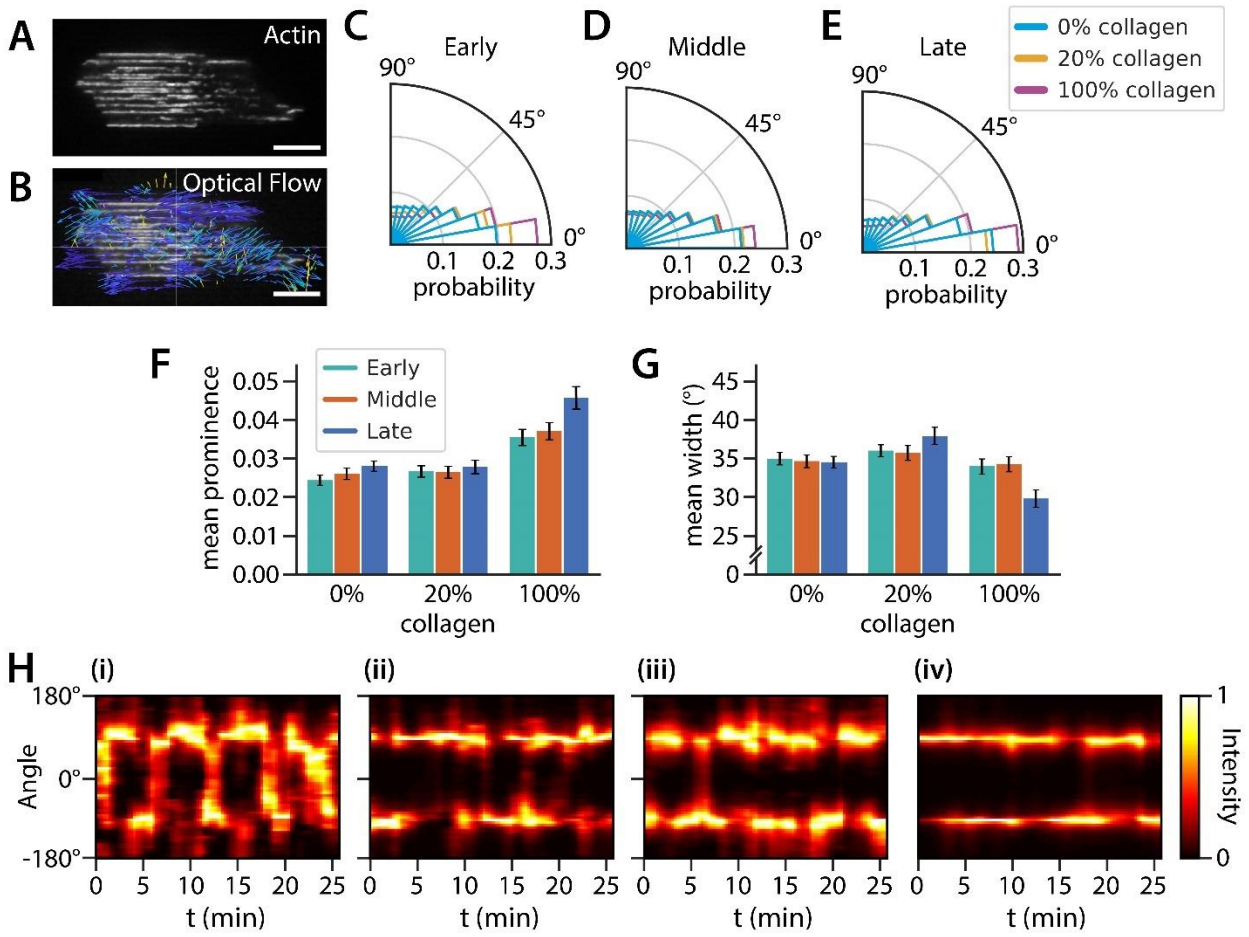

Figure 5.3. Nanotopography can guide actin polymerization even in the absence of added ECM coating, although collagen IV coating can limit actin-polymerization oscillations perpendicular to the ridge axis. A. Representative image of fluorescently labeled F-actin plated on nanoridges with 100% collagen coating and imaged in the late timeframe. B. Corresponding image of OF vectors depicting the actin flux between adjacent image frames. Scale bars: 10 μm. C-E. Polar histograms showing fractions of actin polymerization propagating at different orientations relative to the ridge axis (0°) in the early, middle, and late experimental timeframes, respectively. F. Histogram of the mean prominence of the polar histograms (i.e., the value along the polar axis), as a function of experimental timeframe and the coating condition. G. Histogram of the mean width of the polar histograms (i.e., the width normal to the polar axis), as a function of experimental timeframe and the coating condition. F and G share the same color coding. H. Kymographs showing the actin polymerization flux throughout representative cells as a function of the angle relative to the nanoridge axis and of time. i-ii. Heat maps of a cell on uncoated nanoridges in the early and late experimental timeframes, respectively. iii-iv. Heat maps of a cell on nanoridges with 100% collagen coating in the early and late experimental timeframes, respectively.

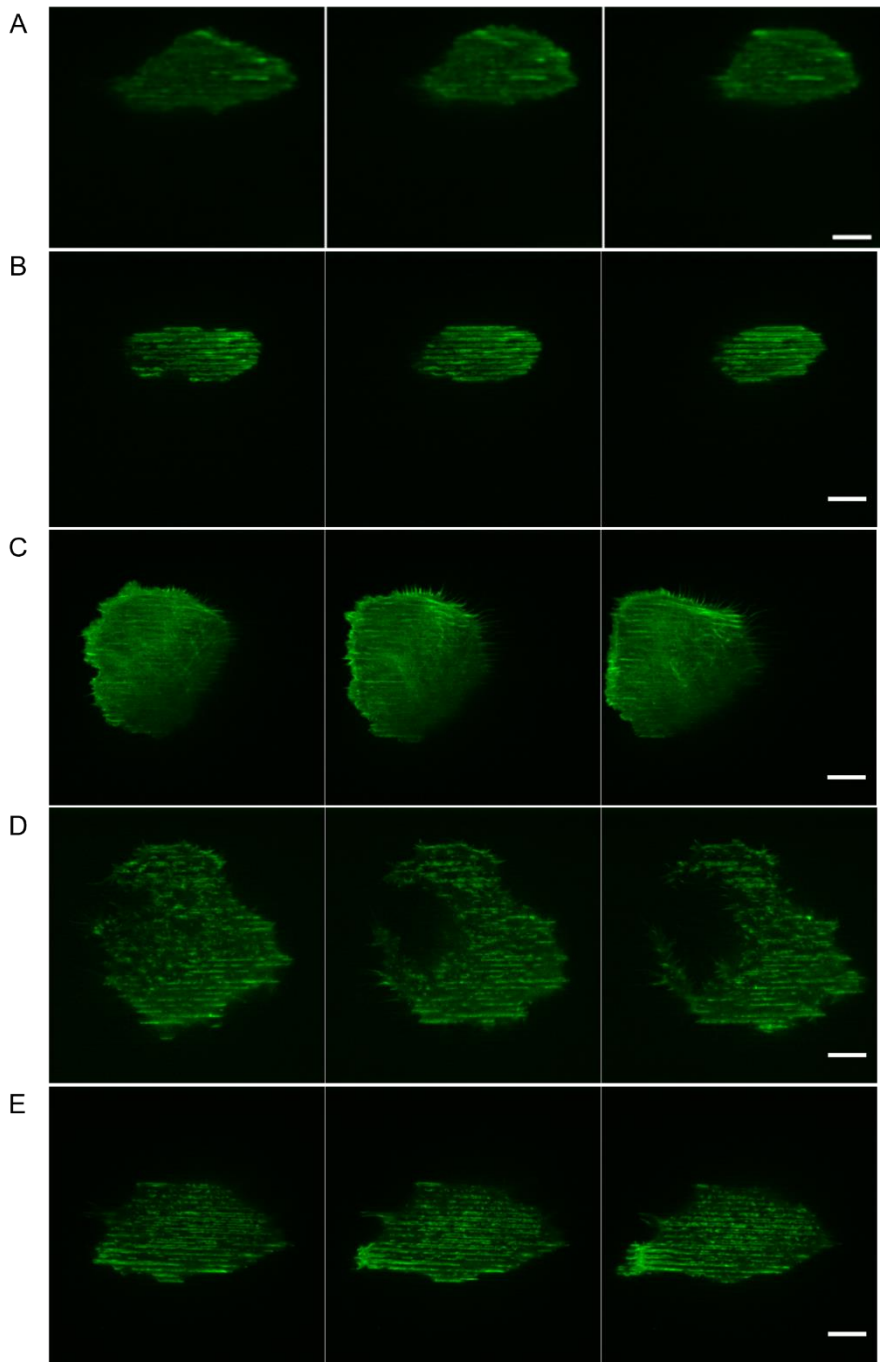

Figure 5.4. Actin distribution at the ventral surface of MCF10A cells migrating on nanoridges. Fluorescently labeled F-actin enables visualization of the dynamic cytoskeletal response to the nanoridges. The time between successive images is 15 min. A. Cell on uncoated nanoridges. B-D. Cells on nanoridges with 20% collagen coating. E. Cell on nanoridges with 100% collagen coating. Scale bars: 10 μm.

5.2.5. The Cell-Trajectory Phenotype Is Not Linked to the Actin-Flow Direction

The trajectories in Fig. 5.2B fall into three distinct categories: trajectories in which the cells move tens or even hundreds of microns in a straight path; trajectories in which the cells exhibit no directional bias; and trajectories in which the cells move straight for a period of time and then reverse to move the opposite direction. To quantify these trajectories, we use the autocorrelation function $R(t')$

$$R(t') = \frac{1}{T-t'} \sum_{t=0}^{t=T-t'} \frac{v(t) \cdot v(t+t')}{|v(t)|\,|v(t+t')|}, \tag{5.1}$$

where $v(t)$ is the instantaneous velocity of the cell at time t and T is the total time spanned by the trajectory spans. $R(t')$ ranges from -1 to 1, and quantifies how similar a trajectory is to itself when separated by a timestep of t'. A completely straight trajectory has $R(t') = 1$ for all values of t', as seen in Fig. 5.5A. A completely random trajectory has $R(t') \to 0$ as $t' \to \infty$, as seen in Fig. 5.5B. Finally, a reversing trajectory will exhibit a sign change in $R(t')$ from positive to negative at the time of the turn, as seen in Fig. 5.5C. We classified the trajectories into these three phenotypes based on $\bar{R}$, the average value of $R(t')$. Straight trajectories were defined as having $\bar{R} > 0.9$, random trajectories were defined as having $0.25 < \bar{R} < 0.9$, and reversing trajectories were defined as having $\bar{R} < 0.25$. These classifications were chosen based on the set of trajectories, and the ranges of $\bar{R}$ for each category could change if T were different. The value of $\bar{R}$ is greater for a random trajectory than for a reversing trajectory because even in the case of random motion there is a persistence time for directional changes, such that $R(t')$ remains close to unity for small enough values of t'. The same holds true for a reversing trajectory, but the fact that the dot product changes its sign but maintains its magnitude following a reversal tends to

lead to a smaller value of $\bar{R}$, as long as the reversal does not occur too early or too late in the trajectory. Most reversing trajectories had $\bar{R} < 0$.

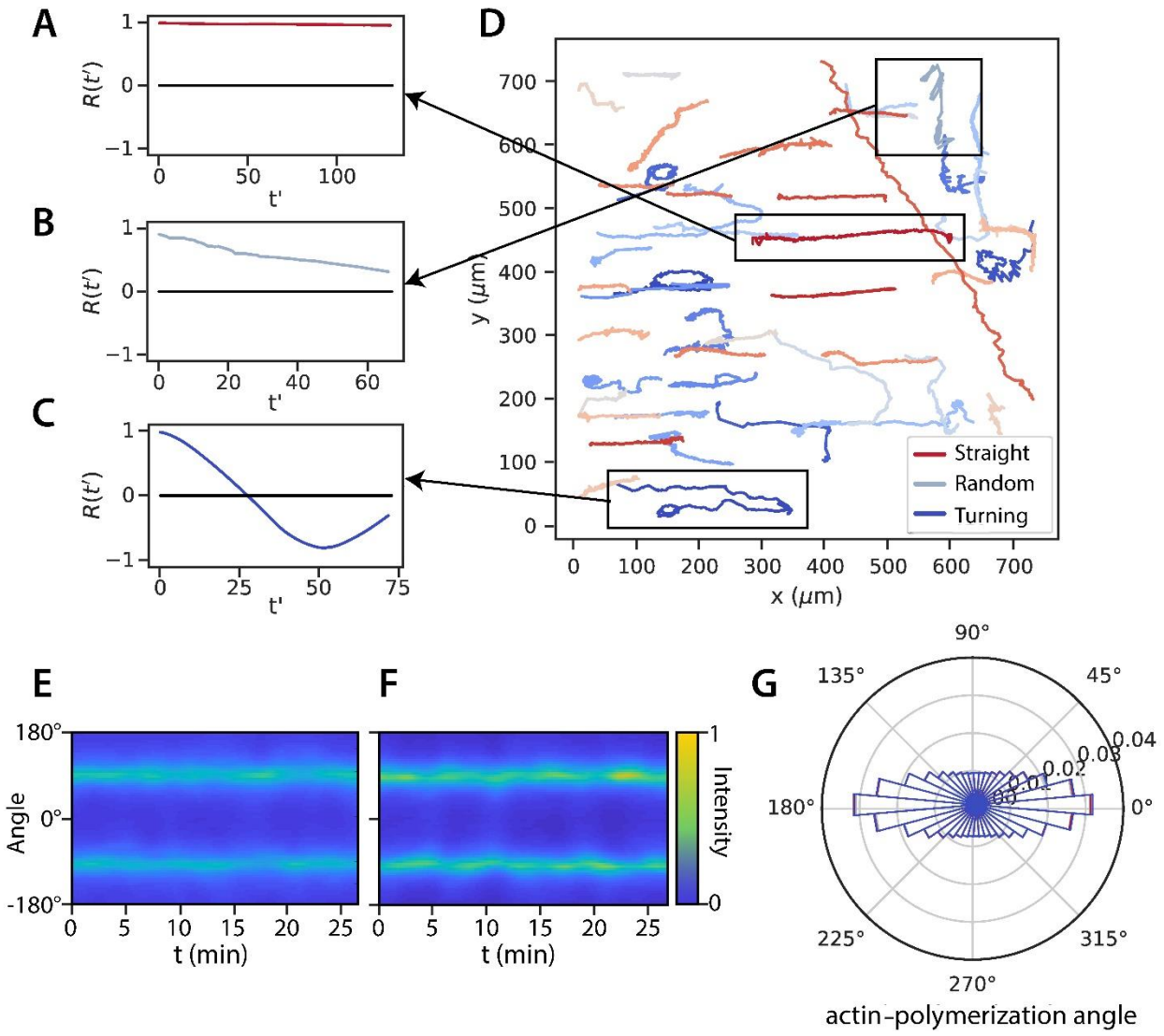

Figure 5.5. Cells with different trajectory phenotypes have similar actin OF distributions. The autocorrelation function $R(t')$ is distinctly different for each type of trajectory: A. straight; B. random; and C. turning. D. Representative cell trajectories. The trajectories are classified in the three categories based on the value of $\bar{R}$. The kymographs of actin optical flow for: E. a straight trajectory; and F. a random trajectory very similar. G. The overall OF distribution for all trajectories classified by trajectory type. The color coding of migratory phenotypes in D is the same in A-C and G. There are no significant differences among the distributions.

Once the trajectories were classified by phenotype, we compared the actin OF for those phenotypes. In representative individual cases, we found that the actin-flow kymographs look similar for straight (Fig. 5.5E) and random (Fig. 5.5F) trajectories. Both of these kymographs have peaks at 0° and 180°, i.e. along the nanoridges. In fact, Fig. 5.5G shows that the angular distribution of actin-flow vectors is essentially indistinguishable among the different trajectory phenotypes.

5.3. Discussion

This study examined the effect of collagen IV, an ECM ligand, on the cellular response to nanoridges. We studied the spreading and migration of MCF10A cells, as well as the guidance of these processes, as quantified by shape and motion orientation relative to the nanoridges. We investigated how esotaxis was affected during spreading and migration, as well as by the density of collagen IV.

We previously found that when *D. discoideum* cells are plated on nanoridges, cells that are more elongated on the nanoridges are most likely to be oriented along the ridge axis.[130] Here, elongation and orientation were not strongly linked for MCF10A cells soon after plating. Although the distributions for the early timeframe show that cells on the uncoated nanoridges are more round and exhibit a greater likelihood of orienting towards the perpendicular direction with respect to the ridge axis (greater than 45°) (Fig. 5.1B,E,F), cells on the collagen-coated nanoridges frequently deviated from the ridge axis at large angles (but usually less than 45°). As time progressed, the correlation between eccentricity and orientation became weaker. After 24 h, and continuing through the end of our observations, the proportion of elongated cells remained

lower on uncoated nanoridges than on nanoridges coated with collagen, even though the proportion of cells aligned with the nanoridges was similar for all coating conditions (Fig. 5.1). These results suggest that cell elongation and orientation on nanoridges can be decoupled to a certain extent. The extent to which adhesion and nanotopography are responsible for the ability of MCF10A cells to be guided with limited cell spreading remains an open question. The protein surface density is expected to be lower on uncoated nanoridges than on collagen-coated nanoridges throughout the course of our observations, despite the ability of human epithelial cells to produce ECM proteins. Although the lower density of adhesive cues on the uncoated nanoridges resulted in a larger population of MCF10A cells with lower eccentricity than on collagen-coated nanoridges, the uncoated nanoridges did not lead to a greater population of misaligned cells. The slight deficiency in orientation of recently plated cells on uncoated nanoridges supports the idea that adhesion facilitates a small degree of enhancement of contact guidance. However, spreading and migrating cells on uncoated nanoridges exhibited alignment with the nanoridges that was similar to the alignment on nanoridges with 20% or 100% collagen, especially ~10-15 h after plating. The extent of alignment shortly after plating, both of the cells themselves and of the polymerizing actin, suggests that strong, stable adhesive interactions are not the main determinant of guidance. These results could be indicative of characteristics of the sensing capabilities of the cytoskeletal machinery that can sustain oriented spreading and directed migration despite momentary or transient actin flow at an aberrant angle relative to ECM cues. The similarity in cell orientation distributions with respect to the topographic cue for cells recently plated on uncoated and collagen-coated nanoridges indicates that the initial guidance is not influenced by the presence of ECM ligands. In the case of the *D. discoideum* cells, which lack integrins, and are often studied on untreated surfaces, even cells with low

eccentricity are apt to orient along the nanoridge axis, although the difference in preference for elongated cells was evident.[130] Taken together, these studies support the idea that nanotopography is capable of driving a directional bias in cells that employ distinct molecules and mechanisms for interactions with the underlying substrate.

The cell tracks we measured illustrate the strong guidance of cell migration by nanoridges, often over distances of greater than 100 μm. The majority of cells in this study traveled at speeds below 0.5 μm/min (Fig. 5.2C). The cell speeds depend on the properties of the substrate, so changes to the topographical cue, the substrate material, or the protein coating density (as shown in the figure) will change the velocity distribution of the cells. Cells that traveled at higher velocities in this study frequently exhibited a round cell shape. These cells were observed on nanoridges with different collagen coating densities (Fig. 5.6A; cell circled in yellow). The low prevalence of cells moving at these speeds could be the result of the limited ability of MCF10A cells to employ amoeboid migratory characteristics, such as reduced adhesion complexes and contractility under the experimental conditions.

A variety of morphologies were exhibited by migrating MCF10A cells, including a fan-like shape. We observed cells that spread wider in the dimension perpendicular to the ridge axis, yet migrated along the ridges (Fig. 5.6B). Other cells frequently altered their shape, some simultaneously exhibiting both concave and convex regions (Fig. 5.6; see also Fig. 5.4D with fluorescently labeled actin shown). Several of these morphologies are suggestive of increased contractility, demonstrating that a single pair of nanotopographic and chemical cues can elicit multiple morphological and migratory responses. These cells were often observed turning while migrating on the ridges, with a lower directional persistence than cells of other shapes. However,

we did not collect enough data on migrating cells of specific morphologies to determine whether cell shape is correlated strongly to specific migratory guidance, speed, or persistence, or that any specific coating density drove cells to adapt specific morphologies for migration. It is likely that different cell shapes are indicative of different interactions with the ECM or external physical cues, and it has also been shown that an individual cell can alter its morphological and migratory characteristics within a short period of time.[360,361]

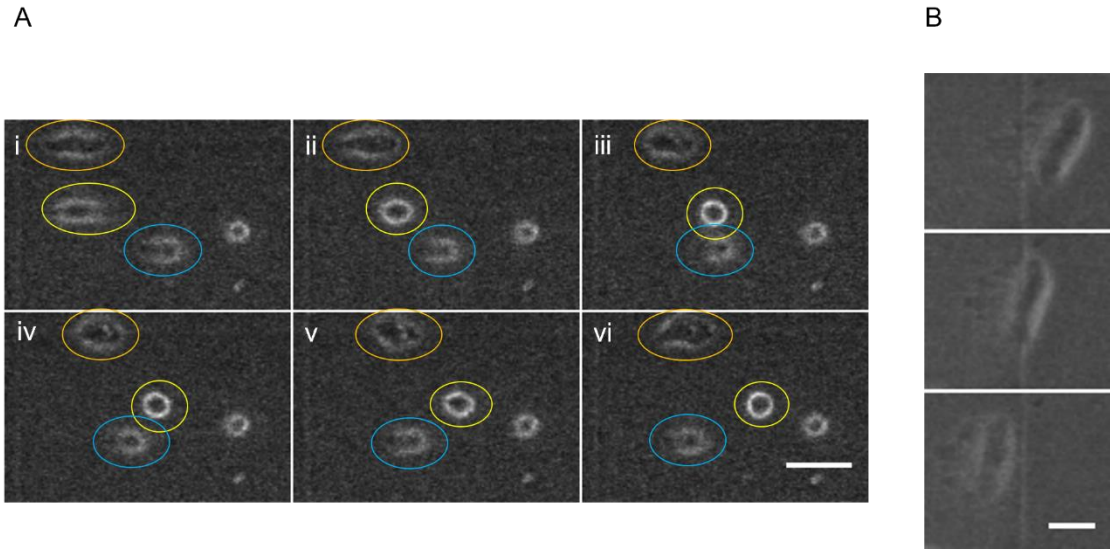

Figure 5.6. Various morphologies during epithelial cell migration on nanoridges. A. Montage of movie frames, taken 18 min apart, showing three cells (circled in orange, yellow, and blue) migrating on uncoated ridges. The cells circled in orange and yellow move to the right and the cell circled in blue moves to the left. The ridges are oriented horizontally in the image. Scale bar: 50 μm. B. Montage of movie frames, taken 18 min apart, showing a cell migrating on nanoridges with 100% collagen coating. The cell moves from right to left. The ridges are oriented horizontally in the image. Protrusions are visible at the leading edge of the cell. Scale bar: 25 μm.

The limited availability of strong adhesive cues on the nanotopographical substrates had some effect on the morphological and migratory responses of cells, but a less substantial impact on guidance, suggesting that cellular components other than just adhesion molecules contribute to the sensing of topography. Similar to the morphology data, although fewer cells are migratory on the uncoated nanoridges (Fig. 5.2A), the cells that do migrate are strongly biased to move along the nanoridge direction during acclimation to the nanotopography (Fig. 5.2D-F). A prior study of tumor-associated fibroblasts (TAFs) on nanoridges showed that oriented cell spreading was due to the alignment of stress fibers formed along the ridge axis, which, in turn, was influenced by the formation of focal adhesions guided by the nanoridges.[155] However, that same study found that topography guided the actin cytoskeleton directly by influencing the direction of motion of an actin crosslinker.[155] Rose plots of our OF data reveal that the predominant motion of actin polymerization is along the ridges, regardless of the coating condition. The OF data further show that after less than 12 h, in cells plated on uncoated nanoridges the actin motion was largely guided by the nanotopographic cues (Fig. 5.3C), even though many of the cells had yet to spread on the surface. The actin is not as well organized in cells recently plated on uncoated nanoridges as in cells recently plated on collagen-coated ridges, which often featured streak-like filaments on both sides of a single nanoridge (Fig. 5.3A); however, the F-actin polymerization in cells on the uncoated ridges was still biased along the nanoridges. Comparison of the OF kymographs of representative cells on uncoated nanoridges and nanoridges with 100% collagen coating soon after plating (Fig. 5.3Hi and 5.3Hiii, respectively) illustrates that actin in the cell on uncoated nanoridges swept out in other directions in an almost periodic manner, but still largely moved along the nanoridge axis. In cells recently plated on uncoated nanoridges, actin motion is restricted to one direction on the ridges for several minutes, followed by a 180° switch and a

sweep of other angles, before returning to the original direction (Fig. 5.3Hi). This process repeats throughout the 30-min movie. Actin in cells on nanoridges coated with 100% collagen showed considerably less propensity to explore polymerization in other directions. Actin flux traveled along nanoridges with 100% collagen coating in both directions throughout the period of observation (Fig. 5.3Hii,iv). These results support the idea that cells can sense nanotopographic cues even in the absence of strong adhesion and organized adhesion complexes. The greater confinement of actin dynamics along the nanoridges that occurs well after plating on our substrates could be the result of expression of additional ECM proteins by the MCF10A cells[362] or progressive adsorption of serum proteins on the substrate. The reorganization of preexisting or expressed proteins could also enable enhanced sensing of the nanotopography on the collagen-coated substrates. The same is true of actin on uncoated nanoridges well after plating (Fig. 5.3Hiii). From these results, we find that although nanoridges generally guided actin flux, a lack of strong adhesion to the substrate causes fluctuations and probing behavior of the actin away from the topographic cues. Stronger adhesion seems to restrict cytoskeletal probing, limiting fluctuations of actin flux away from nanoridges.

Earlier work that focused on how substrate stiffness and ECM-ligand density affect focal adhesion properties surmised that cytoskeletal organization contributed to traction force and focal-adhesion size.[363] The maturation of nascent focal adhesions can be advanced (or canceled) through the molecular clutch to the cytoskeleton to allow mechanical sensing of the external environment and the activation of signaling pathways.[44] Our results indicate that nanotopography is sufficient to drive the preferential orientation of actin. However, the fluctuations of actin flux at angles nearly perpendicular to the ridges on uncoated substrates illustrate that low adhesion requires cytoskeletal sensing at all angles as the cell seeks to spread without the adhesions

necessary to stabilize the morphological changes. Despite probing that occurs away from the ridges, most actin dynamics on uncoated surfaces heed the topographical cues and move along the ridge axis.

Both cell motion and the actin dynamics (of motile and nonmotile cells) were separately shown to be bidirectionally guided along the nanoridges (Fig. 5.2D-F and 5.3C-E, respectively). Cell migratory characteristics were not explained by underlying differences in actin organization or dynamics. Kymographs and rose plots of the dynamics of fluorescently labeled actin collected from migrating cells with distinct behaviors (persistent, guided motion, motion in one direction followed by a reversal of direction, and random motion) did not reveal distinct actin orientational motion. It should be noted that the framework of the experiment meant that actin videos were collected hours after the migration videos were recorded. Actin dynamics at the ventral cell surface does not appear to determine the classification of migratory behavior.

The relationship among adhesion, the cytoskeleton, and cell shape has been investigated under a variety of substrate conditions.[220,364-366] Chen *et al.* determined that cytoskeletal tension spawned from morphological changes regulates focal-adhesion formation, and that the integrin ligand density on the substrate does not control the extent of cell spreading.[220] Chaudhuri and coworkers found that the density of binding sites affects cell spreading on substrates with appropriate viscoelastic properties, and that actin polymerization and actomyosin contractility (as well as specific integrins)[367] modulate this substrate-dependent response.[364] A study of fibroblasts on fibronectin-coated micropillars revealed that actin localized around the individual pillars before, and did not noticeably change after, the gradual formation of adhesions in the intervening flat region.[365] Our findings regarding the localization of F-actin along the nanoridges

and the flow of actin polymerization along the nanoridges indicate that the cytoskeleton can organize in response to the nanoridges without strong integrin engagement with the ECM. Adhesion formation, regardless of ligand density, enables the morphological changes presaged by the cytoskeletal orientation.

Because our results support the integrin-independence of nanotopography sensing by actin, we must consider other possible facilitators of this cytoskeletal capability. The plasma membrane senses and responds to nanotopography. Deformation of the membrane results from contact with nanotopographic cues, and the membrane experiences increased tension.[368] The deformation of the plasma membrane usually includes changes in curvature of the lipid bilayer at the sites of cell contact with the topographic cues. Membrane curvature depends on the organization and packing of lipids that differ in size, shape, and polarity.[251] The curvature of the membrane can attract curvature-sensitive proteins, but bound proteins can further disrupt membrane curvature.[369] Changes in membrane curvature as a result of topography-induced deformations could lead to corresponding changes in charge distributions on the membrane due to the repositioning of negatively charged lipids or positively or negatively charged domains of proteins inserted into the lipid bilayer. In fact, a recent study found that tuning the attractive or repulsive interactions between membrane proteins facilitated curvature switching (between concave and convex).[370] Actin polymerization can localize to regions of high membrane curvature, aided by the curvature sensitivity of some actin-binding proteins.[257,371] Distinct actin organization along nanoscale sawteeth among cancer cell lines was suggested to result because of differences in membrane deformability.[196] Curvature sensing by actin is independent of the presence of negatively charged PIP2 at the membrane.[371] Although it is likely that membrane curvature serves a key role in sensing topography, the importance of actin sensing should not be

understated. In fact, the actin cytoskeleton mitigates the tensile stress exerted on the membrane.[368] Actin dynamics is the primary sensor of texture and does not rely on integrins to sense the physical environment of the cell.

5.4. Methods

5.4.1. MAP

The nanoridges were created using MAP, as described elsewhere.[107] A drop of a resin mixture containing acrylate monomers ethoxylated(6)trimethylolpropane triacrylate (CAS: 28961-43-5, Sartomer) and tris(2-hydroxyethyl)isocyanurate triacrylate (CAS: 40220-08-4, Sartomer) (1/1 w/w), and a small amount of the photoinitiator Irgacure TPO-L (CAS: 84434-11-7, BASF) (3% w/w total solution) was placed on the surface of a microscope slide that had previously been treated with an oxygen plasma and functionalized with acrylate groups. An ultrafast, near-infrared laser (Coherent Mira 900-F Ti:sapphire; 200 fs pulses; 76 MHz repetition rate; wavelength set to 800 nm) was focused through a microscope objective with high numerical aperture (Zeiss α Plan-Fluar 100×, NA: 1.45), enabling multiphoton absorption in the focal region. Patterning was achieved using a LabVIEW (National Instruments) program that controlled the stage position. Once patterning was complete, the material was developed in ethanol twice (3 min. each). The patterned substrate was then baked at 110 °C overnight to harden.

5.4.2. Functionalization and Molding of the MAP-Fabricated Pattern

The ridges fabricated with MAP were functionalized with ethylenediamine (CAS: 107-15-3, Sigma-Aldrich) and, subsequently, perfluorooctadecanoic acid (CAS: 16517-11-6, Alfa

Aesar), as detailed more extensively in Chapter two. The substrate was rinsed in ethanol after each functionalization step, and then was baked at 110 °C for over 1 h. As has been described previously,[142] a hard polydimethyl siloxane (*h*-PDMS) mixture was prepared from a mixture of vinylmethylsiloxane (CAS: 67762-94-1, Gelest) and methylhydrosiloxane (CAS: 68037-59-2, Gelest), each copolymerized with dimethylsiloxane. A platinum catalyst (CAS: 68478-92-2, Gelest) and modulator (CAS: 2554-06-5, Sigma-Aldrich) were also added. Hexane was added to decrease viscosity and improve the resolution of the molding process. This mixture was spin-coated onto the patterned substrate and allowed to sit at room temperature for 2 h prior to baking at 60 °C for 1 h. A mixture (10:1) of the elastomer base and curing agent of Sylgard 184 (Dow Corning) was then poured atop the *h*-PDMS film, and the pre-mold mixture was baked at 60 °C for 70 min. The relief mold was then peeled from the acrylate pattern.

5.4.3. Replication via Nanoimprint Lithography

Replicas were produced by placing a drop of the same acrylate resin on the relief pattern in the PDMS mold and pressing down on the drop with a coverslip functionalized with acrylate groups. After the sandwiched drop was secured, the resin was exposed to ultraviolet light (Blak-Ray, B-100AP, 100 W, 365 nm). The total exposure time was 5 min and the replica pattern was peeled away from the mold. The acrylic replicas were soaked in ethanol for at least 12 h, and subsequently dried in an oven at 110 °C for 1 h. The nanotopographic surfaces were then soaked in 1 mL of distilled water (Invitrogen, Catalog: 10977015) for at least 12 h.

5.4.4. Coating Nanoridge Substrates with Collagen IV

Nanoridged substrates that were to be left uncoated received no further treatment. For all other samples, mouse collagen IV (Engelbreth-Holm-Swarm lathrytic mouse tumor; 0.05 M HCl; Corning; Prod.: 354233) was used to coat the surfaces. The density/concentration of the collagen stock solution, the area to be coated, and the coating density were the factors used to determine the volume of the original collagen solution that should be used. The calculated volume of collagen stock was diluted in 0.05 M HCl to a volume that covered the entire area of the cover slip that would be in contact with cells during the experiments. A coating density of 3.25 μg/cm^2 was determined by identifying when cell morphology and behavior on flat acrylic films coated with collagen resembled those properties on collagen-coated glass. A lower coating density of 0.65 μg/cm^2 was selected to test how cell shape and migration change on the nanoridges. The diluted collagen IV solution was allowed to sit on the substrates, which were placed on ice, for approximately 1 h. The solution was then aspirated. The substrates were then rinsed with distilled water and aspirated twice. The substrates subsequently sat on ice or were stored at 4 °C prior to experiments.

5.4.5. Cell Culture

The MCF10A LifeAct-GFP cells were cultured in a cell medium composed of DMEM/F12 (Gibco, Catalog: 11330057), 5% horse serum (v/v) (Gibco, Catalog: 26050088), 10 μg/mL insulin (Gibco, Catalog: 12585014), 20 ng/mL epidermal growth factor (EGF; PeproTech, Catalog: AF-100-15), 0.5 μg/mL hydrocortisone (Sigma-Aldrich, Product: H4001), and 0.1 μg/mL cholera toxin (Sigma, C8052). Puromycin dihydrochloride (A. G. Scientific;

Product: P-1033-SOL) was subsequently added to the medium (0.5 μg/mL). The cells were stored in a humidified incubator set at 37 °C and sustained with 5% CO_2.

5.4.6. Imaging

Prior to plating the cells on the substrates, the cell medium was aspirated and the cells were rinsed with Dulbecco's phosphate buffered saline (Quality Biological, Product: 114-057-101). The cells were trypsinized (Gibco, Catalog: 25200056) and centrifuged in the cell medium. The cell density was adjusted to 10^4 cells/mL, and 2 mL of cell solution added to the dish or plate to which the substrate was attached.

Cells were imaged within 1.5 h of plating using a PerkinElmer UltraView VoX confocal spinning disk system attached to a Nikon Ti inverted microscope. Culture conditions were maintained in a Tokai Hit stage-top incubator (37 °C, 5% CO_2, humidity). The cells were imaged for at least 3 h with a 10× phase-contrast objective (Nikon CFI Plan Fluor, NA 0.3) to monitor migration. Images were collected with a rate of 1 frame every 3 min. Next, individual cells were selected for imaging at 100× (1.49 NA, oil-immersion objective) in bright-field and fluorescence modes (488-nm laser power: 9%) at a rate of 1 frame every 10 s. After imaging individual cells, migration data were again collected at 10× in phase-contrast for at least 12 h. Then, actin dynamics (fluorescence) data from individual cells were again recorded. The imaging switched between migration and actin-dynamics data collection one more time.

5.4.7. Analysis

Cell tracking and shape detection were performed on the bright-field movies of MCF10A cells on collagen-coated nanoridges, in a manner employed previously.[320] To remove the ridges

from the image, we thresholded the image in Fourier space and applied a low-pass box filter. An inverse Fourier transform was then applied to render an image without any ridges. Next, the image was binarized using the Otsu thresholding method.[372] Using these binarized images, the cell shapes and centroids were captured using *regionprops* from the Python library scikit-image. To obtain cell tracks, the centroid data were processed using a tracking algorithm from the Python library, *trackpy*.

An OF algorithm, which was described in detail previously,[245,319] was used to quantify the flux of actin polymerization within cells. This adapted algorithm is based on the Lucas-Kanade method.[233] The algorithm identifies the spatial fluorescence intensity gradient within a given image frame as well as the intensity gradient between consecutive image frames, the difference image. Combining these two gradients determines the optical flow. Optical flow reveals the velocities of regions of intensity in images, allowing us to account for both changes in intensity of actin and changes in location.

5.5. Acknowledgements

We thank Drs. Stuart S. Martin and Michele Vitolo of the University of Maryland School of Medicine for the generous gift of MCF10A LifeAct-GFP cells.

Chapter 6: Conclusion: A Perspective on Esotaxis

6.1. Introduction

The responsibilities of cells often include specifications, like time and location, required for proper execution of the functions. The inability to satisfy the specifications can lead to negative outcomes for the cell or for an entire organism. Many cell functions entail cell motion or migration. The importance of directed motion applies to all types of cells regardless of the distance they generally travel. Epithelial cells remain stationed in their tissue, yet if they cannot follow the cues to close a wound properly, pathogens can enter and infection can spread. However, there are cues, usually provided by other cells, to guide cells and to facilitate the performance of their roles. There are four important aspects of the cellular processing of a cue: generation of a signal; sensing the signal; transmitting the signal (the connection between detection of the signal and taking some action in response); and executing the signal (taking action in response to the interpreted message of the signal).[13] Directed cell migration is the guided motion of cells in response to a cue or cues. Many processes affecting the survival of an organism, such as development, immune response, and wound healing, depend on the efficient, successful migration of cells. However, directed cell migration can also be exploited to drive negative health outcomes.

A variety of cues can guide migrating cells to a target location. Motion driven by soluble molecules (chemical signaling, chemotaxis), electric fields (electrotaxis or galvanotaxis), surface chemistry (haptotaxis), and surface stiffness (durotaxis) are usually dependent on a gradient. The

cue must be strong enough for the cell to continue to sense a change in the intensity of the cue. Beyond a certain sensitivity limit, the cell cannot distinguish the strength of the stimulus from the front to the rear of the cell. Even topography, the primary focus of this work, can be sensed as a gradient, in which a cell can move toward or away from a denser arrangement of topographic cues,[25] such as ECM fibers. Substrate parameters, including surface chemistry, stiffness, and topography, that are amenable to microscale patterning have the potential to be used to guide cell motion across long distances.[131]

Although the focus of this chapter is the nanotopographic guidance of cell motion and its underlying mechanisms, topography impacts other important cell functions, and cellular interactions with nanotopography can influence health outcomes. Nanotopography has been shown to affect cell differentiation,[305] proliferation,[373] and gene expression.[373] Negative health outcomes can result from interactions with nanotopographic cues. The construction and arrangement of aligned ECM fibers by fibroblasts promotes the invasion of neighboring tissue.[374] Tumor-associated fibroblasts (TAFs) will be discussed in greater detail later in this chapter.

The rearrangement of the ECM is an example of the negative impact of topography based on aberrant cellular behavior and the manipulation of native biomaterials. Foreign materials can also serve as nanotopographic cues that promote disease. Elongate mineral particles (EMPs) are generally defined as having an aspect ratio greater than 3.[375] Asbestos are also categorized as EMPs.[375] Asbestos are a family of naturally occurring silicate mineral fibers used in building materials that cause diseases of the lungs and potentially other tissues that range in severity but include mesothelioma.[375] These diseases often affect workers in manufacturing plants and construction-related jobs.[375] Even if particles do not share certain characteristics with asbestos

(they are then referred to as nonasbestiform), they can still be categorized as EMPs if they satisfy the aspect-ratio threshold. EMPs have also been associated with mesothelioma-related diseases.[375] Cancer research with a focus on EMPs determined that longer, thinner particles are likely to promote tumorigenesis and shorter, nonfibrous particles are less of a threat.[376] Studies suggest that particles longer than 5 μm and thinner than 0.1 μm are biopersistent (can remain intact within the body for extended time) and are the most dangerous.[375] Long fibers drive increased cell proliferation, synthesis of growth regulatory proteins, and protein expression of protooncogenes.[376] EMPs in drinking water are excreted in the urine, although their detection in fish kidneys suggests that excretion of the particles is not completely successful.[377] It has been proposed that interaction with EMPs initiates cellular pathways than involve the release of reactive oxygen species and programmed cell death.[376] Furthermore, the iron content in crocidolite and amosite—two types of asbestiform EMPs—drive iron-related processes in cells that lead to oxidative damage that alters deoxyribonucleic acid and lipid properties.[376] The fact that disease progression depends so strongly on the dimensions and shape of EMPs suggests that nanoscale and microscale topography influences cellular responses that promote aberrant health outcomes. Cell–EMP interactions will be described in more detail later in the chapter.

Cells encounter an array of topographic cues *in vivo* that vary in scale and shape. The network of ECM fibers can be sparsely distributed, yet aligned, or an impenetrable knot. The cell can respond to the topography of both of the aforementioned stimuli. In the case of the dense fiber matrix, if the cell is incapable of, or chooses not to, break down this ECM, the cell can still travel along the barrier. Although the cell can potentially turn away from this obstacle, the fibrous knot can serve as a directional cue along which the cell can migrate and away from which there might be an absence of cues. On the other hand, a cell on an array of aligned fibers

would not experience restricted motion in any direction. Several dimensional properties of the ECM fibers are much smaller than the cell (many cells are on the scale of tens on microns). However, despite the apparent freedom of motion, the cell will often migrate along the oriented topographical cue. Microthigmotaxis, is the guided migration of cells through nano- or micro-topographical cues on substrates. In this chapter, we investigate the sustained motion of cells along microscale and nanoscale topography.

6.2. Fabrication of Nanotopographic Substrates

There are a variety of methods to produce substrates with micro- and nano-scale topographical features, including electrospinning, nanoparticle synthesis and deposition, and even heat treatment of films composed of material mixtures. However, perhaps the most common techniques, especially for uniform patterning with precise control over topographical dimensions, are photolithography-based. These methods include standard photolithography (with a photomask), multiphoton lithography, and electron-beam (e-beam) lithography. The properties of the desired pattern (as well as the instruments available to construct it) often dictate the method by which the pattern is fabricated. Soft-lithography-based approaches are frequently used for replication or stamping to consistently and precisely reproduce the same pattern for experimental studies. These techniques can be used to mold and replicate complex, 2.5-dimensional patterns fabricated from an array of methods. The studies of cellular response to nanotopography described in detail here employed patterns fabricated using multiphoton absorption polymerization (MAP), a technique described in detail elsewhere.[107] This technique involves a photopolymerizable material, usually containing monomers and a photoinitiator, patterned by exposure to an ultrafast laser focused through a microscope objective. The

wavelength of the laser must meet the requirement that absorption of two (or more) photons with the equivalent energy will excite the photoinitiator to the electronic state that will lead to the formation of a radical (or cation) to polymerize the material. The simultaneous absorption of more than one photon by a molecule is an unlikely phenomenon, and the pulses of an ultrafast laser serve to concentrate the photons temporally. By the same token, the laser is focused through a microscope objective with a high numerical aperture to concentrate the photons spatially. This setup results in polymerization of the material within the focal region of the microscope objective, allowing for 3D control over patterning. Control of the microscope stage and of the laser exposure with a mechanical shutter, both operated with computer software, allow one to produce arbitrary patterns using MAP. The ability to vary the height of fabricated structures without the use of sacrificial layers or multiple rounds of material deposition and patterning is an attribute of this technique that most other methods cannot claim.

Replication of the MAP-fabricated patterns was accomplished by using a soft lithography/replica molding technique known as solvent-assisted nanotransfer molding.[142] A mixture of siloxanes was used to produce a hard polydimethylsiloxane (h-PDMS) elastomer that improves upon the stiffness/elasticity and hardness of Sylgard 184[141] (the name of a commercially available and widely used silicone elastomer produced by Dow Corning). The addition of hexane as a solvent to this h-PDMS mixture reduces the viscosity and surface tension, and enables replication with high resolution and fidelity.[119] The h-PDMS layer spin-coated onto the original MAP pattern was then combined with Sylgard 184 to produce a mold of the nanotopographical pattern.[142] To make replicas of the original pattern, a technique known as nanoimprint lithography was used, in which a drop of photopolymerizable resin was sandwiched between a glass coverslip and the PDMS mold and then exposed to UV light.[142] This method

enables the replication and production of nanotopographic surfaces on a relatively large scale. The resolution of these techniques can be higher than 25 nm.[142]

6.3. Nanotopography-Based Directed Cell Migration, Microthigmotaxis

Across a variety of species—from amoebae through mammals—and cell types, it has been demonstrated that cells can orient and migrate along nanotopographical cues. *Dictyostelium discoideum*, a social amoeba also referred to as a slime mold, preferentially spreads and moves in the direction parallel to a nanoridge pattern[130] that features periodic lines of material with uniform thickness separated by grooves or valleys that are also uniformly spaced. Shape changes and motion are strongly influenced by the topography; that is, the cells that elongate the most and move the fastest are those that were oriented with the ridges.[130] In accordance with these observations, protrusive motion at the cell front and retraction at the rear of the cell, which often seem synchronized in directed migration, were observed more prevalently in cells aligned with the nanoridges.[130] Although the leading-edge protrusions and rear retractions occur more frequently on cells oriented with the nanoridges, the shape changes of cells on topographic substrates are wave-like and oscillatory, similar to behavior observed on flat surfaces.[130] (The *D. discoideum* cells used in this study were genetically altered to prevent chemical signaling between cells, ensuring that the ridges were the only factor that could influence directed motion.)[130]

Moving from one end of the spectrum of species, describing the guided motion by nanotopography of an organism that spends a portion of its life cycle in a unicellular state, we have found that human cells can also undergo microthigmotaxis. Cells of a human breast epithelial cell line, MCF10A, as well as those of a metastatic mutant line derived from MCF10A

(known as MCF10CA1 or M4), exhibit a preference to move parallel to the orientation of nanoridges.[196] Osteosarcoma cells (U2OS cell line) elongate on, and are strongly aligned with, nanoridges, and ovarian tumor cells (HEY-T30 cell line) exhibit persistent migration on these nanotopographic substrates.[334] Interestingly, these results demonstrate that disease-promoting cells can be influenced by nanotopography to undergo directed cell motion. Like *D. discoideum* cells, the breast-cancer cell lines moved faster when migrating along the ridge direction.[196]

Directed cell migration is the result of protrusions and retractions of the cell front and rear, respectively, that constructively achieve a net cell displacement in response to one of the external cues described above. This series of 'constructive' protrusions and retractions requires the coordination of many biomolecules within the cell, including the cytoskeleton and signaling cascades. In fact, various properties of the cellular environment can influence the organization and/or motion of these biomolecules to drive cell migration in response to extracellular cues.

In this brief review, we will describe the concept of "esotaxis," how this phenomenon affects directed cell migration, and how esotaxis can result from cellular interactions with nanotopographic cues. The prefix "eso-" is derived from ancient Greek and means "from within." With respect to a cell, eso- refers to subcellular components. Although the ambiguity of "within" can be interpreted as describing organelles – for example, the position of the nucleus or microtubule-organizing center (MTOC) relative to the leading edge of the cell – for the purposes of this discussion, we will generally focus on the scale of the distribution of biomolecules within the cell. The suffix "-taxis" is generally accepted to refer to directed motion in fields of study relating to biology. This definition was used when the term esotaxis was first applied to the wave-like dynamics of actin.[131] However, "taxis" was originally used to describe organization or

arrangement (of soldiers; also ancient Greek), and this definition is equally fitting in understanding how external cues, like nanotopography, affect the cell and can contribute to directed migration.

6.4. Esotaxis Is Ubiquitous

To explain the directed migration and biased leading-edge protrusions and rear-edge retractions of *D. discoideum* cells oriented along nanoridges, our group examined the organization and dynamics of F-actin in cells on these substrates, because virtually all shape changes involve at least some cytoskeletal rearrangement, and actin polymerization and depolymerization drive migration in *Dicty* cells. We found that actin polymerization is constrained to within 500 nm of each side of a ridge.[130] Not only did actin nucleate at these nanotopographic cues, but its polymerization was biased along the ridge axis.[130] Perhaps most surprisingly, even if cell motion was perpendicular to the nanotopography, actin was still oriented along the ridge axis.[130] From these results, we see that external physical cues in the cell environment can direct the organization and orientation of actin inside the cell. The fact that cells can move in a direction perpendicular to the nanotopography despite alignment of the actin cytoskeleton emphasizes that esotaxis does not compel immediate, complete microthigmotaxis in response to the sensing of the ridges. Tracks illustrating the displacement of *D. discoideum* cells on nanoridges show that not every instantaneous motion of the cells is aligned with the nanotopography and that migration is not perfectly straight. Additionally, cells are not equally influenced by the ridges. Some cells move in a straighter, more aligned path than do others. The orientation of actin with the nanotopography biases the direction of cell motion to some extent, increasing the likelihood that a cell moving perpendicularly with respect to the ridges will turn to

be aligned with the cue and then will move along that axis. The cell tracks also indicate that actin polymerization is not the sole determinant of the direction of motion.

Epithelial cells feature distinct actin organization on nanoridges as compared to on flat surfaces. MCF10A cells often form stress fibers throughout the cell body when plated on flat surfaces, and branched actin at the cell front leads to the formation of a broad lamellipodium.[245] On nanoridges, actin streaks form near the ridges throughout the region of contact with the substrate, and these streaks align with the direction of the nanoridges.[245] Perhaps most surprisingly, the morphology of actin structures within the cell is locally influenced by the nanotopography. In an MCF10A cell that encounters a flat surface on one side and a ridged surface on the other, actin will organize in response to the underlying substrate in that region, so that half the cell will feature aligned actin streaks and the other will exhibit diffuse stress fibers that lack a consistent directional bias.[245] Just as lateral proximity to topographic cues influences the esotactic influence on actin aggregation, the axial distance from the stimulus also determines how much actin concentrates at a specific location, as was observed during imaging of different planes of an MCF10A cell in contact with an EMP.[378]

6.5. Quantification of Contact Guidance and Esotaxis

In characterizing and quantifying esotaxis to understand the impact of nanotopography on cytoskeletal dynamics, we must also examine the response at the cellular level. Accordingly, shape detection and cell-tracking software are often applied to cells in studies of esotaxis. These techniques allow cellular properties such as speed and eccentricity to be quantified reliably. Orientation is especially important, in that this property explicitly illustrates the extent to which the cell responds to nanotopographic cues. In some studies, the orientations of fluorescently-

labeled cytoskeletal components are quantified using weighted averages across all cytoskeletal structures.[155] Orientation is generally quantified with respect to the nanoridge direction, but several studies quantified the orientation in comparison to all other cytoskeletal structures within the cell.[155,321] The distribution of speeds of cell migration can provide insight into the migratory phenotype – often categorized as amoeboid and mesenchymal, although other terms have also been used – that the cells employ . Slow motion is often associated with adhesion-based migration, whereas faster movement usually involves weak or no adhesive interactions with the substrate. However, even within a given motility phenotype, velocity data can reveal how nanotopography affects cell motion. Shape analysis can also distinguish how nanoridges influence cells of different migratory phenotypes. Data can be compared among cells or, more frequently, across surfaces (patterned and unpatterned). For intracellular proteins, the position with respect to topographical features is often an important detail to determine. How far away from the nanoridges can F-actin be observed, for instance? Is actin more likely to polymerize at the tops of ridges or near the valleys? Fluorescence intensity can indicate regions in the cell where the labeled molecule is concentrated, and intensity values can be used to quantify or estimate the degree of an esotactic response to topography. The fluorescence intensity within a cell in contact with nanotopographic cues can be compared to the intensity elsewhere in the cell.[378] Image segmentation using binary masks derived from fluorescence and bright-field images can separate fluorescence data for cellular regions proximal to and distant from topographical cues.[378] This image analysis technique produces two separate fluorescence images. One image only includes regions near the nanotopography, and the other image omits these regions and illustrates all other regions of the cell.[378] This technique is especially useful for situations in which a large portion of a cell is not in contact with nanotopography, such as a cell

at the edge of a nanoridge pattern or one that encounters an elongate mineral particle. Quantification of fluorescence differences near and far from a cue facilitates comparisons across cell types and nanotopographies.[378]

Not all cells of a given type, on a specific topography, and in a single experiment will exhibit the same esotactic and microthigmotactic responses. An individual cell is even capable of changing its behavior while under observation. Cellular and subcellular data are almost always presented as histograms or distributions, and occasionally as averages. Normalization of the data to enable comparisons across experimental conditions can be achieved by using the maximum observed value or the value obtained from the control. Certain information can be obtained by normalizing each cell individually, such as protein activity or ion-flux changes through fluorescence intensity fluctuations, using the time- or whole-cell-average value.

Cell tracks illustrate the characteristics of cell motion, and enable facile visualization of displacement and persistence, and possibly of guidance and/or directional bias. The data connected to the tracks usually allows for quantification of migratory properties, including speed and mean-square displacement, as well uncommon or study-specific analytical values or indices. Tracking software is often used to examine motion of the entire cell as a unit. However, there are image-analysis techniques that can capture, identify, or quantify isolated motions within specific regions of the cell. Principal-component analysis was used to identify types of boundary motions and to determine and quantify the likelihood that specific types of boundary motion contribute to contact guidance observed in cells on nanoridges.[130]

Intracellular proteins and other biomolecules, and even ions, can move in an organized manner, and often exhibit wavelike behavior. Improved imaging technology and the

development of transient and transduced or transfected cellular and molecular labeling in recent decades has enabled the capture of these dynamics. One relatively simple method to illustrate dynamics is to create a time-lapse image that merges multiple frames of a video and color-codes the fluorescence by frame to show the motion over time. Another popular technique to visualize dynamics, whether on the cellular or subcellular scale, is through the creation of kymographs. From the collection of a video (or images that can be compiled to form a video) containing the dynamics of interest, a kymograph is created by selecting a region of interest. This area is generally much larger in one dimension than the other, effectively creating a region of interest demarcated by a rectangle in which the width is negligible. The dimensions of the rectangular regions used to create kymographs in Fig. 4.2 differed by nearly an order of magnitude. Instead of a rectangle, many kymograph programs and plugins require the user to draw a line to select the motion for analysis, which further emphasizes the 1D nature of this analysis tool. The frames of the movie that feature only this area of highlighted dynamics are then stacked sequentially either vertically or horizontally, so that one dimension of this stack is the long side of the rectangular region of interest and the other dimension is time. Another version of kymographs has been used with color-coding to illustrate how the change in fluorescence intensity depends on position. An important limitation of kymographs is that they generally only depict dynamics in one dimension.[245] If, for instance, fluorescently-labeled actin moved perpendicular to the ridges but the kymograph was created by selecting a region parallel to the ridge axis, this perpendicular motion would not be captured.[245]

Tracking algorithms have also been used to characterize the motion of individual bands or clusters of fluorescently labeled proteins. One study used the mean-square displacement of

fluorescent bands to fit to an equation in which the parameters characterized the diffusion properties of a labeled protein within the cell.[155]

Analytical tools can also be applied to identify and quantify the changes in cell shape that are captured in videos. Active-contour, or snake, algorithms can be used to detect cell-boundary positions following several steps that include object-scale and fluorescence-intensity adjustments and spatial-gradient and vector-field determination.[130] The active-contour algorithm uses multiple parameters to optimize the iterative cell-boundary detection process.[130] The cell boundary and fluorescence-intensity gradient can be applied together to determine a center-of-mass of the labeled protein within the cell. Center-of-mass calculations for fluorescently labeled molecules have been used for cell tracking and for the determination of a preferred orientation or localization.

Examining the influence of nanotopography on cell behavior as a function of time is an important focus of many studies, because the rate at which subcellular processes occur can influence the execution of important cellular functions, and changes in these rates can be significant. Oscillations of fluorescence intensity can be illustrated graphically for easy visualization of its wave-like properties. Mean-normalized autocovariance (MNA) is a pixelwise measurement that compares the fluorescence intensity within a region over time.[156] This method identifies locations at which concentrated actin persists for extended periods of time. Using MNA, one can determine whether nanotopographic cues drive prolonged actin polymerization and localization. In theory, this technique could also be used to quantify time-dependent cellular processes, such as cell division, in which the position of a labeled molecule is important.

Advances in the field of computer vision have been applied to identify and quantify these coordinated actin dynamics. Optical flow (OF) is one of the techniques that has been used to identify and quantify these changes. One approach to quantifying this motion in images was formulated by Lucas and Kanade in 1981, the aim of which was to improve image registration and minimize the difference between images by using the spatial intensity gradient to iteratively improve the estimation of the vector needed to achieve this minimization.[233] When optical flow is applied to fluorescence intensity, for example, the goal is first to determine the displacement of individual sources of fluorescence and the rate at which they move. The calculations to determine the flow of fluorescence intensity requires the assumption that all the pixels within a narrow window surrounding a specific set of coordinates will share the same flow vector.[245] The optical-flow vector field is determined using spatial and temporal gradients.[245] The spatial gradient displays changes in fluorescence intensity throughout the image or region of interest at a given time. The negative spatial gradient will map vectors directed away from regions of high local intensity.[245] The temporal gradient marks how the intensity changes with time. This concept is illustrated by the creation of a difference image, produced from a pair of image frames from a movie, with regions colored in to indicate positive and negative changes in brightness.[245] OF analysis provides information on the pixel-scale motion of fluorescence intensity over time.[245]

The OF data includes the orientation of actin flow with respect to the nanoridges and it is useful to map the distribution of the angle values. Circular distributions are usually used to map angular variables, and the von Mises model is perhaps the most popular for univariate circular distributions, but if the system requires it, multivariate generalizations have been attempted.[379] Because the actin motion is bidirectionally guided on the ridges, the angular data was fit to a

bimodal von Mises distribution with a constant offset of the two peaks spaced 180° apart.[245] Away from the peaks, the distribution is treated as a uniform distribution.[245] The distribution is positioned based on the value of the main component, which is equivalent to the mean angle of the OF data. The other peak of the distribution is situated 180° away from the main component.[245] A concentration parameter determines the width of the distribution, which is proportional to the inverse of the concentration parameter. Generally, we expect a large value for the concentration parameter when analyzing the data for cells on nanoridges because of the strong bidirectional guidance, so that the distribution more closely approximates a normal, rather than uniform, distribution.

OF vectors show the changes in position and intensity of the fluorescently labeled molecules, with the magnitude of the vectors indicating the magnitude of these changes and the colors representing the strength of orientation parallel or perpendicular to the ridges.[245] However, individual vectors do not provide information on the micron-scale activity of a group of molecules that would be relevant for interaction with multiple nanotopographic features.[245] The OF algorithm that was applied in these studies incorporated a Gaussian weight matrix that was applied to each pixel to emphasize neighboring pixels over more distant pixels when determining the OF-vector magnitude and direction at a given pixel location within the cell.[245] The weight matrix is adjustable based on experimental conditions, the scale of the motion of interest, and noise.[245] Increasing the size of the weight matrix can change the scale of the motion of interest from pixels to microns.[319] Additionally, by clustering similar OF vectors, micron-scale structures can be separated, and the micron-scale dynamics of a collection of molecules can be characterized and quantified by tracking the clusters.[245] Thresholds placed on the clustering and tracking can protect against analyzing non-collective motion of groups of the fluorescently

labeled molecules.[245] The clusters will still contain OF vectors with an array of orientations, which can reveal micro-scale structures.[245] Locating clusters that share maximum alignment allows the identification of coordinated molecular motion.[245] Tracked clusters of actin from OF analysis had speeds similar to those of actin waves measured in kymographs for two different cell lines.[245] OF analysis, clustering, and tracking enable the interpretation of pixel-scale motions in fluorescence images to identify and characterize the collective motion of molecules in two or even three dimensions.

6.6. Guidance of Cytoskeletal Dynamics and Wave-Like Motion

Cytoskeletal localization and orientation relative to nanoridges provide valuable insight into how these structures influence contact guidance and directed cell migration. However, cell signaling, actin polymerization and depolymerization, focal-adhesion maturation, myosin-orchestrated contraction, and other cellular processes are dynamic, and characterizing these temporal activities might offer a deeper understanding of the response of cells to this nanotopography. For example, a model that examined membrane–actin interactions with the substrate and response to curvature found that topography can alter the direction of, or fragment, actin waves.[380] The ability to probe subcellular dynamics is increasingly accessible, with improved spatial and temporal resolution in developed and developing microscopy techniques and the availability of labels for a library of intracellular molecules.

Actin polymerization in *D. discoideum* cells migrating on nanoridges was observed to exhibit wave-like behavior, with the F-actin appearing as streaks and propagating in the same direction in the grooves along both sides of the ridge.[130] These actin waves were coupled with cell motion.[318] The wave was observed to remain at the leading edge of a *D. discoideum* cell that

turned to change directions.[318] MCF10A cells demonstrate similar actin streaks along nanoridges, whereas on flat substrates these cells experience oscillations in actin polymerization in all directions at the cell boundary.[245] Kymographs of actin dynamics in these cells on nanoridges show stable polymerized actin that does not move perpendicularly to the ridge axis.[245] OF analysis showed dynamic actin at the leading edge of the cell that can potentially contribute to the formation of protrusions and that confirmed that the preferred direction of actin polymerization is along the ridges.[245] Although nanoridges guided the motion of actin waves, these nanostructures did not alter the speed of the actin waves from those observed in MCF10A cells on flat substrates.[245]

6.7. Response of Other Cellular Molecules to Nanotopography

Focal adhesions (FAs) also respond to nanotopographic cues. Signaling pathways that are activated during FA formation can influence intrinsic steps in cell motion and can, therefore, affect directed migration in response to nanotopography. For example, mouse fibroblasts that cannot produce FAK still elongate on nanoridges, but their aspect ratio is significantly smaller than that of wild-type fibroblasts.[334] Fluorescent labeling of various FA proteins showed that nanoridges drive the formation of mature FAs at the leading edge of U2OS cells, and FAs also localize near the nanoridges throughout the cell body.[334] Another study found that nanoridges cause focal adhesions to concentrate at the front and rear of elongated human mesenchymal stem cells (hMSCs), as compared to a more uniform distribution on flat substrates.[381] Fluorescence imaging in U2OS cells also revealed that the FAs orient parallel to the nanoridges.[334]

Myosin motors move along actin filaments and can pull together filaments of the actin network, effectively contracting the cytoskeleton and regions of the cell. Myosin contributes to

certain aspects of cell migration based on this contractile function. However, *D. discoideum* cells in which myosin II is knocked out (myosin II$^-$) are still guided in their motion on nanoridges, relative to cells in which myosin II is present.[130] On the other hand, blocking the contractile function of myosin II by inhibiting Rho-associated protein kinase (ROCK), an activator of myosin through phosphorylation of its light chain, stopped actin oscillations in B cells on nanoridges.[156] Furthermore, overall actin accumulation on nanoridges is reduced when myosin function is impaired in these cells.[156] These results suggest that myosin II modulates some aspects of the dynamic actin cytoskeletal response to nanotopography, but does not universally govern nanotopography-driven directed migration, which generally requires some degree of esotactic guidance of actin.

Phosphatidylinositol-3,4,5-trisphosphate (PIP3) is a phospholipid involved in cell signaling. PI3K produces PIP3 through phosphorylation of phosphatidylinositol-4,5-bisphosphate (PIP2). Spatiotemporal control of the concentration of PIP2 by PI3K and phospholipase C (which cleaves PIP2 to form diacylglycerol and inositol-1,4,5-trisphosphate) regulates numerous cellular functions.[382] Together with phosphoinositide 3-kinases and phosphoinositide-dependent kinases, PIP3 is involved in the activation of Akt (also known as PKB),[383] which regulates other signaling molecules necessary for a variety of cellular processes, including cell migration.

PIP3 also exhibits wave-like properties.[318] The wave behavior of PIP3 in *D. discoideum* is coordinated with actin waves, and also localizes at the leading edge of the cell and is coupled with cell motion.[318] Fluorescent labeling of the pleckstrin homology (PH) domain of Akt, which

can bind to PIP3 and, therefore, serve as a marker for the localization of PIP3, shows strong Akt fluorescence throughout U2OS cells on nanoridges.[334]

6.8. Immune cells

Many cells involved in immune response are highly migratory, as they must travel in search of pathogens or other immune cells to execute their functions.[8,384,385] Beyond its involvement in migration, the actin cytoskeleton is also essential for the antigen processing[8,386] and signaling-molecule production[8,387,388] and distribution[387,388] necessary for the identification of targets and recruitment of other immune cells for the activation of the immune response. The inability of the cytoskeleton to function properly in immune cells is associated with numerous diseases.[38] As immune cells must travel throughout the body, the extracellular environments that these cells encounter in distinct tissues and organs vary in composition. Additionally, many types of immune cells must make contact with other cells, and these interactions can potentially impact the immune response. We investigated how nanotopography modulates the behavior and function of immune cells.[155,156,245,319,321,378] Additionally, studying cytoskeletal response to topography in combination with other subcellular components can help to elucidate the mechanisms involved in immune response.

B cells describe several classes of B-lymphocytes that differ in how they are produced and where they develop and operate within the body.[389] The types of B cells also vary in the immunoglobulins or antibodies they produce, the properties of which determine the kinds of antigens that can be targeted and whether other cells must participate in antibody production.[389] B cells form from progenitors that are derived from hematopoietic stem cells (HSCs).[389] The different classes of B cells share the functions of detecting or recognizing antigens and producing

antibodies and other chemicals to signal the immune response. However, each lineage of B cells also has its own functions and responsibilities regarding specific antibodies or signals and regions of coverage.[389]

B-cell receptors (BCRs) on the membrane of B cells are transmembrane receptors that include the immunoglobulin and molecules and complexes of molecules that transduce the signal. The immunoglobulins are glycosylated proteins that contain two light and two heavy chains connected by multiple disulfide linkages.[389] The antigen-binding region of the immunoglobulin is often antigen-specific and, therefore, varies depending upon the antigen target.[389] The C-terminus regions of the heavy chains are positioned closer to the membrane, and distinguish the isotype of immunoglobulin (A, D, E, G, and M).[389] BCRs can be activated to influence the cell to perform its function. These proteins are responsible for antigen recognition and activation of the immune response.

The arrangement of the BCRs affects the immune response of a B cell. The nanotopographic features of other cells, foreign objects, or potential antigens (or even the physical properties of the surrounding environment) can influence how B cells respond to contact. Flat and nanoridged surfaces were coated with the fragment antigen-binding $F(ab')_2$ region of the anti-mouse immunoglobulin M+G (IgM+G) antibody, which can bind to BCRs, to test whether the nanotopographic organization of BCR cues influence the B cell response.[156] The actions taken by B cells during this process involved significant morphological and organizational changes, so dynamic actin, as was observed in these experiments, is likely necessary to achieve B-cell activation. Although B cells on flat substrates had the highest fluorescent actin intensity around the cell periphery, cells on nanoridges exhibited increased

actin near the nanoridges,[156] similar to the actin localization observed in MCF10A cells.[245] There was greater fluorescence intensity of the labeled F-actin within 1 μm of the ridges.[156] Additionally, the nanotopographic cues promoted strong radial oscillations of actin-fluorescence intensity throughout the cell.[156] On the other hand, B cells on flat surfaces had patches of actin fluorescence oscillations that lacked a biased, consistent direction of motion.[156] The magnitude of the intensity fluctuations during these dynamic actin oscillations was much larger in cells on the nanoridges than in cells on flat substrates.[156] Mean-subtraction and normalization of the intensity fluctuations showed that the peak-to-peak oscillations on flat substrates were less than half the magnitude of those observed in cells on nanoridges.[156] Additionally, the peak fluorescence intensity of labeled actin near the ridges, when weighted against the mean fluorescence throughout the cell, was higher than the similarly weighted fluorescence intensity observed around the periphery of cells on flat substrates.[156] Additionally, the dense actin accumulations near the nanoridges remained for longer durations compared to actin away from the nanotopography and in concentrated regions in B cells on flat surfaces.[156] Flat substrates coated with the IgM+G antibody did not induce the same organized, periodic actin fluorescence intensity oscillations that were promoted on the nanoridges.[156] A surface coating that stimulates BCRs increases actin dynamics, and nanotopographic cues on these activating surfaces further amplified the cycles of actin polymerization and depolymerization.[156] Inhibiting signaling molecules/proteins associated with BCRs did not influence the same response from the B cells.[156] These results indicate that B-cell activation (through BCR engagement and the ensuing signaling) increases the sensitivity of the actin cytoskeleton to nanotopographic cues in the extracellular environment. However, actin also controls the behavior of B-cell receptors[390-392] (and pre-BCRs in pre-B cells).[393] Cortical actin controls the clustering of BCRs by restricting

motion on the plasma membrane.[392] In turn, nanotopography can also modify the organization of BCRs. On streptavidin-coated substrates, B-cells labeled with Fab' fragments further tagged with Alexa Fluor 546 exhibited localization of BCRs near the ridges.[156] The fluorescence intensity on flat surfaces was uniform.[156] However, on nanoridged substrates, the fluorescence was most intense ~1 μm from the ridges, exhibiting enhanced clustering in proximity to the localization of actin polymerization.[156] This observation suggests that the responses of actin and BCRs to nanotopography are spatially coordinated.[156]

Signaling molecules and ions are critical to B-cell activation. It has been shown that disruptions in signal delivery in the various pathways can lead to scheduled apoptosis of B cells.[394] Calcium is a key factor in modulating activation, based on the magnitude and duration of its flux, and B-cell fate is likely distinguished by characteristic operation of calcium channels and signaling pathways.[395] Calcium concentrations available from specific channels are crucial for the proper function of other signaling molecules and transcription factors, and defects in these calcium supplies can impair B-cell activation upon BCR stimulation.[396] Additionally, calcium is known to regulate actin dynamics indirectly through the modulation of phosphatidylinositol-4,5-bisphosphate at the plasma membrane, which in turn recruits neural Wiskott-Aldrich syndrome protein (N-WASP).[397] N-WASP then promotes cortical actin polymerization.[397] B cells loaded with a fluorescent calcium sensor exhibited a nanotopographic dependence on Ca^{2+} oscillations when plated on antibody-coated substrates.[156] Cells on flat surfaces experienced periods between Ca^{2+} flux peaks that were approximately four times shorter than those of cells on nanoridges.[156] This observation indicates that physical cues can potentially disrupt, distort, or delay signaling in activated B cells. Inhibiting actin polymerization further slowed Ca^{2+} oscillations on all substrates.[156] Meanwhile, inhibition of Ca^{2+} GTPase, a protein

involved in regulating transport of calcium across the cell, decreased oscillations/dynamics and the overall concentration of F-actin.[156] These results reinforce the idea that the behavior and activity of the cytoskeleton, membrane receptors, and signaling molecules/ions are interdependent, and that nanotopographic cues in the cell environment can further modulate these cellular components and, thus, the overall response of immune cells.

Like B cells, T cells also form from progenitors that arise from HSCs.[398] Early progenitors derived from HSCs have the potential to form various types of immune cells, and multiple differentiation steps occur that eventually lead to a progenitor that is committed to the T-cell lineage, but not before one of these progenitors enters the thymus.[398] Once cells have committed to the T-cell lineage, they continue to differentiate until they join one of the main T-cell populations, at which point they exit the thymus and enter the peripheral lymphoid organs.[398] T cells are often distinguished by specific receptors expressed on the cell membrane. These receptors are known as clusters of differentiation (CDs), and each unique protein cluster has an identification number. The two main groups of T cells are often distinguished based on their expression of either CD4 ($CD4^+$ T helper cells) or CD8 ($CD8^+$ cytotoxic T cells).[399] Upon activation through the presentation of an antigen on the surface of an antigen-presenting cell (APC), helper T cells release cytokines to initiate the immune response.[399] Naïve T cells preferentially migrate to second lymphoid organs, which collect antigens that are presented to the T cells by APCs.[400] Before the cytokine release, this naïve helper T cell must divide multiple times to produce enough cells to fulfill its immunological role.[401] Information from the APC will help to determine differentiation steps of these helper T cells to optimize the immune response to the specific pathogen, with the instructions conveyed across generations of cells through gene regulation.[401] Subsets of T helper cells are distinguished by specific cytokines that induce a

lineage and that they also release to recruit other cells in the immune response.[401] These subsets also differ in the types of pathogens they target and the harmful effects they can incur upon their own organism.[401] Helper T cells can recruit other T cells, various types of innate immune cells, and even nonimmune cells to remove pathogens.[401] Cytotoxic T lymphocytes are also known as killer T cells. As the name suggests, this class of T cells is responsible for killing cells that are considered a threat, again based on detection of specific antigens.[399] The $CD8^+$ T cells are activated in a similar manner as that described for the helper T cells.[399] Cytotoxic T cells employ several mechanisms to kill target cells. The first method involves a surface ligand that can bind to a receptor (sometimes referred to as a death receptor) on the target cell, at which point the receptor and its adaptor proteins recruit molecules that lead to apoptosis.[402] Another technique used by the killer T cells is the production and release of multiple molecules that combine to also induce apoptosis.[402] The protein perforin forms pores in the target cell membrane and granzyme molecules, a family of serine proteinases, then enter the cell through these perforin channels to induce the granule-mediated cell death.[402] The mechanism is somewhat more complicated, as granzymes can enter target cells through receptor-mediated endocytosis and perforin can drive the release of granzymes stored in vesicles within the target cell.[402] Cytotoxic T cells can also release cytokines with cytotoxic activity.[402] A third type of T cell, the regulatory T cell, has drawn a great deal of research interest, despite its small population.[399] Regulatory T cells can suppress immune and autoimmune response by releasing cytokines or other molecules that can inhibit or modulate immune-cell activity or function or drive the cell to undergo apoptosis using mechanisms similar to those of cytotoxic T lymphocytes.[403]

During the process of activation, an antigen peptide is presented to T cells on membrane proteins known as major histocompatibility complex (MHC)-derived molecules on the surface of

another cell, and the antigen is sensed by the T-cell receptors (TCR).[399] To prevent indiscriminate killing of any cell expressing the antigen, the cytotoxic T cells require molecular signaling by helper T cells to activate.[399] Helper T-cell activation through TCR stimulation requires antigen presentation on a different class of MHC-derived molecules than those sensed by cytotoxic T cells.[399] The class of MHC molecules to which helper T cells respond are more restricted in their expression and other membrane proteins must be present on the APCs to activate the helper T cells.[399] A single TCR can recognize many ligands and different antigen peptide/MHC molecules can distinctly influence T-cell gene expression and modulate T-cell functions, often based on the affinity of these ligands for the TCR and other co-receptors (such as the CDs).[399] Complete binding of a ligand and the TCR will effect the phosphorylation of all immunoreceptor tyrosine-based activation motifs (ITAMs) of CD3 (a common co-receptor of TCRs involved in activating T cells) and activation of Src (tyrosine) kinases to fully activate the T cell.[399] Phosphorylation of tyrosine residues by protein tyrosine kinases of the Src, Syk, and Tec families is a key process in the activation of T cells and the signaling pathways that are initiated upon engagement of the TCR and other co-receptors.[404,405] ITAMs are key sites on these immunoreceptors where phosphorylation must occur to induce the downstream signaling upon TCR ligation.[405] Quiescent T cells maintain an equilibrium of tyrosine kinase and phosphatase activity[404] During antigen binding to the TCR, phosphatases, including some CDs, are driven away from the region around the TCR to increase kinase-driven T-cell activation.[404] Phosphorylated ITAMs are locations for engagement with other molecules that can also participate in phosphorylation and further signaling steps.[405] Signaling pathways that are initiated upon engagement with the TCR include early involvement of ZAP-70 (zeta-chain-associated protein kinase-70), which is activated by a tyrosine kinase of the Src family.[405] Before

phosphorylation of ZAP-70, it binds to the phosphorylated ITAM through corresponding Src-homology 2 (SH2) domains and protects the ITAM from dephosphorylation.[404] ZAP-70 is itself a protein tyrosine kinase (Syk family) and the phosphorylation of ZAP-70 boosts its catalytic activity.[404] The phosphorylation responsibilities of ZAP-70 include tyrosine residues on adaptor proteins of the TCR[405] and potentially other protein tyrosine kinases downstream.[404] These phosphorylation actions can even impact Rho GTPases and alter the organization of cortical actin.[404] ZAP-70 is recruited to the ITAM shortly after TCR ligation, so it is an early indicator of T-cell activation.

Properties of the APC-T-cell contact zone can determine which molecules can occupy the region around the TCR, and co-receptors or even adaptor or effector proteins can be excluded from this zone based on molecular size.[404] This suggests that surface topography of the APC can potentially modulate T-cell activation and function. Based on this hypothesis, T-cell response to nanotopographic substrates was studied. Nanoridges that are coated with anti-CD3, a stimulatory antibody, cause Jurkat T cells to spread and activate.[321] Unlike cells on coated flat surfaces, the nanoridges drive cells to spread asymmetrically and undergo increased elongation.[321] However, the cell-spread area is actually larger on flat surfaces than on nanoridges.[321] The nanotopographic cues do not alter the rate at which cells spread on the activating substrates.[321] When a non-stimulatory protein coating, poly L-lysine (PLL), is used instead, cell spread areas are smaller than those measured on anti-CD3 coatings for both flat and nanoridged surfaces.[321] Non-stimulating nanoridges induced cells to spread over a larger area than on flat substrates with the same coating.[321]

After spreading on nanoridges, T cells that are fixed and stained with phalloidin exhibit concentrated actin on the sides and at the bases of the nanoridges.[321] Actin accumulation is not evident at the tops of the nanoridges.[321] Comparable aggregation is not observed in T cells on flat substrates, based on peak-to-mean fluorescence intensity ratios.[321] Actin concentrations near the centers of T-cells are low compared to amounts near the cell edges, based on fluorescence images, regardless of whether the cells encounter flat substrates or nanoridges.[321] However, actin dynamics respond differently to these surfaces. T-cells on flat surfaces exhibit actin retrograde flow when moving on the substrate.[321] OF analysis of a representative T cell on a flat substrate showed patches of actin flow with varying orientations relative to an arbitrary axis within a single cell.[321] Generally, actin flow in cells on flat surfaces is uniformly distributed across all angles.[321] Nanoridges disrupt the retrograde motion of actin so that the flow is disorganized, and flow perpendicular to the ridges is restricted.[321] In fact, even if a cell spreads more in the direction perpendicular to the ridges, actin flow is still mostly oriented parallel to the nanoridges.[321] The temporal coefficient of variation (CV) values of fluorescence intensity show that actin in T cells on nanoridges is more dynamic than in cells on flat surfaces.[321] Microtubules also contribute to T-cell performance of vital immunological functions, and regulate actin flow and force generation through Rho GTPases.[321] T-cell polarization and persistent migration depend on effective microtubule function, and protrusion characteristics and uropod formation in these cells are also influenced by microtubules.[406] Depending on the specificity of the antigen presented, the T cell microtubule organizing center will reorient itself toward the TCR-peptide/MHC contact zone, even though this same behavior was not simultaneously observed in the antigen-presenting B cell.[407] Using fluorescent labeling of EB3, a protein that binds to the plus-ends of microtubules and regulates microtubule dynamics, microtubules have been similarly

shown to grow and orient along nanoridges.[321] The microtubule network is also strongly aligned in cells on nanoridges, with small differences between the orientation angle of individual EB3 tracks and the average orientation angle (weighted by track length).[321] Similar tracks of microtubule dynamics on flat substrates are not biased by an arbitrary axis.[321] However, microtubules in cells on these substrates are also well aligned and organized with each other within the microtubule network, although not as strongly as in cells on nanoridges.[321] Once again, these results demonstrate that nanotopography can modulate the organization and dynamics of other components of the cytoskeleton.

Signaling molecules involved in T-cell activation and TCR stimulation have an interdependent relationship with F-actin and its dynamics. The localization of actin at the base and sides of the nanoridges suggests that these could be sites of clustering of TCRs and associated signaling molecules. Imaging of labeled ZAP-70, a molecule involved in the signaling cascade of TCR stimulation and T-cell activation, displayed colocalization with F-actin at the ridges.[321] ZAP-70 clustering was observed at the nanoridges, based on the peak-to-mean fluorescence intensity ratio data.[321] In T cells on flat substrates, ZAP-70 appeared to be uniformly distributed.[321] Signaling-molecule organization and distribution can seemingly also be modulated by nanotopography.

Macrophages are a class of immune cell with multiple lineages that form in several anatomical locations at different stages of development, with a lack of consensus on their origin.[408] These cells are involved in tissue formation during development and their everyday roles include the regulation of metabolism and brain function, detection and repair of tissue damage, and immune response to pathogens.[408] However, macrophages can also exacerbate or

cause disease.[408] Macrophages are present throughout the body. In the event of the entrance of a foreign pathogen into a tissue, resident macrophages respond and inflammatory monocytes are recruited to the tissue, at which point they differentiate into macrophages.[409] Together, the macrophages participate in removal of the pathogen and also aid in tissue repair.[409] However, the resident macrophages simultaneously regulate metabolic homeostasis during the immune response.[408] Once the threat has subsided, the macrophages that were derived from the circulating monocytes can further differentiate to aid in the return to normal tissue homeostasis, depart from the tissue, or die.[409] The immune response of macrophages is strongly dependent on the tissue environment,[409] and it is possible that the physical properties of the surroundings can modulate the macrophage response.

Nanoridges drive THP-1 macrophages to spread and orient along the ridge direction.[378] Actin in these cells localizes at the ridges,[378] and representative images of macrophages on these nanotopographies exhibit the most intense fluorescence in proximity to the ridges both near the center of the cell and in protrusions at the cell boundary. These results demonstrate that immune cells can have a similar morphological and cytoskeletal response to nanotopography as do other types of mammalian cells, and even cells of other taxonomic classes, phyla, or kingdoms.

Neutrophils are a type of granulocyte, forming in the bone marrow after differentiation steps from hematopoietic stem cells.[410] Hundreds of billions of neutrophils are produced on a daily basis in adult humans, and this number can be adjusted by other immune cells during and after infections through phagocytosis by macrophages and the modulation of cytokine levels by macrophages and T cells.[410] Additional signaling pathways that influence neutrophil production are still being identified, but neutrophil occupancy in the bone marrow is another factor that

influences their production.[411] Neutrophils also exert influence on other immune cells. To organize the immune response of dendritic cells, macrophages, B cells, and T cells, neutrophils release chemokines to recruit immune cells to the site of injury or infection and secrete other cytokines to instruct cells to activate, differentiate, or proliferate.[412] In some circumstances, cell–cell contacts are also employed to deliver signals[412] In addition to their coordination with other immune cells, neutrophils also eliminate pathogens through phagocytosis and the release of reactive oxygen species (ROS), cytotoxic groups of enzymes (granules), and neutrophil extracellular traps (NETs).[411] The granules include anti-microbial peptides and enzymes that inhibit bacterial growth and break down the bacterial cell wall.[411] In the event of injury, if the neutrophils do not encounter a pathogen shortly after activation (less than 1 h), their aim shifts to breaking down tissue through the release of proteases and the inactivation of anti-proteases with the ROS.[412] Destruction of the ECM around the injury facilitates the capture of bacteria by neutrophils and other immune cells.[412] Neutrophils emit signals at the outset of the threat, but they continue to communicate throughout the immune response, sending out instructions to slow all levels of neutrophil involvement and to coordinate repair of the tissue by macrophages and epithelial cells.[412] The decision to undergo NETosis (release of self-antigens and anti-microbial peptides) or apoptosis (programmed cell death) depends upon the stimuli encountered by the neutrophils and likely determines whether the immune response will be pro-inflammatory (and auto-immune) or anti-inflammatory, respectively.[411]

Neutrophils are migratory, traveling through the bloodstream to sites of infection or inflammation in tissues. The physical properties of the extracellular environments through which neutrophils travel vary greatly. Flow rate and shear stress will depend on the type of blood vessel and its dimensions and location. ECM characteristics will be distinct in different tissues.

Displaying versatility in their migratory mode, neutrophils have been found to alter their use of membrane adhesion molecules depending on the extracellular terrain, as well as the chemical signals that the cells receive, which are also dependent on the physical properties of each individual blood vessel.[413] Modulation of neutrophil adhesion to the endothelial walls of the vasculature during migration, referred to as the multistep adhesion cascade, includes rolling, spreading, and crawling.[411] Spreading facilitates engagement with more adhesion molecules on the neutrophil and endothelial cell.[411] Neutrophils modify the availability of specific surface receptors to tune adhesion and they can release cytokines to induce changes in the availability of specific molecules or receptors on the surfaces of endothelial cells they traverse.[413] Endothelial cells exert a similar influence on the neutrophils, presenting chemokines on their membrane to drive neutrophil arrival.[413] Neutrophils also manipulate regions of their membrane in various ways to slow themselves and allow them to withstand the strong fluid forces in some blood vessels.[411] Once near the target tissue, neutrophils can exit the vasculature through the vessel wall, undergoing transmigration between endothelial cell–cell junctions or, occasionally, through individual endothelial cells.[411] These behaviors demonstrate the tendency of neutrophils to manipulate their shape and, likely, their cytoskeleton and the significance of nanotopography on neutrophil migration. The endothelial cells can alter their shape and extend protrusions on their membranes to expose more adhesion molecules to the migrating neutrophils.[411] Because they travel through different tissues and vasculature across the entire body, neutrophils encounter a variety of complex topographical cues. Yet the fact that endothelial cells change their shape while neutrophils traverse them demonstrates that the topographical cues themselves can be dynamic and that the neutrophils must exhibit versatility in their migratory properties and adapt their motion on the fly to execute their functions.

Actin in HL60 cells (neutrophil cell line) on nanoridges exhibits a lot of the same characteristics as in the other cell types discussed above, including *D. discoideum* and MCF10A cells. Actin fluorescence appears as streaks, and the actin polymerization propagates along the ridges and resists perpendicular motion.[245] Dynamic actin is also observed at the leading of the cell.[245] The speed of actin waves in HL60 cells on nanoridges is similar to that observed in cells on flat surfaces.[245] The actin fluorescence intensity in these cells oscillates on flat surfaces, with uniformly distributed motion in all directions based on kymograph data.[245] OF analysis indicates that there is some degree of nonuniform, asymmetric actin motion even on flat surfaces.[245]

Immune cells also have the capability to cause or exacerbate damage to the body. Autoimmune diseases often involve immune cells damaging otherwise healthy tissue, but many cancers also involve malignant behavior of immune cells. Tumor cells release signaling molecules that can modify the behavior of immune cells in and around the tumor microenvironment (TME). Under normal conditions, macrophages are responsible for the detection, capture, and breakdown of dead cells, debris, and foreign material or organisms. Macrophages also instruct other immune cells to perform their functions. Tumor-associated macrophages (TAMs), on the other hand, produce factors, cytokines, and other molecules that promote angiogenesis, ECM degradation, and tumor-cell behaviors or properties that lead to the progression of cancer.[88]

Fibroblasts are responsible for producing ECM components and constructing connective tissue, and also repair injured tissue.[414] To remodel the ECM, fibroblasts extend protrusions whose tips apply compressive force and whose sides pull on the ECM fibers.[415] Another function of fibroblasts is the synthesis of molecules to activate other cells for growth and development

and immune response.[414] Although not usually considered immune cells, fibroblasts play a critical role in initiating the immune response at wound sites. Fibroblasts interact with an array of immune cells throughout most tissues of the body, and the secretion of certain cytokines by tissue-specific subsets of fibroblasts selectively regulates the activation, maintenance, and/or suppression of an immune response by specific classes of immune cells in different parts of the body.[416] Unfortunately, fibroblasts can also further the progression of cancer. Cancer cells recruit fibroblasts to the TME through the secretion of certain cytokines, including transforming growth factor-β (TGF-β), which also drives the conversion of fibroblasts to TAFs.[417] As with normal fibroblasts, there are distinct classes of TAFs that can vary by anatomical location and/or in functional capabilities.[418] Regular fibroblasts and TAFs generally share the same responsibilities, but with different agendas. Both are responsible for synthesizing or modifying the ECM and both communicate with immune cells. Tumor-associated fibroblasts synthesize most of the ECM within the TME. The upregulation and downregulation of specific ECM genes that are predictive of tumorigenesis and poor prognosis are associated with the presence of TAFs in the TME.[419] Normal and tumor-associated fibroblasts produce different amounts of an array of ECM components,[420] which helps to explain the changes in the TAF-constructed ECM found in the TME. The properties of this maladaptive ECM inhibit drug treatment and immune response, restrict fluid flow in the interstitium and nearby vasculature, and promote tumor growth.[418] Signaling from cancer cells also communicates whether TAFs should deposit more ECM proteins or degrade and rearrange the existing ECM.[417] TAFs release immunosuppressive cytokines that deter the activity of certain immune cells within the TME.[418] Alternatively, some classes of TAFs can recruit distinct types of immune cells that also perform immunosuppressive functions.[418] Furthermore, TAFs actually guide tumor cells toward neighboring tissue/stroma for

invasion. Chemical signals from TAFs promote cancer-cell migration, and direct cadherin contacts from TAFs to cancer cells exert a pulling force that extracts the tumor cells from the bulk.[421] Secretion of TGF-β by TAFs drives an epithelial-to-mesenchymal transition in many types of cancer cells, which leads to pro-migratory and invasive behavior.[422] TAF interaction with topography is particularly interesting, given that these cells produce and/or remodel the ECM with properties that promote invasion. Aligned ECM fibers guide cancer cell migration and invasion.[421]

TAFs also respond to nanoridges, spreading in a polarized manner and preferentially elongating along the ridge direction.[155] The structural support allowing this oriented spreading is provided by aligned stress fibers. In TAFs on nanoridges, most stress fibers are strongly oriented along the ridge direction and are also organized relative to other stress fibers.[155] These results suggest that nanotopography drives the coordinated, aligned reorganization of the cytoskeleton, which is dramatically different from the behavior of TAF stress fibers on flat surfaces, which are oriented randomly and exhibit minimal organization with one another.[155] Stress fibers are formed by the crosslinking and bundling of actin filaments, which are achieved by the incorporation of α-actinin and myosin II. Stress fibers exert mechanical tension on the cell. The nanoridges guide the aligned organization of stress fibers along the ridge direction.[155] Therefore, cell spreading and elongation are restricted to occur parallel to the nanoridges. Stress fibers are generally anchored to the membrane, and linked to the ECM, by FAs at one or both ends, suggesting that FAs influence the localization and orientation of stress fibers. Fluorescent labeling of paxillin, an adaptor protein found in FAs, revealed that nanoridges induce the orientation of FAs along the ridge direction and the localization of FAs near the tops of the ridges.[155] FAs that form on the

tops of ridges are generally longer than those in the grooves, the latter of which have lengths similar to those observed on flat substrates.[155]

The effect of nanotopography on the dynamics of actin polymerization was discussed above. However, nanotopography can affect the dynamics of cellular components and cytoskeletal structures beyond individual actin filaments. The speed of motion and the frequency and duration of activity can vary among components, cells, and environmental conditions. By fluorescently labeling palladin, an actin-crosslinker protein that localizes to stress-fiber puncta and ends,[57,58] Azatov *et al.* were able to quantify stress-fiber dynamics, and determined that stress fibers move faster and are more dynamic on nanotopography than on flat surfaces.[155] The angles between the instantaneous velocities of tracks and the ridge axis were measured to determine how well stress-fiber motion conforms to the direction of the ridges, and the angles between the instantaneous velocities of tracks and prior displacements were used to quantify the persistence of stress-fiber motion in a given direction.[155] Flat substrates did not induce a preferred direction of stress fiber motion.[155] Gaussian fits to the distributions of angles for stress fibers in cells on nanoridges peaked at ~0°.[155] The nanoridges drove stress-fiber motion along the ridge direction and this guidance increased with time.[155] These results demonstrate that nanotopography guides the crosslinked actin in stress fibers in addition to the polymerization in individual actin filaments. Stress-fiber motion is also fastest when moving in the direction of the ridges,[155] suggesting that nanotopography can influence the rate at which cytoskeletal dynamics occurs.

Immune cells engage with nanotopographic cues in a variety of settings. Topography influences the characteristics of immune cell migration, whether cells encounter ECM fibers or

other components of damaged tissue or the cells they must traverse in the vasculature. Additionally, the shape and physical properties of immune cells during communication can influence the efficacy of information transfer and the immune response. The shape of many of the immune cells that were investigated exhibited contact guidance in response to nanoridges. Esotaxis was observed in all immune cell types, with actin filaments organizing and orienting in response to the topographic cues. Other components of the cytoskeleton, including microtubules and the bundled actin in stress fibers, also demonstrated a bias to the nanoridges. Aside from the cytoskeleton, immunoreceptors on the plasma membrane could organize and potentially cluster in response to topography. Even signaling molecules were affected by topographical cues. Most interestingly, the organization of the cytoskeleton and these other molecules were often interdependent and, in some cases, influenced cell shape and orientation on the nanoridges. These results illustrate the importance of esotaxis and topography-driven contact guidance in multiple aspects of immune response.

6.9. Different Topographical Cues

6.9.1. Sawteeth

Nanoridges are perhaps the most common topographic cue used in studies to examine esotaxis and the role that guidance of actin and other cellular proteins serve in directed cell migration. In most cases, at least one dimension or physical property (e.g., curvature) of the ridges is intended to mimic those of ECM proteins. Nanoridges resemble the topography of the rearranged ECM that promotes cancer-cell invasion of neighboring tissue. Of course, the extracellular environment is almost always more complex than rows of aligned fibers, especially when these fibers are uniform in height and spacing. In fact, researchers have fabricated patterns

with a range of characteristic topographical features to gain further insight into the effects of physical cues on cellular and cytoskeletal behavior.

Sawteeth, as the name suggests, are a type of topographic cue that resembles the teeth of a saw rising out from the substrate. This topographical pattern serves to emulate a prevalence of three-dimensional (3D) complexity found in the *in vivo* extracellular environment, such as the deposition of ECM fibers overlaid above other fibers. Design of this nanotopography is not easily achieved by most common lithographic techniques, which usually allow for limited control in the *z* dimension.

The asymmetric shape of individual sawteeth drives a unique cell-motion response. Unlike the nanoridges, on which cells exhibit bidirectional migration along the ridge direction, asymmetric sawteeth promote a unidirectional bias of cell migration in *D. discoideum* and neutrophil-like cells (HL60),[131] as well as in multiple cancer cell lines (and non-tumorigenic MCF10A cells).[196] As was observed with cells on the ridges, the cell velocity and eccentricity of *D. discoideum* on sawteeth are predictors of how well cells follow the nanotopographic cues.[131] Cells that are more eccentric exhibit the strongest preference in direction of motion.[131] In the panel of cancer cells, the various cell types also moved fastest in their preferred direction of motion along the sawteeth.[196] Additionally, in these cancer-cell lines, cells with persistent motion (those with a large displacement from their original position, relative to total motion) generally exhibited a strong bias in migration, either up or down the sawteeth.[196]

Although nanoridges guide cell motion and actin polymerization bidirectionally, it is well established that other forms of extracellular cues, such as chemoattractants, can direct cells to travel in one direction. Chemotaxis and durotaxis (migration stimulated by sensing changes in

stiffness) both require the existence of a gradient of the strength of the cue. To direct cell motion in one direction using topography, the cell would similarly need to sense a topographical gradient. Asymmetric sawteeth provide such a gradient locally, such that unidirectional guidance can be achieved over arbitrarily long distances.

Fluorescent labeling of F-actin in *D. discoideum* cells on sawteeth substrates revealed that actin localizes to within 500 nm of the sides of the sawteeth ridges, appearing as streaks oriented along the row of sawteeth.[131] Time-lapse actin movies clarified that these streaks are actually actin polymerization waves, with the wavefront probing its surroundings across a range of angles.[131] Waves on opposite sides of a row of sawteeth can be coupled, depending on the width of this nanotopographic feature.[131] Emphasizing the importance of esotaxis on directed cell migration on the sawteeth (microthigmotaxis), the flux of actin polymerization waves moves in the same direction as does the cell (actin guidance is actually stronger than the bias on cell motion).[131] This behavior was also observed in multiple cancer-cell lines whose F-actin was fluorescently labeled.[196] These findings of unidirectional guidance of both actin and cell motion are perhaps the strongest evidence of esotaxis – and, specifically, the directional bias of actin – driving nanotopography-induced directed cell motion. Rearrangements of the cytoskeleton and the motion of actin are necessary for the development of protrusions, which both sense the cellular environment and initiate the process of pushing the cell forward to migrate. Many of the cell types extend lamellipodia – which are formed by actin pushing out on the cell membrane at the leading edge – while moving on the sawteeth, strongly suggesting that actin guidance drives directed cell motion. Cells that utilize pseudopodia can also potentially sense changes in the height of nanotopographic cues at the leading edge. Of course, even without protrusions, actin can sense, and be guided by, the sawtooth nanotopography through the basal cell membrane. On

nanoridges, actin and cellular guidance are biased bidirectionally along the ridge direction. However, the direction of actin dynamics is not always the direction of cellular orientation.[130] Driving the motion of actin in one direction along the sawteeth likely restricts the formation of protrusions to that same side of the cell, thereby inducing the cell to move in that direction. Whether non-protrusive actin sensing of topography can guide the direction of cell motion, and, if so, by which mechanistic detail (retrograde actomyosin flow, rear actomyosin contractility, or other driving force), requires further investigation.

A 3D phase-field model was created to investigate the factors responsible for unidirectional cell guidance on sawteeth substrates further.[320] This model employed two fields to characterize the state of the cell: a scalar phase field that demarcates the boundary of the cell from its surroundings and a polarization vector field.[320] The vector field determined the orientation and organization of actin filaments within the cell.[320] The model set restrictions that ensured that the substrate and the cell did not share the same space and only examined actin dynamics at the membrane–substrate boundary.[320] To determine which factors drive unidirectional cell guidance, the model incorporated adjustable parameters that modulated the actin-polymerization rate, the angle of actin polymerization with respect to the substrate, and the actomyosin contractility.[320] Based on this model, it was determined that the asymmetric sawtooth nanotopography drives the spontaneous polarization of cells down or perpendicular to the sawteeth.[320] Actin polymerization that is tangential to the nanotopography influences the spontaneous polarization on sawteeth.[320] The stability of the cell state prevents this phenomenon from occurring on flat surfaces.[320]

If the cell was given an initial polarization up the sawteeth, the cell could either migrate persistently up the sawteeth, begin to move up the sawteeth and turn and reverse course down the sawteeth, or stop.[320] The actin polymerization rate and the preferred angle of actin polymerization were adjusted to determine how these parameters influence which direction the cell traveled on the sawteeth with this initial upward polarization.[320] Exceeding a threshold rate of actin polymerization permitted the cell to continue to move up the sawteeth.[320] At lower actin polymerization rates, a cell that began to move up the sawteeth would be inclined to turn around and move in another direction.[320] If the cell turned away from moving up the sawteeth, it did not always move down the sawteeth and instead sometimes moved at angles relative to the topographic cues.[320] If an initial polarization was not forced upon the cell, it would always move down the sawteeth, indicating the preferred direction of motion for cells on this type of nanotopography.[320]

A more simplistic toy model was produced that incorporated the main observations of the phase-field model.[320] A motivation for creating the toy model was to improve the predictive capabilities of cell behavior under hypothetical topographic and cellular conditions.[320] Extrapolated positions from the results of the toy model could be confirmed in experiments and the phase-field model.[320]

A specific focus of the toy model was to determine the stability of guided motion on the sawteeth.[320] The equations of motion for cells in this model, on flat substrates or asymmetric nanotopography, were formulated as functions of a parameter related to the actin polymerization rate.[320] On a flat surface, the equation produces three stable fixed points and two unstable fixed points expressing velocity as a function of the actin polymerization parameter.[320] The equation

for the cell on the sawtooth substrate adds a function that depends on the cell position, the spatial frequency of the pattern, and a factor that modulates the influence of the sawtooth topographical cue to the equation of motion on a flat surface.[320] This cell position function exerts a positive bias on the cell.[320] For 1D motion, the equations for the toy model reproduce behaviors from the phase-field model that were dependent on values of the actin polymerization rate.[320] Above a threshold rate of actin polymerization, the cell could move up or down the sawteeth.[320] Below a different polymerization rate, the cell would not move.[320] Between these values, the cell would only move down the sawteeth.[320] Extending these toy model equations to two dimensions revealed that motion up the sawteeth is always unstable.[320] The cell would eventually make a U-turn and move down the sawteeth.[320] The amount of time required for this directional change increases (and eventually diverges) with a larger actin polymerization rate and decreases with taller sawteeth.[320]

Using only two parameters to describe properties of the sawteeth and another parameter relating to the actin polymerization rate, the toy model predicted the instability of motion up the sawteeth, a hysteretic boundary between motion up and down the sawteeth, and a threshold sawtooth height preventing upward motion.[320] Together, the phase-field and toy models demonstrate the prognosticative potential of mathematical models to predict cell behavior in response to nanotopographic cues.

6.9.2. Wavy Ridges

Many ECM fibers in the body are not straight. The fibers often have some level of curvature that repeats periodically in a wavelike manner. The waviness of ECM fibers can be an indicator of tissue health.[334] To characterize the differences in ECM fiber properties in healthy

and diseased tissue, second harmonic generation microscopy was used to image collagen in the mammary fat pads of lean (wild-type) and obese mice, as well as in the central and peripheral regions of mouse tumors.[334] Most collagen fibers near the center of tumors were relatively straight, whereas the majority toward the periphery were wavy.[334] A similar distinction was observed between the curvature of collagen fibers in the mammary fat pads of obese and lean (wild-type) mice. Fibrils in the mammary fat pads of obese mice were generally much shorter in amplitude and wavelength than those in mammary fat pads of lean mice.[334] Measurements of the wave properties of ECM fibers in high- and low-grade ovarian tumors, as well as in the fat pads of obese and lean mice, demonstrated that fibrils with shorter wavelength and amplitude are characteristic of less healthy tissue and disease of greater severity.[334] Fibers with larger wavelength and amplitude are found in healthier tissue, and indicate a better prognosis in the case of disease.[334]

Wavy, fibril-like ridged substrates (600-nm high, 300-nm wide, and 3-μm spacing) fabricated using MAP promoted cell elongation and orientation along the wave axis in U2OS cells, as well as persistent migration in HEY-T30 cells.[334] However, the properties of these substrates dictated how well cells could spread, orient, and migrate, which will be discussed in more detail in a subsequent section.

The study on wavy ridges also examined how the cytoskeleton, and other biomolecules that influence cell shape and motion, respond to the curvature of the ridges to facilitate contact guidance. ABPs associated with branched actin in lamellipodia exhibited a strong preference for localization at the curved peaks of the fibril-like waveform topographies.[334] Inhibition of Arp2/3 prevented the barbed ends of actin filaments from collecting at the wave peaks, and caused a

decrease in U2OS cell elongation and HEY-T30 directional migration on the small-amplitude wavy ridges.[334] Inhibition of formin-family actin nucleators prevented stress-fiber formation on the wave substrates, which also reduced cell elongation.[334] These results demonstrated that the sensing and esotaxis of actin and ABPs at the wave peaks, where the curvature is maximal, was the most important factor for the cytoskeleton to influence cellular contact guidance.[334] Myosin II is involved in the formation of stress fibers and its contractility regulates the organization of FAs and stress fibers.[334] Minifilaments of myosin II localized periodically at stress fibers near the ventral surface of cells in wavy ridges, as well as at subcortical stress fibers.[334] Localization of the lamellipodial actin-assembly machinery at the wave peaks was observed on all fibril-like ECM waveform ridges, and was more prevalent than at the leading edges of cells.[334] Inhibition of PI3K prevented cells from spreading on the ridged substrates and orienting in the direction of the wave axis,[334] demonstrating that this kinase is necessary for contact guidance. Fluorescent labeling of the PH domain of Akt revealed that a PIP3 gradient is not necessary for cell polarization on these nanotopographies.[334] However, the GFP-PH-Akt showed that PIP3 preferentially localizes at the curved peaks of the wavy substrates, as opposed to the straighter regions between peaks,[334] indicating that curvature can drive PIP3 gradients within the cell.

The localization of PIP3 at the wave peaks of ECM fibril-like substrates drove the assembly of actin (helped by similar localization of ABPs) and myosin filaments, as well as a branched actin network.[334] Actomyosin retrograde flow directed perpendicular to the wave axis toward the node of the wave influenced the formation of FAs and stress fibers, which, in turn, determine cell polarization and elongation based on their organization in response to the topography.[334]

6.9.3. EMPs

EMPs differ from the nanotopographic patterns that have been discussed so far in several important ways. First, EMPs are naturally occurring, and are physiologically relevant due to potential human encounters with these particles or with others that bear a strong resemblance to the EMPs studied. Another important characteristic of EMPs is that they present a nanotopographic cue that lacks uniform, periodic dimensions that extend well beyond the scale of the cells. The particles can span all or part of the surface area of the cell, but with a low enough density of EMPs on the surface, the cell can spread and not sense additional cues, which is a different situation for the cells than is the perceptually oceanic topography on the patterned substrates. Despite this difference, EMPs still evoke an esotactic response in epithelial cells and macrophages. Actin was found to localize near the particles, and the EMPs also triggered actin waves.[378] Several types of EMPs were examined. Three tremolite samples were studied, two asbestiform and one nonasbestiform. Samples of a nonasbestiform riebeckite and a crocidolite—considered the most dangerous type of asbestiform EMPs—were also tested.[378] Each type of EMP increased the actin activity in macrophages and the actin fluorescence intensity in these cells was enhanced in the cell–particle contact region.[378] These observations demonstrate that cells can sense local topography beyond those that feature homogeneous, periodic dimensions that extend well beyond the scale of the cell.

6.10. Dimensions Matter

The dimensions of nanotopographic cues determine the cellular response. Ridges spaced too closely together or too far apart have limited influence on cellular contact guidance or directed migration in *D. discoideum* cells.[130] Similar results were observed in TAFs, for which

there are lower and upper thresholds to the nanoridge spacings between which cells are maximally oriented and elongated along the ridge direction.[155] Although a range of ridge spacings drive cell elongation and orientation along the nanoridges, a spacing of 3 μm prompted the largest cell elongation with strongest alignment with the ridge axis.[155] Narrower ridge spacings (1 and 1.8 μm) do not drive T cell spreading as strongly as wider spacings (3 and 5 μm) on both activating and non-stimulatory surfaces.[321] The thickness or height of an individual ridge also contributes to the cell's ability to sense and be guided by the substrate.

The size of the cell is connected to the influence of nanotopographic dimensions. If the cell is much smaller than the width of a groove, the cell will not be compelled to interact with the ridges, and so it is as if it were not textured. On the other hand, if the gap between ridges is much smaller than the cell, it is similarly difficult for the surface to guide the cells. A given cell type will have its own range of optimal nanotopographic dimensions for contact guidance and directed migration. *D. discoideum*, for instance, responds best to nanoridges spaced approximately 1.5 μm apart[130] (in this paper, spacing refers to periodicity, the distance between the same edge of adjacent ridges). Changes to other dimensions, such as ridge thickness or height, can similarly alter the capacity of a given cell type to respond to the substrate cues. The varied interactions based on dimensions are the result of processes involving intracellular molecules, networks, and pathways, and how these components help the cell to perceive the physical nature of the extracellular environment. We have previously modeled the cell-shape oscillations of *D. discoideum* as being resonant with the nanoridge grating, treating the system as an overdamped harmonic oscillator.[130] In the model, when the ridge spacing decreased to 0, the force exerted on the cell membrane by the topography was not biased – as would be the case on a flat surface – because moments in which force was exerted on the cell would not be correlated

with one another.[130] When the ridge spacing was adjusted to large values, the force on the cell was also not biased in a single direction, because the correlation of instances of force exertion was independent of angle.[130] These calculations explain the cell-scale physical basis for the dependence of contact guidance on ridge spacing, in addition to our understanding that focuses on cytoskeletal and molecular organization.

The cell-scale dependence on nanotopographic dimensions that influence shape and motion and their guidance is the result of how these external physical cues influence the organization of the cytoskeleton, as well as of other molecules and networks within the cell. Actin dynamics on both sides of a nanoridge (a few hundred nm in thickness) were observed to be correlated.[130] Yet when a *D. discoideum* cell encounters a microridge (at least 1 μm thick) with bordering grooves that are on the scale of several hundred nm, actin polymerization does not always extend into the grooves on both sides of the microridge, and moves independently if not penetrating into both grooves.[130] Actin dynamics can also depend on nanotopographic dimensions. Jurkat T-cells exhibit greater actin dynamics, based on the temporal variation in fluorescence intensity, on nanoridges with a 1.8-μm spacing than on ridges with a wider spacing.[321] The larger spacings are also more permissive of actin dynamics oriented away from the ridge axis, demonstrated by the wider von Mises distributions of OF data obtained from cells on these substrates.[321] Nanoridges with narrower spacings are better at guiding actin flow along the direction of the ridges.[321] The region of enhanced actin concentration extends approximately 1 μm away from the ridge in B cells, although the actin-fluorescence intensity is greatest at the ridge.[156] BCRs often cluster in the area adjacent to dense actin regions. Accordingly, on nanoridge substrates, BCRs aggregate most intensely approximately 1 μm from the ridges.[156] In addition to BCR clustering directly adjacent to the ridges, BCRs in B cells on 3-μm-spaced

nanoridges exhibit a preference to cluster 1 μm away from the ridges.[156] However, on 5-μm-spaced nanoridges, BCRs preferentially organize at distances of 1 and 2 μm from the ridges.[156] Smaller spacings restrict the distribution of BCRs and limit the distance from the nanotopographic features at which they can cluster. The wider distribution of BCRs upon encountering less dense topography could have ramifications for B-cell response that depends on the surface properties of antigen-presenting cells. The extent of oriented and ordered stress fibers in TAFs has a biphasic dependence on ridge spacing, with maximal alignment observed in cells on 3-μm-spaced nanoridges.[155] This scale matches the dimensions that induce the largest cell elongation and the narrowest deviation in cell orientation with respect to the ridge axis.[155] The guidance of stress-fiber dynamics also depends on the nanoridge spacing. Cells on substrates with small (1 μm) and large (10 μm) ridge spacings were most likely to exhibit stress fiber motion away from the ridge axis.[155] The 3-μm spacing again exhibited the best guidance in TAFs, with the smallest standard deviation in the orientation angle of stress fiber dynamics with respect to the direction of the nanoridges.[155] Furthermore, although stress fibers move faster along the ridge axis for all nanoridge spacings, 3-μm-spaced micro/nanoridge topographies drive faster stress fiber dynamics than do other dimensional configurations.[155] The ridge spacing also influence the orientation, localization, and length of FAs in TAFs.[155] On nanoridges with spacings between 1 and 2 μm, FAs were most strongly aligned with the direction of the ridges and are most likely to form on top of the ridges.[155] The strong alignment of FAs formed on top of ridges is likely due to restrictions caused by the plasticity of the membrane, and possibly by steric requirements for the organization of FA proteins. On surfaces with larger ridge spacings, TAF FAs can still form on top of ridges, and are still nearly aligned with the ridge axis.[155] However, on these surfaces FAs can also form in the grooves, and are not as restricted in their

organization as they are on top of ridges, resulting in larger angles of orientation with respect to the ridges.[155] For a given ridge spacing, FA length is also dependent on whether the FA formed on top of the ridge or in the groove near the ridge wall.[155] Nanogrooves with microridges of similar thickness do not induce the dense organization of microtubules and focal adhesions in MCF10A cells that are observed for nanoridges.[142] Microtubules in Jurkat T-cells were found to grow and move in stronger alignment with the nanoridges on substrates with narrower ridge spacings.[321] Aligned motion of microtubules was also more strongly coordinated in cells on the topographies with smaller spacings, as the deviations from the average instantaneous angle of motion were smaller on these substrates (using data weighted by track length).[321] The speed of microtubule dynamics might also be influenced by nanotopographic dimensions, with faster instantaneous speeds observed for EB3 tracks in T-cells on 1.8-μm-spaced nanoridges.[321] The response of signaling molecules to nanotopography can also depend on its dimensionality. Nanoridges with a spacing of 1.8 μm induce greater accumulation of ZAP-70 in Jurkat T-cells than do nanoridges spaced farther apart (3 and 5 μm), based on the fluorescence intensity data.[321] The actin localization observed at the base of 1.8-μm-spaced ridges[321] suggests that this line of T-cells can exhibit a high degree of cortical plasticity. Conforming to nanotopography with narrower spacing could result in regions of higher curvature that might induce greater clustering of signaling molecules.

The importance of dimensions for influencing cell guidance has also been observed with other nanotopographic cues. The length and height of sawteeth features can elicit cell motion in opposite directions, and a change in size can also alter the likelihood of biased motion. Longer and taller sawteeth (8 μm long, 2.4 μm high) drive most *D. discoideum* and human neutrophil-like (HL60) cells to move up the slope from tail to tip.[131] Some fraction of *D. discoideum* cells

tend to move perpendicularly to the sawtooth axis.[131] Because the rows of sawteeth are in registry, traveling along a column at the base of each sawtooth resembles migration in the groove between widely spaced ridges (here, the sawteeth peaks). Sawteeth with a length of 6 μm elicited a similar guidance preference as that of 8-μm-long sawteeth.[131] On the other hand, *D. discoideum* cells tend to move down the sawtooth slope when the feature dimensions are shorter (2 μm long, 1 μm high).[131] However, the cell speed is related to directional bias on these shorter sawteeth, as faster cells are more likely to move in either direction.[131] These distinct directions of cell motion reflect the change in behavior of actin on the sawteeth of different dimensions. Actin waves form at the bottom of longer sawteeth and travel upward, whereas waves develop near tips of short sawteeth and flow downward.[131] Engineering the dimensions of nanotopographic features to be much larger than the scale of the cell can also alter the cellular response. On a row of sawteeth hundreds of microns wide, cells preferred to move perpendicular to the sawtooth axis in the "groove" formed where the peak of one tooth meets the tail of the next.[131] Creating a space between the end of one sawtooth and the beginning of the next can also increase the likelihood of this perpendicular motion occurring.

Adjustments of the sawtooth dimensions in the 3D phase-field model identified the corresponding expected cellular response, as well as the cell migration properties that modified the guidance outcome.[320] Taller sawteeth usually drove cell motion downward.[320] However, a phase diagram of the preferred guidance direction based on the model parameters of actin polymerization rate and sawtooth height showed that faster cell speeds, often linked to a greater rate of actin polymerization, increased the sawtooth height that the cell was able to climb.[320] Polar histograms of the average velocity distributions from experimental data of *D. discoideum* cells on sawteeth showed that faster cells are more unidirectionally guided on this

nanotopography than slower cells.[131,320] The height of the sawteeth can be used as a means to control the direction of motion of the fastest cells and tune the velocity cutoff of the cells that can be guided.[320]

The ramifications of changes in the wave properties of ECM fibers on cell behavior were studied on fibril-like substrates.[334] One of the objectives was to identify how wavy nanotopography contributes to disease progression.[334] ECM-fibril waveform nanotopographies with different wave amplitude and wavelength were produced to determine whether there exists a range of these wave properties over which cell response is strongly influenced.[334] Nanotopographies with small wave amplitude and short wavelengths drive greater elongation and orientation along the wave axis in U2OS cells (an osteosarcoma cell line), and greater migrational persistence in HEY-T30 cells (ovarian tumor cell line).[334] Does one of these properties, amplitude and wavelength, exert a stronger influence on cell behavior? On ECM fibril-like waveform substrates with a wave amplitude of 15 μm, guided cell polarization and persistent migration increase with increasing ridge wavelength.[334] However, cells are also biased when the nanotopography featured a short wavelength if the amplitude was also shorter.[334] Therefore, the wave amplitude of these fibril-like substrates is the greater determinant in driving contact guidance of the cells.[334] The strongest bias was observed on ECM fibril-like waveforms with a wave amplitude below 7.5 μm, and guidance was inhibited at amplitudes above 15 μm.[334]

Normalized average fluorescence intensity data for the ABPs and Akt showed greater accumulation of these proteins at the curved peaks of small-amplitude wavy ridge substrates as compared to large-amplitude waveforms, as well as increased coverage of the straighter regions between wave peaks.[334] The fact that proteins associated with the lamellipodial machinery and

migration-dependent signaling pathways contact a greater percentage of the nanotopographic cues on the small-wave-amplitude ridges suggests why these nanotopographies elicit stronger contact guidance from cells.[334]

The organization and orientation of FAs is strongly dependent on the waviness of the fibril-like ECM substrates. Like nanoridges, small-wave nanotopographies induce the formation of mature FAs, whereas on large-wave substrates, smaller nascent FAs are observed.[334] On small-wave ECM fibril waveforms, FAs localize most strongly at the shoulders adjacent to the wave peaks.[334] The FAs on these topographies are generally oriented nearly parallel (±30°) to the wave axis.[334] In contrast to the FA behavior on the ridge substrates with smaller wave dimensions, the large-wave fibril-like ECMs direct FA formation near the wave peaks with an orientation that was more aligned to the perpendicular axis (greater than ±45° with respect to the wave axis).[334] The wavy ridges regulate the location and orientation of FAs and localization of FAs to wave peaks on large-amplitude wavy ridges plays a role in the inability of the cells to polarize on these substrates.

Since the functions of FAs and stress fibers are intertwined, it seemed likely that stress-fiber organization would also depend on the wave properties of the fibril-like ridge substrates. Staining for F-actin and employing an image-analysis tool based on the concept of the nematic tensor and a tangent vector determined from intensity gradients,[423] it was found that small-wave substrates drove stronger anisotropic organization of stress fibers.[334] That is, stress fibers were more aligned in the same direction on the small-amplitude wavy ridges.[334] On large-wave fibril-like ECM substrates, there was a broader distribution of stress-fiber orientation angles and a larger average angle, with greater deviation from the wave axis.[334] The wavy substrates with

large amplitudes also drove the stress fibers to bend around the wave peaks, which correlated with FA organization perpendicular to the wave axis and explains why the cell aspect ratio decreased on this topography.[334] On the other hand, cells on small-wave fibril-like ECM substrates formed shorter cortical stress fibers due to the localization of FAs near the peak shoulders or the inability of stress fibers to maintain structural integrity during organization near the wave peak.[334] However, actin bundles deeper in the cell and farther from the cortex and topography were able to organize along the wave axis.[334] Together, these stress-fiber behaviors on the small-amplitude wavy ridges exert the mechanical forces necessary to drive greater cell elongation and alignment along the wave axis.[334] Wave dimensions also influenced the organization of myosin proximal to stress fibers. Although myosin IIA localized periodically along stress fibers in cells on both large- and small-wave substrates, the large-wave substrates also induced the organization and alignment of myosin II near subcortical branched actin that connected stress fibers located at wave peaks and bases.

Localization of PIP3, Arp2/3, and FAs at the wave peaks and the organization of myosin II "ribbons" around the branched-actin meshwork between the wave peak and base on large-wave ECM substrates resembled the assembly of migration machinery in the mesenchymal phenotype.[334] However, this arrangement of molecular components was oriented perpendicular to the wave axis and we referred to this misaligned assembly as "cryptic leading edges."[334] Timelapse movies of cells on these large-wave substrates showed that GFP-labeled myosin IIA localized near the wave peaks and nearby regions of the cell and then flowed perpendicular to the wave axis toward the base of the wave, at which point subcortical stress fibers formed that spanned a half-wavelength.[334] If the cell could spread enough to span an entire wavelength,

retrograde actomyosin flow at the wave trough would be oriented in the opposite direction of the flow at the wave peak, both directed toward the base, or node, of the wave.[334]

PIP3 and Arp2/3 behaved similarly on small-wave ECM substrates, localizing at the wave peaks.[334] Even though the FAs preferred to form near the peak shoulders, myosin II still localized near wave peaks, and retrograde flow was similarly oriented in the direction observed on the large-amplitude wavy ridges.[334] The centripetal flow toward the base of the wave from the wave peak was similarly mirrored by flow in the opposite direction from the wave trough.[334] However, because of the small wave amplitude, the flow quickly led to the formation of longer subcortical stress fibers that spanned multiple wavelengths and their contractility strongly influenced cell elongation along these small-wave substrates.[334]

The physiological significance of nanotopographic dimensions is perhaps most clearly demonstrated by the study of EMPs. Esotaxis was studied on EMPs with various shapes and thicknesses.[378] The cytoskeletal response depends on particle thickness, with thinner particles eliciting stronger actin fluorescence proximal to the EMP.[378] Asbestiform EMPs with thinner fibers elicit weak actin localization in the epithelial cells, whereas EMPs with thicker fibers do not induce an esotactic response in these cells.[378] Although a crocidolite EMP sample featured particles with a measured fiber diameter as low as ~200 nm, a Jamestown tremolite EMP sample, with measured particle diameters as low as ~400 nm and as high as ~900 nm, actually evoked the strongest actin response (compared to regions of interest without EMPs) from macrophages.[378] Of all the EMPs studied, only proximity to Jamestown tremolite EMPs evoked a higher percentage of brighter actin fluorescence compared to other regions of the macrophage cells.[378] In other words, of all the EMP types that were used in experiments to identify the locations of

the brightest fluorescent actin pixels in macrophages, only the Jamestown tremolite particles spurred an increased probability of localization of the brightest actin fluorescence pixels at the EMPs compared to other regions of the cell.[378] These results support the idea that the morphological and dimensional properties of particles that enter the body (through inhalation or some other means) can influence how the particles affect nearby cells, and are consequently processed.[378]

The fact that cell motion varies on these different topographical cues demonstrates that contact guidance depends on feature dimensions. Accordingly, there is the potential to control and modulate cell migration through engineering of cellular environments.

6.11. Esotactic Response Varies by Cell Type

In the natural 3D extracellular environment, the organization of the ECM can create barriers and narrow openings that might limit certain cells' passage based on the compressibility of the cell nucleus.[14] Different cell types might have different expression levels of integrins (or lack them altogether), actin-binding proteins, or other molecules necessary for mechanotransduction. Cells might exhibit different membrane stiffness and cortical plasticity or require different mechanical force thresholds to activate signaling pathways. Realistically, of course, these variations can be observed within a single cell type or line, based on factors that cannot necessarily be controlled by the experimental conditions. However, there are characteristics that can generally be applied to distinguish among cell lines and predict behavior on a specific nanotopographic cue.

A corollary to the concept that feature dimensions determine whether cells and subcellular components can be guided is that not all cells sense and react to a specific nanotopographic cue in the same manner. MCF10A cells exhibit stronger guidance on nanoridges than do M4 cells (the metastatic mutant).[196] The morphologies of these cell lines are different on flat surfaces, and nanotopography does not reduce the distinction.[196] Furthermore, protrusions of the two cell types do not interact with physical cues in the same manner. Lamellipodia in MCF10A cells do not conform as sharply to nanotopography and often anchor to the tops of nanoridges, whereas lamellipodia in M4 fit into the grooves and cling to the walls of each ridge.[196] MCF10A cells spread along the ridges and their lamellipodia are restricted to forming on either side of the elongated cell.[196] On the other hand, M4 cells spread more in the direction perpendicular to the ridges, with lamellipodia that also span multiple ridges.[196] The difference between the confinement of protrusions in these cells likely influences why MCF10A exhibit stronger contact guidance on nanoridges than do M4 cells.[196] Although MCF10A and M4 cells spread preferentially in a specific orientation with respect to the ridge direction, T cells are equally likely to spread parallel and perpendicular to anti-CD3-coated nanoridges.[321]

Migratory and morphological differences on nanotopography between cell lines can often be explained by distinct esotactic responses. For instance, if actin is more restricted to the walls of nanoridges in macrophages than in epithelial cells, perhaps macrophages will have a stronger response to contact with elongate mineral particles (EMPs).[378] MCF10A cells exhibit little or no actin response to EMPs.[378] The EMP types to which these epithelial cells exhibit some level of esotactic response might contain valleys between fibrils that comprise the particle fibers, thereby allowing the cortex to reach into these voids and improve the sensing of these particles and strengthening the esotactic response.[378] In contrast, THP-1 macrophages exhibit a strong

esotactic response to EMPs, with regions of concentrated F-actin localized near the fibers.[378] The actin response in these macrophages is often dynamic in character when in contact with several different types of EMPs, fluctuating in intensity and position on the particles as time passes.[378] The macrophages are not as sensitive as epithelial cells to EMP dimensions, as all five types of particles studied elicited enhanced actin-fluorescence intensity.[378] Differences have also been observed regarding the locations at which esotaxis occurs within a cell. In neutrophil-like HL60 cells, actin is generally concentrated in the front of the cells on both flat and nanotopographic surfaces.[245] As a result, actin streaks are generally only found near the cell front of HL60 cells on nanoridges, compared to the streaks observed throughout MCF10A cells on the same nanotopography.[245] The actin dynamics also differ in these neutrophil and epithelial cell lines. Actin-based protrusions occur on the scale of seconds in HL60 cells and minutes in MCF10A cells.[245] The location of actin dynamics also varies between epithelial cells and macrophages during interactions with EMPs. Actin fluorescence localized at different positions on an EMP and fluctuated in intensity throughout the contact area in macrophages, whereas actin fluorescence in response to an EMP did not fluctuate significantly in intensity or position along the EMP in epithelial cells and was mostly concentrated at the cell boundary.[378]

Divergent cell behavior is perhaps more evident on nanosawteeth. Although *D. discoideum* and HL60 cells preferentially migrate in the same direction on sawteeth, even when that direction changed upon encountering surfaces with different sawtooth dimensions,[131] the degree of bias was not uniform among cancer cell lines studied, and some of these cells were driven to migrate in the opposite direction along the sawteeth.[196] The various cancer cell lines exhibited different morphologies, protrusions, and other migration characteristics, demonstrating that differences in these cell lines at the intracellular level determine the response to a specific

nanotopographic cue. The study using a phase-field model to investigate the cellular response to the sawteeth topography identified two major morphological phenotypes – the crescent and the wedge – that depend on the contractility of the cell.[320] Cell types that are more contractile in nature, such as M4 cells, often exhibit the crescent shape when in contact with sawteeth, and cells with lower contractility, such as *D. discoideum*, often display the wedge shape.[131,196,320] Furthermore, although most cell types demonstrate stronger directional bias on sawteeth when migrating at high speeds, MCF10A cells move slowly in all directions.[196] Despite exhibiting a preference to move up the sawteeth, this guidance is weak for MCF10A cells.[196] Similarly, M4 cells are the exception with respect to persistent motion leading to a strong directional bias on sawteeth. Even when M4 cells migrate persistently they do not demonstrate a directional preference on the sawteeth.[196]

When the morphologies of two of the cancer-cell lines, MDA-MB-231 (a carcinoma cell line derived from pleural effusion) and M4 (MCF10CA1; metastatic mutant of the MCF10A, benign human epithelial, cell line) cells, were studied on nanosawteeth substrates using scanning electron microscopy (SEM), distinct positioning of protrusions and the cell body were observed, as well as different interactions with individual sawteeth. MDA-MB-231 cells generally remain attached near the tops of sawteeth.[196] The cell body "floats" on the sawteeth, not pushing down into the valleys between rows of sawteeth. The lamellipodium (often only a single protrusion in MDA-MB-231 cells on the sawteeth) spreads across, or bridges, multiple sawteeth in neighboring rows (within the same column; i.e., perpendicular to the length of the sawteeth), and there is limited conformation of the protrusions or the rest of the cell body into the grooves, except to support the cell situated atop the sawteeth.[196] M4 cells can bend regions of the cell body, especially in its protrusions, into the valleys between sawteeth rows.[196] These cells often

form multiple protrusions that can envelop individual sawteeth and can reach down into the grooves between rows of sawteeth.[196] As with the alignment and directed migration of cells on nanoridges, there should be esotactic explanations for these distinct responses of cancer-cell lines to sawteeth.

The direction of esotaxis corresponds to that of microthigmotactic guidance for all of the cell types in which both of these phenomena have been studied. However, the direction of actin waves on the sawteeth differs between the cancer-cell lines MDA-MB-231 and M4.[196] In both *D. discoideum* and MDA-MB-231 cells, actin nucleates at the tail of a sawtooth, flows up the slope along both sides toward the sawtooth head, and then proceeds to the tail of the next sawtooth in the row.[196] On the other hand, in M4 cells, actin nucleates at sawtooth heads and flows down toward the tails before proceeding to the head of the neighboring sawtooth within the row.[196] To some extent, actin in both cell types remains at the nucleation site as the wave flows along the rest of the sawtooth, despite the fact that the starting position and direction of propagation are opposite in the two cases.[196] However, in M4 cells the actin intensity is always strongest at the nucleation site (sawtooth head) even though actin flow traverses the rest of the nanotopographic cue; so far this observation is unique to this cell type.[196] In addition to the differences in dynamics, imaging of the localization of actin in the *z* dimension illustrated that actin in MDA-MB-231 cells does not interact with the sawteeth near the surface of the substrate, whereas the actin in M4 cells surrounds sawteeth down toward the grooves.[196] The distinct appearance of the membrane and actin structures in these cancer cells is believed to result from differences in the stiffness or plasticity of their cortical actin, which can either permit or restrict the cell from reaching down to the base of the sawteeth. *D. discoideum* cells labeled with cAR1-YFP to visualize the membrane also exhibit contact with the entire sawtooth.[131] This observation

suggests that *D. discoideum* has high enough cortical plasticity and low enough membrane stiffness to be able to conform to individual sawteeth of specific height, length, and width, and to organize its cytoskeleton and be guided by the nanotopography to move in a certain direction. Different cell types can also demonstrate the same bias of actin waves on nanotopography with one set of dimensions, and then exhibit distinct behavior when those dimensions are changed. Esotaxis is preferentially directed up the slope of 8-μm sawteeth in both *D. discoideum* and HL60 cells.[131] When the sawteeth are shrunk to 2 μm in length, actin in *D. discoideum* has a downward bias whereas there is bidirectional guidance in HL60 cells.[131]

Differences in the characteristics of guidance of actin dynamics among cell types can still lead to the same migratory bias. For instance, actin waves exist throughout the region of contact with nanotopography in *D. discoideum* cells, whereas actin dynamics is restricted to the lamellipodium in HL60 cells on these substrates.[131] In HL60 cells, the actin-wave speed is directionally dependent with respect to 8-μm sawteeth, which is not the case for *D. discoideum* cells,[131] yet both cell types are biased up the sawteeth.

On nanosawteeth, the esotactic response of microtubules in cancer-cell lines is not uniform. In MDA-MB-231 cells, the microtubules align and wrap around individual sawteeth, whereas in M4 cells there is no such biased organization.[196]

Focal adhesions also have distinct organization in different cell types when migrating on sawteeth.[196] For the most part, confocal images of paxillin in MDA-MB-231 cells showed localization and the strongest intensity atop the sawteeth, near the tips, with limited FA formation at the bases of the sawteeth near the tails or in the grooves between sawteeth.[196] This observation matches with the restriction of the cell body to the tops of the sawteeth, and the

confinement of the FAs can explain the strong alignment of the cells and guidance along the sawteeth.[196] MDA-MB-231 cells likely do not engage much with the bottom of the substrate, due to their inability to conform to the shape of individual sawteeth as a result of a stiff actin cortex. On the other hand, FAs form around the entire sawtooth in M4 cells, demonstrating the ability of these cells to conform to the features of the topography and reach the gaps and valleys and envelop the sawteeth.[196] The cortical plasticity of these cells allows them to interact differently with the nanotopography than do MDA-MB-231 cells. As a result, there is a distinct directional bias for each cell line.

The 3D phase-field model described earlier was used to reproduce the distinct behavior of different cell types on the sawteeth substrates. The cell contractility and actin polymerization rate were tuned to adjust cell shape and guidance direction.[320] The cell contractility parameter modulated the cell shape.[320] Lower levels of cell contractility led to a less polarized, oval shape elongated parallel to the direction of motion.[320] Higher contractility values caused cells to spread perpendicular to the dimension of motion along the sawteeth,[320] a trait that was observed in M4 cells[196] and could be expected in many types of cancer cells, due to their general tendency to be highly contractile.[320] However, some cell types, such as *D.discoideum*, clearly demonstrated the ability to elongate and migrate both parallel and perpendicular to the sawteeth and, in fact, at all intermediate angles.[131,320] By adjusting the initial polarization of the cell, the model could also reproduce cell spreading and migration in all directions.[320] With initial polarization up the sawteeth, a high degree of contractility, and fast rate of actin polymerization, cells migrated persistently up the sawteeth.[320] Across the range of contractility levels studied, the cells experienced an initial peak and rapid drop in velocity—caused by the initial polarization up the

sawteeth and shape changes that occurred—and then velocity recovery, to some extent, and subsequent long-term behavior that depended on the cell contractility.[320]

The study of cancer-cell response to wavy ECM fibril-like substrates suggested that intrinsic actomyosin contractility regulated the ability of cancer cells to elongate and migrate on ECM fibers with wavelike properties.[334] Quantification of the amount of phosphorylation of myosin II regulatory light chain, as an approximation of actomyosin activity, using Western blot analysis enabled the ranking of several cancer cell lines based on estimated contractility.[334] Comparison of these rankings to cell elongation and migration persistence data for the cells on wavy ECM substrates supported the hypothesis. Cell lines with lower actomyosin activity, and thus contractility, levels exhibited reduced elongation and migration persistence on the fibril-like ECM substrates.[334] More contractile cell lines can migrate on substrates with higher wave amplitude than cells with lower characteristic contractility.[334] Perturbations of myosin activity confirmed the importance of contractility on cell response to topographic cues. Blebbistatin inhibition of myosin reduced the wave amplitude at which U2OS cells could still elongate and MDA-MB-231 cells could still migrate persistently on the fibril-like ECM substrates.[334] On the other hand, overexpression of myosin IIA enabled HEY-T30 cells to migrate persistently on wavy substrates of greater amplitude than possible under normal conditions.[334] Results from this study further support the idea that response to topography is cell-type-specific. The arrangement and properties of ECM fibers can vary based on organismal health and anatomical location.[334] The ability of cells to traverse a particular region of ECM—to undergo persistent directed migration in response to the topographic cues (microthigmotaxis)—depends on specific properties of the cell, especially the contractile properties of the cytoskeleton, that are generally characteristic of a cell line or type.[334] However, the perturbation studies demonstrated that the

cellular properties can be modulated, often through changes in expression levels, based on environmental factors that include intercellular signaling.

6.12. Modulation of Other Cues with Nanotopography

6.12.1. Surface Chemistry

Cells can also respond to the surface chemistry of their environment. Focal adhesions have been discussed earlier, but even cells that lack integrin receptors possess other transmembrane proteins that can experience attractive interactions with a surface that are dependent on chemical composition, functional groups, surface charge, and other factors. Because the surface chemistry of the ECM or an *in vitro* substrate can influence the organization of membrane proteins, which can influence signaling pathways and cytoskeletal organization, changes in surface chemistry have the potential to modulate the cellular and cytoskeletal response to nanotopography.

The T-cells discussed above exhibited microthigmotactic and esotactic responses on nanotopographic substrates that were coated with anti-CD3, an antibody known to stimulate T-cell activity.[321] Although the results of the study clearly showed that nanotopography elicits a distinct cellular response compared to flat surfaces, it is also clear that multiple types of cues can be tuned to modulate cellular behavior. Changing the surface coating to PLL reduced the cell-spread area on substrates for all spacings.[321] This non-stimulatory coating reverses the dimensional preferences of T-cell spreading. The cell area is larger on the ridges with wider spacings than on the smaller gratings and flat surfaces.[321] Additionally, more disorganized, less aligned actin dynamics was observed on PLL-coated nanotopographic surfaces, suggesting that

T-cell activation through CD3 is necessary for the esotactic reorganization of the actin cytoskeleton[321] (although other proteins or receptors might influence similar responses). Antigen recognition by lymphocytes is an organized and dynamic process and the formation of the immunological synapse requires a stable, flat interface between the T cell and the target cell.[424] After using its leading edge to make contact with the APC, the T cell polarizes toward the APC,[424] and the two cells form a contact zone that undergoes slow, gradual changes through cytoskeletal dynamics.[425] T-cell polarization toward the APC involves repositioning of the centrosome (MTOC) underneath the immunological synapse,[424] which is accompanied by vesicle transport and the initiation of signaling pathways.[424-426] These slight motions continuously reposition the regions of contact between the cells to engage receptors.[425] The junction forms when MHCs start to bind to peptides and complexes are then transported to form centralized clusters.[427] The organization of the immunological synapse includes a gap between the MHC-antigen cluster and a region of engagement among adhesion molecules from the two cells and another region comprised of CDs, such that the overall configuration takes the form of a bullseye.[426] Repositioning of the centrosome near the immunological synapse was observed frequently on anti-CD3-coated nanoridge substrates, but less often in cells attached to PLL-coated nanotopographic surfaces.[321]

Similarly, the summary of results for B-cells and the response of BCRs and actin to nanotopography were for substrates coated with an antibody capable of being bound by the BCRs that simulated an antigen being presented to the B cells.[156] The activation of the B cells, clustering of the BCRs, and localization of and dynamics of the fluorescently-labeled actin on the nanoridges occurred in the presence of this antigen-like coating.[156] To test whether nanotopography could initiate a similar response through esotactic guidance of the cytoskeleton

without engagement of BCRs, substrates coated with transferrin were tested.[156] Transferrin is a glycoprotein involved in iron uptake and supports iron metabolism in cells.[428] When the substrates were instead coated with transferrin, the cellular and cytoskeletal responses to nanotopography changed.[156] The cells spread on the nanoridges, but the lack of antigen prevented the activation of the BCRs.[156] Without stimulation of the BCRs and activation of the B cells, actin did not localize to the ridges, and the oscillations in actin fluorescence intensity were absent.[156] The ridges alone did not promote or enhance actin localization and dynamics in these cells.[156]

A 2D substrate patterned with adhesive cues via stamping of ECM proteins did not drive polarization and directed migration of U2OS cells.[334] This result demonstrates the importance of nanotopography in contact guidance. However, surface chemistry did influence how cells responded to wavy ECM substrates. Although U2OS cells elongate on small-amplitude, fibril-like waveforms or straight nanoridges coated with either collagen or fibronectin, elongation does not occur when the substrates are coated with concanavalin A, which does not engage integrins.[334] This result is another example that demonstrates how contact guidance can be modulated by tuning surface chemistry.

These previous examples emphasize the importance of surface chemistry on the ability of nanotopography to influence activation, polarization, and migration. Similar results were observed for MCF10A cells on nanoridges upon which the coating density of collagen IV was modulated. Cells on uncoated nanoridges remain round and cells on these substrates are less likely to migrate than cells on ridges coated with collagen IV. The coating density of collagen IV on the nanotopographies does not noticeably influence cell elongation or migration. Despite the

fact that uncoated nanoridges are less likely to drive epithelial cell elongation and migration, cells on these surfaces exhibit similar guidance by the ridges. Even without strong integrin engagement, cells can sense and orient along the nanoridges. Optical flow analysis of actin dynamics showed that the flow of actin is similarly oriented along the ridges, regardless of the presence or density of collagen IV coating. Shortly after cells are plated on the uncoated ridge substrates, actin is already strongly bidirectionally guided along the ridge axis, with accompanying periodic sweeps across different angles to probe the region away from the nanotopography. This sweeping motion dissipates over time and the kymographs of the orientation of actin dynamics for cells on collagen-IV-coated and uncoated nanoridges become less distinguishable. The fidelity of actin motion along the ridge axis is not characteristic of a specific migratory phenotype. Cells that exhibit persistent, turning, and random migratory phenotypes all display similar aligned actin dynamics.

6.12.2. Electric Fields/Electrotaxis

Electric fields are also capable of driving directed cell migration, in a process referred to as electrotaxis or galvanotaxis. This phenomenon has biological relevance in wound healing, for example, in which the electric field directs cells toward the wound site and influences the direction in which cells close and repair the wound.

In an *in vitro* study of HL60 cells, a 10 V/cm EF (a physiologically relevant magnitude) was delivered across an acrylic (flat) substrate through agar/salt bridges.[319] Cells were observed before and after the field direction was switched to monitor the cellular and cytoskeletal response.[319] The initial exposure to the EF activated the HL60 cells and caused them to polarize.[319] Cell motion was oriented toward the cathode, and fluorescently labeled actin was

most concentrated at the cell front toward the outer edge of the protrusion.[319] The actin responded to the switched direction of the EF and smoothly turned 180°, along with the leading edge of the cell, toward the new cathode.[319] Although the actin turned smoothly, OF analysis of the dynamic actin exhibit the nonuniform orientation of OF vectors biased toward the direction of the cathode both before and after the EF switch.[319] The cumulative flow-direction distribution of OF vectors before and after the switching of the EF appeared to be nearly isotropic.[319] This phenomenon was likely due to the variability of cell polarity prior to the application of the EF and of the actin response time across experiments.[319] However, coarse-graining of the OF vectors to visualize the dynamics of larger scale actin structures revealed a bias towards the cathode before and after the EF reversal in the cumulative distribution of OF orientation.[319] Centroid tracking of these coarse-grained structures further emphasized the bias, especially after switching the direction of the EF.

A similar experiment was conducted in which HL60 cells were plated on nanoridges with the EF aligned parallel to the ridge axis.[319] In this case, the actin was more patchy and discontinuous, which seems to have caused the cell to have multiple protrusions that were not uniformly positioned at the leading edge.[319] Upon switching of the direction of the EF, the cell was still able to turn and migrate toward the new cathode, but the process was less organized and smooth on both the cellular and cytoskeletal levels.[319] Most actin fluorescence intensity disappeared from the new cell rear once several minutes elapsed after the EF switch and the cell changed directions.[319] The nanotopography disrupted the actin wave that would have formed at the cell front if the cell had been subjected to an EF on a flat surface. The nanoridges broke that potential wave into smaller, uncoordinated wave patches.[319] The wave speeds were comparable in both scenarios, indicating that the nanoridges do not impede actin motion.[319] Actin dynamics

was strongly restricted to move parallel or nearly parallel to the ridge axis, both before and after the switch of EF direction (especially beyond 5 min),[319] which possibly explains the disruption of a single, organized wave at the leading edge, and the lack of a smooth turn of the actin and the cell after the EF switch. Coarse-graining of OF vectors resulted in a cumulative flow-direction distribution that was more strongly biased in the cathodal direction, both before and after EF reversal, than the bidirectional character of the non-coarse-grained distribution, but the centroid tracking of these coarse-grained actin structures did not strongly support a unidirectional preference.[319] The nanoridges strengthened the guidance of actin dynamics along the axis defined by the electric field vector when the two stimuli were aligned parallel to each other.[319]

Orienting the electric field and the nanoridges in perpendicular directions enabled the investigation of the degree of influence each cue can exert on cellular and cytoskeletal behavior. Additionally, competition between these guiding forces can reveal unique responses from cells that can be elicited through the creative modulation of cues, either individually or combinatorially. The perpendicular arrangement of the EF and the nanoridges resulted in actin dynamics that suggested that nanotopography exerts a stronger influence on the direction of cytoskeletal motion.[319] OF vectors were strongly restricted to the ridge axis in cells, even though the EF was oriented in the perpendicular direction.[319] A representative cell exhibited an exaggerated leading edge oriented in the direction of the cathode (and seemingly reestablished at the opposite end of the cell with the switched EF) but which spread along the perpendicular ridges; i.e., the cell was spread wider from side to side than from front to rear.[319] This example suggests that an EF can drive the orientation of the cell leading edge while the nanoridges simultaneously bias cell spreading. However, the cumulative flow-direction distribution of the coarse-grained OF data and of the tracked centroids of cells (based on cell boundary and shape

detection and center-of-mass determination from the actin fluorescence intensity) showed a broadening of the distribution along the axis perpendicular to the ridges (i.e., the EF axis), which suggests that the EF exerts some influence on the direction of actin dynamics that would otherwise be more strongly directed along the nanoridges in its absence.[319] Indeed, although actin-polymerization waves moved preferentially along the nanoridges, the nucleation of new waves was biased to occur on the side of the cell closest to the cathode, allowing the cell to migrate in that direction. This phenomenon is more noticeable after the EF reversal.[319] The representative cell on the perpendicular EF–ridge setup exhibited limited actin fluorescence intensity on the edge of the cell facing the anode, except for a short window of time after the EF switch. Similar isolation of the actin concentration was observed in a representative cell on a flat substrate.[319] The fluorescence disparity between the leading and trailing edges, although present, was not as stark in the representative cell on the parallel EF–ridge configuration.[319] These results suggest that the reversal of the EF directs the nucleation of actin polymerization away from previously actin-rich regions, and that the new cathodal direction and the nanoridges determine the characteristics of cell shape and actin organization and dynamics at the leading edge.[319]

In general, when HL60 cells experience electrotactic guidance, actin polymerization occurs on the side of the cell situated near the cathode, and cell polarization and migration are usually oriented in this direction as well. Actin guidance by the EF is stronger after field reversal, and always responds to the new cathode upon the EF switch.[319] That is, cytoskeletal organization and dynamics are sensitive to an EF and changes in its orientation.[319] Additionally, the guidance of actin polymerization by EFs is not immediate. The response to the EF often takes at least several minutes, and the required time and the strength of the response varies from cell to cell.[319] Once the cytoskeleton responds to the EF, the guidance still occurs gradually, and the quantified

bias is greater if the measurement is taken over a larger window of time.[319] Nanoridges disrupt the actin polymerization at the leading edge of the cell that would otherwise coordinate its motion under EF guidance resulting in small, 1D patches of actin whose motion is restricted to propagating along the ridges.[319] Nanotopography exerts a stronger influence on the orientation of polymerized actin dynamics than do EFs, but the EF still biases guided nucleation of some proportion of actin even during competition with nanotopographic cues.

6.13. Summary and Outlook

The study of esotaxis gives us perspective about the extent to which every detail and property of the extracellular environment influences cell behavior. Even expression of adhesion proteins can be altered as a result of contact with nanotopographic cues, in addition to the effect of surface chemistry and stiffness.[381] Nanotopography breaks the symmetry that a cell would otherwise experience on a flat surface of uniform composition.[245] This symmetry breaking serves as a location where cellular processes can initiate, such as the nucleation of F-actin or the clustering of membrane proteins, and then expand, such as actin streaks moving along a fiber.[245] This localization of a molecular response can then lead to cell-scale changes, such as motion along the topographical cue.

Visualization of esotaxis through the labeling and imaging of actin and other molecules involved in cell motion, as well as analytical tools that illustrate the dynamics of these molecules, allows us to understand the migratory behavior of cells in response to nanotopography. Additionally, imaging methods, including SEM and other high-resolution techniques, that provide perspective of the morphological properties of cells on these substrates clarify the extent to which actin and other intracellular molecules can engage with specific

features of a nanotopographic cue. Fabrication of patterned nanotopographies with unique features and the subsequent cellular studies have the potential to reveal the morphological and migratory responses of cells to the features, the underlying influence on the cytoskeleton and other molecules, and yet undiscovered relationships among signaling molecules, actin, ABPs, and transmembrane proteins.

Microscale and nanoscale topographies have dimensions that are smaller than the size of the cell, yet they can guide cell motion over arbitrarily long distances (microthigmotaxis). The ability to sense and be guided by nanotopography has been observed in cells of many eukaryotic organisms. The actin cytoskeleton can sense nanotopographic features and dimensions and specifically organize in response to those properties. Additionally, actin polymerization exhibits wavelike dynamics that are influenced by nanotopographic cues. The guidance of the organization and dynamics of the cytoskeleton is defined as esotaxis. In addition to actin, other components of the cytoskeleton, as well as ABPs, transmembrane proteins, adaptor molecules, and signaling molecules, can be guided by nanotopography. Esotaxis is ubiquitous across cell types and many eukaryotic organisms. Despite traveling across many regions of the body and encountering many different extracellular environments, immune cells exhibit esotactic guidance of the cytoskeleton and transmembrane receptors to efficiently traverse the complex terrain and sense signals from other cells to perform their immunological functions. Most frequently studied on nanoridges, actin generally polymerizes adjacent to the ridges and the actin structures and polymerization waves are oriented along the ridge axis.

The dimensions of nanoridges determine the extent of guidance. Spaced too close together or too far apart, actin will not organize as efficiently and directed cell motion will

decrease. Topographic dimensions are also important for other patterned substrates. Asymmetric nanosawtooth topographies bias cell motion in one direction. Changing the sawtooth height (and length) can reverse the preferred direction of motion by influencing the location of actin wave nucleation and the direction of propagation. Cellular response to wavy fibril-like ridges also depends on the wave properties of the topography. Smaller wave amplitude and larger wavelength, which increase the similarity of the pattern to nanoridges, drive cell elongation and migration persistence on the fibril-like ECM substrates. Localization of PIP3, ABPs, FAs, and myosin II near wave peaks leads to the formation of leading-edge assemblies at the wave peaks. Wave dimensions determine whether retrograde flow from the cryptic leading edges or stress fiber contractility along the wave axis dominates the actomyosin flow direction and whether cells are well guided by the wave ridges.

Different cell lines or types can respond to the same nanotopographic substrate in different ways. Guidance might be improved with a slightly larger or smaller spacing. Migration on asymmetric nanosawteeth might be biased in the opposite direction compared to another cell. The differences in migration guidance and esotaxis often result from intrinsic characteristics of the different cell lines, such as membrane deformability, cortical plasticity, and actomyosin contractility. For instance, cells that cannot penetrate into grooves as well as others might not be able to form FAs at the base of asymmetric nanotopographic features or might not envelop these features with cytoskeletal components. As a result, for two different cells on the same substrate, one might be sensing an entirely different nanotopographic environment. Additionally, baseline differences in the expression of FA proteins or signaling molecules for two different cell types could also lead to disparities in guidance efficiency. Even within a given cell type, cells exhibit a

distribution of responses to nanotopography, resulting from slight changes in protein and gene expression.

Esotaxis is a local phenomenon that can influence global changes in the cell. A cell partially situated on a flat substrate and a ridged pattern will exhibit actin organization characteristic of contact with that type of topography in each respective region of the cell. The organization of actin responds to the local environment. The dynamics of actin on the basal surface of the cell in contact with nanoridges will not form the same structures as actin closer to the dorsal surface. The local properties of the dynamics and organization of the cytoskeleton or other molecules can influence global changes in the cell. Guidance or localization of cytoskeletal proteins, signaling molecules, or transmembrane proteins can initiate signaling pathways, molecular gradients, and modulation of protein expression. These changes can influence the cell to undergo directed migration or perform other cell functions, such as proliferation or differentiation.

Actin serves as a sensor of nanotopography. Transmembrane proteins are often credited with the ability to sense the extracellular environment. Integrins and the adhesion complexes they form are frequently highlighted when describing the process of sensing nanotopography. Modulating the availability of collagen IV ligands for integrin binding, we found that FA formation is vital for epithelial cell elongation and migration along nanoridges. However, under conditions with limited availability of ECM ligands, cell orientation and migration are still strongly aligned with the nanoridges. Analysis of actin dynamics on the ridges showed that despite periodic sweeps or probes of actin motion away from the ridge axis, actin flow along the nanoridges is dominant. OF analysis showed that actin dynamics and orientation is not predictive

of migratory behavior. Despite the ability of actin to sense topographic and other physical cues without strong engagement of integrins, surface chemistry can be used to modulate cellular behavior on nanotopography.

Incorporating EFs into esotaxis studies further reveals the strength of the influence of nanotopography on cellular and cytoskeletal guidance in a multi-cue environment. An EF guides cell motion toward the cathode on flat surfaces, and actin is concentrated near the leading edge of the cell. Coarse-graining of the OF data showed that the dynamics of actin structures are oriented toward the cathode. When the field is reversed, the actin turns 180° toward the new cathode with a new leading edge, and large-scale actin dynamics are oriented in this direction. Combining nanoridges and an EF, sharing the same orientation, strengthens the guidance of actin along the axis of the EF, compared to EF guidance in the absence of the topography. However, the ridges break up actin waves into patches, leading to the formation of multiple protrusions. Reversal of the EF causes the cell to switch directions, but the turning of actin in the opposite direction is not as smooth because the ridges strongly restrict esotaxis away from the ridge axis. Changing the orientation of the EF to be perpendicular to the nanoridges showed that the nanoridges exert a stronger influence on actin guidance than the EF. The perpendicular configuration creates a similar front–rear disparity in actin concentration as is observed in cells on flat surfaces. The nanotopography is the dominant influence on actin dynamics, but the EF also exerts some sway over the direction of actin flow. Actin polymerization is biased toward the cathode which influences the direction of cell polarization and migration. Guidance of actin by an EF is always stronger after field reversal.

The current technological capabilities in the fields of lithography, microfluidics, materials, microscopy, and spectroscopy, as well as other analytical techniques, foster aspirations of the widespread availability of all-in-one adaptive cellular environments for cell studies, as well as for diagnostics and therapeutics. The ability to program or reprogram a nanotopographic pattern *in situ* means that multiple experimental conditions can be tested on the same cells. The incorporation of other cues would allow one to selectively control the complexity of the extracellular environment or finely tune the cellular motion and esotaxis. Live detection of protein organization and distribution or cytokine and protease release would provide real-time feedback of the effects of changes to the extracellular conditions on cell behavior, which could inform additional changes to substrate and environment.

The mechanism of actin sensing must still be elucidated. The nanotopographic cue that the cell senses depends on how much of the topography the cell contacts. Therefore, it is likely that the sensory capabilities of actin depend on activities and properties of the membrane. Manipulation of membrane composition might reveal the limits of esotaxis. Limiting membrane deformation and reducing cortical plasticity could reduce sensitivity to physical guidance cues, including topography and substrate stiffness. Increasing deformability and plasticity would increase detection of nanotopographic features. For instance, it would be interesting to determine the behavior of M4 cells on nanosawteeth, which were already shown to conform well to the topographic cues, if the flexibility of the membrane and the actin cortex were increased.

More work must be performed to further clarify the interactions among the cytoskeleton, FAs, ABPs, and signaling molecules in response to nanotopography. Investigation of the cell response to other individual nanotopographic cues can be beneficial to reveal other properties of

esotaxis. However, examining cells in extracellular environments with more complexity (e.g., more stimuli, multiple or irregular nanotopographic patterns, additional dimensionality) would also be beneficial.

Bibliography

(1) Gillies, T. E.; Cabernard, C. Cell division orientation in animals. *Curr Biol* **2011**, *21* (15), R599-609.

(2) Shafqat-Abbasi, H.; Kowalewski, J. M.; Kiss, A.; Gong, X.; Hernandez-Varas, P.; Berge, U.; Jafari-Mamaghani, M.; Lock, J. G.; Stromblad, S. An analysis toolbox to explore mesenchymal migration heterogeneity reveals adaptive switching between distinct modes. *Elife* **2016**, *5*, e11384.

(3) Theveneau, E.; Mayor, R. Neural crest delamination and migration: From epithelium-to-mesenchyme transition to collective cell migration. *Dev Biol* **2012**, *366* (1), 34-54.

(4) Lim, L.; Pakan, J. M. P.; Selten, M. M.; Marques-Smith, A.; Llorca, A.; Bae, S. E.; Rochefort, N. L.; Marin, O. Optimization of interneuron function by direct coupling of cell migration and axonal targeting. *Nat Neurosci* **2018**, *21* (7), 920-931.

(5) Silva, C. G.; Peyre, E.; Nguyen, L. Cell migration promotes dynamic cellular interactions to control cerebral cortex morphogenesis. *Nat Rev Neurosci* **2019**, *20* (6), 318-329.

(6) Enoch, S.; Leaper, D. J. Basic science of wound healing. *Surgery (Oxford)* **2008**, *26* (2), 31-37.

(7) Trepat, X.; Chen, Z.; Jacobson, K. Cell migration. *Compr Physiol* **2012**, *2* (4), 2369-2392.

(8) Liu, J.; Zhang, X.; Cheng, Y.; Cao, X. Dendritic cell migration in inflammation and immunity. *Cell Mol Immunol* **2021**, *18* (11), 2461-2471.

(9) Theveneau, E.; Mayor, R. Collective cell migration of epithelial and mesenchymal cells. *Cell Mol Life Sci* **2013**, *70* (19), 3481-3492.

(10) Sahlgren, C.; Gustaffson, M. V.; Jin, S.; Poellinger, L.; Lendahl, U. Notch signaling mediates hypoxia-induced tumor cell migration and invasion. *Proc Natl Acad Sci U S A* **2008**, *105* (17), 6392-6397.

(11) Bodor, D. L.; Ponisch, W.; Endres, R. G.; Paluch, E. K. Of cell shapes and motion: The physical basis of animal cell migration. *Dev Cell* **2020**, *52* (5), 550-562.

(12) Weiss, P.; Garber, B. Shape and movement of mesenchyme cells as functions of the physical structure of the medium. Contributions to a quantitative morphology. *Proc Natl Acad Sci U S A* **1952**, *38*, 264-280.

(13) SenGupta, S.; Parent, C. A.; Bear, J. E. The principles of directed cell migration. *Nat Rev Mol Cell Biol* **2021**, *22* (8), 529-547.

(14) Yamada, K. M.; Sixt, M. Mechanisms of 3D cell migration. *Nat Rev Mol Cell Biol* **2019**, *20* (12), 738-752.

(15) Ridley, A. J.; Schwartz, M. A.; Burridge, K.; Firtel, R. A.; Ginsberg, M. H.; Borisy, G.; Parsons, J. T.; Horwtiz, A. R. Cell migration: Integrating signals from front to back. *Science* **2003**, *302*, 1704-1709.

(16) van Helvert, S.; Storm, C.; Friedl, P. Mechanoreciprocity in cell migration. *Nat Cell Biol* **2018**, *20* (1), 8-20.

(17) Horwitz, A. R.; Parsons, J. T. Cell migration--Movin' on. *Science* **1999**, *286* (5442), 1102-1103.

(18) Seo, J.; Kim, K. S.; Park, J. W.; Cho, J. Y.; Chang, H.; Fukuda, J.; Hong, K. Y.; Chun, Y. S. Metastasis-on-a-chip reveals adipocyte-derived lipids trigger cancer cell migration via HIF-1alpha activation in cancer cells. *Biomaterials* **2021**, *269*, 120622.

(19) Roycroft, A.; Mayor, R. Molecular basis of contact inhibition of locomotion. *Cell Mol Life Sci* **2016**, *73* (6), 1119-1130.

(20) Bagorda, A.; Parent, C. A. Eukaryotic chemotaxis at a glance. *J Cell Sci* **2008**, *121* (Pt 16), 2621-2624.

(21) Espina, J. A.; Marchant, C. L.; Barriga, E. H. Durotaxis: the mechanical control of directed cell migration. *FEBS J* **2022**, *289* (10), 2736-2754.

(22) Yang, Y.; Wang, K.; Gu, X.; Leong, K. W. Biophysical regulation of cell behavior-cross talk between substrate stiffness and nanotopography. *Engineering (Beijing)* **2017**, *3* (1), 36-54.

(23) Carter, S. B. Haptotaxis and the mechanism of cell motility. *Nature* **1967**, *213*, 256-260.

(24) Tai, G.; Reid, B.; Cao, L.; Zhao, M. Electrotaxis and Wound Healing: Experimental Methods to Study Electric Fields as a Directional Signal for Cell Migration. In *Chemotaxis: Methods and Protocols*, Jin, T., Hereld, D. Eds.; Springer Protocols: Methods in Molecular Biology, Humana Press, 2009; pp 77-97.

(25) Park, J.; Kim, D. H.; Levchenko, A. Topotaxis: A new mechanism of directed cell migration in topographic ECM gradients. *Biophys J* **2018**, *114* (6), 1257-1263.

(26) Guo, Z.; Pan, F.; Peng, L.; Tian, S.; Jiao, J.; Liao, L.; Lu, C.; Zhai, G.; Wu, Z.; Dong, H.; Xu, X.; Wu, J.; Chen, P.; Bai, X.; Lin, D.; Xu, L.; Li, E.; Zhang, K. Systematic proteome and lysine succinylome analysis reveals the enhanced cell migration by hyposuccinylation in esophageal squamous cell cancer. *Mol Cell Proteomics* **2021**, 100053.

(27) Pollard, T. D. Actin and Actin-Binding Proteins. *Cold Spring Harb Perspect Biol* **2016**, *8* (8), a018226.

(28) Pagliuso, A.; Cossart, P.; Stavru, F. The ever-growing complexity of the mitochondrial fission machinery. *Cell Mol Life Sci* **2018**, *75* (3), 355-374.

(29) Gurel, P. S.; Hatch, A. L.; Higgs, H. N. Connecting the cytoskeleton to the endoplasmic reticulum and Golgi. *Curr Biol* **2014**, *24* (14), R660-R672.

(30) Dominguez, R.; Holmes, K. C. Actin structure and function. *Annu Rev Biophys* **2011**, *40*, 169-186.

(31) Kudryashov, D. S.; Reisler, E. ATP and ADP actin states. *Biopolymers* **2013**, *99* (4), 245-256.

(32) Pollard, T. D.; Borisy, G. G. Cellular motility driven by assembly and disassembly of actin filaments. *Cell* **2003**, *112*, 453-465.

(33) Schaks, M.; Giannone, G.; Rottner, K. Actin dynamics in cell migration. *Essays Biochem* **2019**, *63* (5), 483-495.

(34) Ammer, A. G.; Weed, S. A. Cortactin branches out: roles in regulating protrusive actin dynamics. *Cell Motil Cytoskeleton* **2008**, *65* (9), 687-707.

(35) Paavilainen, V. O.; Bertling, E.; Falck, S.; Lappalainen, P. Regulation of cytoskeletal dynamics by actin-monomer-binding proteins. *Trends Cell Biol* **2004**, *14* (7), 386-394.

(36) Devreotes, P.; Horwitz, A. R. Signaling networks that regulate cell migration. *Cold Spring Harb Perspect Biol* **2015**, *7* (8), a005959.

(37) Helfer, E.; Nevalainen, E. M.; Naumanen, P.; Romero, S.; Didry, D.; Pantaloni, D.; Lappalainen, P.; Carlier, M. F. Mammalian twinfilin sequesters ADP-G-actin and caps filament barbed ends: implications in motility. *EMBO J* **2006**, *25* (6), 1184-1195.

(38) Moulding, D. A.; Record, J.; Malinova, D.; Thrasher, A. J. Actin cytoskeletal defects in immunodeficiency. *Immunol Rev* **2013**, *256*, 282-299.

(39) Hall, A. Rho GTPases and the actin cytoskeleton. *Science* **1998**, *279*, 509-514.

(40) Mackay, D. J.; Hall, A. Rho GTPases. *J Biol Chem* **1998**, *273* (33), 20685-20688.

(41) Hodge, R. G.; Ridley, A. J. Regulating Rho GTPases and their regulators. *Nat Rev Mol Cell Biol* **2016**, *17* (8), 496-510.

(42) Robert-Paganin, J.; Pylypenko, O.; Kikuti, C.; Sweeney, H. L.; Houdusse, A. Force generation by myosin motors: A structural perspective. *Chem Rev* **2020**, *120* (1), 5-35.

(43) Houdusse, A.; Sweeney, H. L. How myosin generates force on actin filaments. *Trends Biochem Sci* **2016**, *41* (12), 989-997.

(44) Wehrle-Haller, B. Structure and function of focal adhesions. *Curr Opin Cell Biol* **2012**, *24* (1), 116-124.

(45) Wozniak, M. A.; Modzelewska, K.; Kwong, L.; Keely, P. J. Focal adhesion regulation of cell behavior. *Biochim Biophys Acta* **2004**, *1692* (2-3), 103-119.

(46) Chrzanowska-Wodnicka, M.; Burridge, K. Rho-stimulated contractility drives the formation of stress fibers and focal adhesions. *J Cell Biol* **1996**, *133* (6), 1403-1415.

(47) Burridge, K.; Guilluy, C. Focal adhesions, stress fibers and mechanical tension. *Exp Cell Res* **2016**, *343* (1), 14-20.

(48) Barczyk, M.; Carracedo, S.; Gullberg, D. Integrins. *Cell Tissue Res* **2010**, *339* (1), 269-280.

(49) Kanchanawong, P.; Shtengel, G.; Pasapera, A. M.; Ramko, E. B.; Davidson, M. W.; Hess, H. F.; Waterman, C. M. Nanoscale architecture of integrin-based cell adhesions. *Nature* **2010**, *468* (7323), 580-584.

(50) Burridge, K.; Wittchen, E. S. The tension mounts: stress fibers as force-generating mechanotransducers. *J Cell Biol* **2013**, *200* (1), 9-19.

(51) Klapholz, B.; Brown, N. H. Talin - the master of integrin adhesions. *J Cell Sci* **2017**, *130* (15), 2435-2446.

(52) Hansen, M. D.; Kwiatkowski, A. V. Control of actin dynamics by allosteric regulation of actin binding proteins. *Int Rev Cell Mol Biol* **2013**, *303*, 1-25.

(53) Ziegler, W. H.; Liddington, R. C.; Critchley, D. R. The structure and regulation of vinculin. *Trends Cell Biol* **2006**, *16* (9), 453-460.

(54) Ezratty, E. J.; Bertaux, C.; Marcantonio, E. E.; Gundersen, G. G. Clathrin mediates integrin endocytosis for focal adhesion disassembly in migrating cells. *J Cell Biol* **2009**, *187* (5), 733-747.

(55) Tojkander, S.; Gateva, G.; Lappalainen, P. Actin stress fibers--assembly, dynamics and biological roles. *J Cell Sci* **2012**, *125* (Pt 8), 1855-1864.

(56) Livne, A.; Geiger, B. The inner workings of stress fibers - from contractile machinery to focal adhesions and back. *J Cell Sci* **2016**, *129* (7), 1293-1304.

(57) Goicoechea, S. M.; Arneman, D.; Otey, C. A. The role of palladin in actin organization and cell motility. *Eur J Cell Biol* **2008**, *87* (8-9), 517-525.

(58) Parast, M. M.; Otey, C. A. Characterization of palladin, a novel protein localized to stress fibers and cell adhesions. *J Cell Biol* **2000**, *150* (3), 643-655.

(59) Wade, R. H. On and around microtubules: An overview. *Mol Biotechnol* **2009**, *43* (2), 177-191.

(60) Valiron, O.; Caudron, N.; Job, D. Microtubule dynamics. *Cell Mol Life Sci* **2001**, *58*, 2069-2084.

(61) Olmsted, J. B.; Borisy, G. G. Microtubules. *Annu Rev Biochem* **1973**, *42* (1), 507-540.

(62) Luo, T.; Mohan, K.; Iglesias, P. A.; Robinson, D. N. Molecular mechanisms of cellular mechanosensing. *Nat Mater* **2013**, *12* (11), 1064-1071.

(63) Balaban, N. Q.; Schwarz, U. S.; Riveline, D.; Goichberg, P.; Tzur, G.; Sabanay, I.; Mahalu, D.; Safran, S.; Bershadsky, A.; Addadi, L.; Geiger, B. Force and focal adhesion assembly: A close relationship studied using elastic micropatterned substrates. *Nat Cell Biol* **2001**, *3*, 466-472.

(64) Tadijan, A.; Samarzija, I.; Humphries, J. D.; Humphries, M. J.; Ambriovic-Ristov, A. KANK family proteins in cancer. *Int J Biochem Cell Biol* **2021**, *131*, 105903.

(65) Edwards, D. C.; Sanders, L. C.; Bokoch, G. M.; Gill, G. N. Activation of LIM kinase by Pak1 couples Rac/Cdc42 GTPase signalling to actin cytoskeletal dynamics. *Nat Cell Biol* **1999**, *1*, 253-259.

(66) Chin, Y. R.; Toker, A. The actin-bundling protein palladin is an Akt1-specific substrate that regulates breast cancer cell migration. *Mol Cell* **2010**, *38* (3), 333-344.

(67) Cox, T. R.; Erler, J. T. Remodeling and homeostasis of the extracellular matrix: Implications for fibrotic diseases and cancer. *Dis Model Mech* **2011**, *4* (2), 165-178.

(68) Jenkins, T. L.; Little, D. Synthetic scaffolds for musculoskeletal tissue engineering: Cellular responses to fiber parameters. *NPJ Regen Med* **2019**, *4*, 15.

(69) Kalluri, R. Basement membranes: Structure, assembly and role in tumour angiogenesis. *Nat Rev Cancer* **2003**, *3* (6), 422-433.

(70) Wolf, K.; Alexander, S.; Schacht, V.; Coussens, L. M.; von Andrian, U. H.; van Rheenen, J.; Deryugina, E.; Friedl, P. Collagen-based cell migration models in vitro and in vivo. *Semin Cell Dev Biol* **2009**, *20* (8), 931-941.

(71) Buchheit, C. L.; Weigel, K. J.; Schafer, Z. T. Cancer cell survival during detachment from the ECM: Multiple barriers to tumour progression. *Nat Rev Cancer* **2014**, *14* (9), 632-641.

(72) Keselowsky, B. G.; Collard, D. M.; García, A. J. Integrin binding specificity regulates biomaterial surface chemistry effects on cell differentiation. *Proc Natl Acad Sci U S A* **2005**, *102* (17), 5953-5957.

(73) LeBaron, R. G.; Athanasiou, K. A. Extracellular matrix cell adhesion peptides: Functional applications in orthopedic materials. *Tissue Eng* **2000**, *6* (2), 85-103.

(74) Li, Y.; Burridge, K. Cell-cycle-dependent regulation of cell adhesions: Adhering to the schedule. *Bioessays* **2019**, *41* (1), e1800165.

(75) Taufalele, P. V.; VanderBurgh, J. A.; Munoz, A.; Zanotelli, M. R.; Reinhart-King, C. A. Fiber alignment drives changes in architectural and mechanical features in collagen matrices. *PLoS One* **2019**, *14* (5), e0216537.

(76) Pankov, R.; Yamada, K. M. Fibronectin at a glance. *J Cell Sci* **2002**, *115* (Pt 20), 3861-3863.

(77) Rocha-Mendoza, I.; Yankelevich, D. R.; Wang, M.; Reiser, K. M.; Frank, C. W.; Knoesen, A. Sum frequency vibrational spectroscopy: The molecular origins of the optical second-order nonlinearity of collagen. *Biophys J* **2007**, *93* (12), 4433-4444.

(78) Shoulders, M. D.; Raines, R. T. Collagen structure and stability. *Annu Rev Biochem* **2009**, *78* (1), 929-958.

(79) Boryskina, O. P.; Bolbukh, T. V.; Semenov, M. A.; Gasan, A. I.; Maleev, V. Y. Energies of peptide–peptide and peptide–water hydrogen bonds in collagen: Evidences from infrared spectroscopy, quartz piezogravimetry and differential scanning calorimetry. *J Mol Struct* **2007**, *827* (1-3), 1-10.

(80) Falk, M.; Hartman, J., K. A.; Lord, R. C. Hydration of deoxyribonucleic acid: I. A gravimetric study. *J Am Chem Soc* **1962**, *84* (20), 3843-3846.

(81) Ricard-Blum, S. The collagen family. *Cold Spring Harb Perspect Biol* **2011**, *3* (1), a004978.

(82) Khoshnoodi, J.; Pedchenko, V.; Hudson, B. G. Mammalian collagen IV. *Microsc Res Tech* **2008**, *71* (5), 357-370.

(83) Bozec, L.; van der Heijden, G.; Horton, M. Collagen fibrils: Nanoscale ropes. *Biophys J* **2007**, *92* (1), 70-75.

(84) Hudson, B. G.; Reeders, S. T.; Tryggvason, K. Type IV collagen: Structure, gene organization, and role in human diseases. Molecular basis of Goodpasture and Alport syndromes and diffuse leiomyomatosis. *J Biol Chem* **1993**, *268* (35), 26033-26036.

(85) Roy, A.; Gauld, J. W. Molecular dynamics investigation on the effects of protonation and lysyl hydroxylation on sulfilimine cross-links in collagen IV. *ACS Omega* **2022**, *7* (44), 39680-39689.

(86) Trueb, B.; Odermatt, B. F. Loss of type VI collagen in experimental and most spontaneous human fibrosarcomas. *Int J Cancer* **2000**, *86*, 331-336.

(87) Wolf, J.; Carsons, S. E. Distribution of type VI collagen expression in synovial tissue and cultured synoviocytes: Relation to fibronectin expression. *Ann Rheum Dis* **1991**, *50*, 493-496.

(88) Mantovani, A.; Schioppa, T.; Porta, C.; Allavena, P.; Sica, A. Role of tumor-associated macrophages in tumor progression and invasion. *Cancer Metastasis Rev* **2006**, *25* (3), 315-322.

(89) Hoffmann, E. J.; Ponik, S. M. Biomechanical contributions to macrophage activation in the tumor microenvironment. *Front Oncol* **2020**, *10*, 787.

(90) Schlesinger, E.; Ciaccio, N.; Desai, T. A. Polycaprolactone thin-film drug delivery systems: Empirical and predictive models for device design. *Mater Sci Eng C Mater Biol Appl* **2015**, *57*, 232-239.

(91) Yeh, C.-C.; Chen, C.-N.; Li, Y.-T.; Chang, C.-W.; Cheng, M.-Y.; Chang, H.-I. The effect of polymer molecular weight and UV radiation on physical properties and bioactivities of PCL films. *Cell Polym* **2011**, *30* (5), 261-276.

(92) Arbeiter, D.; Eickner, T.; Oschatz, S.; Reske, T.; Specht, O.; Teske, M.; Senz, V.; Schmitz, K.-P.; Grabow, N. Physico chemical and phase separation characterization of high molecular PLLA blended with low molecular PCL obtained from solvent cast processes. *Mater Res Express* **2020**, *7* (9), 095302.

(93) Shao, Y.; Fu, J. Integrated micro/nanoengineered functional biomaterials for cell mechanics and mechanobiology: A materials perspective. *Adv Mater* **2014**, *26* (10), 1494-1533.

(94) Tsai, Y. T.; Wu, C. Y.; Guan, Z. Y.; Sun, H. Y.; Cheng, N. C.; Yeh, S. Y.; Chen, H. Y. Topologically controlled cell differentiation based on vapor-deposited polymer coatings. *Langmuir* **2017**, *33* (36), 8943-8949.

(95) Schnell, E.; Klinkhammer, K.; Balzer, S.; Brook, G.; Klee, D.; Dalton, P.; Mey, J. Guidance of glial cell migration and axonal growth on electrospun nanofibers of poly-epsilon-caprolactone and a collagen/poly-epsilon-caprolactone blend. *Biomaterials* **2007**, *28* (19), 3012-3025.

(96) He, W.; Ma, Z.; Yong, T.; Teo, W. E.; Ramakrishna, S. Fabrication of collagen-coated biodegradable polymer nanofiber mesh and its potential for endothelial cells growth. *Biomaterials* **2005**, *26* (36), 7606-7615.

(97) Linnola, R. J.; Sund, M.; Ylonen, R.; Cand, M.; Pihlajaniemi, T. Adhesion of soluble fibronectin, laminin, and collagen type IV to intraocular lens materials. *J Cataract Refractive Surg* **1999**, *25*, 1486-1491.

(98) Dalby, M. J.; Riehle, M. O.; Sutherland, D. S.; Agheli, H.; Curtis, A. S. G. Morphological and microarray analysis of human fibroblasts cultured on nanocolumns produced by colloidal lithography. *Eur Cells Mater* **2005**, *9*, 1-8.

(99) Champion, J. A.; Mitragotri, S. Role of target geometry in phagocytosis. *Proc Natl Acad Sci U S A* **2006**, *103* (13), 4930-4934.

(100) Champion, J. A.; Mitragotri, S. Shape induced inhibition of phagocytosis of polymer particles. *Pharm Res* **2009**, *26* (1), 244-249.

(101) Plotnikov, S. V.; Pasapera, A. M.; Sabass, B.; Waterman, C. M. Force fluctuations within focal adhesions mediate ECM-rigidity sensing to guide directed cell migration. *Cell* **2012**, *151* (7), 1513-1527.

(102) Gulati, K.; Li, T.; Ivanovski, S. Consume or conserve: Microroughness of titanium implants toward fabrication of dual micro-nanotopography. *ACS Biomater Sci Eng* **2018**, *4* (9), 3125-3131.

(103) Ricoult, S. G.; Kennedy, T. E.; Juncker, D. Substrate-bound protein gradients to study haptotaxis. *Front Bioeng Biotechnol* **2015**, *3*, 40.

(104) Garmire, E. Nonlinear optics in daily life. *Opt Express* **2013**, *21* (25), 30532-30544.

(105) Zhang, Y.-L.; Chen, Q.-D.; Xia, H.; Sun, H.-B. Designable 3D nanofabrication by femtosecond laser direct writing. *Nano Today* **2010**, *5* (5), 435-448.

(106) LaFratta, C. N.; Fourkas, J. T.; Baldacchini, T.; Farrer, R. A. Multiphoton fabrication. *Angew Chem Int Ed Engl* **2007**, *46* (33), 6238-6258.

(107) Li, L.; Fourkas, J. T. Multiphoton polymerization. *Mater Today* **2007**, *10* (6), 30-37.

(108) Spangenberg, A.; Hobeika, N.; Stehlin, F.; Pierre Malval, J.; Wieder, F.; Prabhakaran, P.; Baldeck, P.; Sopper, O. Recent Advances in Two-Photon Stereolithography. In *Updates in Advanced Lithography*, 2013.

(109) Iosin, M.; Scheul, T.; Nizak, C.; Stephan, O.; Astilean, S.; Baldeck, P. Laser microstructuration of three-dimensional enzyme reactors in microfluidic channels. *Microfluid Nanofluid* **2010**, *10* (3), 685-690.

(110) Vurth, L.; Baldeck, P.; Stéphan, O.; Vitrant, G. Two-photon induced fabrication of gold microstructures in polystyrene sulfonate thin films using a ruthenium(II) dye as photoinitiator. *Appl Phys Lett* **2008**, *92* (17).

(111) Baldacchini, T.; Pons, A.-C.; Pons, J.; LaFratta, C. N.; Fourkas, J. T.; Sun, Y.; Naughton, M. J. Multiphoton laser direct writing of two-dimensional silver structures. *Opt Express* **2005**, *13* (4), 1275-1280.

(112) LaFratta, C. N.; Li, L.; Fourkas, J. T. Soft-lithographic replication of 3D microstructures with closed loops. *Proc Natl Acad Sci U S A* **2006**, *103* (23), 8589-8594.

(113) Xing, J.-F.; Dong, X.-Z.; Chen, W.-Q.; Duan, X.-M.; Takeyasu, N.; Tanaka, T.; Kawata, S. Improving spatial resolution of two-photon microfabrication by using photoinitiator with high initiating efficiency. *Appl Phys Lett* **2007**, *90* (13), 131106.

(114) Li, L.; Gattass, R. R.; Gershgoren, E.; Hwang, H.; Fourkas, J. T. Achieving lambda/20 resolution by one-color initiation and deactivation of polymerization. *Science* **2009**, *324* (5929), 910-913.

(115) Papagiakoumou, E.; de Sars, V.; Oron, D.; Emiliani, V. Patterned two-photon illumination by spatiotemporal shaping of ultrashort pulses. *Opt Express* **2008**, *16* (26), 22039-22047.

(116) Somers, P.; Liang, Z.; Johnson, J. E.; Boudouris, B. W.; Pan, L.; Xu, X. Rapid, continuous projection multi-photon 3D printing enabled by spatiotemporal focusing of femtosecond pulses. *Light Sci Appl* **2021**, *10* (1), 199.

(117) Li, Y.-C.; Cheng, L.-C.; Chang, C.-Y.; Lien, C.-H.; Campagnola, P. J.; Chen, S.-J. Fast multiphoton fabrication of freeform polymer microstructures by spatiotemporal focusing and patterned excitation. *Opt Express* **2012**, *20* (17), 19030-19038.

(118) Losic, D.; Mitchell, J. G.; Lal, R.; Voelcker, N. H. Rapid fabrication of micro- and nanoscale patterns by replica molding from diatom biosilica. *Adv Funct Mater* **2007**, *17* (14), 2439-2446.

(119) Kang, H.; Lee, J.; Park, J.; Lee, H. H. An improved method of preparing composite poly(dimethylsiloxane) moulds. *Nanotechnology* **2006**, *17* (1), 197-200.

(120) Mempel, T. R.; Henrickson, S. E.; von Andrian, U. H. T-cell priming by dendritic cells in lymph nodes occurs in three distinct phases. *Nature* **2004**, *427*, 154-159.

(121) Watt, F. M.; Huck, W. T. Role of the extracellular matrix in regulating stem cell fate. *Nat Rev Mol Cell Biol* **2013**, *14* (8), 467-473.

(122) Rozario, T.; DeSimone, D. W. The extracellular matrix in development and morphogenesis: a dynamic view. *Dev Biol* **2010**, *341* (1), 126-140.

(123) Lammermann, T.; Afonso, P. V.; Angermann, B. R.; Wang, J. M.; Kastenmuller, W.; Parent, C. A.; Germain, R. N. Neutrophil swarms require LTB4 and integrins at sites of cell death in vivo. *Nature* **2013**, *498* (7454), 371-375.

(124) Maquart, F. X.; Monboisse, J. C. Extracellular matrix and wound healing. *Pathol Biol (Paris)* **2014**, *62* (2), 91-95.

(125) Sorokin, L. The impact of the extracellular matrix on inflammation. *Nat Rev Immunol* **2010**, *10* (10), 712-723.

(126) Provenzano, P. P.; Eliceiri, K. W.; Campbell, J. M.; Inman, D. R.; White, J. G.; Keely, P. J. Collagen reorganization at the tumor-stromal interface facilitates local invasion. *BMC Med* **2006**, *4* (1), 38.

(127) Oudin, M. J.; Jonas, O.; Kosciuk, T.; Broye, L. C.; Guido, B. C.; Wyckoff, J.; Riquelme, D.; Lamar, J. M.; Asokan, S. B.; Whittaker, C.; Ma, D.; Langer, R.; Cima, M. J.; Wisinski, K. B.;

Hynes, R. O.; Lauffenburger, D. A.; Keely, P. J.; Bear, J. E.; Gertler, F. B. Tumor cell-driven extracellular matrix remodeling drives haptotaxis during metastatic progression. *Cancer Discov* **2016**, *6* (5), 516-531.

(128) Kilian, K. A.; Bugarija, B.; Lahn, B. T.; Mrksich, M. Geometric cues for directing the differentiation of mesenchymal stem cells. *Proc Natl Acad Sci U S A* **2010**, *107* (11), 4872-4877.

(129) Elliott, H.; Fischer, R. S.; Myers, K. A.; Desai, R. A.; Gao, L.; Chen, C. S.; Adelstein, R. S.; Waterman, C. M.; Danuser, G. Myosin II controls cellular branching morphogenesis and migration in three dimensions by minimizing cell-surface curvature. *Nat Cell Biol* **2015**, *17* (2), 137-147.

(130) Driscoll, M. K.; Sun, X.; Guven, C.; Fourkas, J. T.; Losert, W. Cellular contact guidance through dynamic sensing of nanotopography. *ACS Nano* **2014**, *8* (4), 3546-3555.

(131) Sun, X.; Driscoll, M. K.; Guven, C.; Das, S.; Parent, C. A.; Fourkas, J. T.; Losert, W. Asymmetric nanotopography biases cytoskeletal dynamics and promotes unidirectional cell guidance. *Proc Natl Acad Sci U S A* **2015**, *112* (41), 12557-12562.

(132) Ghassemi, S.; Meacci, G.; Liu, S.; Gondarenko, A. A.; Mathur, A.; Roca-Cusachs, P.; Sheetz, M. P.; Hone, J. Cells test substrate rigidity by local contractions on submicrometer pillars. *Proc Natl Acad Sci U S A* **2012**, *109* (14), 5328-5333.

(133) Dalby, M. J.; Gadegaard, N.; Tare, R.; Andar, A.; Riehle, M. O.; Herzyk, P.; Wilkinson, C. D.; Oreffo, R. O. The control of human mesenchymal cell differentiation using nanoscale symmetry and disorder. *Nat Mater* **2007**, *6* (12), 997-1003.

(134) Kim, D. H.; Lipke, E. A.; Kim, P.; Cheong, R.; Thompson, S.; Delannoy, M.; Suh, K. Y.; Tung, L.; Levchenko, A. Nanoscale cues regulate the structure and function of macroscopic cardiac tissue constructs. *Proc Natl Acad Sci U S A* **2010**, *107* (2), 565-570.

(135) Williams, C. G.; Malik, A. N.; Kim, T. K.; Manson, P. N.; Elisseeff, J. H. Variable cytocompatibility of six cell lines with photoinitiators used for polymerizing hydrogels and cell encapsulation. *Biomaterials* **2005**, *26* (11), 1211-1218.

(136) Sabnis, A.; Rahimi, M.; Chapman, C.; Nguyen, K. T. Cytocompatibility studies of an in situ photopolymerized thermoresponsive hydrogel nanoparticle system using human aortic smooth muscle cells. *J Biomed Mater Res A* **2009**, *91* (1), 52-59.

(137) Kim, D.-H.; Kim, P.; Song, I.; Cha, J. M.; Lee, S. H.; Kim, B.; Suh, K. Y. Guided three-dimensional growth of functional cardiomyocytes on polyethylene glycol nanostructures. *Langmuir* **2006**, *22* (12), 5419-5426.

(138) Peleg, B.; Disanza, A.; Scita, G.; Gov, N. Propagating cell-membrane waves driven by curved activators of actin polymerization. *PLoS One* **2011**, *6* (4), e18635.

(139) Gadegaard, N.; Mosler, S.; Larsen, N. B. Biomimetic polymer nanostructures by injection molding. *Macromol Mater Eng* **2003**, *288* (1), 76-83.

(140) Fourkas, J. T. Fundamentals of two-photon fabrication. In *Three-Dimensional Microfabrication Using Two-Photon Polymerization*, Baldacchini, T. Ed.; William Andrew Publishing, 2016; pp 45-61.

(141) Schmid, H.; Michel, B. Siloxane polymers for high-resolution, high-accuracy soft lithography. *Macromolecules* **2000**, *33* (8), 3042-3049.

(142) Sun, X.; Hourwitz, M. J.; Baker, E. M.; Schmidt, B. U. S.; Losert, W.; Fourkas, J. T. Replication of biocompatible, nanotopographic surfaces. *Sci Rep* **2018**, *8* (1), 564.

(143) Li, L.; Driscoll, M.; Kumi, G.; Hernandez, R.; Gaskell, K. J.; Losert, W.; Fourkas, J. T. Binary and gray-scale patterning of chemical functionality on polymer films. *J Am Chem Soc* **2008**, *130* (41), 13512-13513.

(144) Pitts, J. D.; Howell, A. R.; Taboada, R.; Banerjee, I.; Wang, J.; Goodman, S. L.; Campagnola, P. J. New Photoactivators for Multiphoton Excited Three-dimensional Submicron Cross-linking of Proteins: Bovine Serum Albumin and Type 1 Collagen. *Photochem Photobiol* **2002**, *76* (2), 135-144.

(145) Basu, S.; Rodionov, V.; Terasaki, M.; Campagnola, P. J. Multiphoton-excited microfabrication in live cells via Rose Bengal cross-linking of cytoplasmic proteins. *Opt Lett* **2005**, *30* (2), 159-161.

(146) Bayindir, Z.; Sun, Y.; Naughton, M. J.; LaFratta, C. N.; Baldacchini, T.; Fourkas, J. T.; Stewart, J.; Saleh, B. E. A.; Teich, M. C. Polymer microcantilevers fabricated via multiphoton absorption polymerization. *Appl Phys Lett* **2005**, *86*, 064105.

(147) Yip, A. K.; Iwasaki, K.; Ursekar, C.; Machiyama, H.; Saxena, M.; Chen, H.; Harada, I.; Chiam, K. H.; Sawada, Y. Cellular response to substrate rigidity is governed by either stress or strain. *Biophys J* **2013**, *104* (1), 19-29.

(148) Wenger, M. P.; Bozec, L.; Horton, M. A.; Mesquida, P. Mechanical properties of collagen fibrils. *Biophys J* **2007**, *93* (4), 1255-1263.

(149) Hua, F.; Sun, Y.; Gaur, A.; Meitl, M. A.; Bilhaut, L.; Rotkina, L.; Wang, J.; Geil, P.; Shim, M.; Rogers, J. A.; Shim, A. Polymer imprint lithography with molecular-scale resolution. *Nano Lett* **2004**, *4* (12), 2467-2471.

(150) Elhadj, S.; Rioux, R. M.; Dickey, M. D.; DeYoreo, J. J.; Whitesides, G. M. Subnanometer replica molding of molecular steps on ionic crystals. *Nano Lett* **2010**, *10* (10), 4140-4145.

(151) Berg, J. Wettability. Marcel Dekker: 1993.

(152) Lee, J. N.; Park, C.; Whitesides, G. M. Solvent compatibility of poly(dimethylsiloxane)-based microfluidic devices. *Anal Chem* **2003**, *75* (23), 6544-6554.

(153) Chaudhury, M. K.; Whitesides, G. M. Direct measurement of interfacial interactions between semispherical lenses and flat sheets of poly(dimethylsiloxane) and their chemical derivatives. *Langmuir* **1991**, *7* (5), 1013-1025.

(154) Gates, B. D.; Whitesides, G. M. Replication of vertical features smaller than 2 nm by soft lithography. *J Am Chem Soc* **2003**, *125* (49), 14986-14987.

(155) Azatov, M.; Sun, X.; Suberi, A.; Fourkas, J. T.; Upadhyaya, A. Topography on a subcellular scale modulates cellular adhesions and actin stress fiber dynamics in tumor associated fibroblasts. *Phys Biol* **2017**, *14* (6), 065003.

(156) Ketchum, C. M.; Sun, X.; Suberi, A.; Fourkas, J. T.; Song, W.; Upadhyaya, A. Subcellular topography modulates actin dynamics and signaling in B-cells. *Mol Biol Cell* **2018**, *29* (13), 1732-1742.

(157) McCann, C. P.; Rericha, E. C.; Wang, C.; Losert, W.; Parent, C. A. Dictyostelium cells migrate similarly on surfaces of varying chemical composition. *PLoS One* **2014**, *9* (2), e87981.

(158) Qin, S. The applications of multiphoton absorption polymerization. University of Maryland-College Park, 2013.

(159) Schneider, C. A.; Rasband, W. S.; Eliceiri, K. W. NIH Image to ImageJ: 25 years of image analysis. *Nat Methods* **2012**, *9* (7), 671-675.

(160) Amini-Nik, S.; Cambridge, E.; Yu, W.; Guo, A.; Whetstone, H.; Nadesan, P.; Poon, R.; Hinz, B.; Alman, B. A. beta-Catenin-regulated myeloid cell adhesion and migration determine wound healing. *J Clin Invest* **2014**, *124* (6), 2599-2610.

(161) Friedl, P.; Alexander, S. Cancer invasion and the microenvironment: Plasticity and reciprocity. *Cell* **2011**, *147* (5), 992-1009.

(162) Scarpa, E.; Mayor, R. Collective cell migration in development. *J Cell Biol* **2016**, *212* (2), 143-155.

(163) Petrie, R. J.; Doyle, A. D.; Yamada, K. M. Random versus directionally persistent cell migration. *Nat Rev Mol Cell Biol* **2009**, *10* (8), 538-549.

(164) Chen, S.; Li, N.; Hsu, S. F.; Zhang, J.; Lai, P. Y.; Chan, C. K.; Chen, W. Intrinsic fluctuations of cell migration under different cellular densities. *Soft Matter* **2014**, *10* (19), 3421-3425.

(165) Parent, C. A. Making all the right moves: Chemotaxis in neutrophils and Dictyostelium. *Curr Opin Cell Biol* **2004**, *16* (1), 4-13.

(166) Sunyer, R.; Conte, V.; Escribano, J.; Elosegui-Artola, A.; Labernadie, A.; Valon, L.; Navajas, D.; Garcia-Aznar, J. M.; Munoz, J. J.; Roca-Cusachs, P.; Trepat, X. Collective cell durotaxis emerges from long-range intercellular force transmission. *Science* **2016**, *353* (6304), 1157-1161.

(167) Shanley, L. J.; Walczysko, P.; Bain, M.; MacEwan, D. J.; Zhao, M. Influx of extracellular Ca2+ is necessary for electrotaxis in Dictyostelium. *J Cell Sci* **2006**, *119* (Pt 22), 4741-4748.

(168) Kim, D. H.; Provenzano, P. P.; Smith, C. L.; Levchenko, A. Matrix nanotopography as a regulator of cell function. *J Cell Biol* **2012**, *197* (3), 351-360.

(169) Nguyen, A. T.; Sathe, S. R.; Yim, E. K. From nano to micro: Topographical scale and its impact on cell adhesion, morphology and contact guidance. *J Phys Condens Matter* **2016**, *28* (18), 183001.

(170) Doyle, A. D.; Carvajal, N.; Jin, A.; Matsumoto, K.; Yamada, K. M. Local 3D matrix microenvironment regulates cell migration through spatiotemporal dynamics of contractility-dependent adhesions. *Nat Commun* **2015**, *6*, 8720.

(171) Provenzano, P. P.; Inman, D. R.; Eliceiri, K. W.; Trier, S. M.; Keely, P. J. Contact guidance mediated three-dimensional cell migration is regulated by Rho/ROCK-dependent matrix reorganization. *Biophys J* **2008**, *95* (11), 5374-5384.

(172) Alexander, S.; Koehl, G. E.; Hirschberg, M.; Geissler, E. K.; Friedl, P. Dynamic imaging of cancer growth and invasion: A modified skin-fold chamber model. *Histochem Cell Biol* **2008**, *130* (6), 1147-1154.

(173) Ray, A.; Slama, Z. M.; Morford, R. K.; Madden, S. A.; Provenzano, P. P. Enhanced directional migration of cancer stem cells in 3D aligned collagen matrices. *Biophys J* **2017**, *112* (5), 1023-1036.

(174) Wolf, K.; Te Lindert, M.; Krause, M.; Alexander, S.; Te Riet, J.; Willis, A. L.; Hoffman, R. M.; Figdor, C. G.; Weiss, S. J.; Friedl, P. Physical limits of cell migration: Control by ECM space and nuclear deformation and tuning by proteolysis and traction force. *J Cell Biol* **2013**, *201* (7), 1069-1084.

(175) Dvir, T.; Timko, B. P.; Kohane, D. S.; Langer, R. Nanotechnological strategies for engineering complex tissues. *Nat Nanotechnol* **2011**, *6* (1), 13-22.

(176) Potthoff, E.; Franco, D.; D'Alessandro, V.; Starck, C.; Falk, V.; Zambelli, T.; Vorholt, J. A.; Poulikakos, D.; Ferrari, A. Toward a rational design of surface textures promoting endothelialization. *Nano Lett* **2014**, *14* (2), 1069-1079.

(177) Ramirez-San Juan, G. R.; Oakes, P. W.; Gardel, M. L.; Forscher, P. Contact guidance requires spatial control of leading-edge protrusion. *Mol Biol Cell* **2017**, *28* (8), 1043-1053.

(178) Ray, A.; Lee, O.; Win, Z.; Edwards, R. M.; Alford, P. W.; Kim, D. H.; Provenzano, P. P. Anisotropic forces from spatially constrained focal adhesions mediate contact guidance directed cell migration. *Nat Commun* **2017**, *8*, 14923.

(179) Onesto, V.; Cancedda, L.; Coluccio, M. L.; Nanni, M.; Pesce, M.; Malara, N.; Cesarelli, M.; Di Fabrizio, E.; Amato, F.; Gentile, F. Nano-topography enhances communication in neural cells networks. *Sci Rep* **2017**, *7* (1), 9841.

(180) Teo, B. K. K.; Wong, S. T.; Lim, C. K.; Kung, T. Y. S.; Yap, C. H.; Ramagopal, Y.; Romer, L. H.; Yim, E. K. F. Nanotopography modulates mechanotransduction of stem cells and induces differentiation through focal adhesion kinase. *ACS Nano* **2013**, *7* (6), 4785-4798.

(181) Yang, K.; Yu, S. J.; Lee, J. S.; Lee, H. R.; Chang, G. E.; Seo, J.; Lee, T.; Cheong, E.; Im, S. G.; Cho, S. W. Electroconductive nanoscale topography for enhanced neuronal differentiation and electrophysiological maturation of human neural stem cells. *Nanoscale* **2017**, *9* (47), 18737-18752.

(182) Vicente-Manzanares, M.; Webb, D. J.; Horwitz, A. R. Cell migration at a glance. *J Cell Sci* **2005**, *118* (Pt 21), 4917-4919.

(183) Mitra, S. K.; Hanson, D. A.; Schlaepfer, D. D. Focal adhesion kinase: In command and control of cell motility. *Nat Rev Mol Cell Biol* **2005**, *6* (1), 56-68.

(184) Kim, D. H.; Han, K.; Gupta, K.; Kwon, K. W.; Suh, K. Y.; Levchenko, A. Mechanosensitivity of fibroblast cell shape and movement to anisotropic substratum topography gradients. *Biomaterials* **2009**, *30* (29), 5433-5444.

(185) Park, J.; Kim, H. N.; Kim, D. H.; Levchenko, A.; Suh, K. Y. Quantitative analysis of the combined effect of substrate rigidity and topographic guidance on cell morphology. *IEEE Trans Nanobioscience* **2012**, *11* (1), 28-36.

(186) Ventre, M.; Natale, C. F.; Rianna, C.; Netti, P. A. Topographic cell instructive patterns to control cell adhesion, polarization and migration. *J R Soc Interface* **2014**, *11* (100), 20140687.

(187) Kadota, M.; Yang, H. H.; Gomez, B.; Sato, M.; Clifford, R. J.; Meerzaman, D.; Dunn, B. K.; Wakefield, L. M.; Lee, M. P. Delineating genetic alterations for tumor progression in the MCF10A series of breast cancer cell lines. *PLoS One* **2010**, *5* (2), e9201.

(188) Marella, N. V.; Malyavantham, K. S.; Wang, J.; Matsui, S.; Liang, P.; Berezney, R. Cytogenetic and cDNA microarray expression analysis of MCF10 human breast cancer progression cell lines. *Cancer Res* **2009**, *69* (14), 5946-5953.

(189) Tang, B.; Vu, M.; Booker, T.; Santner, S. J.; Miller, F. R.; Anver, M. R.; Wakefield, L. M. TGF-beta switches from tumor suppressor to prometastatic factor in a model of breast cancer progression. *J Clin Invest* **2003**, *112* (7), 1116-1124.

(190) Foulkes, W. D.; Smith, I. E.; Reis-Filho, J. S. Triple-negative breast cancer. *N Engl J Med* **2010**, *363* (20), 1938-1948.

(191) Santner, S. J.; Dawson, P. J.; Tait, L.; Soule, H. D.; Eliason, J.; Mohamed, A. N.; Wolman, S. R.; Heppner, G. H.; Miller, F. R. Malignant MCF10CA1 cell lines derived from premalignant human breast epithelial MCF10AT cells. *Breast Cancer Res Treat* **2001**, *65*, 101-110.

(192) Song, K. H.; Kwon, K. W.; Choi, J. C.; Jung, J.; Park, Y.; Suh, K. Y.; Doh, J. T cells sense biophysical cues using lamellipodia and filopodia to optimize intraluminal path finding. *Integr Biol (Camb)* **2014**, *6* (4), 450-459.

(193) Tan, J.; Saltzman, M. Topographical control of human neutrophil motility on micropatterned materials with various surface chemistry. In *The Biomaterials: Silver Jubilee Compendium*, Williams, D. F., Ed.; Elsevier Science: 2002; pp 191-201.

(194) Arocena, M.; Rajnicek, A. M.; Collinson, J. M. Requirement of Pax6 for the integration of guidance cues in cell migration. *R Soc Open Sci* **2017**, *4* (10), 170625.

(195) Tzvetkova-Chevolleau, T.; Stephanou, A.; Fuard, D.; Ohayon, J.; Schiavone, P.; Tracqui, P. The motility of normal and cancer cells in response to the combined influence of the substrate rigidity and anisotropic microstructure. *Biomaterials* **2008**, *29* (10), 1541-1551.

(196) Chen, S.; Hourwitz, M. J.; Campanello, L.; Fourkas, J. T.; Losert, W.; Parent, C. A. Actin cytoskeleton and focal adhesions regulate the biased migration of breast cancer cells on nanoscale asymmetric sawteeth. *ACS Nano* **2019**, *13* (2), 1454-1468.

(197) Friedl, P. Prespecification and plasticity: Shifting mechanisms of cell migration. *Curr Opin Cell Biol* **2004**, *16* (1), 14-23.

(198) Friedl, P.; Wolf, K. Plasticity of cell migration: A multiscale tuning model. *J Cell Biol* **2010**, *188* (1), 11-19.

(199) Kao, J.; Salari, K.; Bocanegra, M.; Choi, Y. L.; Girard, L.; Gandhi, J.; Kwei, K. A.; Hernandez-Boussard, T.; Wang, P.; Gazdar, A. F.; Minna, J. D.; Pollack, J. R. Molecular profiling of breast cancer cell lines defines relevant tumor models and provides a resource for cancer gene discovery. *PLoS One* **2009**, *4* (7), e6146.

(200) Bear, J. E.; Haugh, J. M. Directed migration of mesenchymal cells: Where signaling and the cytoskeleton meet. *Curr Opin Cell Biol* **2014**, *30*, 74-82.

(201) Sun, X. Cellular contact guidance through dynamic sensing of nanotopographies via actin polymerization waves. University of Maryland-College Park, 2015.

(202) Kim, D. H.; Seo, C. H.; Han, K.; Kwon, K. W.; Levchenko, A.; Suh, K. Y. Guided cell migration on microtextured substrates with variable local density and anisotropy. *Adv Funct Mater* **2009**, *19* (10), 1579-1586.

(203) Park, J.; Kim, D. H.; Kim, H. N.; Wang, C. J.; Kwak, M. K.; Hur, E.; Suh, K. Y.; An, S. S.; Levchenko, A. Directed migration of cancer cells guided by the graded texture of the underlying matrix. *Nat Mater* **2016**, *15* (7), 792-801.

(204) Comelles, J.; Caballero, D.; Voituriez, R.; Hortiguela, V.; Wollrab, V.; Godeau, A. L.; Samitier, J.; Martinez, E.; Riveline, D. Cells as active particles in asymmetric potentials: Motility under external gradients. *Biophys J* **2014**, *107* (7), 1513-1522.

(205) Caballero, D.; Voituriez, R.; Riveline, D. Protrusion fluctuations direct cell motion. *Biophys J* **2014**, *107* (1), 34-42.

(206) Caballero, D.; Voituriez, R.; Riveline, D. The cell ratchet: Interplay between efficient protrusions and adhesion determines cell motion. *Cell Adh Migr* **2015**, *9* (5), 327-334.

(207) Maiuri, P.; Rupprecht, J. F.; Wieser, S.; Ruprecht, V.; Benichou, O.; Carpi, N.; Coppey, M.; De Beco, S.; Gov, N.; Heisenberg, C. P.; Lage Crespo, C.; Lautenschlaeger, F.; Le Berre, M.; Lennon-Dumenil, A. M.; Raab, M.; Thiam, H. R.; Piel, M.; Sixt, M.; Voituriez, R. Actin flows mediate a universal coupling between cell speed and cell persistence. *Cell* **2015**, *161* (2), 374-386.

(208) Bettinger, C. J.; Orrick, B.; Misra, A.; Langer, R.; Borenstein, J. T. Microfabrication of poly (glycerol-sebacate) for contact guidance applications. *Biomaterials* **2006**, *27* (12), 2558-2565.

(209) Oakley, C.; Brunette, D. M. The sequence of alignment of microtubules, focal contacts, and actin filaments in fibroblasts spreading on smooth and grooved titanium substrata. *J Cell Sci* **1993**, *106*, 343-354.

(210) Ezratty, E. J.; Partridge, M. A.; Gundersen, G. G. Microtubule-induced focal adhesion disassembly is mediated by dynamin and focal adhesion kinase. *Nat Cell Biol* **2005**, *7* (6), 581-590.

(211) Weiner, O. D.; Marganski, W. A.; Wu, L. F.; Altschuler, S. J.; Kirschner, M. W. An actin-based wave generator organizes cell motility. *PLoS Biol* **2007**, *5* (9), e221.

(212) Doubrovinski, K.; Kruse, K. Cell motility resulting from spontaneous polymerization waves. *Phys Rev Lett* **2011**, *107* (25), 258103.

(213) Kruse, K. Cell Crawling Driven by Spontaneous Actin Polymerization Waves. In *Physical Models of Cell Motility*, 1 ed.; Aranson, I. S. Ed.; Biological and Medical Physics, Biomedical Engineering, Springer Cham, 2015; pp 69-93.

(214) Bretschneider, T.; Diez, S.; Anderson, K.; Heuser, J.; Clarke, M.; Muller-Taubenberger, A.; Kohler, J.; Gerisch, G. Dynamic actin patterns and Arp2/3 assembly at the substrate-attached surface of motile cells. *Curr Biol* **2004**, *14* (1), 1-10.

(215) Ohara, P. T.; Buck, R. C. Contact guidance in vitro: A light, transmission, and scanning electron microscopic study. *Exp Cell Res* **1979**, *121*, 235-249.

(216) Kubow, K. E.; Shuklis, V. D.; Sales, D. J.; Horwitz, A. R. Contact guidance persists under myosin inhibition due to the local alignment of adhesions and individual protrusions. *Sci Rep* **2017**, *7* (1), 14380.

(217) Zimerman, B.; Arnold, M.; Ulmer, J.; Blummel, J.; Besser, A.; Spatz, J. P.; Geiger, B. Formation of focal adhesion-stress fibre complexes coordinated by adhesive and non-adhesive surface domains. *IEE Proc Nanobiotechnol* **2004**, *151* (2), 62-66.

(218) Deakin, N. O.; Turner, C. E. Paxillin comes of age. *J Cell Sci* **2008**, *121* (Pt 15), 2435-2444.

(219) Galbraith, C. G.; Yamada, K. M.; Sheetz, M. P. The relationship between force and focal complex development. *J Cell Biol* **2002**, *159* (4), 695-705.

(220) Chen, C. S.; Alonso, J. L.; Ostuni, E.; Whitesides, G. M.; Ingber, D. E. Cell shape provides global control of focal adhesion assembly. *Biochem Biophys Res Commun* **2003**, *307* (2), 355-361.

(221) Gallant, N. D.; Michael, K. E.; Garcia, A. J. Cell adhesion strengthening: Contributions of adhesive area, integrin binding, and focal adhesion assembly. *Mol Biol Cell* **2005**, *16* (9), 4329-4340.

(222) Goffin, J. M.; Pittet, P.; Csucs, G.; Lussi, J. W.; Meister, J. J.; Hinz, B. Focal adhesion size controls tension-dependent recruitment of alpha-smooth muscle actin to stress fibers. *J Cell Biol* **2006**, *172* (2), 259-268.

(223) Xia, N.; Thodeti, C. K.; Hunt, T. P.; Xu, Q.; Ho, M.; Whitesides, G. M.; Westervelt, R.; Ingber, D. E. Directional control of cell motility through focal adhesion positioning and spatial control of Rac activation. *FASEB J* **2008**, *22* (6), 1649-1659.

(224) Wu, Z.; Su, M.; Tong, C.; Wu, M.; Liu, J. Membrane shape-mediated wave propagation of cortical protein dynamics. *Nat Commun* **2018**, *9* (1), 136.

(225) Yang, Y.; Wu, M. Rhythmicity and waves in the cortex of single cells. *Philos Trans R Soc B* **2018**, *373* (1747), 20170116.

(226) Gov, N. S. Guided by curvature: Shaping cells by coupling curved membrane proteins and cytoskeletal forces. *Philos Trans R Soc B* **2018**, *373* (1747), 20170115.

(227) Xi, W.; Sonam, S.; Lim, C. T.; Ladoux, B. Tubular microscaffolds for studying collective cell migration. *Methods Cell Biol* **2018**, *146*, 3-21.

(228) Yevick, H. G.; Duclos, G.; Bonnet, I.; Silberzan, P. Architecture and migration of an epithelium on a cylindrical wire. *Proc Natl Acad Sci U S A* **2015**, *112* (19), 5944-5949.

(229) Baldacchini, T. Three-Dimensional Microfabrication Using Two-Photon Polymerization: Fundamentals, Technology, and Applications. 1 ed.; William Andrew: Oxford, 2015; p 512.

(230) Efron, B. Bootstrap methods: Another look at the jackknife. *Ann Stat* **1979**, *7* (1), 1-26.

(231) Efron, B.; Tibshirani, R. J. *An Introduction to the Bootstrap*; Chapman & Hall, 1993.

(232) Horn, B. K. P.; Schunk, B. G. Determining optical flow. *Artif Intell* **1981**, *17*, 185-203.

(233) Lucas, B. D.; Kanade, T. An iterative image registration technique with an application to stereo vision. In IJCAI'81: 7th international joint conference on Artificial intelligence, Vancouver, Canada; 1981.

(234) Maruthamuthu, V.; Aratyn-Schaus, Y.; Gardel, M. L. Conserved F-actin dynamics and force transmission at cell adhesions. *Curr Opin Cell Biol* **2010**, *22* (5), 583-588.

(235) Lam Hui, K.; Kwak, S. I.; Upadhyaya, A. Adhesion-dependent modulation of actin dynamics in Jurkat T cells. *Cytoskeleton (Hoboken)* **2014**, *71* (2), 119-135.

(236) Muller, J.; Sixt, M. Cell Migration: Making the Waves. *Curr Biol* **2017**, *27* (1), R24-R25.

(237) Inagaki, N.; Katsuno, H. Actin Waves: Origin of Cell Polarization and Migration? *Trends Cell Biol* **2017**, *27* (7), 515-526.

(238) Discher, D. E.; Janmey, P.; Wang, Y. Tissue cells feel and respond to the stiffness of their substrate. *Science* **2005**, *310*, 1139-1143.

(239) Doyle, A. D.; Wang, F. W.; Matsumoto, K.; Yamada, K. M. One-dimensional topography underlies three-dimensional fibrillar cell migration. *J Cell Biol* **2009**, *184* (4), 481-490.

(240) Lu, P.; Weaver, V. M.; Werb, Z. The extracellular matrix: A dynamic niche in cancer progression. *J Cell Biol* **2012**, *196* (4), 395-406.

(241) Petrie, R. J.; Yamada, K. M. Fibroblasts lead the way: A unified view of 3D cell motility. *Trends Cell Biol* **2015**, *25* (11), 666-674.

(242) Wolf, K.; Friedl, P. Extracellular matrix determinants of proteolytic and non-proteolytic cell migration. *Trends Cell Biol* **2011**, *21* (12), 736-744.

(243) Charras, G.; Sahai, E. Physical influences of the extracellular environment on cell migration. *Nat Rev Mol Cell Biol* **2014**, *15* (12), 813-824.

(244) Vig, D. K.; Hamby, A. E.; Wolgemuth, C. W. On the quantification of cellular velocity fields. *Biophys J* **2016**, *110* (7), 1469-1475.

(245) Lee, R. M.; Campanello, L.; Hourwitz, M. J.; Alvarez, P.; Omidvar, A.; Fourkas, J. T.; Losert, W. Quantifying topography-guided actin dynamics across scales using optical flow. *Mol Biol Cell* **2020**, *31* (16), 1753-1764.

(246) Blair, D.; Dufresne, E. *Crocker-Grier particle tracking algorithm*; The MATLAB Particle Tracking Code Repository, Available at: https://site.physics.georgetown.edu/matlab/, 2018. (accessed 9 August, 2018).

(247) Meyer, W. H.; Howard, T. H. Actin polymerization and its relationship to locomotion and chemokinetic response in maturing human promyelocytic leukemia cells. *Blood* **1987**, *70* (2), 363-367.

(248) Lee, R. M.; Stuelten, C. H.; Parent, C. A.; Losert, W. Collective cell migration over long time scales reveals distinct phenotypes. *Converg Sci Phys Oncol* **2016**, *2* (2), 025001.

(249) Begemann, I.; Saha, T.; Lamparter, L.; Rathmann, I.; Grill, D.; Golbach, L.; Rasch, C.; Keller, U.; Trappmann, B.; Matis, M.; Gerke, V.; Klingauf, J.; Galic, M. Mechanochemical self-organization determines search pattern in migratory cells. *Nat Phys* **2019**, *15* (8), 848-857.

(250) Vogel, V.; Sheetz, M. Local force and geometry sensing regulate cell functions. *Nat Rev Mol Cell Biol* **2006**, *7* (4), 265-275.

(251) McMahon, H. T.; Boucrot, E. Membrane curvature at a glance. *J Cell Sci* **2015**, *128* (6), 1065-1070.

(252) Bridges, A. A.; Jentzsch, M. S.; Oakes, P. W.; Occhipinti, P.; Gladfelter, A. S. Micron-scale plasma membrane curvature is recognized by the septin cytoskeleton. *J Cell Biol* **2016**, *213* (1), 23-32.

(253) Zimmerberg, J.; McLaughlin, S. Membrane curvature: How BAR domains bend bilayers. *Curr Biol* **2004**, *14* (6), R250-R252.

(254) Graziano, B. R.; Weiner, O. D. Self-organization of protrusions and polarity during eukaryotic chemotaxis. *Curr Opin Cell Biol* **2014**, *30*, 60-67.

(255) Miki, H.; Yamaguchi, H.; Suetsugu, S.; Takenawa, T. IRSp53 is an essential intermediate between Rac and WAVE in the regulation of membrane ruffling. *Nature* **2000**, *408*, 732-735.

(256) Habermann, B. The BAR-domain family of proteins: A case of bending and binding? *EMBO Rep* **2004**, *5* (3), 250-255.

(257) Lou, H. Y.; Zhao, W.; Li, X.; Duan, L.; Powers, A.; Akamatsu, M.; Santoro, F.; McGuire, A. F.; Cui, Y.; Drubin, D. G.; Cui, B. Membrane curvature underlies actin reorganization in response to nanoscale surface topography. *Proc Natl Acad Sci U S A* **2019**, *116* (46), 23143-23151.

(258) Simoncelli, E. P.; Adelson, E. H.; Heeger, D. J. Probability distributions of optical flow. In *1991 IEEE Computer Society Conference on Computer Vision and Pattern Recognition*, Mauii, Hawaii, June, 1991, 1991; IEEE Computer Society: pp 310-315.

(259) Barron, J. L.; Fleet, D. J.; Beauchemin, S. S.; Burkitt, T. A. Performance of optical flow techniques. In *1992 IEEE Computer Society Conference on Computer Vision and Pattern Recognition*, January, 1992, 1992; IEEE Computer Society: pp 236-237.

(260) Crocker, J. C.; Grier, D. G. Methods of digital video microscopy for colloidal studies. *J Colloid Interface Sci* **1996**, *179*, 298-310.

(261) Lee, R.; Campanello, L.; Hourwitz, M.; Alvarez, P.; Omidvar, A.; Fourkas, J.; Losert, W. Data for: Quantifying topography-guided actin dynamics across scales using optical flow. 1 ed.; Mendeley Data: 2020.

(262) Luster, A. D.; Alon, R.; von Andrian, U. H. Immune cell migration in inflammation: present and future therapeutic targets. *Nat Immunol* **2005**, *6* (12), 1182-1190.

(263) Seetharaman, S.; Etienne-Manneville, S. Cytoskeletal crosstalk in cell migration. *Trends Cell Biol* **2020**, *30* (9), 720-735.

(264) Yamaguchi, H.; Condeelis, J. Regulation of the actin cytoskeleton in cancer cell migration and invasion. *Biochim Biophys Acta* **2007**, *1773* (5), 642-652.

(265) Chen, H.; Zhu, G.; Li, Y.; Padia, R. N.; Dong, Z.; Pan, Z. K.; Liu, K.; Huang, S. Extracellular signal-regulated kinase signaling pathway regulates breast cancer cell migration by maintaining slug expression. *Cancer Res* **2009**, *69* (24), 9228-9235.

(266) Zohrabian, V. M.; Forzani, B.; Chau, Z.; Murali, R.; Jhanwar-Uniyal, M. Rho/ROCK and MAPK signaling pathways are involved in glioblastoma cell migration and proliferation. *Anticancer Res* **2009**, *29*, 119-124.

(267) Mostafavi-Pour, Z.; Askari, J. A.; Parkinson, S. J.; Parker, P. J.; Ng, T. T.; Humphries, M. J. Integrin-specific signaling pathways controlling focal adhesion formation and cell migration. *J Cell Biol* **2003**, *161* (1), 155-167.

(268) Li, Y.; Wang, J. P.; Santen, R. J.; Kim, T. H.; Park, H.; Fan, P.; Yue, W. Estrogen stimulation of cell migration involves multiple signaling pathway interactions. *Endocrinology* **2010**, *151* (11), 5146-5156.

(269) Yamauchi, J.; Chan, J. R.; Shooter, E. M. Neurotrophins regulate Schwann cell migration by activating divergent signaling pathways dependent on Rho GTPases. *Proc Natl Acad Sci U S A* **2004**, *101* (23), 8774-8779.

(270) Dumstrei, K.; Mennecke, R.; Raz, E. Signaling pathways controlling primordial germ cell migration in zebrafish. *J Cell Sci* **2004**, *117* (Pt 20), 4787-4795.

(271) Zhao, X.; Guan, J. L. Focal adhesion kinase and its signaling pathways in cell migration and angiogenesis. *Adv Drug Deliv Rev* **2011**, *63* (8), 610-615.

(272) Harris, J.; Honigberg, L.; Robinson, N.; Kenyon, C. Neuronal cell migration in C. elegans: Regulation of Hox gene expression and cell position. *Development* **1996**, *122*, 3117-3131.

(273) Mannaerts, I.; Schroyen, B.; Verhulst, S.; Van Lommel, L.; Schuit, F.; Nyssen, M.; van Grunsven, L. A. Gene expression profiling of early hepatic stellate cell activation reveals a role for Igfbp3 in cell migration. *PLoS One* **2013**, *8* (12), e84071.

(274) Rhoads, J. M.; Niu, X.; Odle, J.; Graves, L. M. Role of mTOR signaling in intestinal cell migration. *Am J Physiol Gastrointest Liver Physiol* **2006**, *291* (3), G510-G517.

(275) Burrows, C.; Abd Latip, N.; Lam, S. J.; Carpenter, L.; Sawicka, K.; Tzolovsky, G.; Gabra, H.; Bushell, M.; Glover, D. M.; Willis, A. E.; Blagden, S. P. The RNA binding protein Larp1

regulates cell division, apoptosis and cell migration. *Nucleic Acids Res* **2010**, *38* (16), 5542-5553.

(276) Yan, S.; Golumba-Nagy, V.; Kotschenreuther, K.; Thiele, J.; Refaian, N.; Shuya, D.; Gloyer, L.; Dittrich-Salamon, M.; Meyer, A.; Heindl, L. M.; Kofler, D. M. Membrane-bound IL-6R is upregulated on Th17 cells and inhibits Treg cell migration by regulating post-translational modification of VASP in autoimmune arthritis. *Cell Mol Life Sci* **2022**, *79* (1), 3.

(277) Snider, N. T.; Omary, M. B. Post-translational modifications of intermediate filament proteins: Mechanisms and functions. *Nat Rev Mol Cell Biol* **2014**, *15* (3), 163-177.

(278) Verma, N. K.; Dempsey, E.; Conroy, J.; Olwell, P.; McElligott, A. M.; Davies, A. M.; Kelleher, D.; Butini, S.; Campiani, G.; Williams, D. C.; Zisterer, D. M.; Lawler, M.; Volkov, Y. A new microtubule-targeting compound PBOX-15 inhibits T-cell migration via post-translational modifications of tubulin. *J Mol Med* **2008**, *86* (4), 457-469.

(279) Stemmler, M. P.; Eccles, R. L.; Brabletz, S.; Brabletz, T. Non-redundant functions of EMT transcription factors. *Nat Cell Biol* **2019**, *21* (1), 102-112.

(280) Sanchez-Tillo, E.; Liu, Y.; de Barrios, O.; Siles, L.; Fanlo, L.; Cuatrecasas, M.; Darling, D. S.; Dean, D. C.; Castells, A.; Postigo, A. EMT-activating transcription factors in cancer: Beyond EMT and tumor invasiveness. *Cell Mol Life Sci* **2012**, *69* (20), 3429-3456.

(281) Di Cio, S.; Gautrot, J. E. Cell sensing of physical properties at the nanoscale: Mechanisms and control of cell adhesion and phenotype. *Acta Biomater* **2016**, *30*, 26-48.

(282) Moe, A. A.; Suryana, M.; Marcy, G.; Lim, S. K.; Ankam, S.; Goh, J. Z.; Jin, J.; Teo, B. K.; Law, J. B.; Low, H. Y.; Goh, E. L.; Sheetz, M. P.; Yim, E. K. Microarray with micro- and nano-topographies enables identification of the optimal topography for directing the differentiation of primary murine neural progenitor cells. *Small* **2012**, *8* (19), 3050-3061.

(283) Lim, S. H.; Liu, X. Y.; Song, H.; Yarema, K. J.; Mao, H. Q. The effect of nanofiber-guided cell alignment on the preferential differentiation of neural stem cells. *Biomaterials* **2010**, *31* (34), 9031-9039.

(284) Yin, Z.; Chen, X.; Chen, J. L.; Shen, W. L.; Hieu Nguyen, T. M.; Gao, L.; Ouyang, H. W. The regulation of tendon stem cell differentiation by the alignment of nanofibers. *Biomaterials* **2010**, *31* (8), 2163-2175.

(285) Chiarugi, P.; Giannoni, E. Anoikis: a necessary death program for anchorage-dependent cells. *Biochem Pharmacol* **2008**, *76* (11), 1352-1364.

(286) Taddei, M. L.; Giannoni, E.; Fiaschi, T.; Chiarugi, P. Anoikis: An emerging hallmark in health and diseases. *J Pathol* **2012**, *226* (2), 380-393.

(287) Zhong, X.; Rescorla, F. J. Cell surface adhesion molecules and adhesion-initiated signaling: Understanding of anoikis resistance mechanisms and therapeutic opportunities. *Cell Signal* **2012**, *24* (2), 393-401.

(288) Perlikos, F.; Harrington, K. J.; Syrigos, K. N. Key molecular mechanisms in lung cancer invasion and metastasis: A comprehensive review. *Crit Rev Oncol Hematol* **2013**, *87* (1), 1-11.

(289) Chatterjee, K.; Lin-Gibson, S.; Wallace, W. E.; Parekh, S. H.; Lee, Y. J.; Cicerone, M. T.; Young, M. F.; Simon, C. G., Jr. The effect of 3D hydrogel scaffold modulus on osteoblast differentiation and mineralization revealed by combinatorial screening. *Biomaterials* **2010**, *31* (19), 5051-5062.

(290) Trichet, L.; Le Digabel, J.; Hawkins, R. J.; Vedula, S. R.; Gupta, M.; Ribrault, C.; Hersen, P.; Voituriez, R.; Ladoux, B. Evidence of a large-scale mechanosensing mechanism for cellular adaptation to substrate stiffness. *Proc Natl Acad Sci U S A* **2012**, *109* (18), 6933-6938.

(291) Kulangara, K.; Leong, K. W. Substrate topography shapes cell function. *Soft Matter* **2009**, *5* (21), 4072-4076.

(292) Chua, J. S.; Chng, C. P.; Moe, A. A.; Tann, J. Y.; Goh, E. L.; Chiam, K. H.; Yim, E. K. Extending neurites sense the depth of the underlying topography during neuronal differentiation and contact guidance. *Biomaterials* **2014**, *35* (27), 7750-7761.

(293) Heydarkhan-Hagvall, S.; Choi, C. H.; Dunn, J.; Heydarkhan, S.; Schenke-Layland, K.; MacLellan, W. R.; Beygui, R. E. Influence of systematically varied nano-scale topography on cell morphology and adhesion. *Cell Commun Adhes* **2007**, *14* (5), 181-194.

(294) Curtis, A.; Wilkinson, C. Topographical control of cells. *Biomaterials* **1997**, *18* (24), 1573-1583.

(295) Hou, Y.; Xie, W.; Yu, L.; Camacho, L. C.; Nie, C.; Zhang, M.; Haag, R.; Wei, Q. Surface roughness gradients reveal topography-specific mechanosensitive responses in human mesenchymal stem cells. *Small* **2020**, *16* (10), e1905422.

(296) Huang, J.; Chen, Y.; Tang, C.; Fei, Y.; Wu, H.; Ruan, D.; Paul, M. E.; Chen, X.; Yin, Z.; Heng, B. C.; Chen, W.; Shen, W. The relationship between substrate topography and stem cell differentiation in the musculoskeletal system. *Cell Mol Life Sci* **2019**, *76* (3), 505-521.

(297) Hoffman-Kim, D.; Mitchel, J. A.; Bellamkonda, R. V. Topography, cell response, and nerve regeneration. *Annu Rev Biomed Eng* **2010**, *12*, 203-231.

(298) Liu, X.; Lim, J. Y.; Donahue, H. J.; Dhurjati, R.; Mastro, A. M.; Vogler, E. A. Influence of substratum surface chemistry/energy and topography on the human fetal osteoblastic cell line hFOB 1.19: Phenotypic and genotypic responses observed in vitro. *Biomaterials* **2007**, *28* (31), 4535-4550.

(299) Lara Rodriguez, L.; Schneider, I. C. Directed cell migration in multi-cue environments. *Integr Biol (Camb)* **2013**, *5* (11), 1306-1323.

(300) DuFort, C. C.; Paszek, M. J.; Weaver, V. M. Balancing forces: Architectural control of mechanotransduction. *Nat Rev Mol Cell Biol* **2011**, *12* (5), 308-319.

(301) Gjorevski, N.; Nelson, C. M. Bidirectional extracellular matrix signaling during tissue morphogenesis. *Cytokine Growth Factor Rev* **2009**, *20* (5-6), 459-465.

(302) Albuschies, J.; Vogel, V. The role of filopodia in the recognition of nanotopographies. *Sci Rep* **2013**, *3*, 1658.

(303) Guadarrama Bello, D.; Fouillen, A.; Badia, A.; Nanci, A. A nanoporous titanium surface promotes the maturation of focal adhesions and formation of filopodia with distinctive nanoscale protrusions by osteogenic cells. *Acta Biomater* **2017**, *60*, 339-349.

(304) Bhingardive, V.; Kossover, A.; Iraqi, M.; Khand, B.; Le Saux, G.; Porgador, A.; Schvartzman, M. Antibody-functionalized nanowires: A tuner for the activation of T cells. *Nano Lett* **2021**, *21* (10), 4241-4248.

(305) Zhang, W.; Yang, Y.; Cui, B. New perspectives on the roles of nanoscale surface topography in modulating intracellular signaling. *Curr Opin Solid State Mater Sci* **2021**, *25* (1), 100873.

(306) Chen, Y.; Wang, J.; Li, X.; Hu, N.; Voelcker, N. H.; Xie, X.; Elnathan, R. Emerging roles of 1D vertical nanostructures in orchestrating immune cell functions. *Adv Mater* **2020**, *32* (40), e2001668.

(307) Farrell, M. V.; Webster, S.; Gaus, K.; Goyette, J. T cell membrane heterogeneity aids antigen recognition and T cell activation. *Front Cell Dev Biol* **2020**, *8*, 609.

(308) Aramesh, M.; Stoycheva, D.; Sandu, I.; Ihle, S. J.; Zund, T.; Shiu, J. Y.; Forro, C.; Asghari, M.; Bernero, M.; Lickert, S.; Oxenius, A.; Vogel, V.; Klotzsch, E. Nanoconfinement of microvilli alters gene expression and boosts T cell activation. *Proc Natl Acad Sci U S A* **2021**, *118* (40), e2107535118.

(309) Lehoux, S.; Castier, Y.; Tedgui, A. Molecular mechanisms of the vascular responses to haemodynamic forces. *J Intern Med* **2006**, *259* (4), 381-392.

(310) Chachisvilis, M.; Zhang, Y.-L.; Frangos, J. A. G protein-coupled receptors sense fluid shear stress in endothelial cells. *Proc Natl Acad Sci U S A* **2006**, *103* (42), 15463-15468.

(311) Peter, B. J.; Kent, H. M.; Mills, I. G.; Vallis, Y.; Butler, P. J. G.; Evans, P. R.; McMahon, H. T. BAR domains as sensors of membrane curvature: The amphiphysin BAR structure. *Science* **2004**, *303*, 495-499.

(312) Bhatia, V. K.; Madsen, K. L.; Bolinger, P. Y.; Kunding, A.; Hedegard, P.; Gether, U.; Stamou, D. Amphipathic motifs in BAR domains are essential for membrane curvature sensing. *EMBO J* **2009**, *28* (21), 3303-3314.

(313) Bhatia, V. K.; Hatzakis, N. S.; Stamou, D. A unifying mechanism accounts for sensing of membrane curvature by BAR domains, amphipathic helices and membrane-anchored proteins. *Semin Cell Dev Biol* **2010**, *21* (4), 381-390.

(314) Ozdemir, T.; Xu, L. C.; Siedlecki, C.; Brown, J. L. Substrate curvature sensing through myosin IIa upregulates early osteogenesis. *Integr Biol (Camb)* **2013**, *5* (11), 1407-1416.

(315) Bade, N. D.; Xu, T.; Kamien, R. D.; Assoian, R. K.; Stebe, K. J. Gaussian curvature directs stress fiber orientation and cell migration. *Biophys J* **2018**, *114* (6), 1467-1476.

(316) Galbraith, C. G.; Sheetz, M. P. Forces on adhesive contacts affect cell function. *Curr Opin Cell Biol* **1998**, *10*, 566-571.

(317) Sun, X.; Alushin, G. M. Cellular force-sensing through actin filaments. *FEBS J* **2023**, *290* (10), 2576-2589.

(318) Yang, Q.; Miao, Y.; Campanello, L. J.; Hourwitz, M. J.; Abubaker-Sharif, B.; Bull, A. L.; Devreotes, P. N.; Fourkas, J. T.; Losert, W. Cortical waves mediate the cellular response to electric fields. *Elife* **2022**, *11*, e73198.

(319) Bull, A. L.; Campanello, L.; Hourwitz, M. J.; Yang, Q.; Zhao, M.; Fourkas, J. T.; Losert, W. Actin dynamics as a multiscale integrator of cellular guidance cues. *Front Cell Dev Biol* **2022**, *10*, 873567.

(320) Herr, C.; Winkler, B.; Ziebert, F.; Aranson, I. S.; Fourkas, J. T.; Losert, W. Spontaneous polarization and cell guidance on asymmetric nanotopography. *Commun Phys* **2022**, *5* (1), 114.

(321) Wheatley, B. A.; Rey-Suarez, I.; Hourwitz, M. J.; Kerr, S.; Shroff, H.; Fourkas, J. T.; Upadhyaya, A. Nanotopography modulates cytoskeletal organization and dynamics during T cell activation. *Mol Biol Cell* **2022**, *33* (10), ar88.

(322) Yang, Q.; Miao, Y.; Banerjee, P.; Hourwitz, M. J.; Hu, M.; Qing, Q.; Iglesias, P. A.; Fourkas, J. T.; Losert, W.; Devreotes, P. N. Nanotopography modulates intracellular excitable systems through cytoskeleton actuation. *Proc Natl Acad Sci U S A* **2023**, *120* (19), e2218906120.

(323) Heng, Y. W.; Koh, C. G. Actin cytoskeleton dynamics and the cell division cycle. *Int J Biochem Cell Biol* **2010**, *42* (10), 1622-1633.

(324) Rizzelli, F.; Malabarba, M. G.; Sigismund, S.; Mapelli, M. The crosstalk between microtubules, actin and membranes shapes cell division. *Open Biol* **2020**, *10* (3), 190314.

(325) Chew, T. G.; Lorthongpanich, C.; Ang, W. X.; Knowles, B. B.; Solter, D. Symmetric cell division of the mouse zygote requires an actin network. *Cytoskeleton (Hoboken)* **2012**, *69* (12), 1040-1046.

(326) Parisis, N.; Krasinska, L.; Harker, B.; Urbach, S.; Rossignol, M.; Camasses, A.; Dewar, J.; Morin, N.; Fisher, D. Initiation of DNA replication requires actin dynamics and formin activity. *EMBO J* **2017**, *36* (21), 3212-3231.

(327) Hurst, V.; Shimada, K.; Gasser, S. M. Nuclear actin and actin-binding proteins in DNA repair. *Trends Cell Biol* **2019**, *29* (6), 462-476.

(328) Schuh, M. An actin-dependent mechanism for long-range vesicle transport. *Nat Cell Biol* **2011**, *13* (12), 1431-1436.

(329) Drummond, I. A. Polycystins, focal adhesions, and extracellular matrix interactions. *Biochim Biophys Acta* **2011**, *1812*, 1322-1326.

(330) Sharif-Naeini, R.; Folgering, J. H. A.; Bichet, D.; Duprat, F.; Lauritzen, I.; Arhatte, M.; Jodar, M.; Dedman, A.; Chatelain, F. C.; Schulte, U.; Retailleau, K.; Loufrani, L.; Patel, A.; Sachs, F.; Delmas, P.; Peters, D. J. M.; Honoré, E. Polycystin-1 and -2 dosage regulates pressure sensing. *Cell* **2009**, *139* (3), 587-596.

(331) Tu, C. L.; Chang, W.; Bikle, D. D. The calcium-sensing receptor-dependent regulation of cell-cell adhesion and keratinocyte differentiation requires Rho and filamin A. *J Invest Dermatol* **2011**, *131* (5), 1119-1128.

(332) Leiphart, R. J.; Chen, D.; Peredo, A. P.; Loneker, A. E.; Janmey, P. A. Mechanosensing at cellular interfaces. *Langmuir* **2019**, *35* (23), 7509-7519.

(333) Ringer, P.; Colo, G.; Fassler, R.; Grashoff, C. Sensing the mechano-chemical properties of the extracellular matrix. *Matrix Biol* **2017**, *64*, 6-16.

(334) Fischer, R. S.; Sun, X.; Baird, M. A.; Hourwitz, M. J.; Seo, B. R.; Pasapera, A. M.; Mehta, S. B.; Losert, W.; Fischbach, C.; Fourkas, J. T.; Waterman, C. M. Contractility, focal adhesion orientation, and stress fiber orientation drive cancer cell polarity and migration along wavy ECM substrates. *Proc Natl Acad Sci U S A* **2021**, *118* (22), e2021135118.

(335) Sengupta, P. K.; Smith, E. M.; Kim, K.; Murnane, M. J.; Smith, B. D. DNA hypermethylation near the transcription start site of collagen alpha2(I) gene occurs in both cancer cell lines and primary colorectal cancers. *Cancer Res* **2003**, *63*, 1789-1797.

(336) Miranti, C. K.; Brugge, J. S. Sensing the environment: A historical perspective on integrin signal transduction. *Nat Cell Biol* **2002**, *4*, E83-E90.

(337) Friedl, P.; Brocker, E. B.; Zanker, K. S. Integrins, cell matrix interactions and cell migration strategies: Fundamental differences in leukocytes and tumor cells. *Cell Adhes Commun* **1998**, *6* (2-3), 225-236.

(338) Schmidt, S.; Friedl, P. Interstitial cell migration: Integrin-dependent and alternative adhesion mechanisms. *Cell Tissue Res* **2010**, *339* (1), 83-92.

(339) Friedl, P.; Weigelin, B. Interstitial leukocyte migration and immune function. *Nat Immunol* **2008**, *9* (9), 960-969.

(340) Holle, A. W.; Govindan Kutty Devi, N.; Clar, K.; Fan, A.; Saif, T.; Kemkemer, R.; Spatz, J. P. Cancer cells invade confined microchannels via a self-directed mesenchymal-to-amoeboid transition. *Nano Lett* **2019**, *19* (4), 2280-2290.

(341) Renkawitz, J.; Schumann, K.; Weber, M.; Lammermann, T.; Pflicke, H.; Piel, M.; Polleux, J.; Spatz, J. P.; Sixt, M. Adaptive force transmission in amoeboid cell migration. *Nat Cell Biol* **2009**, *11* (12), 1438-1443.

(342) Pankova, K.; Rosel, D.; Novotny, M.; Brabek, J. The molecular mechanisms of transition between mesenchymal and amoeboid invasiveness in tumor cells. *Cell Mol Life Sci* **2010**, *67* (1), 63-71.

(343) Wolf, K.; Mazo, I.; Leung, H.; Engelke, K.; von Andrian, U. H.; Deryugina, E. I.; Strongin, A. Y.; Brocker, E. B.; Friedl, P. Compensation mechanism in tumor cell migration: Mesenchymal-amoeboid transition after blocking of pericellular proteolysis. *J Cell Biol* **2003**, *160* (2), 267-277.

(344) Graziani, V.; Rodriguez-Hernandez, I.; Maiques, O.; Sanz-Moreno, V. The amoeboid state as part of the epithelial-to-mesenchymal transition programme. *Trends Cell Biol* **2022**, *32* (3), 228-242.

(345) Gadea, G.; Sanz-Moreno, V.; Self, A.; Godi, A.; Marshall, C. J. DOCK10-mediated Cdc42 activation is necessary for amoeboid invasion of melanoma cells. *Curr Biol* **2008**, *18* (19), 1456-1465.

(346) Alexandrova, A. Y.; Chikina, A. S.; Svitkina, T. M. Actin cytoskeleton in mesenchymal-to-amoeboid transition of cancer cells. *Int Rev Cell Mol Biol* **2020**, *356*, 197-256.

(347) Orgaz, J. L.; Pandya, P.; Dalmeida, R.; Karagiannis, P.; Sanchez-Laorden, B.; Viros, A.; Albrengues, J.; Nestle, F. O.; Ridley, A. J.; Gaggioli, C.; Marais, R.; Karagiannis, S. N.; Sanz-Moreno, V. Diverse matrix metalloproteinase functions regulate cancer amoeboid migration. *Nat Commun* **2014**, *5*, 4255.

(348) Talkenberger, K.; Cavalcanti-Adam, E. A.; Voss-Böhme, A.; Deutsch, A. Amoeboid-mesenchymal migration plasticity promotes invasion only in complex heterogeneous microenvironments. *Sci Rep* **2017**, *7* (1), 9237.

(349) Wang, M.; Cheng, B.; Yang, Y.; Liu, H.; Huang, G.; Han, L.; Li, F.; Xu, F. Microchannel stiffness and confinement jointly induce the mesenchymal-amoeboid transition of cancer cell migration. *Nano Lett* **2019**, *19* (9), 5949-5958.

(350) Liu, Y. J.; Le Berre, M.; Lautenschlaeger, F.; Maiuri, P.; Callan-Jones, A.; Heuze, M.; Takaki, T.; Voituriez, R.; Piel, M. Confinement and low adhesion induce fast amoeboid migration of slow mesenchymal cells. *Cell* **2015**, *160* (4), 659-672.

(351) Renkawitz, J.; Kopf, A.; Stopp, J.; de Vries, I.; Driscoll, M. K.; Merrin, J.; Hauschild, R.; Welf, E. S.; Danuser, G.; Fiolka, R.; Sixt, M. Nuclear positioning facilitates amoeboid migration along the path of least resistance. *Nature* **2019**, *568* (7753), 546-550.

(352) Walzer, T.; Galibert, L.; Comeau, M. R.; De Smedt, T. Plexin C1 engagement on mouse dendritic cells by viral semaphorin A39R induces actin cytoskeleton rearrangement and inhibits integrin-mediated adhesion and chemokine-induced migration. *J Immunol* **2005**, *174* (1), 51-59.

(353) Kwon, K. W.; Park, H.; Song, K. H.; Choi, J. C.; Ahn, H.; Park, M. J.; Suh, K. Y.; Doh, J. Nanotopography-guided migration of T cells. *J Immunol* **2012**, *189* (5), 2266-2273.

(354) Song, K. H.; Park, S. J.; Kim, D. S.; Doh, J. Sinusoidal wavy surfaces for curvature-guided migration of T lymphocytes. *Biomaterials* **2015**, *51*, 151-160.

(355) Wolfenson, H.; Iskratsch, T.; Sheetz, M. P. Early events in cell spreading as a model for quantitative analysis of biomechanical events. *Biophys J* **2014**, *107* (11), 2508-2514.

(356) Hielscher, A. C.; Qiu, C.; Gerecht, S. Breast cancer cell-derived matrix supports vascular morphogenesis. *Am J Physiol Cell Physiol* **2012**, *302* (8), C1243-C1256.

(357) DiMilla, P. A.; Stone, J. A.; Quinn, J. A.; Albelda, S. M.; Lauffenburger, D. A. Maximal migration of human smooth muscle cells on fibronectin and type IV collagen occurs at an intermediate attachment strength. *J Cell Biol* **1993**, *122* (3), 729-737.

(358) Riching, K. M.; Cox, B. L.; Salick, M. R.; Pehlke, C.; Riching, A. S.; Ponik, S. M.; Bass, B. R.; Crone, W. C.; Jiang, Y.; Weaver, A. M.; Eliceiri, K. W.; Keely, P. J. 3D collagen alignment limits protrusions to enhance breast cancer cell persistence. *Biophys J* **2014**, *107* (11), 2546-2558.

(359) Wang, W. Y.; Pearson, A. T.; Kutys, M. L.; Choi, C. K.; Wozniak, M. A.; Baker, B. M.; Chen, C. S. Extracellular matrix alignment dictates the organization of focal adhesions and directs uniaxial cell migration. *APL Bioeng* **2018**, *2* (4), 046107.

(360) Barnhart, E. L.; Lee, K. C.; Keren, K.; Mogilner, A.; Theriot, J. A. An adhesion-dependent switch between mechanisms that determine motile cell shape. *PLoS Biol* **2011**, *9* (5), e1001059.

(361) Bergert, M.; Chandradoss, S. D.; Desai, R. A.; Paluch, E. Cell mechanics control rapid transitions between blebs and lamellipodia during migration. *Proc Natl Acad Sci U S A* **2012**, *109* (36), 14434-14439.

(362) Stahl, S.; Weitzman, S.; Jones, J. C. R. The role of laminin-5 and its receptors in mammary epithelial cell branching morphogenesis. *J Cell Sci* **1997**, *110*, 55-63.

(363) Han, S. J.; Bielawski, K. S.; Ting, L. H.; Rodriguez, M. L.; Sniadecki, N. J. Decoupling substrate stiffness, spread area, and micropost density: a close spatial relationship between traction forces and focal adhesions. *Biophys J* **2012**, *103* (4), 640-648.

(364) Chaudhuri, O.; Gu, L.; Darnell, M.; Klumpers, D.; Bencherif, S. A.; Weaver, J. C.; Huebsch, N.; Mooney, D. J. Substrate stress relaxation regulates cell spreading. *Nat Commun* **2015**, *6*, 6364.

(365) Ghibaudo, M.; Di Meglio, J. M.; Hersen, P.; Ladoux, B. Mechanics of cell spreading within 3D-micropatterned environments. *Lab Chip* **2011**, *11* (5), 805-812.

(366) Gong, Z.; Szczesny, S. E.; Caliari, S. R.; Charrier, E. E.; Chaudhuri, O.; Cao, X.; Lin, Y.; Mauck, R. L.; Janmey, P. A.; Burdick, J. A.; Shenoy, V. B. Matching material and cellular timescales maximizes cell spreading on viscoelastic substrates. *Proc Natl Acad Sci U S A* **2018**, *115* (12), E2686-E2695.

(367) Elosegui-Artola, A.; Bazellieres, E.; Allen, M. D.; Andreu, I.; Oria, R.; Sunyer, R.; Gomm, J. J.; Marshall, J. F.; Jones, J. L.; Trepat, X.; Roca-Cusachs, P. Rigidity sensing and adaptation through regulation of integrin types. *Nat Mater* **2014**, *13* (6), 631-637.

(368) Le Roux, A. L.; Quiroga, X.; Walani, N.; Arroyo, M.; Roca-Cusachs, P. The plasma membrane as a mechanochemical transducer. *Philos Trans R Soc B* **2019**, *374* (1779), 20180221.

(369) Drin, G.; Antonny, B. Amphipathic helices and membrane curvature. *FEBS Lett* **2010**, *584* (9), 1840-1847.

(370) Yuan, F.; Lee, C. T.; Sangani, A.; Houser, J. R.; Wang, L.; Lafer, E. M.; Rangamani, P.; Stachowiak, J. C. The ins and outs of membrane bending by intrinsically disordered proteins. *Sci Adv* **2023**, *9* (27), eadg3485.

(371) Takano, K.; Toyooka, K.; Suetsugu, S. EFC/F-BAR proteins and the N-WASP-WIP complex induce membrane curvature-dependent actin polymerization. *EMBO J* **2008**, *27* (21), 2817-2828.

(372) Otsu, N. A threshold selection method from gray-level histograms. *IEEE Trans Syst Man Cyb* **1979**, *SMC-9* (1), 62-66.

(373) Jing, L.; Wang, X.; Leng, B.; Zhan, N.; Liu, H.; Wang, S.; Lu, Y.; Sun, J.; Huang, D. Engineered Nanotopography on the Microfibers of 3D-Printed PCL Scaffolds to Modulate Cellular Responses and Establish an In Vitro Tumor Model. *ACS Appl Bio Mater* **2021**, *4* (2), 1381-1394.

(374) Erdogan, B.; Ao, M.; White, L. M.; Means, A. L.; Brewer, B. M.; Yang, L.; Washington, M. K.; Shi, C.; Franco, O. E.; Weaver, A. M.; Hayward, S. W.; Li, D.; Webb, D. J. Cancer-associated fibroblasts promote directional cancer cell migration by aligning fibronectin. *J Cell Biol* **2017**, *216* (11), 3799-3816.

(375) Andujar, P.; Lacourt, A.; Brochard, P.; Pairon, J. C.; Jaurand, M. C.; Jean, D. Five years update on relationships between malignant pleural mesothelioma and exposure to asbestos and other elongated mineral particles. *J Toxicol Environ Health B Crit Rev* **2016**, *19* (5-6), 151-172.

(376) Mossman, B. T. Mechanistic in vitro studies: What they have told us about carcinogenic properties of elongated mineral particles (EMPs). *Toxicol Appl Pharmacol* **2018**, *361*, 62-67.

(377) Aust, A. E.; Cook, P. M.; Dodson, R. F. Morphological and chemical mechanisms of elongated mineral particle toxicities. *J Toxicol Environ Health B Crit Rev* **2011**, *14* (1-4), 40-75.

(378) Gu, S.; Bull, A.; Perry, J. K.; Huang, A.; Hourwitz, M. J.; Abostate, M.; Fourkas, J. T.; Korchevskiy, A. A.; Wylie, A. G.; Losert, W. Excitable systems: A new perspective on the cellular impact of elongate mineral particles. *Environ Res* **2023**, *230*, 115353.

(379) Mardia, K. V.; Hughes, G.; Taylor, C. C.; Singh, H. A multivariate von mises distribution with applications to bioinformatics. *Canadian Journal of Statistics* **2009**, *36* (1), 99-109.

(380) Naoz, M.; Gov, N. S. Cell-Substrate Patterns Driven by Curvature-Sensitive Actin Polymerization: Waves and Podosomes. *Cells* **2020**, *9* (3), 782.

(381) Yim, E. K.; Darling, E. M.; Kulangara, K.; Guilak, F.; Leong, K. W. Nanotopography-induced changes in focal adhesions, cytoskeletal organization, and mechanical properties of human mesenchymal stem cells. *Biomaterials* **2010**, *31* (6), 1299-1306.

(382) Sun, Y.; Thapa, N.; Hedman, A. C.; Anderson, R. A. Phosphatidylinositol 4,5-bisphosphate: targeted production and signaling. *Bioessays* **2013**, *35* (6), 513-522.

(383) Stokoe, D.; Stephens, L. R.; Copeland, T.; Gaffney, P. R. J.; Reese, C. B.; Painter, G. F.; Holmes, A. B.; McCormick, F.; Hawkins, P. T. Dual role of phosphatidylinositol-3,4,5-trisphosphate in the activation of protein kinase B. *Science* **1997**, *277*, 567-570.

(384) de Winde, C. M.; Munday, C.; Acton, S. E. Molecular mechanisms of dendritic cell migration in immunity and cancer. *Med Microbiol Immunol* **2020**, *209* (4), 515-529.

(385) Bros, M.; Haas, K.; Moll, L.; Grabbe, S. RhoA as a Key Regulator of Innate and Adaptive Immunity. *Cells* **2019**, *8* (7), 733.

(386) Upadhyaya, A. Mechanosensing in the immune response. *Semin Cell Dev Biol* **2017**, *71*, 137-145.

(387) Li, J.; Yin, W.; Jing, Y.; Kang, D.; Yang, L.; Cheng, J.; Yu, Z.; Peng, Z.; Li, X.; Wen, Y.; Sun, X.; Ren, B.; Liu, C. The Coordination Between B Cell Receptor Signaling and the Actin Cytoskeleton During B Cell Activation. *Front Immunol* **2019**, *9*, 3096.

(388) Bhanja, A.; Rey-Suarez, I.; Song, W.; Upadhyaya, A. Bidirectional feedback between BCR signaling and actin cytoskeletal dynamics. *FEBS J* **2022**, *289* (15), 4430-4446.

(389) Hoffman, W.; Lakkis, F. G.; Chalasani, G. B Cells, Antibodies, and More. *Clin J Am Soc Nephrol* **2016**, *11* (1), 137-154.

(390) Mattila, P. K.; Feest, C.; Depoil, D.; Treanor, B.; Montaner, B.; Otipoby, K. L.; Carter, R.; Justement, L. B.; Bruckbauer, A.; Batista, F. D. The actin and tetraspanin networks organize receptor nanoclusters to regulate B cell receptor-mediated signaling. *Immunity* **2013**, *38* (3), 461-474.

(391) Ketchum, C.; Miller, H.; Song, W.; Upadhyaya, A. Ligand mobility regulates B cell receptor clustering and signaling activation. *Biophys J* **2014**, *106* (1), 26-36.

(392) Gold, M. R.; Reth, M. G. Antigen Receptor Function in the Context of the Nanoscale Organization of the B Cell Membrane. *Annu Rev Immunol* **2019**, *37*, 97-123.

(393) Rossi, B.; Espeli, M.; Schiff, C.; Gauthier, L. Clustering of pre-B cell integrins induces galectin-1-dependent pre-B cell receptor relocalization and activation. *J Immunol* **2006**, *177* (2), 796-803.

(394) Akkaya, M.; Traba, J.; Roesler, A. S.; Miozzo, P.; Akkaya, B.; Theall, B. P.; Sohn, H.; Pena, M.; Smelkinson, M.; Kabat, J.; Dahlstrom, E.; Dorward, D. W.; Skinner, J.; Sack, M. N.; Pierce, S. K. Second signals rescue B cells from activation-induced mitochondrial dysfunction and death. *Nat Immunol* **2018**, *19* (8), 871-884.

(395) Scharenberg, A. M.; Humphries, L. A.; Rawlings, D. J. Calcium signalling and cell-fate choice in B cells. *Nat Rev Immunol* **2007**, *7* (10), 778-789.

(396) Mahtani, T.; Treanor, B. Beyond the CRAC: Diversification of ion signaling in B cells. *Immunol Rev* **2019**, *291* (1), 104-122.

(397) Wollman, R.; Meyer, T. Coordinated oscillations in cortical actin and Ca2+ correlate with cycles of vesicle secretion. *Nat Cell Biol* **2012**, *14* (12), 1261-1269.

(398) Koch, U.; Radtke, F. Mechanisms of T cell development and transformation. *Annu Rev Cell Dev Biol* **2011**, *27*, 539-562.

(399) Andersen, M. H.; Schrama, D.; Thor Straten, P.; Becker, J. C. Cytotoxic T cells. *J Invest Dermatol* **2006**, *126* (1), 32-41.

(400) Mackay, I. R.; Rosen, F. S. T-cell function and migration: Two sides of the same coin. *N Engl J Med* **2000**, *343* (14), 1020-1034.

(401) Reiner, S. L. Development in motion: helper T cells at work. *Cell* **2007**, *129* (1), 33-36.

(402) Barry, M.; Bleackley, R. C. Cytotoxic T lymphocytes: all roads lead to death. *Nat Rev Immunol* **2002**, *2* (6), 401-409.

(403) Vignali, D. A.; Collison, L. W.; Workman, C. J. How regulatory T cells work. *Nat Rev Immunol* **2008**, *8* (7), 523-532.

(404) Acuto, O.; Cantrell, D. T cell activation and the cytoskeleton. *Annu Rev Immunol* **2000**, *18*, 165-184.

(405) Smith-Garvin, J. E.; Koretzky, G. A.; Jordan, M. S. T cell activation. *Annu Rev Immunol* **2009**, *27*, 591-619.

(406) Takesono, A.; Heasman, S. J.; Wojciak-Stothard, B.; Garg, R.; Ridley, A. J. Microtubules regulate migratory polarity through Rho/ROCK signaling in T cells. *PLoS One* **2010**, *5* (1), e8774.

(407) Kupfer, A.; Swain, S. L.; Singer, S. J. The specific direct interaction of helper T cells and antigen-presenting B cells: II. Reorientation of the microtubule organizing center and reorganization of the membrane-associated cytoskeleton inside the bound helper T cells. *J Exp Med* **1987**, *165*, 1565-1580.

(408) Wynn, T. A.; Chawla, A.; Pollard, J. W. Macrophage biology in development, homeostasis and disease. *Nature* **2013**, *496* (7446), 445-455.

(409) Murray, P. J. Macrophage Polarization. *Annu Rev Physiol* **2017**, *79*, 541-566.

(410) Borregaard, N. Neutrophils, from marrow to microbes. *Immunity* **2010**, *33* (5), 657-670.

(411) Mayadas, T. N.; Cullere, X.; Lowell, C. A. The multifaceted functions of neutrophils. *Annu Rev Pathol* **2014**, *9*, 181-218.

(412) Nathan, C. Neutrophils and immunity: challenges and opportunities. *Nat Rev Immunol* **2006**, *6* (3), 173-182.

(413) Witko-Sarsat, V.; Rieu, P.; Descamps-Latscha, B.; Lesavre, P.; Halbwachs-Mecarelli, L. Neutrophils: Molecules, functions, and pathophysiological aspects. *Lab Invest* **2000**, *80* (5), 617-653.

(414) Plikus, M. V.; Wang, X.; Sinha, S.; Forte, E.; Thompson, S. M.; Herzog, E. L.; Driskell, R. R.; Rosenthal, N.; Biernaskie, J.; Horsley, V. Fibroblasts: Origins, definitions, and functions in health and disease. *Cell* **2021**, *184* (15), 3852-3872.

(415) Shakiba, D.; Alisafaei, F.; Savadipour, A.; Rowe, R. A.; Liu, Z.; Pryse, K. M.; Shenoy, V. B.; Elson, E. L.; Genin, G. M. The Balance between Actomyosin Contractility and Microtubule Polymerization Regulates Hierarchical Protrusions That Govern Efficient Fibroblast-Collagen Interactions. *ACS Nano* **2020**, *14* (7), 7868-7879.

(416) Buechler, M. B.; Turley, S. J. A short field guide to fibroblast function in immunity. *Semin Immunol* **2018**, *35*, 48-58.

(417) Najafi, M.; Farhood, B.; Mortezaee, K. Extracellular matrix (ECM) stiffness and degradation as cancer drivers. *J Cell Biochem* **2019**, *120* (3), 2782-2790.

(418) Biffi, G.; Tuveson, D. A. Diversity and Biology of Cancer-Associated Fibroblasts. *Physiol Rev* **2021**, *101* (1), 147-176.

(419) Chakravarthy, A.; Khan, L.; Bensler, N. P.; Bose, P.; De Carvalho, D. D. TGF-beta-associated extracellular matrix genes link cancer-associated fibroblasts to immune evasion and immunotherapy failure. *Nat Commun* **2018**, *9* (1), 4692.

(420) Fullár, A.; Dudás, J.; Oláh, L.; Hollósi, P.; Papp, Z.; Sobel, G.; Karászi, K.; Paku, S.; Baghy, K.; Kovalszky, I. Remodeling of extracellular matrix by normal and tumor-associated fibroblasts promotes cervical cancer progression. *BMC Cancer* **2015**, *15*, 256.

(421) Barbazan, J.; Matic Vignjevic, D. Cancer associated fibroblasts: is the force the path to the dark side? *Curr Opin Cell Biol* **2019**, *56*, 71-79.

(422) Erdogan, B.; Webb, D. J. Cancer-associated fibroblasts modulate growth factor signaling and extracellular matrix remodeling to regulate tumor metastasis. *Biochem Soc Trans* **2017**, *45* (1), 229-236.

(423) Boudaoud, A.; Burian, A.; Borowska-Wykret, D.; Uyttewaal, M.; Wrzalik, R.; Kwiatkowska, D.; Hamant, O. FibrilTool, an ImageJ plug-in to quantify fibrillar structures in raw microscopy images. *Nat Protoc* **2014**, *9* (2), 457-463.

(424) Huppa, J. B.; Davis, M. M. T-cell-antigen recognition and the immunological synapse. *Nat Rev Immunol* **2003**, *3* (12), 973-983.

(425) Friedl, P.; den Boer, A. T.; Gunzer, M. Tuning immune responses: diversity and adaptation of the immunological synapse. *Nat Rev Immunol* **2005**, *5* (7), 532-545.

(426) Dustin, M. L. The immunological synapse. *Cancer Immunol Res* **2014**, *2* (11), 1023-1033.

(427) Grakoui, A.; Bromley, S. K.; Sumen, C.; Davis, M. M.; Shaw, A. S.; Allen, P. M.; Dustin, M. L. The immunological synapse: A molecular machine controlling T cell activation. *Science* **1999**, *285* (5425), 221-227.

(428) Aisen, P. Transferrin receptor 1. *Int J Biochem Cell Biol* **2004**, *36* (11), 2137-2143.